

STP 612

thermal fatigue of materials and components

Spera / Mowbray



american society for testing and materials

THERMAL FATIGUE OF MATERIALS AND COMPONENTS

A symposium
sponsored by ASTM
Committee E-9 on Thermal Fatigue of
Materials and Components
AMERICAN SOCIETY FOR
TESTING AND MATERIALS
Philadelphia, Pa., 17-18 Nov. 1975

ASTM SPECIAL TECHNICAL PUBLICATION 612
D. A. Spera, NASA Lewis Research Center, and
D. F. Mowbray, General Electric Co., editors

List price \$27.00
04-612000-30



AMERICAN SOCIETY FOR TESTING AND MATERIALS
1916 Race Street, Philadelphia, Pa. 19103

© by AMERICAN SOCIETY FOR TESTING AND MATERIALS 1976
Library of Congress Catalog Card Number: 76-21535

NOTE

The Society is not responsible, as a body,
for the statements and opinions
advanced in this publication.

Printed in Baltimore, Md.
Nov. 1976

Foreword

The Symposium on Thermal Fatigue of Materials and Components was presented at the meeting held in New Orleans, 17-18 Nov. 1975. The symposium was sponsored by The American Society for Testing and Materials through its Committee E-9 on Fatigue. D. A. Spera, National Aeronautics and Space Administration Lewis Research Center, and D. F. Mowbray, General Electric Co., presided as symposium co-chairmen.

Related ASTM Publications

**Fatigue Crack Growth Under Spectrum Loads, STP 595 (1976), \$34.50
(04-595000-30)**

**Manual on Statistical Planning and Analysis for Fatigue Experiments,
STP 588 (1976), \$15.00 (04-588000-30)**

Handbook on Fatigue Testing, STP 566 (1974), \$17.25 (04-566000-30)

A Note of Appreciation to Reviewers

This publication is made possible by the authors and, also, the unheralded efforts of the reviewers. This body of technical experts whose dedication, sacrifice of time and effort, and collective wisdom in reviewing the papers must be acknowledged. The quality level of ASTM publications is a direct function of their respected opinions. On behalf of ASTM we acknowledge with appreciation their contribution.

ASTM Committee on Publications

Editorial Staff

Jane B. Wheeler, *Managing Editor*
Helen M. Hoersch, *Associate Editor*
Ellen J. McGlinchey, *Assistant Editor*
Kathleen P. Turner, *Assistant Editor*
Sheila G. Pulver, *Editorial Assistant*

Contents

Introduction

What is Thermal Fatigue? —D. A. SPERA	3
Nonlinear Analysis of a Tapered Disk Thermal Fatigue Specimen — D. F. MOWBRAY AND J. E. MCCONNELEE	10
Thermal Stress Concentration Factors in Large Shafts —D. C. GONYEA	30
Low-Cycle Fatigue Analysis of the Turbine Disk for the National Aeronautics and Space Administration High-Temperature Turbine Rig —S. TEPPER	38
Thermal Fatigue and Its Failure Prediction for Brittle Ceramics — D. P. H. HASSELMAN, R. BADALIANCE, AND E. P. CHEN	55
Description of a Computerized Method for Predicting Thermal Fatigue Life of Metals —D. A. SPERA AND E. C. COX	69
A Study of Thermal Fatigue Mechanisms —M. A. H. HOWES	86
Thermal-Stress Fatigue Behavior of Twenty-Six Superalloys — P. T. BIZON AND D. A. SPERA	106
Effect of Microstructure on the Thermal Fatigue Resistance of a Cast Cobalt-Base Alloy, Mar-M509 —C. G. BECK AND A. T. SANTHANAM	123
Some Thermal Fatigue Characteristics of Mild Steel for Heat Exchangers —J. S. LAUB	141
Low-Cycle Thermal Mechanical Fatigue Testing —S. W. HOPKINS	157
Thermal-Mechanical, Low-Cycle Fatigue of AISI 1010 Steel —C. E. JASKE	170
Thermomechanical Fatigue Crack Propagation in an Anisotropic (Directionally Solidified) Nickel-Base Superalloy —A. E. GEMMA, B. S. LANGER, AND G. R. LEVERANT	199
Vacuum Thermal-Mechanical Fatigue Behavior of Two Iron-Base Alloys —K. D. SHEFFLER	214
Instability Effects in Thermal Fatigue —L. F. COFFIN	227
Life Prediction of Thermal-Mechanical Fatigue Using Strainrange Partitioning —G. R. HALFORD AND S. S. MANSON	239
Summary	255
Index	260

Introduction

Most low-cycle fatigue problems in high-temperature machinery involve thermal as well as mechanical loadings. By thermal loadings it is meant that the material is subjected to cyclic temperature simultaneous with the cyclic stress. Analysis of these loadings and consideration of the attendant fatigue damage becomes very complex and often gross simplifications are introduced. Usually this involves the use of isothermal data and life prediction techniques evolved from isothermal testing. In fact, fatigue studies in the laboratory have generally bypassed real thermal fatigue loadings in favor of easier isothermal testing.

It would appear that recent rapid advances in analysis methods (for example, finite element computer programs) and testing equipment (for example, servohydraulic test systems) obviate some of the reasons for resorting to isothermal fatigue in the analysis of thermal fatigue problems. Indeed, there is now increased emphasis on studying thermal fatigue. In light of these developments, a symposium on the topic of thermal fatigue seemed both appropriate and timely. ASTM Committee E-9 on Fatigue through its Subcommittee E09.08 on Fatigue Under Cyclic Strain undertook the symposium organization in hope that it would serve as a review of the current state of the art in thermal fatigue.

The symposium, as it has developed, focuses on four important aspects of thermal fatigue: (a) stress and deformation analysis; (b) life prediction techniques; (c) materials behavior; and (d) thermal-mechanical testing. The papers on stress analysis span the domain of complexity from strictly elastic to elastic-plastic-creep analysis. Life prediction techniques include applications of the creep damage and strain range partitioning approaches to thermal fatigue analysis. Papers on material behavior studies span the range of materials from the most common structural material, low-carbon steel, to advanced superalloys and ceramics. A number of papers deal with the subject of thermal-mechanical fatigue test systems. These systems allow one to study thermal fatigue with control not possible just a few years ago. As a result, we can expect to see considerable emphasis on this topic in the future. The present papers describe the equipment and testing procedures developed and demonstrate valuable data. In addition to the technical papers, the first paper in the volume (the opening address) gives a very interesting historical sketch of the development of thermal fatigue testing and analysis.

The results of the symposium as presented in this volume should be

2 THERMAL FATIGUE OF MATERIALS AND COMPONENTS

of use to several groups within the scientific community, most notably to the mechanical design engineer contending with the analysis of thermal fatigue problems, the materials engineer faced with selecting the proper materials to resist thermal fatigue loadings, and the laboratory test engineer who is establishing facilities for conducting thermal fatigue tests. It is our belief that the results presented in this volume will also serve as a stimulus for future meetings on the topic of thermal fatigue.

D. F. Mowbray

Mechanics of Materials Unit, Materials and Processes Laboratory, General Electric Company, Schenectady, N.Y.; symposium cochairman and also coeditor of this publication.

D. A. Spera¹

What is Thermal Fatigue?

REFERENCE: Spera, D. A., "What is Thermal Fatigue?" *Thermal Fatigue of Materials and Components, ASTM STP 612*, D. A. Spera and D. F. Mowbray, Eds., American Society for Testing and Materials, 1976, pp. 3-9.

ABSTRACT: Definitions are suggested for terms such as thermal fatigue, thermal-mechanical fatigue, and thermal-stress fatigue. Historical developments in the field of thermal fatigue from 1838 to the present are reviewed. It is hypothesized that we have advanced from qualitative to quantitative understanding of the thermal fatigue process and can now make life predictions with factor-of-two reliability for conventional metals.

KEY WORDS: thermal fatigue, fatigue (materials), definitions, fatigue life

The purpose of the symposium which produced this volume was to exchange ideas on methods for determining and improving the resistance of materials and mechanical components to that combination of failure mechanisms which we know as thermal fatigue. To various people at various times, thermal fatigue is also known as thermal stress fatigue, thermal strain fatigue, creep fatigue, thermal cracking, thermal shock, thermal rupture, thermal endurance, low-cycle thermal fatigue, heat checking, craze cracking, fire cracking, and just plain high-temperature fatigue. Considering this assortment of names, it is appropriate for us to discuss the terminology we will need in order to communicate effectively with one another on this complicated subject.

First, a few simple definitions will be suggested which may be useful, particularly to those who have had little contact with the study of thermal fatigue. If these definitions help us, we may wish to continue using them. If not, let us try to improve them. I believe they are relevant to present studies of thermal fatigue phenomena. And what is just as important, they contain a certain measure of respect for the historical development of our field. After giving the definitions, I will briefly review the development of terms during the past 137 years of our technical history.

¹ Consultant, Fatigue Branch, Lewis Research Center, Cleveland, Ohio 44135.

Suggested Definitions

First, let me suggest this definition for thermal fatigue: "Thermal fatigue is the gradual deterioration and eventual cracking of a material by alternate heating and cooling during which free thermal expansion is partially or completely constrained." Constraint of thermal expansion causes thermal stresses which may eventually initiate and propagate fatigue cracks. Thermal fatigue may be classified under the more general heading of low-cycle fatigue, because thermal fatigue cracks usually start in less than 50 000 cycles. In addition, a thermal fatigue cycle usually contains significant inelastic strain. Thus, I suggest we start defining our terms by dividing the subject of low-cycle fatigue into two branches, defining one as "thermal fatigue" if the temperature is not constant with time, and the other as "isothermal fatigue" if it is. As an example, thermal fatigue might result from the starting and stopping of a piece of high-temperature equipment, while isothermal fatigue might be the consequence of vibration during steady-state operation.

Constraint of free thermal expansion and contraction is a necessary ingredient in the thermal fatigue process. For convenience, constraints may be grouped into two general categories: external and internal. External constraints are those provided by boundary forces applied to the surfaces of the body which is being heated and cooled. This type of constraint is more typical of specimen testing than it is of components in service. Designers of high-temperature equipment usually take considerable care to provide for overall thermal expansion and contraction through the use of clearances, sliding supports, bellows, and other mechanical devices. Thus, thermal fatigue with external constraint is primarily a laboratory testing practice in which external forces on a test specimen are used to simulate internal thermal stresses in an actual component.

In a typical thermal fatigue test with external constraint, a uniaxial specimen—usually tubular or hourglass in shape—is heated and cooled uniformly across its test section while constraining forces are applied through end grips. This test technique is referred to as "thermal-mechanical fatigue testing." End constraints may be as simple as a semirigid frame which only allows the specimen to lengthen and shorten in accordance with the elastic compliance of the frame. This simple device is often called a Coffin-type thermal fatigue apparatus, after its developer, Dr. L. F. Coffin, Jr., [1].² Today, the simple constraining frame has given way to the modern servocontrolled fatigue machine in which temperature and strain cycles may be applied independently according to predetermined programs. Whether the apparatus is simple or complex, thermal-mechanical fatigue is always characterized by external constraint

² The italic numbers in brackets refer to the list of references appended to this paper.

forces. Therefore, let me suggest this second definition: "Thermal-mechanical fatigue is thermal fatigue in which constraints on thermal expansion are external."

The second general category of thermal fatigue failures are those with internal constraints. Internal constraints on the expansion and contraction of an element of material are provided by adjacent material elements which are either at a different temperature or are made of a different material (for example, fiber-reinforced composites), or both. Internal constraints are typical of high-temperature machine components which are subjected to rapid heating and cooling, usually by some type of working fluid. Large thermal gradients may be produced in these components which will, in turn, produce self-equilibrating thermal stresses. In the laboratory, relatively high rates of surface heating and cooling are usually necessary to reproduce these internal constraints. Specimens are often shaped to simulate a significant feature of the component being studied and to accentuate thermal gradients. For example, thermal fatigue cracking of the leading edge of a gas-turbine blade may be simulated in the laboratory by a wedge specimen flame-heated along its apex edge. Often, the component is tested directly, since it provides its own internal constraints. Because self-equilibrating thermal stresses are characteristic of thermal fatigue with internal constraints, we may add this third definition: "Thermal-stress fatigue is thermal fatigue in which constraints on thermal expansion are internal."

Figure 1 is a summary of the suggested terminology. We may divide the general field of low-cycle fatigue into thermal and isothermal categories, depending on whether temperature is cyclic or constant, respectively. The

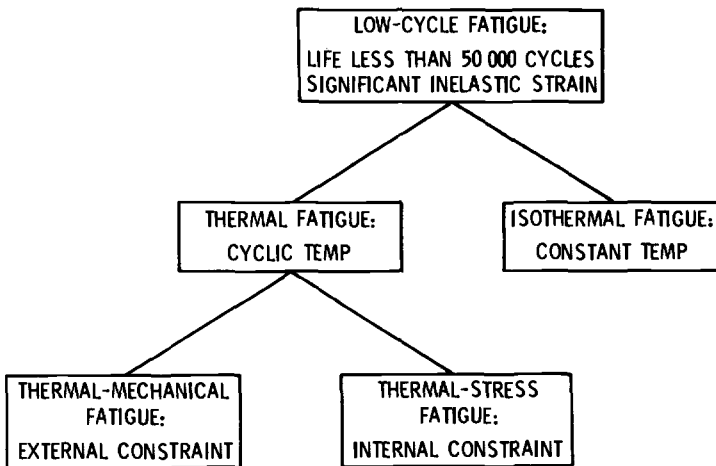


FIG. 1—Proposed terminology for high temperature fatigue.

thermal fatigue category may then be subdivided into thermal-mechanical fatigue and thermal-stress fatigue, depending on whether constraints are external or internal, respectively.

Historical Review

Having suggested some definitions, let us briefly review the development of the field of thermal fatigue and the origin of some of the terms just defined. Much of the information which follows was taken from a 1956 literature survey prepared by Harry Majors, Jr., of the University of Alabama [2]. The study of material failure as a result of thermal cycling goes back to 1838, at least. In that year, Duhamel published the first equations for calculating the thermal stresses in a body subjected to non-uniform heating [3]. However, it was not until 1894 that fracture was combined with thermal stress in a quantitative way. This was done in Germany by Winkelmann and Schott who studied what we now call thermal shock of ceramic materials, using only rapid heating [4]. Eight years later, Hovestadt and Everhart of the United States published an analysis for thermal shock of glass through rapid cooling [5]. And that was the trend of the thermal stress failure literature for the next 30 or more years: thermal shock of materials by either rapid heating alone or rapid cooling alone. Most—but not all—of the materials studied were ceramics and glass. The earliest reported study of the thermal shock behavior of ductile metals was probably that by Bollenrath and co-workers in 1938, again in Germany [6].

It was not until 1935, almost a century after Duhamel's publication on thermal stress, that alternate heating and cooling were discussed in the literature as a cause of cyclic thermal strains. This discussion appeared in a text on plasticity in crystals, written by Erich Schmid and Walter Boas [7]. These authors noted that, when a noncubic crystal is alternately heated and cooled, it gradually increases in size, provided no phase changes take place. Theoretically, a high-temperature component made of such an anisotropic material would produce within itself ever-increasing thermal stresses and eventual cracking. And this cracking would occur even if the component were heated and cooled slowly, without temperature gradients and without external constraints. Nine years later, Boas and a co-worker by the name of R. W. Honeycombe showed that this was indeed the case for bearings made from a particular tin alloy. Their paper, published in 1944, was given the rather liberal title of "Thermal Fatigue of Metals" [8]. This was probably the first time this phrase appeared in the literature.

As we have seen, then, the original definition of thermal fatigue, credited to Walter Boas in 1944, was very restrictive. It applied only to failure in a noncubic lattice material slowly heated and cooled without

any external constraint. During the next decade, this limited definition would be gradually expanded because engineers had a need for a term to describe high-temperature material failures that were cyclic in nature.

We can guess that it was difficult at first to combine two concepts that had developed separately: the concept of thermal stress and the concept of fatigue failure. As an example, let me quote from an old report from the archives of my laboratory at the Lewis Research Center of the National Aeronautics and Space Administration. At the time this report was written in 1947, our laboratory was called the Aircraft Engine Research Laboratory of the National Advisory Committee for Aeronautics (NACA). The title of this report is "Investigation of Rim Cracking in Turbine Wheels with Welded Blades," and the principal author was Morton Millenson. To explain the cause of cracking in certain gas turbine disks, Millenson pointed to cyclic plastic strains, as follows: "Subsequent cycles of starting and stopping will cause alternate compressive and tensile flow and progressively weaken the material until cracking occurs in a manner somewhat similar to the fatigue of metals . . ." I can guess that Millenson's coauthor would have used a more definite phrase than "somewhat similar to the fatigue of metals" had it been solely up to him. The coauthor of this 1947 report [9] was a young man by the name of S. S. Manson. It would not be long before Manson conceived and directed fatigue research programs at our laboratory and established an international reputation in the field of high-temperature material behavior.

The terminology was changing and developing, however, as it always does to fill needs. The earliest mention of thermal fatigue in our files at the Lewis Research Center was in 1949, when John Weeton, a colleague of Millenson and Manson, used the term to describe one of the failure mechanisms he observed in combustor liners for gas turbines [10]. In 1950, the term thermal cracking was used by Harry Wetenkamp and his co-workers at the University of Illinois in their study of the failure of railway car wheels caused by the heating action of brakes [11]. In 1952, Helmut Thielsch wrote a survey article for the Welding Research Council on the subjects of thermal fatigue and thermal shock [12]. Later that same year, in a lecture delivered at the University of Michigan, Manson spoke on the behavior of materials under conditions of thermal stress [13]. He stated that thermal shock is the failure of a material after a single cycle of thermal stress while thermal fatigue requires repeated thermal stress cycles.

Today, that lecture at Michigan is remembered, not for the thermal stress information it contained, but for Manson's proposal that low-cycle fatigue life depends primarily on the imposed range of inelastic strain. He suggested a power law which is known throughout the world today as the Manson-Coffin equation.

I mentioned Coffin earlier as the inventor of an apparatus for thermal-mechanical fatigue testing. Using this apparatus to conduct a broad series of fatigue tests, he also obtained a power-law relationship between inelastic strain range and cycles to failure, and he did so simultaneously with and independently of Manson's work. His two landmark papers on the effects of thermal stress on ductile metals were presented in 1953 [1, 14]. They have served as basic references for just about every paper on thermal fatigue written in the last 20 years. I decided to reread these two pioneering papers to see how Coffin defined and used the term thermal fatigue. To my surprise, in an estimated 25 000 words of text, the phrase "thermal fatigue" never appears once! I asked Coffin about this, and he was just as surprised as I was, not at the absence of any reference to thermal fatigue, however, but at the fact that he had written 25 000 words on the subject!

Whatever his reasons for not mentioning thermal fatigue in 1953, Coffin introduced the term "thermal stress fatigue" in 1954. The occasion was an American Society for Testing and Materials' symposium on the effect of cyclic heating and stressing on metals, which was the predecessor of the symposium which produced this volume. In Coffin's paper [15], the two terms "thermal stress" and "fatigue" were finally wedded, 116 years after Duhamel's original publication.

To summarize the next ten years, let me quote from an excellent British text on thermal stress, edited in 1964 by P. P. Benham and Russell Hoyle of the Imperial College of Science and Technology. There is a chapter in this book on the subjects of thermal fatigue and thermal shock, written by H. G. Baron of the Royal Armament Research and Development Establishment [16]. Baron ends this chapter with the following observation: "The subject of thermal fatigue has advanced in the last decade (that is, from 1954 to 1964) from a position of almost total obscurity to one in which many of the controlling factors are qualitatively understood, and in which order-of-magnitude estimates can sometimes be made of the number of thermal cycles which will produce cracks."

This, then, was the situation as of 1964, as seen by a specialist in our field: qualitative understanding, sometimes leading to order-of-magnitude life estimates.

Conclusions

Now another decade has passed, the second since Manson and Coffin introduced life analysis to thermal fatigue. To conclude, let me offer the following hypothesis. In this second decade, we have advanced from qualitative to quantitative understanding, and from order-of-magnitude life estimates to factor-of-two life predictions, at least for conventional

metals. This is an optimistic—but I think realistic—hypothesis which requires further evaluation.

References

- [1] Coffin, L. F., Jr. and Wesley, R. P., *Transactions, American Society of Mechanical Engineers*, Vol. 76, Aug. 1954, pp. 923–930.
- [2] Majors, H., Jr., "Thermal Shock and Fatigue—A Literature Survey," Technical Report No. 1, Office of Ordnance Research Project No. 1230, Sept. 1956.
- [3] Duhamel, J. M. C. in *Memoires de l'Institut de France*, Vol. 5, 1838, p. 440.
- [4] Winklemann, A. and Schott, O., *Annalen der Physikalischen Chemie*, Vol. 51, 1894, p. 730.
- [5] Hovestadt, H. and Everhart, J. D. in *Jena Glass*, Macmillan, New York, 1902, p. 228.
- [6] Bollenrath, F., Cornelius, H., and Bungardt, W., *Jahrbuch der Deutschen Luftfahrtforschung*, 1938, Vol. II, pp. 326–338.
- [7] Schmid, E. and Boas, W. in *Kristallplastizitaet*, Verlag Julius Springer, Berlin, 1935, p. 202.
- [8] Boas, W. and Honeycombe, R. W. K., *Nature*, Vol. 153, April 1944, pp. 494–495.
- [9] Millenson, M. B. and Manson, S. S., "Investigation of Rim Cracking in Turbine Wheels with Welded Blades," NACA RM E6L 17, National Advisory Committee for Aeronautics, Feb. 1947.
- [10] Weeton, J. W., "Mechanisms of Failure of High Nickel-Alloy Turbojet Combustion Liners," NACA TN 1938, National Advisory Committee for Aeronautics, Oct. 1949.
- [11] Wetenkamp, H. R., Sidebottom, O. M., and Schrader, H. J., "The Effect of Brake Shoe Action on Thermal Cracking and on Failure of Wrought Steel Railway Car Wheels," Bulletin 387, Engineering Experiment Station, University of Illinois, Urbana, Vol. 47, No. 77, June 1950.
- [12] Thielsch, H., "Thermal Fatigue and Thermal Shock," Welding Research Council Bulletin, Series No. 10, April 1952.
- [13] Manson, S. S., "Behavior of Materials Under Conditions of Thermal Stress," NACA TN-2933, National Advisory Committee for Aeronautics, July 1953.
- [14] Coffin, L. F., Jr., *Transactions, American Society of Mechanical Engineers*, Vol. 76, Aug. 1954, pp. 931–950.
- [15] Coffin, L. F., Jr. in *Symposium on Effect of Cyclic Heating and Stressing on Metals at Elevated Temperatures, ASTM STP 165*, American Society for Testing Materials, June 1954, pp. 31–52.
- [16] Baron, H. G. in *Thermal Stress*, P. P. Benham and R. Hoyle, Eds., Pitman and Sons, London, 1964, p. 204.

*D. F. Mowbray*¹ and *J. E. McConnelee*¹

Nonlinear Analysis of a Tapered Disk Thermal Fatigue Specimen

REFERENCE: Mowbray, D. F. and McConnelee, J. E., "Nonlinear Analysis of a Tapered Disk Thermal Fatigue Specimen," *Thermal Fatigue of Materials and Components, ASTM STP 612*, D. A. Spera and D. F. Mowbray, Eds., American Society for Testing and Materials, 1976, pp. 10-29.

ABSTRACT: Calculations of the stress-strain response of a common tapered disk thermal fatigue specimen are presented. The calculations were made by complete nonlinear finite element solution and by a simpler method employing the elastic strain-invariance principle. The results are used to show the effect of several common test variables on the resulting stress-strain response, to assess the effect of various material behavior and structural analysis assumptions on the stress-strain response, and to explore the application of several high-temperature fatigue damage prediction methods to transient thermal fatigue loading.

KEY WORDS: thermal fatigue, fatigue (materials), disks, thermal analysis, stress analysis

A common testing approach for generating thermal fatigue data under transient thermal conditions incorporates the combination of tapered disk specimens and fluidized baths [1,2].² The specimens are subjected to alternate heating and cooling shocks by immersion in the fluidized baths at differing temperatures. Results from this type of test have close applicability to turbine thermal fatigue problems because the strain-time-temperature history produced in the specimens is similar to those existing in turbine parts such as blades and stator vanes. Unfortunately, direct measurement of stress or strain or both are not possible so that results obtained from such tests cannot be expressed in a quantitative manner. Quantification requires highly complex analysis when temperature and loading conditions induce nonlinear deformations. The analysis must consider the non-uniform, three-dimensional geometry in the thermal and stress analysis,

¹ Manager, Mechanics of Materials Unit, and Manager, Component Analysis and Test Unit, respectively, Materials and Processes Laboratory, General Electric Co., Schenectady, N. Y. 12345.

² The italic numbers in brackets refer to the list of references appended to this paper.

factor in material property variations with temperature, and account for the accumulation of time independent and time-dependent nonlinear deformations.

Considerable work has been completed in the past on the analysis of the tapered disk test [3-5]. However, many approximations were used in the structural analysis method and material behavior representation. The present paper offers some expansion on and refinements of these past efforts. The finite element (FE) method was employed to improve the accuracy of heat transfer and stress analyses. Sensitivity studies were conducted to determine the effect of several different material behavior assumptions on the results.

Two analysis methods were utilized. They differ in the degree of approximation made and information obtained. One was based on an approach utilizing linear axisymmetric finite element stress analysis to determine the total strain history of the peripheral fiber. The nonlinear strain components and stress of this fiber were found by treating it as a uniaxial bar subjected to the calculated strain history. The second method involved use of an axisymmetric FE computer program with capability for treating nonlinear, time-dependent material behavior. This method generated a complete stress-strain solution. However, it was very costly in terms of computation time so that the former, simpler approach was utilized in the bulk of the analysis. In the subsequent discussion, the simpler approach will be referred to as the uniaxial, elastic strain invariance (UESI) method and the complete finite element solution as the axisymmetric, FE method.

The results of the analyses are used to

- (a) show the effects of several common test variables on the resulting stress-strain response,
- (b) assess the effect of various material behavior and structural analysis assumptions on the resulting stress-strain response, and
- (c) explore the application of several high temperature fatigue damage prediction methods to transient thermal fatigue loading.

Tapered Disk Specimen and Test

The tapered disk specimen is shown in Fig. 1. The overall diameter and center thickness are 1.5 times the original dimensions employed by Glennly et al [1]. The fourfold variation in peripheral radius (R_p) was incorporated in the test as a means of achieving a variation in cyclic strain range for fixed minimum and maximum cycle temperatures.

In the testing, the disk specimens are subjected to alternate heating and cooling shocks by transferring them between hot and cold fluidized baths of aluminum oxide sand. In the tests analyzed herein, the minimum temperature (T_{\min}) was always held at 70°F for an exposure time (t_e) of 4 min.

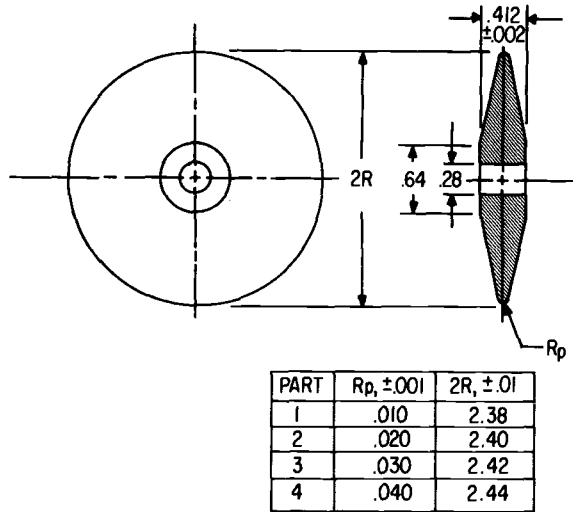


FIG. 1—Tapered disk thermal fatigue specimen.

The hot bath or maximum temperature (T_{\max}) was varied between 1500 and 1900°F, with exposure times (t_h) of 1 or 4 min.

The test material analyzed is the cast cobalt-base superalloy, FSX414. This alloy has been described in Ref 6. Table 1 gives a summary of static properties over the temperature range of interest.

TABLE 1—Mechanical properties for FSX-414.

Temperature °F	Tensile			Rupture		
	Tensile Strength, ksi	0.2% Yield Strength, ksi	Reduction of Area, %	σ , ksi	t_R , h	Reduction of Area, %
80	106	60	18
800	86	41	18
1000	79	36	19
1200	74	33	21
1400	65	31	23	21.0	2150	39
1600	45	30	28	10.0	1150	12
1800	4.5	1870	4

Analysis Methods

Both analysis methods started with the transient temperature fields determined by FE computation. Temperature-dependent values of thermal

conductivity and specific heat were utilized, and the heating and cooling shocks were simulated by applying time-independent values of convective heat transfer coefficient on all exterior surfaces. The brief transfer time from the hot to cold bath was included by specifying a convective heat transfer coefficient corresponding to still air during the first 3.5 s of the cooling shock. The thermal properties employed are given in Table 2. (The heat transfer coefficients are those measured in the baths.) Axisym-

TABLE 2—*Thermal and physical properties for FSX 414.*

Temperature, °F	Thermal Conductivity, Btu/ft ² /in./h/°F	Coefficient of Expansion × 10 ⁶	Elastic Modulus, 10 ⁶ psi
200	85	7.2	27.4
400	101	7.55	26.4
600	116	7.9	25.3
800	129	8.25	24.3
1000	142	8.55	23.1
1200	154	8.75	22.0
1400	165	9.05	20.7
1600	176	9.3	19.4
1800	187	9.5	17.8
Convective heat transfer coefficients, Btu/°F in. ² h			
1. Hot bath, ≤1688°F	0.80		
2. Hot bath, >1688°F	1.04		
3. Cold bath	0.80		
4. Still air	0.08		
Specific heat, Btu/lb-mass °F	0.12		
Density lb-mass/in. ³	0.312		

metry in the temperature and stress fields was assumed. An example FE grid is shown in Fig. 2. The elements employed are of the constant stress type.

Comparisons of calculated time-temperature response and thermocouple measurements at several locations within a disk are shown in Fig. 3. In general, these comparisons show a good correspondence between calculations and measurement.

In the initial seconds of each shock, the maximum temperature change develops at the disk periphery so that the maximum strains also develop at this location. The difference between the peripheral (T_e) and volume average temperature (T_{avg}) is proportional to the peripheral strain. Example plots of this difference as a function of time are shown in Fig. 4. Maxima are reached in 5 to 15 s and complete dissipation of the gradient in 1 to 2 min.

The heat transfer and stress analysis programs used are all compatible so that the same finite element models were used in all analyses, with one

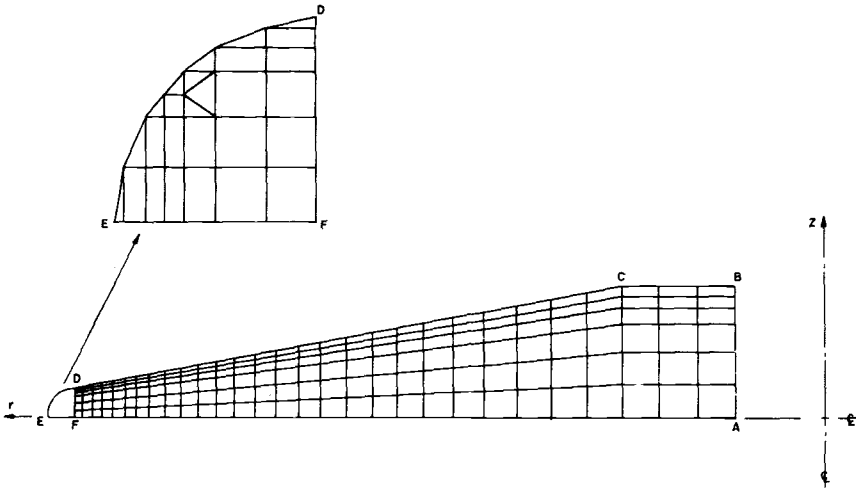


FIG. 2—Example finite element grid ($R_p = 0.04$ in.).

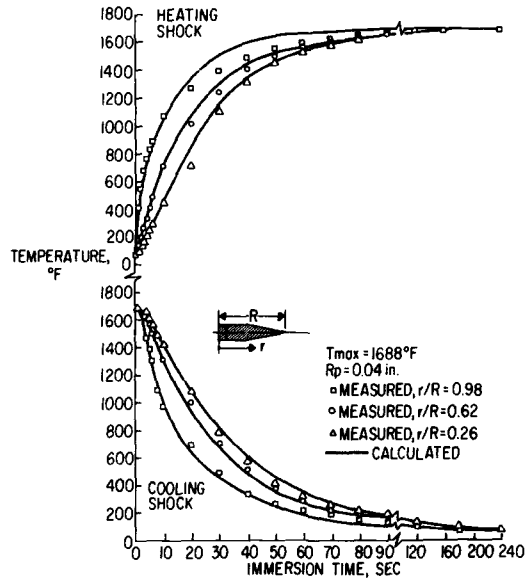


FIG. 3—Comparison of measured and calculated time-temperature response of a disk specimen.

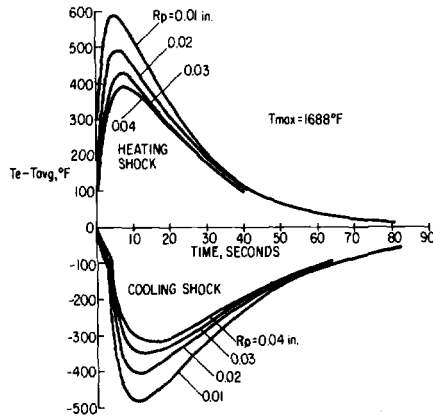


FIG. 4—Calculated time-temperature curves for disk specimens.

exception. The exception was involved with the nonlinear FE analysis. In order to reduce cost for this case, a simpler model was employed after preliminary comparisons with results from the full model demonstrated the adequacy of the reduced model.

Before proceeding with specific descriptions of the two analysis methods, two assumptions about material behavior required in both analysis methods will be discussed. One is concerned with the Bauschinger effect and the second with a method for stress transfer in creep analysis. Figure 5 illustrates schematically the nature of the assumptions involved.

With regard to the Bauschinger effect, the stress level at which reversed plastic flow commences must be specified if strain hardening is included in the analysis. Three common assumptions are illustrated by Points *a*, *b*, and *c* in Fig. 5a [7]. Point *a* corresponds to a kinematic theory, Point *c* to the isotropic theory, and Point *b* implies yielding in tension and compression to be independent of each other.

The kinematic theory allows for the characteristic in cyclic plasticity of a translating yield surface, whereas the other two theories do not. Despite this feature, a recent investigation [8] has shown the isotropic theory to be better able to predict subsequent yielding behavior. Observation of the data examined in Ref 8 indicates that the independent tension and yield theory will provide better predictions than the kinematic or isotropic theories.

All three assumptions were explored in the current calculations with the UESI method. Differences in results were not large so that, for computing convenience, the bulk of the computations were carried out using the independent tension and compression yield assumption (Point *b* in Fig. 5a).

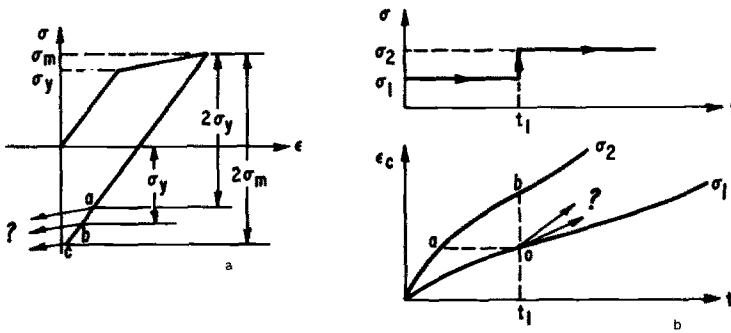


FIG. 5—Schematic illustrations of material behavior considerations in nonlinear, cyclic temperature analysis: (a) Bauschinger effect and (b) stress transfer in creep analysis.

The FE analysis method employed the isotropic hardening assumption only.

In both analysis methods, creep strain was specified in the form of the hyperbolic sine law

$$\epsilon_c = 2At^{1/2} \sinh G\sigma \tag{1}$$

where A and G are functions of temperature, evaluated by means of non-linear regression analysis of available creep data. For the FSX414 alloy, the following specific functional forms were found to provide a good fit to available data

$$\begin{aligned} A &= P - Q/(T + 460) \\ G &= 1/(U - VT) \end{aligned} \tag{2}$$

where P , Q , U , and V are regression parameters.

The creep relationship being nonlinear requires that one specify a rule for determining creep rate after a change of stress level occurs. Two commonly employed assumptions in the treatment of this problem are called the strain hardening and time hardening rules. These are indicated in Fig. 5b by Lines oa and ob , respectively. The strain hardening rule is generally thought to be the most accurate and the most physically acceptable [9]. It was therefore used in the present analyses. Time hardening was utilized in selected examples, and the difference in results will be shown.

UESI Method

In this method, the total strain-time-temperature histories were ob-

tained by elastic analysis using the elastic strain-invariance principle [10]. The said principle assumes that strains computed by elastic analysis are the correct total strains, even though the stresses are affected by plastic flow. This principle is known to yield accurate predictions of total strain for purely thermal axisymmetric loading such as in the disk test.

Total strain solutions were obtained by elastic FE analysis at various times in the temperature transients. The temperature-dependent values of elastic modulus and coefficient of thermal expansion used in the analyses are listed in Table 2.

The nonlinear part of the analysis treated the peripheral fiber as a uniaxial bar subject to prescribed strain-time-temperature histories. It is noted that similar reasoning is employed with success in fatigue notch analysis [11]. A typical example of the cycle experienced by the disk periphery is shown in Fig. 6 where strain is plotted against temperature, with time indicated by crosshatching.

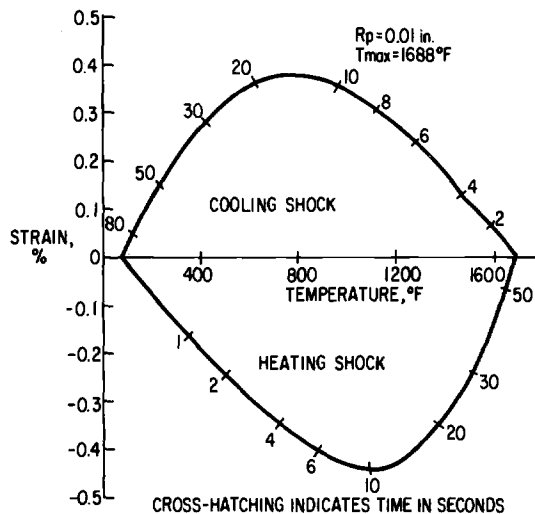


FIG. 6—Example strain-temperature cycle for peripheral fiber.

The method of solution was patterned after that given by Spera [4]. Total strain is considered to be the sum of three components; that is

$$\epsilon_t = \epsilon_e + \epsilon_p + \epsilon_c \quad (3)$$

where

- ϵ_t = instantaneous total strain,
- ϵ_e = elastic component,

ϵ_p = time independent plastic component, and
 ϵ_c = time-dependent plastic or creep component.

The instantaneous stress, σ , can be specified as a function of the elastic strain via the elastic modulus (E); that is

$$\sigma = E\epsilon_e \quad (4)$$

Since ϵ_e and E are specified as a function of time, the problem is to determine the instantaneous values of σ , ϵ_p and ϵ_c .

For solution of Eq 3, ϵ_p and ϵ_c were expressed as functions of σ . The time-independent plastic strains (ϵ_p) were determined from the temperature dependent stress-strain curves shown in Fig. 7. In the solution technique, the curves were represented by a series of six stress-strain data

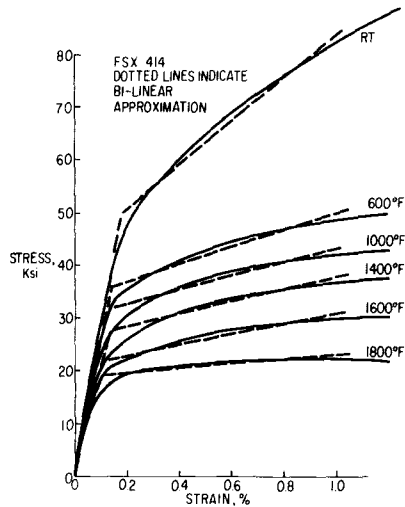


FIG. 7—Stress-strain curves.

points connected by linear lines; curves for intermediate temperatures were defined by linear interpolation. Transfer from one stress-strain curve to another (or one temperature to another) was at constant total strain. Hence, in functional form

$$\epsilon_p = f(\sigma, \epsilon_t, T) \quad (5)$$

As discussed earlier, creep strain was specified in the form of Eq 1.

Since both ϵ_p and ϵ_c are nonlinear functions of stress, a numerical solu-

tion technique was applied. Following Spera's [4] lead, the method of Runge and Kutta [12] was utilized to set up a time incremental calculation procedure.

Axisymmetric FE Method

The finite element computer program used in this analysis is based on incremental plasticity theory and the von Mises yield condition and associated flow rule. Although capable of treating combined isotropic and kinematic hardening, the present analysis was restricted to purely isotropic hardening. The same creep relationships were used as with the UESI method. Creep stress transfer was assumed in accordance with the strain hardening rule. The program is currently restricted to the use of bilinear stress-strain relationships. The bilinear approximations employed in the analysis are indicated by dotted lines in Fig. 7.

As discussed earlier, the finite element model used in the stress-strain calculations was a very much simplified model with only 16 elements and 33 node points. This simplification was used to reduce the cost of the inelastic analysis after preliminary comparisons with results from the complete FE model indicated that this reduced model was adequate to accurately calculate the stress-strain response at the periphery of the disk.

Results and Discussion

The shape of the calculated hysteretic loops were found to be relatively insensitive to analysis method, material behavior assumptions and test conditions. Figure 8 shows an example of a calculated loop in which the UESI method was employed. Temperatures achieved at different locations are indicated by the crosshatching. It is instructive to trace through this loop to gain a feeling for the complexities involved in transient thermal fatigue. Starting at Point *O*, the initial heating shock drives the peripheral material into compression along Path *OA*. At Point *A*, the stress has achieved the proportional limit, and time-independent plastic flow commences. The stress level does not become increasingly negative beyond this point because the proportional limit stresses are decreasing rapidly with the increasing temperature.

Point *B* is the maximum negative strain developed in the heating shock, and thereafter the strain and stress increase. The initial stress increase is elastic. At some Point *B'*, prior to achieving positive stress values, creep commences. Because the temperature is increasing along with the stress, the creep becomes increasingly prominent, and the rise in stress slows down due to concomitant stress relaxation. At some Point *C*, the thermal strain available for increased stress is outweighed by the creep induced relaxation, and the stress decreases in magnitude again. For this example,

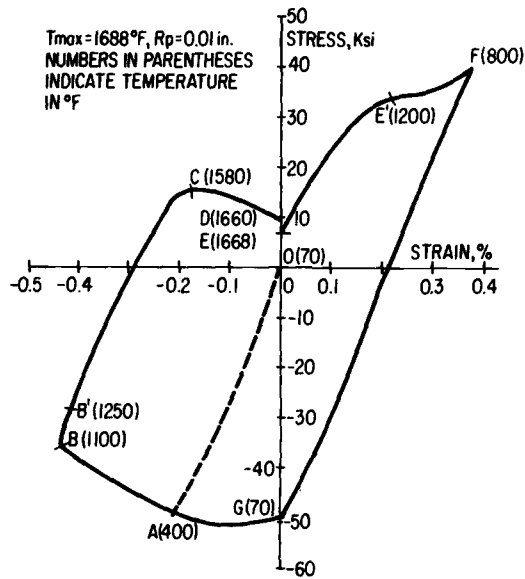
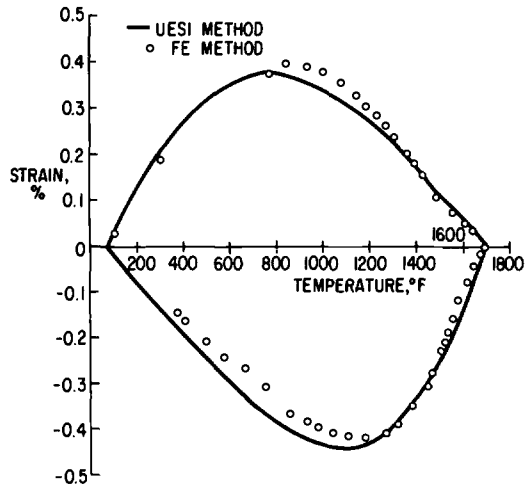


FIG. 8—Calculated hysteretic loop for peripheral fiber.

the stress continues to relax to Point *E* after the strain achieves a zero value (Point *D*).

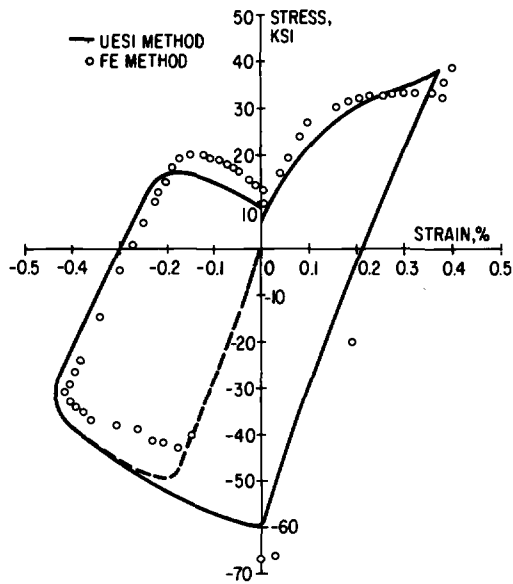
The cooling shock introduces tensile strain and initially increasing tensile stress. Since the cooling shock starts at a high temperature and the stress is increasing, creep occurs initially in the cooling shock. At some point, designated *E'* in Fig. 8, the temperature dips below where creep and stress relaxation will occur. The stress and strain continue to increase to Point *F*, which is the maximum positive strain generated by the cooling shock. The peculiar curvature obtained in loading from Points *E* to *F* is a result of the initial stress relaxation and rapid increases in the flow stress with the decreasing temperature. At Point *F*, the strain begins to decrease, and the fiber unloads elastically. The unloading extends into the compressive stress region to the zero strain position, Point *G*. Close to the zero strain point, compressive plastic flow initiates. Upon reintroduction of the heating shock, time-independent plastic flow continues to the minimum strain position (Point *B*).

A solution from the FE method was obtained for the test conditions discussed in Figs. 6 and 8. This result is compared with the corresponding UESI method solution in Fig. 9. Figure 9*a* shows strain-temperature histories, and Fig. 9*b*, hysteretic loops. For consistent comparison, the hysteretic loop calculated by the UESI method employed isotropic hardening and the bilinear stress-strain curves.



(a) Strain-temperature cycles.

FIG. 9—Comparisons of calculated results using the UESI and FE methods of analysis.



(b) Hysteretic loops.
FIG. 9—Continued.

Examining first the peripheral fiber strain-temperature behavior (Fig. 9a), it can be observed that the two calculational methods predict nearly identical histories. The maximum difference in strain at a given temperature is about 10 percent, with the more rigorous of the solutions indicating more positive magnitudes. This result would appear to justify the assumption of elastic-strain invariance for this problem.

Differences in the calculated hysteretic loops (Fig. 9b) result mainly from the slightly different strain-temperature histories; that is, the FE method calculated loop is of the same proportions but translated in the positive strain direction. Also, the total inelastic strain calculated is nearly equal, with, however, less of it in creep strain for the FE method. The latter shows up as higher stresses in the negative strain region and appears to result from the slightly lower total compressive strain amplitude. In conclusion, it can be stated that treatment of the peripheral fiber as a uniaxial member is a good approximation.

This comparison indicates that the two calculational methods predict the same behavioral trends. In most temperature regions, identical behavior is predicted. On the basis of this result, the simpler UESI method was utilized to investigate the effects of material behavior assumptions and test variables.

The calculated stress-strain response of the peripheral fiber is affected by the choice of assumption used in describing the Bauschinger effect and stress transfer in creep. Example results are illustrated in Figs. 10 and 11. Figure 10, which shows hysteretic loops calculated assuming the three dif-

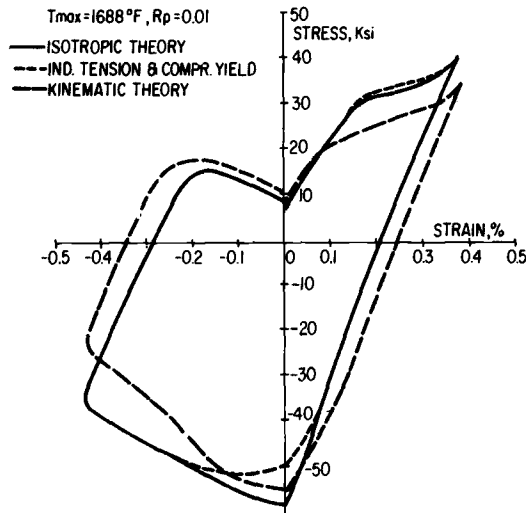


FIG. 10—Hysteretic loops calculated with differing assumptions on the Bauschinger effect (UESI method).

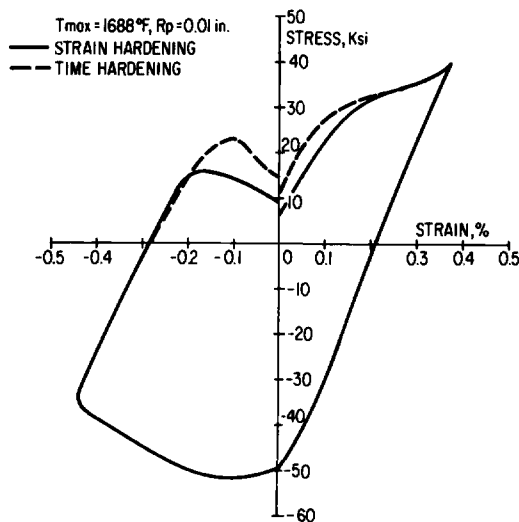


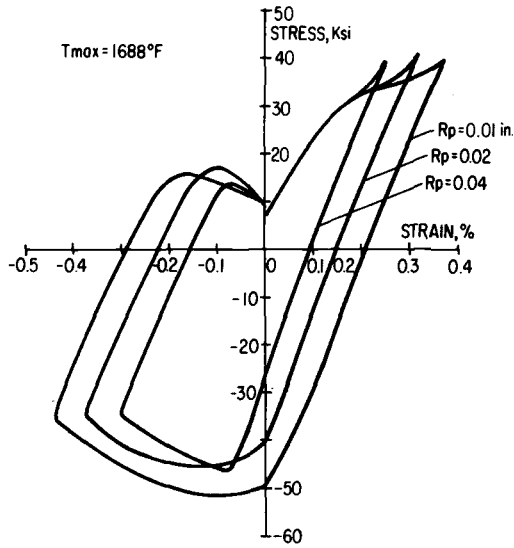
FIG. 11—Hysteretic loops calculated with the strain hardening and time hardening rules for creep-stress transfer (UESI method).

ferent assumptions on the Bauschinger effect previously discussed, indicates that the isotropic hardening and independent tension and yield assumptions predict the same behavior in the tension domain. However, as would be expected, the isotropic theory predicts greater compressive stresses. In contrast, the kinematic theory, which gives rise to a cycle effect, predicts on shakedown (five to six cycles) higher tensile stresses in the high temperature tension domain but lesser stress elsewhere. It also predicts somewhat larger plastic strain ranges.

Figure 11 shows loops resulting from the time and strain hardening assumptions in the creep analysis. Time hardening gives rise to less total creep and, therefore, higher stresses in the high temperature tensile domain. The resulting difference in total inelastic strain range is however, insignificant. In other words, if available elastic strain is not converted to creep, additional time-independent plastic strain results.

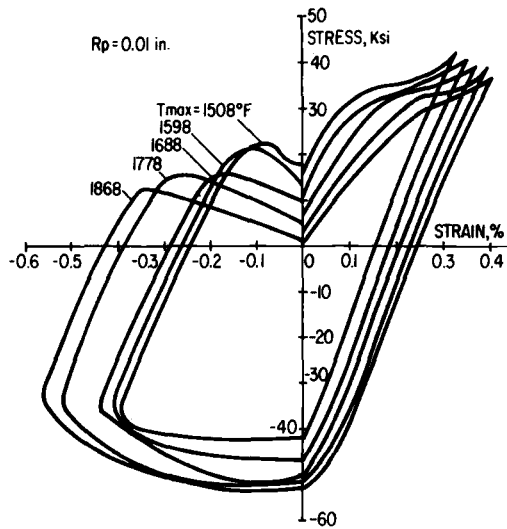
Figure 12 shows examples of loops calculated for other test conditions. Figure 12a of the figure shows the effect of R_p at constant T_{max} and t_h ; Fig. 12b, the effect of T_{max} at constant R_p and t_h ; and Fig. 12c, the difference between $t_h = 1$ and 4 min at constant T_{max} and R_p . Observe that the stresses achieved in each half of the cycle vary little with test condition. The major effect that each variable has on loop size is the total inelastic strain.

Ultimately, one would want to use the results of analyses like these for



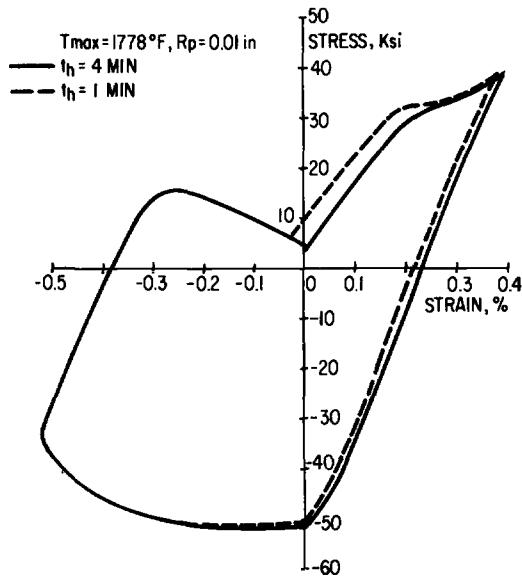
(a) Effect of R_p .

FIG. 12—Calculated hysteresis loops for various test conditions (UESI method).



(b) Effect of T_{max} .

FIG. 12—Continued.



(c) Effect of t_h .
FIG. 12—Continued.

fatigue life predictions. Although it is not the purpose of the present paper to examine fatigue life of the disk specimens, it is pertinent to examine the analysis results in light of potential application of current high temperature life prediction concepts. The following three damage concepts will be considered: (a) creep damage (Spera [4]), (b) strain range partitioning (Manson et al [13]), and (c) frequency modified fatigue life (Coffin [14]).

The creep damage hypothesis assumes that high-temperature fatigue damage is solely the result of creep damage. In his application of it, Spera proposes summing the damage via the linear life fraction rule, with the assumption that creep in compression is additive to that in tension. For varying temperature cycles, the creep damage per cycle, ϕ , is given by

$$\phi = \sum_0^t \frac{\Delta t}{t_r} \quad (6)$$

where

Δt = time increment and

t_r = creep-rupture time for the average stress and temperature within the time increment.

Failure is assumed to occur after N cycles when

$$N\phi = 1.0 \quad (7)$$

Use of this concept then requires knowledge of the isothermal stress-rupture properties in the temperature range of interest but no fatigue properties.

The strain range partitioning concept hypothesizes that the damage process is dependent upon the type of inelastic deformation. The inelastic strains present in a hysteretic loop are partitioned into the following components:

1. ϵ_{pp} , tensile plastic strain reversed by compressive plastic strain (that is, all nontime-dependent deformation).
2. ϵ_{pc} , tensile plastic strain reversed by compressive creep strain, or ϵ_{cp} , tensile creep reversed by compressive plastic strain.
3. ϵ_{cc} , tensile creep strain reversed by compressive creep strain (that is, all time-dependent deformation).

Further assumptions in the concept include relating each of these strain components to life through the Coffin-Manson equation and summing the damage caused by the various strain components in a linear fashion. That is

$$\begin{aligned} N_{pp}\epsilon_{pp}^\alpha &= A \\ N_{cp}\epsilon_{cp}^\beta &= B \end{aligned} \quad (8)$$

etc., and

$$\frac{1}{N_{pp}} + \frac{1}{N_{cp}} + \frac{1}{N_{pc}} + \frac{1}{N_{cc}} = \frac{1}{N_f} \quad (9)$$

In these relations, N_{pp} , N_{cp} , etc., are lives corresponding to the properly subscripted strain components ϵ_{pp} , ϵ_{cp} , etc.; N_f is the life when more than one component is acting.

For thermal loading of the type examined in this paper, only the ϵ_{pp} and ϵ_{cp} components are significant. These correspond to the ϵ_p and ϵ_c components calculated. To use the concept, one would then have to know the isothermal fatigue properties, α , β , A , and B . It has been proposed, on the basis of some initial experimental evidence, that these are independent of temperature [15]; that is, damage from each type of deformation is independent of temperature. This possibility would greatly simplify a damage analysis.

The frequency modified fatigue life approach is based on the hypothesis

that high-temperature fatigue damage is, in the main, environmental damage. The Coffin-Manson relationship is modified, based on the following relationship between frequency and time to failure

$$\nu^k t_f = c_1 \quad (10)$$

where

ν = frequency of cycling,
 t_f = time to failure, and
 k, c = material constants.

It is further assumed that c_1 is a constant for each plastic strain range and that the following relationship exists

$$c_1^\beta \Delta\epsilon_{tp} = c_2 \quad (11)$$

where

$\Delta\epsilon_{tp}$ = the total plastic strain range ($\Delta\epsilon_p + \Delta\epsilon_c$) and
 β, c_2 = material constants.

Taking $\nu t_f = N_f$, the following modified Coffin-Manson form can be arrived at

$$(N_f \nu^{k-1})^\beta \Delta\epsilon_{tp} = c_2 \quad (12)$$

Employment of this concept in transient thermal fatigue analysis requires obtaining values of k , β , and c_2 from isothermal fatigue tests. They are known to be temperature dependent [16] so that a damage analysis would have to assume some average or dominant values.

The analysis methods used in this paper readily provide one with these inelastic strain components. Also, a creep damage computation is easily facilitated. On examining the magnitudes of these quantities, they appear to be quite sensitive to the material behavior assumptions embodied in the stress analysis. As an example, Table 3 presents results for one test condition. It can be observed that $\Delta\epsilon_p$, $\Delta\epsilon_c$, and ϕ vary widely, depending upon the analysis assumptions. As an extreme, the time hardening assumption predicts the lowest creep strain and largest creep damage. Only $\Delta\epsilon_{tp}$ is relatively insensitive to the computation assumptions.

As a final observation, it is noted that none of the concepts examined explicitly treat the effect of mean stress bias. This may be an important omission, since mean stress biases are inevitably present in thermal loadings. The creep damage approach will predict an effect for some cases, but it would seemingly be in the wrong direction because compressive creep is considered additive to tensile.

TABLE 3—Predicted damage variables for the test condition
($T_{max} = 1688^{\circ}F$ and $R_p = 0.01$ in.).

Analysis Method	Material Behavior Assumption		Variables			
	Bauschinger Effect	Creep Stress Transfer	$\Delta\epsilon_{rp}$	$\Delta\epsilon_p$	$\Delta\epsilon_c$	$\phi, \%$
UESI	IT and CY ^a	ϵ -hard	0.495	0.198	0.297	0.22
UESI	IT and CY	t -hard	0.463	0.278	0.185	0.88
UESI	isotropic	ϵ -hard	0.492	0.195	0.297	0.22
UESI	kinematic	ϵ -hard	0.610	0.350	0.260	0.06
FE ^b	isotropic	ϵ -hard	0.532	0.301	0.231	...
UESI ^b	isotropic	ϵ -hard	0.515	0.210	0.305	0.31

^aIndependent tension and compression yield.

^bBilinear stress-strain curves.

In conclusion, it is suggested that each of these damage concepts could be applied to the analysis of thermal fatigue upon obtaining the appropriate isothermal properties. The strain range partitioning concept appears to be the easiest to apply. No statement can be made at this time on the accuracy of each concept. It is apparent that the predictions from any of the concepts would be sensitive to the material behavior assumptions chosen for the stress analysis. The controlling variable in the frequency modified approach appears to be the least sensitive in this regard. Further testing and analysis effort to establish the best (or better) material behavior assumptions appear necessary at this time.

References

- [1] Glenny, E., et al, "A Technique for Thermal Shock and Thermal Fatigue Testing Based on the Use of Fluidized Solids," *Journal of the Institute of Metals*, 1958, Vol. 87, pp. 294-302.
- [2] Howes, M. A. H. in *Fatigue at Elevated Temperatures*, ASTM STP 520, American Society for Testing and Materials, 1973, pp. 242-254.
- [3] Howe, P. W. H. in *Thermal and High-Strain Fatigue*, The Metals and Metallurgy Trust, 1967, pp. 122-141.
- [4] Spera, D. A., "The Calculation of Thermal Fatigue Life Based on Accumulated Creep Damage," NASA TMX-52558, National Aeronautics and Space Administration, 1969.
- [5] Mowbray, D. F. and Woodford, D. A., "Observations and Interpretation of Crack Propagation Under Conditions of Transient Thermal Strain," International Conference on Creep and Fatigue, Institute of Mechanical Engineers, 1973, pp. 179.1-179.11.
- [6] Foster, A. D. and Sims, C. T., *Metal Progress*, 1969, pp. 83-95.
- [7] Mendelsohn, *Plasticity: Theory and Application*, MacMillan, New York, 1968.
- [8] Hunsaker, B., et al, "A Comparison of the Capability of Four Hardening Rules to Predict a Material's Plastic Behavior," Report #75-51. Texas Engineering Experiment Station, June 1975.
- [9] Penney, R. K. and Marriott, D. L., *Design for Creep*, McGraw-Hill, London, 1971.
- [10] Manson, S. S., *Thermal Stress and Low-Cycle Fatigue*, McGraw-Hill, New York, 1966.
- [11] Topper, T. H. et al, *Journal of Materials*, Vol. 4, No. 1, 1969, pp. 200-209.

- [12] Hildebrand, F. B., *Advanced Calculus for Engineers*, Prentice-Hall, Englewood Cliffs, N.J., 1949.
- [13] Manson, S. S., Halford, G. R., and Hirschberg, M. H., "Creep-Fatigue Analysis By Strain Range Partitioning," NASA TMX-67838, National Aeronautics and Space Administration, May 1971.
- [14] Coffin, L. F., Jr., *Journal of Materials*, 1971, Vol. 6, pp. 388-402.
- [15] Halford, G. R., Hirschberg, M. H., and Manson, S. S. in *Fatigue at Elevated Temperatures*, ASTM STP 520, American Society for Testing and Materials, pp. 658-669.
- [16] Coffin, L. F., Jr., *Proceedings*, Institute for Mechanical Engineers, 1974, Vol. 188, pp. 109-127.

D. C. Gonyea¹

Thermal Stress Concentration Factors in Large Shafts

REFERENCE: Gonyea, D. C., "Thermal Stress Concentration Factors in Large Shafts," *Thermal Fatigue of Materials and Components, ASTM STP 612*, D. A. Spera and D. F. Mowbray, Eds., American Society for Testing and Materials, 1976, pp. 30-37.

ABSTRACT: The concentration of thermal stress in a shaft subjected to a ramp surface temperature change has been investigated. The concentration occurs at a step change in shaft diameter, and the temperature and stress responses are calculated by the finite element method. A thermal stress concentration factor (TSCF) is defined, and an analytical expression is given which defines the concentration factor in terms of the geometric parameters. Over the range of transient conditions studied, it is observed that the TSCF is insensitive to the surface temperature ramp rate. A comparison illustrates that the TSCF can be significantly different in numerical value than mechanical stress concentration factors.

KEY WORDS: thermal fatigue, thermal stress, stress analysis, stress concentration

Power generating equipment is frequently subjected to operating conditions that give rise to thermal stresses. In many cases, these thermal stresses are large and limit the operational flexibility of power plants. In connection with these limits, the transient thermal stresses developed in the rotors of large steam turbines have been studied extensively.²⁻⁴ An important aspect of these studies is the use of a thermal stress concentration factor to account for variations in the geometry on the outer surface of the rotor.

The purpose of this paper is to describe the nature of thermal stress concentrations at step changes in the diameters of large rotors. An expression is presented that defines an effective (Von Mises) stress con-

¹ Development engineer, General Electric Company, Schenectady, N.Y. 12305.

² Spencer, R. C. and Timo, D. P., "Starting and Loading of Large Steam Turbines," presented at the 36th Annual Meeting of the American Power Conference, April 1974, Chicago, Ill.

³ Berry, W. R. and Johnson, I., *Journal of Engineering for Power*, July 1964, pp. 361-368.

⁴ Manson, S. S., *Thermal Stress and Low Cycle Fatigue*, McGraw-Hill, New York, 1966.

centration factor in terms of geometric parameters for two idealized rotor shapes, alone and in combination. Thermal stresses are assumed to be developed due to slow uniform heating of the rotor surface.

Modeling Technique

Figure 1 depicts the three general types of geometries that have been studied, and Table 1 lists the actual dimensions utilized in this study. A total of 15 geometries has been investigated which encompasses the range of parameters typically encountered in actual turbine geometries of the author's company.

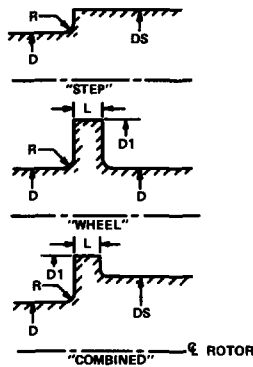


FIG. 1—Sketch of three types of geometries studied and definition of geometric parameters.

TABLE 1—Geometry description and thermal stress concentration factors found using finite element approach. All dimensions are given in units of inches. See Fig. 1 for definition of symbols.

Case	D	DS	D1	R	L	TSCF
1	20	42	...	3	...	3.72
2	20	30	...	3	...	2.66
3	20	30	...	1	...	3.57
4	20	22	...	1	...	1.77
5	20	24	...	1	...	2.33
6	20	20.5	...	0.25	...	1.74
7	12.3	24	...	4	...	2.60
8	22	22	39	0.5625	5	2.03
9	29.25	29.25	39.6	1.25	6.75	1.80
10	22	22	28.25	0.4375	2.25	1.74
11	20	30	40	1	4	4.06
12	20	26	30	1	4	3.39
13	20	23	30	1	4	2.56
14	20	23	26	1	4	2.67
15	20	26	30	1	6	3.19

A two-dimensional, axisymmetric finite element technique is used to study the thermal stress response of these geometries. Figure 2 illustrates the boundary conditions that are applied to the finite element model.

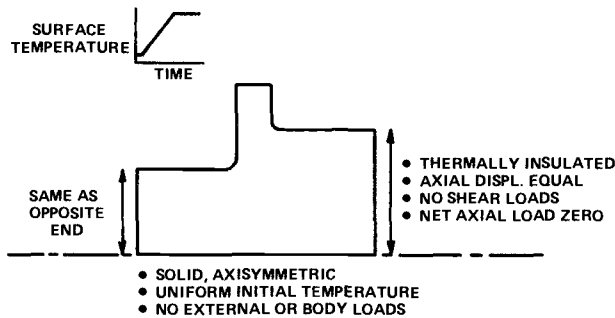


FIG. 2—Thermal and mechanical boundary conditions utilized in finite element study.

Thermal boundary conditions are applied which approximate those experienced by a turbine rotor during startup. Specifically, the surface temperature is assumed to be subjected to a finite linear temperature increase with respect to time. A uniform initial temperature is assumed, and the entire outer surface is given the same temperature variation with time. A solid shaft is used, and the ends of the finite element model are insulated to simulate a long shaft.

The mechanical boundary conditions at each end of the model are such that all axial displacements are equal, no radial shear exists, and the net axial load is identically zero. These conditions, as well as the length of the finite element model, are selected to approximate a long, unrestrained shaft. Examination of the results has shown these conditions to be essentially met. Deviations of up to 3 percent between the finite element results at the end of the shafts and classical solutions were found. In the case of the "wheel" geometry, advantage is taken of axial symmetry in geometry and loading about the center of the wheel. The model is assumed to be free of external and body loads in order to investigate solely the effects of thermal stress.

In the calculations described herein, the material is assumed to be homogeneous and isotropic and the material properties independent of temperature. Nominal values of material properties are used which are typical of turbine rotor alloys. These values are listed in Table 2.

Both the transient thermal and elastic stress analyses utilize the same finite element grid network. The actual computer codes employed in the calculations are programs developed by the author's company which incorporate the standard equation and solution techniques common to most two dimensional finite element codes.

TABLE 2—Numerical values of thermal and mechanical material properties utilized in the analysis.

Thermal conductivity	= 1.65 Btu/h · in. °F
Specific heat capacity	= 0.15 Btu/lb °F
Density	= 0.283 lb/in. ³
Thermal expansion coefficient	= 8×10^{-6} in./in. °F
Young's modulus	= 30×10^6 in./in. °F
Poisson's ratio	= 0.3

Temperatures/Stress Response

Figure 3 illustrates the temperature and stress response that is found to result from the surface ramp temperature change. The interior temperatures lag the surface temperature on heating and reach a quasi-steady

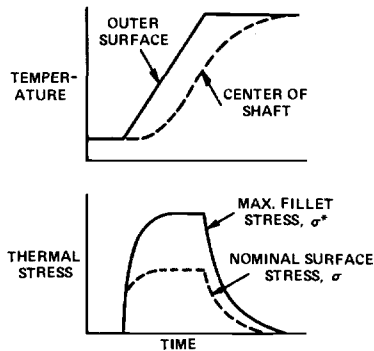


FIG. 3—Temperature and thermal stress response, Von Mises equivalent stress illustrated.

state condition after approximately 2 h. At this time, the calculated stresses reach their maximum values and remain constant until the end of the ramp, at which time the stresses decay as temperature equilibrium is approached.

During heating, compressive surface stresses develop. On the shaft surface removed from the concentration, an equibiaxial state of stress occurs. To account for the complex states of stress both nominally (removed from the fillet) and locally (at the maximum point at the fillet), the Von Mises equivalent⁵ stress is used. The use of Von Mises equivalent

⁵The Von Mises equivalent stress, σ , is defined as

$$\sigma = \frac{1}{\sqrt{2}} [(\sigma_1 - \sigma_2)^2 + (\sigma_2 - \sigma_3)^2 + (\sigma_3 - \sigma_1)^2]^{1/2}$$

where

$\sigma_1, \sigma_2, \sigma_3$ = principal components of stress.

stress is motivated by design considerations which consider the Von Mises equivalent stress as the quantity of interest in evaluating the low-cycle fatigue performance of the rotor due to thermal cycling.²

In addition, a thermal stress concentration factor (TSCF) is defined

$$TSCF = \frac{\sigma_0}{\sigma_\infty} \quad (1)$$

where

TSCF = thermal stress concentration factor,
 σ_0 = maximum Von Mises equivalent stress, and
 σ_∞ = Von Mises equivalent stress removed from the fillet.

In Eq 1, the values of stresses are taken after a quasi-steady-state temperature field develops. During the initial heating portion, the magnitude of the thermal stresses are less than those developed during quasi-steady state. Figure 4 illustrates this initial time dependent nature of the thermal stresses.

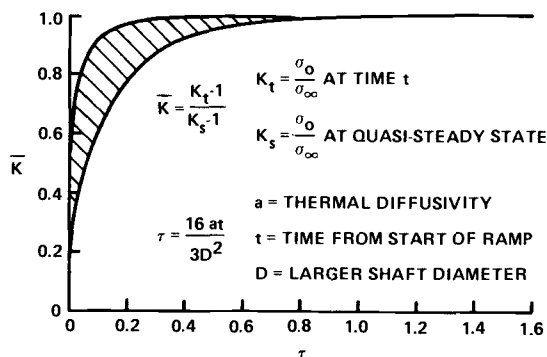


FIG. 4—Time dependence of thermal stress concentration during initial portion of heating. Note that the range illustrated includes wheel, step, and combined geometries.

In addition, the effect of various heating rates on the values of TSCF has been studied. Model 8 was subjected to surface heating rates of 100 and 333°F/h, and the value of TSCF was found to be identical in both situations. Other geometries that have been studied display the same behavior. Hence, TSCF is independent of heating rate when a quasi-steady state temperature field exists.

For other models, a heating rate of 200°F/h is utilized and TSCF determined after 5 h (at the end of the heating). Table 1 lists the values of TSCF determined in this manner for the 15 geometries studied.

The peak value of thermal stress occurs in the fillet region, a distance

of approximately $0.3 R$ from the intersection of fillet radius, R , and the shaft. The surface stress decreases rapidly around the fillet and along the shaft. Figure 5 illustrates this variation of stress in a normalized fashion. The scatterband illustrated includes the results from all geometries studied. Note the large decrease in thermal stress within a distance equal to the radius. This plot is useful for estimating the interaction effects of adjacent regions of concentration for more complex geometries.

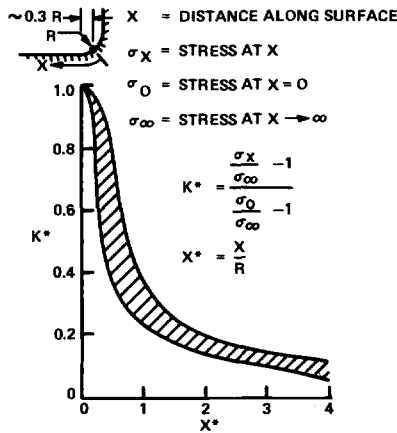


FIG. 5—Normalized distribution of surface stress in region of fillet. All cases investigated included in scatterband.

Approximate Equation for TSCF

Because it is impractical to study all geometries of interest with the finite element approach, an approximate analytical expression has been developed which relates TSCF to the geometric parameters involved. As a starting point, TSCF values associated with the "step" geometry are used to establish a fundamental relationship. The more complex geometries, (the wheel and combined cases) are related to an equivalent step geometry to provide a secondary relationship. This approach follows that of Peterson⁶ in defining the mechanical stress concentration factor for a shaft in bending.

The approximate relationship that has been developed in this manner, using the geometric parameters defined in Fig. 1, is

$$\text{TSCF} = 1 + \sqrt{\frac{D}{R} \left[\frac{DEQ}{D} - 1 \right]}^{\frac{1}{\sqrt{2}}} \quad (2)$$

⁶Peterson, R. E., *Stress Concentration Design Factors*, Wiley, New York, 1953.

where

$$\frac{DEQ}{D} = \begin{cases} DS/D & \text{for step geometry} \\ \text{minimum } [D1/D, DS/D + 0.35 L/DS] & \text{for wheel and combined geometry} \end{cases}$$

It should be noted that TSCF is defined in terms of the nominal equivalent stress at diameter, D , in all cases.

Figure 6 illustrates that Eq 2 describes the results of the finite element studies connected with the step geometries in the range of parameters studied. Figure 7 is a direct comparison of TSCF found by the finite element technique and by the proposed analytical relationship, Eq 2 for all cases studied.

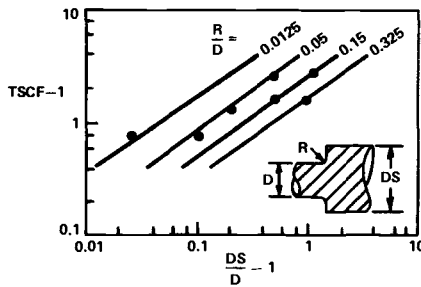


FIG. 6—Comparison of finite element results for step geometry and equation developed to define thermal stress concentration behavior.

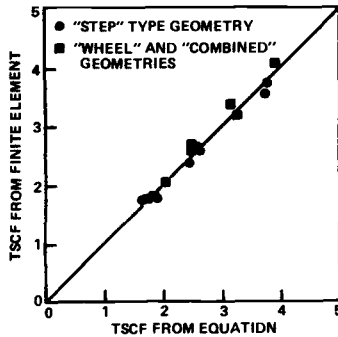


FIG. 7—Comparison of TSCF calculated using the finite element technique from Eq 2.

A comparison of TSCF and the mechanical stress concentration in bending given by Peterson⁶ highlights another aspect of TSCF. Figure 8 illustrates such a comparison. Observe that, for small diameter ratios, the value of TSCF is roughly equal to or less than that of mechanical bending. However, for large diameter ratios, the values of TSCF is signifi-

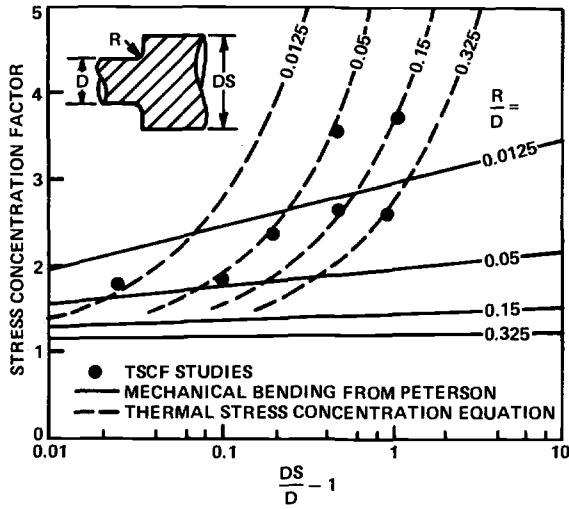


FIG. 8—Comparison of thermal and mechanical stress concentration factors for shaft with step change in diameter.

cantly larger than the corresponding mechanical value. This effect is due principally to a thermal mismatch mechanism that gives rise to additional stress in the case of the thermal loading, particularly for large diameter ratios. The difference in average temperatures between the large and small sections of shaft causes this thermal mismatch. A similar mechanism does not exist for the case of mechanical loading.

Summary

The finite element technique has been used to investigate the nature of thermal stress concentrations in large turbine rotors during temperature transients. On the basis of this analysis, it is tentatively concluded that the thermal stress concentration factor, TSCF, is independent of time and heating rate under conditions of slow uniform heating in which a quasi-steady state temperature field exists. An approximate relationship is given, Eq 2, which defines TSCF in terms of the geometric parameters of the rotor. A normalized plot of the distribution of thermal stress in the vicinity of the fillet region is also given. A comparison of TSCF with the mechanical stress concentration factor due to bending illustrates that there may be a significant difference in numerical values of these two factors. For large diameter ratios, the value of TSCF is larger than that due to bending, owing to an additional thermal stress component which is due to a thermal mismatch mechanism.

*S. Tepper*¹

Low-Cycle Fatigue Analysis of the Turbine Disk for the National Aeronautics and Space Administration High-Temperature Turbine Rig

REFERENCE: Tepper, S., "Low-Cycle Fatigue Analysis of the Turbine Disk for the National Aeronautics and Space Administration High-Temperature Turbine Rig," *Thermal Fatigue of Materials and Components, ASTM STP 612*, D. A. Spera and D. F. Mowbray, Eds., American Society for Testing and Materials, 1976, pp. 38-54.

ABSTRACT: The high-pressure, high-temperature turbine test rig was designed for the National Aeronautics and Space Administration to test turbine components in an environment that simulates current and future gas turbines operating at 41 atm (600 psi) and 2204 °C (4000 °F). This paper illustrates the design approach that led to selection of a typical test rig component: the turbine disk. The final configuration of the rotor assembly and the turbine disk was determined by analysis of low-cycle fatigue and creep.

KEY WORDS: thermal fatigue, creep (materials), disks, thermal cycling tests, plastic analysis, substructures, turbines

During the preliminary design of mechanical components, especially during definition of component configurations, the analyst must establish the controlling conditions that affect the design. This paper summarizes the analytical approaches used in designing the turbine disk for the National Aeronautics and Space Administration (NASA) Lewis Research Center's high-pressure, high-temperature, turbine test rig (HTTR).²

The Larson-Miller parameter (LMP) approach was followed in the creep analysis. Life, as calculated from the plastic analysis, was updated by a more accurate study of stress relaxation and cyclic operation. In the low-cycle fatigue (LCF) analysis, the cycles to failure were determined

¹Senior engineering specialist, Applied Mechanics Group, AiResearch Manufacturing Company of California, Torrance, Calif. 90509.

²"High Pressure High Temperature Turbine Test Rig," NAS3-17736, 19 July 1973.

by the universal slopes method according to Manson and Halford [1]³ and considering the studies of Morrow, Wetzel, and Topper [2,3]. The interaction between creep and LCF, and the strain range partitioning approach are also discussed [4-6].

The Turbine Disk

The HTTR was designed and analyzed in terms of a number of operating conditions. The objective was to test turbine components in an environment simulating current and future gas turbines, with maximum operation at 41 atm (600 psia) and 2204 °C (4000 °F).

The wide range of HTTR operating conditions was imposed by large variations in operating speed, temperature, and pressure. The rotary assembly has three specified operating speeds: idle, 12 000 rpm; maximum cyclic, 16 667 rpm; and maximum operational, 17 500 rpm. Its overspeed design condition is 21 800 rpm. All intermediate speeds between 0 and 17 500 rpm are possible. Cooling is provided by pressurized air, with temperatures varying between 260 and 621 °C (500 and 1150 °F). Inlet pressures may be as high as 41 atm (600 psia).

Because of its critical nature, the Astroloy turbine disk was subjected to many combinations of temperature maps, rotating speeds, pressures, and interface loadings. From the configurations studied, a design with cover sideplates was selected. These sideplates, which are bolted as units to the disk, enclose two chambers through which two separate flows of cooling air are carried to two types of turbine blades.

The two final candidate designs are depicted as finite-element models in Figs. 1 and 2. Once the second design was adopted (Fig. 2) controlling conditions became those that affected the interface between the cover plate, bolt, and disk.

Preliminary Analysis Process

The following initial guidelines are recommended to analysts investigating similar tasks.

Initial Guidelines

Step 1—Establish all specified and tabulated operating conditions. If each contributory action for a given operating condition could be linearly superposed, the following expression could be used during the preliminary design

$$\frac{Se}{Sa} = \sum_{i=1}^n \frac{Si}{Sai} \leq 1$$

³ The italic numbers in brackets refer to the list of references appended to this paper.

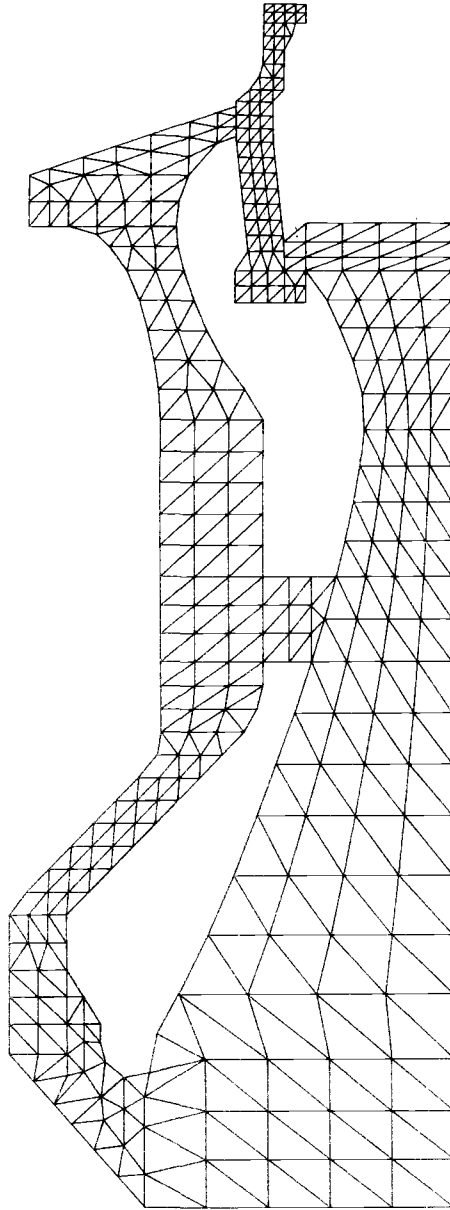


FIG. 1—*Finite-element model of Candidate Disk 1.*

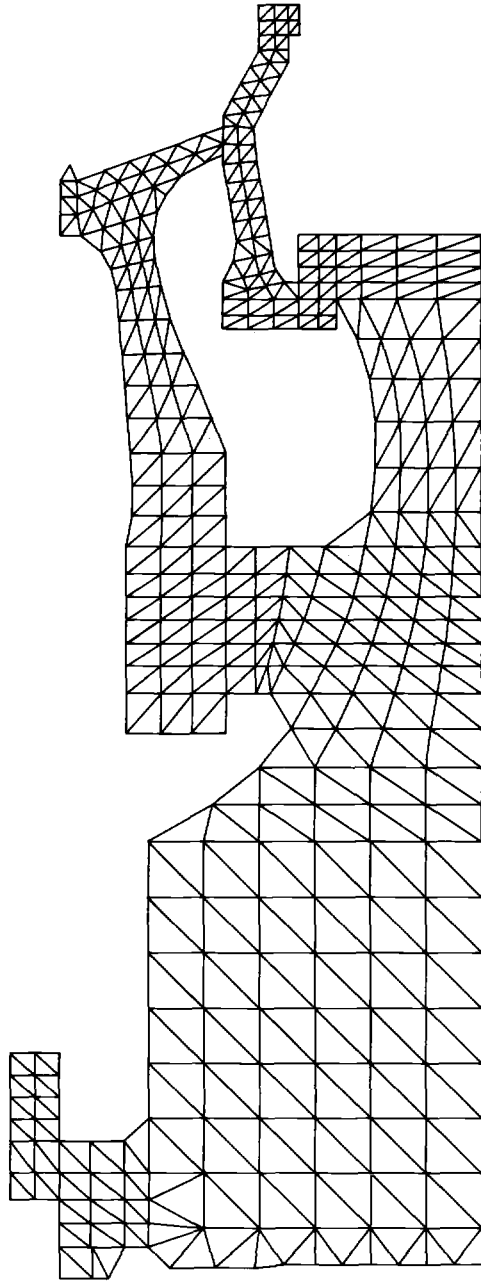


FIG. 2—*Finite-element model of Candidate Disk 2.*

where

S = any design condition, for example, stress and hours of life,

a = allowable value,

e = equivalent total, and

i = corresponding contributory condition.

In this analysis, the only linear contributory load, neglecting differential stiffening effects, is the pressure. For a given temperature distribution and rotational speed, only two conditions were analyzed: zero and maximum pressure. The other two contributory actions were nonlinear, that is, temperature and rotational speed.

Step 2—Establish intermediate operating conditions if the acting loads cannot be linearly superposed. In the present study, seven speeds (six operational and one for overspeed design), four pressure values (two at each side of the disk), and six temperature maps existed. These variables produce a total of 192 combinations. However, not all of these combinations are operational.

Step 3—Discard nonoperational and minor operating conditions. Once the obviously insignificant conditions are eliminated, the discarding of some intermediate operating conditions can be very challenging. An example to be considered would be, which temperature maps are the most significant? Here one must choose between high-temperature conditions with lower temperature gradients, and low-temperature conditions with large temperature gradients. The best method is to keep both extreme conditions and at least one intermediate condition.

Step 4—Retain conditions that define a cyclic operation. Basically, one tends to study or select only the highly loaded conditions because of their relation to ultimate or yield strength and to creep life. This approach is valid when the representative mission profile indicates few cycles. Frequently, however, that is not the case.

The mission profile analyzed here comprises many long and short tests in which the corresponding transients affect each of the contributory parameters—speed, pressure, temperature—and their mutual relationships. Cyclic life is a fundamental condition to satisfy.

Step 5—If conditions allow, start using an elastic model. Once the contributory loads are defined (in this case, speed, pressure, and temperature maps), an elastic finite-element model may be used. This model may be used even if the operating conditions are not linear. Use of an elastic finite-element model assumes that: (a) the possible plastic areas are confined to local small spots and (b) these spots will not create a mechanism between two or more parts of the model.

Elastic models are more economical than plastic models because they run faster in the computer. Also, there are many large computer programs able to accept elastic models. In many cases, an elastic-plastic

solution for a given operating condition is valid if previous elastic-plastic solutions were run and the correct history was kept.

As the conditions just mentioned are met, the analyst may record the results of the most severe condition, as well as the conditions that are important enough to deserve a full elastic-plastic analysis.

Nonlinear Problem And Finite-Element Model

Figure 3 shows the adopted disk configuration in which loads and moments represent blades, bolts, and seals. At the given temperatures and

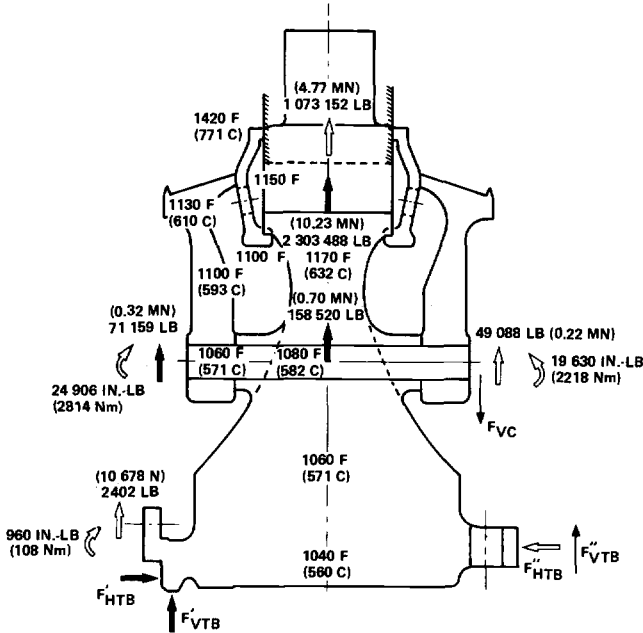
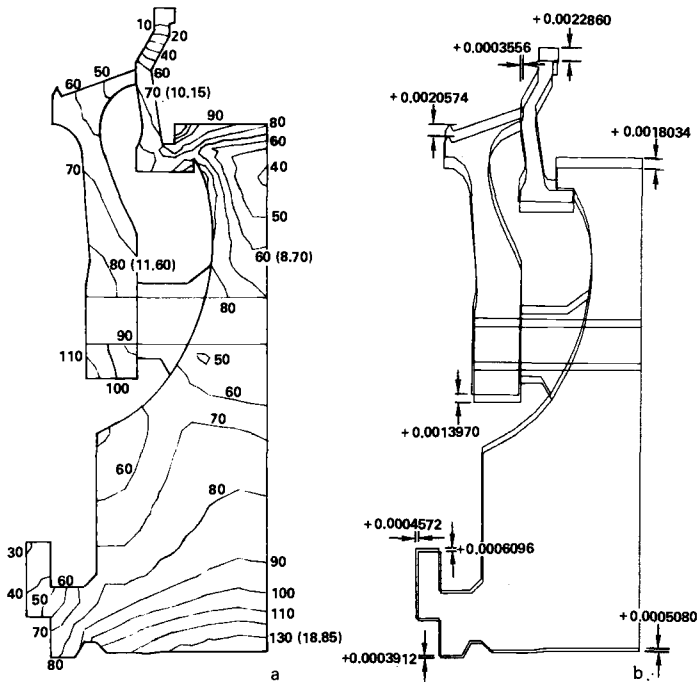


FIG. 3—Rotor interface loads and temperatures at 17 500 rpm.

speed, with an internal pressure of 20 atm (300 psia) in the cavities, the corresponding effective Von Mises stresses and displacements are shown in Figure 4. Figure 5 depicts the estimated plastic flow based on the elastic analysis for 17 500 and 21 800 rpm.

A cyclosymmetric finite-element model of the main disk, side plate, and bolt was used. At 17 500 rpm, the maximum operational speed, plasticity was found only at the disk hub. However, owing to the coarseness limitations of the model, a better representation of the side plate-bolt area was desired. Of particular interest was finding a simple way to examine all important loading combinations without constructing large models. One clear method was to separate the main disk from the



(a) Effective stress, ksi (MPa).
 (b) Displacements, m.

FIG. 4—Effective stresses and displacements at 17 500 rpm.

side plate and establish the matching and boundary loads for a substructure surrounding the area under study.

Also, two other actions (bolt loosening and tightening) were simultaneously analyzed. By using a bolt made of the same material as the disk, the thermal expansion was the same for both. However, the centrifugal field acting on the disk produced two principal stresses (radial σ_r and hoop σ_θ) of the same order, while the bolt is mainly under axial loading. Because the Poisson's ratio effect narrows the disk farther than the bolt, the bolt could become loose if sufficient preloading is not provided.

Once preloading is defined, the effect of the following must be investigated: (a) the different working conditions at room temperature and at idle and maximum operating speeds, (b) the creep associated with the stress and temperature field, and (c) the maximum manufacturing tolerances allowed.

Figure 6 depicts the load distribution at the disk-sideplate interface. The contact pressure loads are transferred through the bolt. Matching

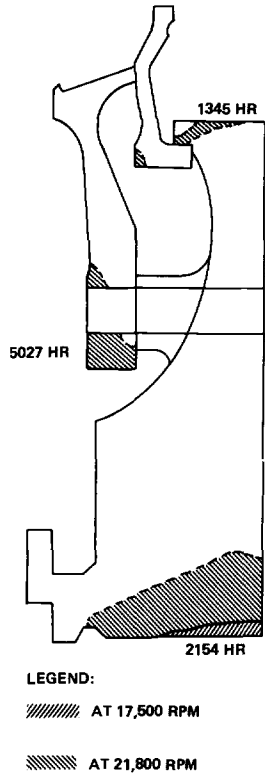


FIG. 5—Plastic flow and life, hour.

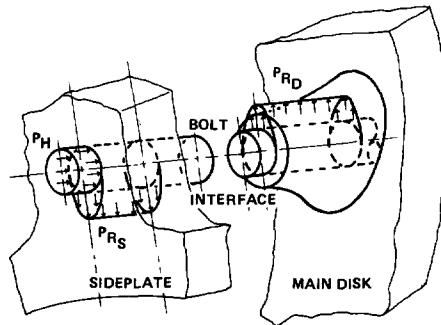


FIG. 6—Distribution loads at interface.

of the resultant loads and the structural displacement was accomplished for the two substructures (main disk and sideplate) under seven load

conditions. Five nonlinear equations were solved in terms of displacements by the Newton method. The five equations are

$$\left\{ \begin{array}{l} \delta_{H(n)}^0 + P_1 \delta_{H(P_1, n)}^P + H_1 \delta_{H(H, n)}^H \approx 0 \\ \delta_{P_1(n)}^0 + P_1 \delta_{P_1(P_1, n)}^P + H_1 \delta_{P_1(H, n)}^H = \delta_{P_1(P_1, H, n)}^R \\ \delta_{P_2(n)}^0 + P_2 \delta_{P_2(P_2, n)}^P \approx \delta_{P_2(P_2, H, n)}^R \\ P_1 + P_2 \approx 0 \\ \delta_{P_1(P_1, P_2, H, n)}^R = \delta_{P_2(P_1, P_2, H, n)}^R \end{array} \right.$$

where

- subscripts = degrees of freedom associated with the loads,
- variables between parenthesis = nonlinear dependencies,
- superscripts = loading configurations,
- ⁰ = free centrifugal field, (17 500 rpm),
- ^R = total resultant displacement along the radial direction, and
- $P_1, P_2,$ and H_1 = loading resultants from the contract pressures $P_{RS}, P_{RD},$ and P_H respectively (see Fig. 6).

The solution of the system of equations gave the shear stresses at the bolt section and the axial preload required to keep the sideplate attached to the disk. Considering the additional preload required to control the thermal expansion, the Poisson's ratio effect, the manufacturing tolerance, and the creep relaxation, the maximum axial stress in the bolt is 75 to 80 ksi. The lower axial stress is about 40 ksi for the worst combination of operating conditions. Bolt retightening time is defined by both creep relaxation and cyclic operation.

First Approach to Creep Study, Substructure Analysis

The region under study was the interface between the main disk and the sideplate. The loads and boundary conditions were established from the preliminary runs by using the finite-element model mentioned previously.

In this approach, an isoparametric elastic-plastic element was implemented in an AiResearch computer program that has been used with satisfactory results during the last four years. Figure 7 shows the temperature map. Figure 8 shows the effective stress maps at 17 500 and 21 800 rpm. By using LMP curves, a first solution for creep life was made.

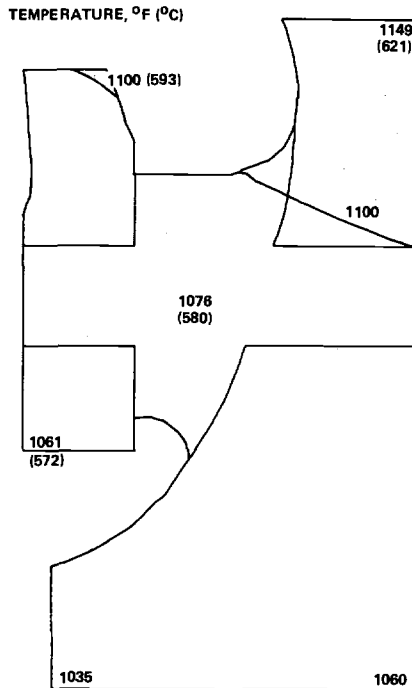


FIG. 7—Temperature map.

These life zones are depicted in Fig. 9 for both 17 500 rpm and 21 800 rpm and the established creep values.

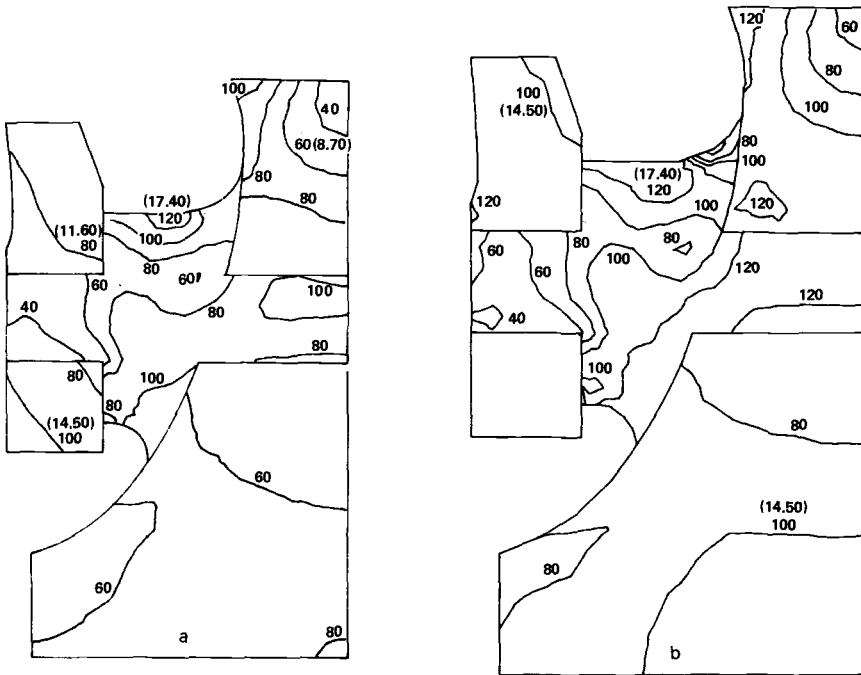
If the LMP curves reflect minimum values, a safety factor of four is common practice. However, it should be noted that the expected life was based on an elastic-plastic solution where no stress relaxation was considered.

Continued Analysis Process

At this point in the analysis, the following guidelines apply.

Step 6—For economy and simplicity, the finite-element model should be established in such a way that possible substructures are easily identifiable. A coarse model is an advantage if a critical area can be further analyzed without reassembling the overall model. Also, computer time, which usually is an exponential function of the number of degrees of freedom (related to the unconstrained nodes), can be substantially reduced by proper substructuring.

Step 7—Define the interface loads between two continuous substructures and then proceed as necessary to increment the number of elements



(a) At 17 500 rpm, ksi (MPa).
 (b) At 21 800 rpm, ksi (MPa).

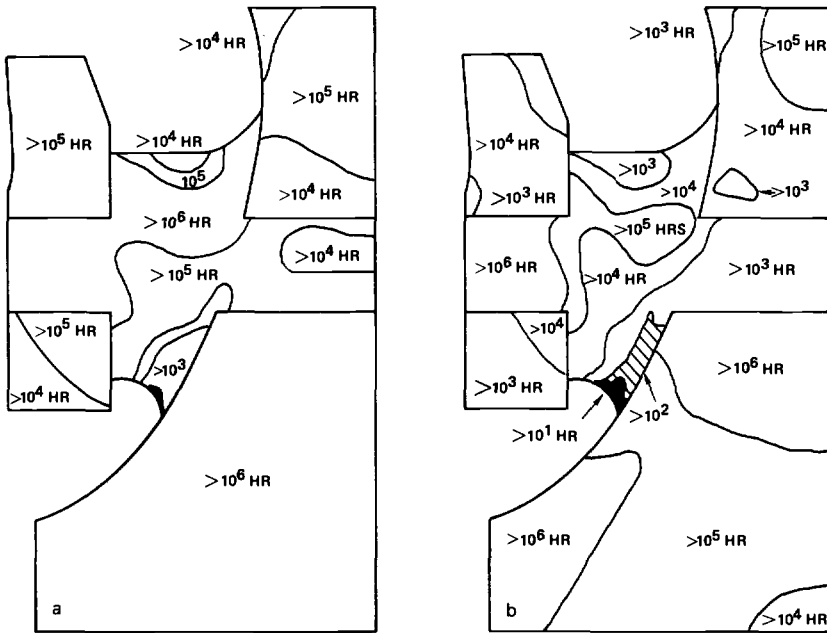
FIG. 8—Effective stresses.

in the substructure. After the runs, recheck the interface and boundary agreements.

Step 8—When plasticity is expected, run the full elastic-plastic analysis for the critical substructure or for the total structure, if required. A first assessment of possible plasticity should compare the effective stress with the corresponding temperature and yield stress at a given point. An effective stress below the yield stress does not guarantee elastic values. However, the analyst will be able to check the different types of stresses involved and the particular area under consideration. If a point shows plasticity, all the substructures (or the structure) should be run in a plastic solution.

Step 9—For the specified creep value (1 percent, 2 percent, rupture, etc.), define the creep life map. Since no stress relaxation is considered at this time, the LMP approach should suffice. A typical LMP expression is

$$\text{LMP} = T(20 + \log t)/1000$$



(a) 17 500 rpm.
(b) 21 800 rpm.

FIG. 9—Plastic regions and hours of life.

where

T = absolute temperature (temperature °F + 460),
 t = expected life in hours, and
 log = logarithm to base 10.

Most of the materials have curves relating stresses to LMP

$$\text{LMP} = f\{\sigma\}_{\epsilon_c}$$

where ϵ_c is a given creep value. Therefore, the life is easily calculated from

$$\log t = 1000 \text{ LMP}/T - 20$$

Step 10—Clearly mark the plastic areas with special emphasis on the following three aspects: (a) plastic areas on the surface, (b) if there is more than one area, mark possible connectivity, and (c) plastic areas that are large in proportion to their surrounding elastic areas.

Second Approach to Creep Study

Depending on the characteristics of the plastic areas, a more complete study that includes stress relaxation could be considered. An AiResearch computer program developed in 1971 allows an incremental time solution of a plastic solution for a finite-element model.

If only creep were considered, the analysis would be complete at this point. However, a local plastic area (Fig. 9a) is always a concern in low-cycle fatigue studies, and a finer analysis is required. In the present case, plastic propagation was not found. The life values obtained were slightly lower than those calculated previously.

First Approach to Low-Cycle Fatigue

This method is based on the classical universal slopes solution developed during the 1960's that provides additional allowance for creep [1]. Because it uses a safety factor of ten, it is considered a conservative approach.

If the plastic area is relatively small and is surrounded by a predominant elastic region, the equivalent (linear) elastic effective stress obtained from the elastic model can be applied by using the Neuber hyperbola method.

It has been shown by Topper et al [2] that Neuber's rule [3] may be applied to inelastic behavior characteristics at a notch root. Neuber states that the theoretical stress concentration factor is equal to the geometric mean of the actual stress and strain concentration factors,

$$K_t = (K_\sigma \times K_\epsilon)^{1/2} \quad (1)$$

Peterson [7] has shown that notch size can affect the fatigue life and that a fatigue concentration factor, K_f , should be used

$$K_f = 1 + \frac{K_t - 1}{1 + \sqrt{a/r}} \quad (2)$$

where

r = root radius and

a = material constant determined empirically.

In applying Neuber's rule to the notch fatigue problem, K_f is used in place of K_t . By substituting the ratios of stress and strain ranges for K_σ and K_ϵ , Eq 1 becomes

$$K_f = \left(\frac{\Delta\sigma\Delta\varepsilon}{\Delta S\Delta E} \right)^{1/2} \quad (3)$$

$$K_f (\Delta S\Delta e E)^{1/2} = (\Delta\sigma\Delta\varepsilon E)^{1/2}$$

where E is the Young's modulus.

If strain, e , is elastic, then

$$K_f \Delta S = (\Delta\sigma \times \Delta\varepsilon \times E)^{1/2} \quad (4)$$

$$\frac{(K_f \Delta S)^2}{E} = \Delta\sigma\Delta\varepsilon \quad (5)$$

For a given load and geometry, the left side of Eq 4 is a constant. The set of solutions of $\Delta\sigma$ and $\Delta\varepsilon$, therefore, form a hyperbola as shown in Fig. 10. The intersection at A in Fig. 10 is the solution if the stress and strain are entirely elastic. Points B and C are the location of true stress

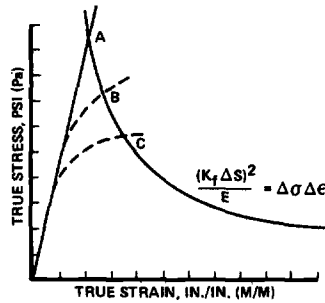


FIG. 10—Neuber's hyperbola rule.

and strain for two different materials that have the same elastic modulus but different strengths.

Crews and Hardrath [8] experimentally demonstrated the validity of using these control hyperbolas to determine the residual stresses and strains after a complete cycle. This work was carried farther by Wetzel [9] in demonstrating the use of control hyperbolas to determine actual stress and strain throughout the load history.

Figure 11 shows how the actual stresses and strains may be followed throughout the load history by returning to the control hyperbolas after each load change. It may also be seen how the hysteresis loop stabilizes and strain hardening has taken place for the particular material.

Manson and Halford [1] developed an empirical relationship between

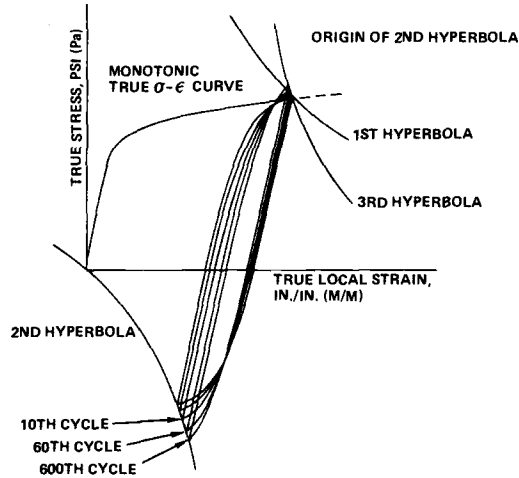


FIG. 11—Cyclic loop.

total strain and the number of cycles required to cause fatigue failure by using conventional tensile properties, as follows

$$\Delta\epsilon_t = 3.5 \frac{UTS}{E} N_f^{-0.12} + D_t^{0.6} N_f^{-0.6} \quad (6)$$

where

- $\Delta\epsilon_t$ = stabilized or final total true strain range,
- UTS = ultimate tensile strength,
- D_t = tensile ductility, and
- N_f = cycles to failure.

This formula has been shown to fit fatigue data for many materials. It is adequate for predicting pure fatigue life where temperature and loading frequencies are such that cyclic creep damage is not a factor. Many investigations have been performed using Eq 6 with acceptable correlation between fatigue life (N_f) and total strain ($\Delta\epsilon_t$).

By using this formula, the value $\Delta\epsilon_t$ can be obtained directly from the plastic analysis without going through the Neuber's hyperbola approach. In analyzing the HTTR, both Neuber's hyperbola and the plastic solution were used. During the selective analysis, however, the analysis was limited to the nominal or equivalent elastic stresses and the Neuber's hyperbola approach.

Second Approach to Low-Cycle Fatigue

Creep and LCF interact. A common and somewhat simplified method was used to determine this interaction. This was the life fractions method that is based on the Miner's rule

$$\varphi = \varphi_C + \varphi_{\text{LCF}} \leq 1 \quad (7)$$

where φ is the life fraction and subscripts C and LCF correspond respectively to creep and low-cycle fatigue

$$\varphi_C = \sum_{K=1}^n \Delta\varphi_{C_K} \quad \varphi_{\text{LCF}} = \sum_{M=1}^m \Delta\varphi_{\text{LCF}_M} \quad (8)$$

$$\Delta\varphi_{C_K} = \frac{h_k}{h_{t_k}} \quad \Delta\varphi_{\text{LCF}_M} = \frac{C_{Y_M}}{C_{Y_{t_M}}} \quad (9)$$

where

- h_k = hours spent at condition k ,
- h_{t_k} = total hours possible at condition k ,
- C_{Y_M} = number of cycles used at condition M , and
- $C_{Y_{t_M}}$ = total number of cycles possible at condition M .

During the initial phases of the analysis, this method is sufficient for a comparison of the design alternatives. As can be observed, the results are the same if most of the cycles are spent at the beginning or at the end of the creep life. This method does not consider the cycle frequency, nor does it consider if the mechanical properties of the material related to the creep can be affected by the cyclic operation.

In Manson and Halford's relationship [1], the number of cycles as calculated by the Eq 6 was adjusted for creep phenomena. This was done by using values related to the effective fraction of each cycle for which the material may be considered to be subjected to the maximum stress, frequency of stress application, and material coefficients.

In recent years, new techniques have been discussed; the most promising among them is strainrange partitioning [4-6]. By this technique, any cyclic behavior can be represented as a combination of four basic types of inelastic strainranges defined as plastic-plastic, plastic-creep, creep-creep, and creep-plastic. However, for a given cycle, not more than three of these types can exist. Each one of these basic types must be tested for a given material. To take full advantage of this new technique, considerable effort must be expended to compile a library of materials for the basic cycle types.

Completing the Analysis Process

In completing an analysis of this type, the following guidelines apply.

Step 11—If the projected plastic zone affects a considerable portion of the model or a critical area, run a finite element-finite difference analysis with a full elastic-plastic model and time increment solution.

Determine if there is any growth of the plastic area and establish the characteristics of stress relaxation. Stress is important, but the significant element in this analysis is strain.

Step 12—From the original elastic analysis related to cyclic operation, calculate the number of cycles to failure by using nominal elastic stresses and the Neuber hyperbolas.

Step 13—Interact creep and LCF by using Eqs 7-9. Define the best design under the worst combination of creep and LCF. By using safety factors like 6 to 10 for LCF and 2.5 to 4 for creep, the analytical design process could stop at this point.

Step 14—If the design requires a more sophisticated approach because of marginal conditions or large number of production units, strainrange partitioning with better creep-LCF interaction could be required.

References

- [1] Manson, S. S. and Halford, G., "A Method of Estimating High Temperature Low-Cycle Fatigue Behavior of Materials," NASA Report TMX 52357, Lewis Research Center, National Aeronautics and Space Administration, Cleveland, Ohio, Jan. 1967.
- [2] Morrow, T., Wetzel, R. M., and Topper, T. H. in *Effects of Environment and Complex Load History on Fatigue Life, ASTM STP 462*, American Society for Testing and Materials, 1970, pp. 74-91.
- [3] Morrow, T., Wetzel, R. M., and Topper, T. H., *Journal of Materials*, Vol. 4, No. 1, March 1969, pp. 200-209.
- [4] Spera, D. A. in *Fatigue at Elevated Temperatures, ASTM STP 520*, American Society for Testing and Materials, 1973, pp. 648-657.
- [5] Manson, S. S. in *Fatigue at Elevated Temperatures, ASTM STP 520*, American Society for Testing and Materials, 1973, pp. 744-782.
- [6] Halford, G. R., Hirschberg, M. H., and Manson, S. S. in *Fatigue at Elevated Temperatures, ASTM STP 520*, American Society for Testing and Materials, 1973, pp. 658-669.
- [7] Peterson, R. E., *Material Research and Standards*, Vol. 3, No. 2, Feb. 1963, pp. 122-139.
- [8] Crews, J. H. and Hardrath, H. F., *Experimental Mechanics*, Vol. 6, No. 6, June 1966, pp. 313-320.
- [9] Wetzel, R. M., *Journal of Materials*, Vol. 3, No. 3, Sept. 1968, pp. 646-657.

D. P. H. Hasselman,¹ R. Badaliance,¹ and E. P. Chen¹

Thermal Fatigue and Its Failure Prediction for Brittle Ceramics

REFERENCE: Hasselman, D. P. H., Badaliance, R., and Chen, E. P., "Thermal Fatigue and Its Failure Prediction for Brittle Ceramics," *Thermal Fatigue of Materials and Components, ASTM STP 612*, D. A. Spera and D. F. Mowbray, Eds., American Society for Testing and Materials, 1976, pp. 55-68.

ABSTRACT: The thermal fatigue behavior of a soda-lime-silica glass subjected to water quench and silicon-nitride subjected to thermal environment of a turbine engine was predicted from data of slow (subcritical) crack growth. A numerical integration technique was developed to calculate the extent of slow crack growth for each thermal cycle over the total duration of the transient thermal stress and temperature, as well as the total number of cycles required for catastrophic failure to occur. Good agreement between the predicted and experimental data was found. The results indicate that, for reliable prediction of thermal fatigue resistance, an estimate of critical flaw-depth based on a statistical (such as the Weibull) theory of brittle fracture is necessary.

KEY WORDS: thermal fatigue, crack propagation, silicon nitrides, silica glass, fracture, fatigue failure.

Structural ceramics and glasses generally exhibit a decrease in load-bearing ability (that is, strength) under conditions of constant [1,2]² or cyclic load [3,4] as well as repeated thermal shock [5,6]. Such behavior is the result of slow crack growth at stress levels below those required for rapid fracture. Considerable progress has been made in the failure prediction of ceramic materials undergoing slow crack growth from information for crack growth behavior. This approach was applied to conditions of steady [7,8] as well as cyclic load [9] and single-cycle thermal shock [10]. This paper presents the results of a feasibility study to extend such techniques to the prediction of thermal fatigue.

¹Director, post-doctoral research associate, and assistant professor, respectively, Ceramics Research Laboratory, Materials Research Center, Lehigh University, Bethlehem, Pa. 18015.

²The italic numbers in brackets refer to the list of references appended to this paper.

Materials*Soda-Lime-Silica Glass*

Soda-lime-silica³ glass in the form of rods with radius of 0.236 cm, identical to the glass studied previously [10], was selected for the present program. Table 1 lists the appropriate physical properties of this glass. Experimental data for slow crack growth were obtained from the literature

TABLE 1—Data for physical properties, crack propagation behavior, and heat transfer required for calculations of thermal fatigue resistance of soda-lime-silica glass rods subjected to a water quench.

PHYSICAL PROPERTIES	
Coefficient of thermal expansion (α)	$9.3 \times 10^{-6} \text{ } ^\circ\text{C}^{-1}$
Young's modulus of elasticity (E)	$6.9 \times 10^{10} \text{ Nm}^{-2}$
Poisson's ratio (ν)	0.25
Thermal conductivity (k)	$2.5 \times 10^{-3} \text{ cal} \cdot \text{ } ^\circ\text{C}^{-1} \text{ cm}^{-1} \text{ s}^{-1}$
Specific heat (c)	$0.22 \text{ cal} \cdot \text{g}^{-1} \text{ } ^\circ\text{C}^{-1}$
Density (ρ)	$2.53 \text{ gcm}^{3/\text{g}}$
Weibull parameter (a)	≈ 8
CRACK PROPAGATION BEHAVIOR	
Fatigue limit (K_0)	$2.49 \times 10^5 \text{ Nm}^{-3/2}$
Critical stress intensity factor (K_{Ic})	$7.49 \times 10^5 \text{ Nm}^{-3/2}$
Preexponential factor (in v_0)	
Low K	$-1.08 \text{ m} \cdot \text{kg} \cdot \text{s units (m/s)}$
High K	$10.3 \text{ m} \cdot \text{kg} \cdot \text{s units (m/s)}$
Velocity constant (b)	
Low K	$0.1888 \text{ m} \cdot \text{kg} \cdot \text{s units (m/s)}$
High K	$0.110 \text{ m} \cdot \text{kg} \cdot \text{s units (m/s)}$
Activation energy (Q)	$1.088 \times 10^5 \text{ J} \cdot \text{mol}^{-1}$
Initial crack depth (a_0)	8 and $10 \mu\text{m}$
HEAT TRANSFER DATA	
Temperature of water bath	33 and $65 \text{ } ^\circ\text{C}$
Cylinder radius (R)	0.236 cm
Heat transfer coefficient	$0.1 \text{ cal} \cdot \text{cm}^{-2} \text{ } ^\circ\text{C}^{-1} \text{ s}^{-1}$

[11]. For computational purposes, the crack growth behavior was described by an exponential equation with two sets of constants for the low and high values of the stress-intensity factor (K_1) expressed by

$$V = v_0 \exp[(bK_1 - Q)/RT] \quad (1)$$

³ R-6, Owens-Illinois.

where

- V = rate of slow crack growth,
- v_0 = preexponential factor,
- b = a constant,
- Q = activation energy,
- R = Boltzmann constant, and
- T = absolute temperature.

Values for b and v_0 corresponding to the high and low K_I are given in Table 1. The experimental data for crack growth suggests that no crack growth occurred below the fatigue limit (K_0).

Strength of the glass rods was measured at liquid nitrogen (N_2) temperature in four-point bending with a span between the central loading points of 2.4 cm. This gave an average value of strength of $2.38 \times 10^8 \text{ Nm}^{-2}$ ranging from a minimum value of 1.94×10^8 to a maximum value of $2.76 \times 10^8 \text{ Nm}^{-2}$ for a total of ten specimens. A statistical analysis of the data gave a value for the Weibull parameter, $q \approx 8$,⁴ also listed in Table 1.

Silicon Nitride

Thermal fatigue data for hot-pressed silicon nitride⁵ were obtained by Ammann et al [12] using a specimen geometry which approximated the shape of a vane in a turbine engine. As shown by Evans et al [13], this rate of slow crack growth in this material could be expressed by

$$V = AK_I^n \exp(-Q/RT) \quad (2)$$

where

- V = crack-velocity in ms^{-1} ,
- A, n = constants, and
- $K_I, Q, R,$ and T = as defined in Eq 1.

Table 2 lists the appropriate values for the constants in Eq 2, together with the values for the physical properties pertinent to the thermal stress calculations and fatigue predictions. Tensile strength at room temperature as reported by Nessler [14] ranged from 2.41 to $3.71 \times 10^8 \text{ Nm}^{-2}$ with an average value of $3.33 \times 10^8 \text{ Nm}^{-2}$.

Thermal Environment

Soda-Lime-Silica Glass

The glass rods were subjected to thermal fatigue by repeated quenching

⁴ This symbol corresponds to the letter m in the original Weibull theory.

⁵ HS-130, Norton Company.

TABLE 2—Data for physical properties and crack propagation behavior required for calculations of thermal fatigue resistance of hotpressed silicon nitride.

PHYSICAL PROPERTIES ^a	
Coefficient of thermal expansion (α)	$4.6 \times 10^{-6} \text{ }^\circ\text{C}^{-1}$
Young's modulus of elasticity (E)	$2.9 \times 10^{11} \text{ Nm}^{-2}$
Poisson's ratio (ν)	0.30
Thermal conductivity (K)	$0.033 \text{ cal} \cdot \text{ }^\circ\text{C}^{-1} \text{ cm}^{-1} \text{ s}^{-1}$
Specific heat (c)	$0.30 \text{ cal} \cdot \text{ g}^{-1} \text{ }^\circ\text{C}^{-1}$
Density (ρ)	$3.2 \text{ ggm}^{3/1}$
CRACK PROPAGATION BEHAVIOR	
Constant (A)	$5 \times 10^{14} \text{ m} \cdot \text{ kg} \cdot \text{ s units (m/s)}$
Constant (n)	6
Activation energy (Q)	$170 \text{ kcal} \cdot \text{ mol}^{-1}$
Critical stress intensity factor (K_{Ic})	
Room temperature	$4.7 \text{ MNm}^{-3/2}$
1000 °C	$5.0 \text{ MNm}^{-3/2}$

^a Representative values at 1000 °C, see text.

from an electrically heated laboratory oven into a water bath thermostatically controlled at constant temperatures of 33 or 65 °C. The ends of the specimens of length 7.5 cm were thermally insulated by wrapping with glass insulating tape in order to eliminate fracture initiation at the specimen ends, leaving a gage section of 5.5 cm subjected to the thermal shock. A total of nine specimens were tested simultaneously by holding them lightly at the wrapped ends in a suitable specimen holder, attached to a pneumatically operated air cylinder, controlled with an electric timer with a frequency of four cycles/h. The specimens were kept in the oven for 12 min in order to assure thermal equilibrium prior to the quench. They were then rapidly transferred (1 s) into the water bath where they were held for approximately 2 min, after which they were slowly transferred back into the oven in order to minimize thermal shock on heating. Upon emergence from the water bath, the specimens were examined for fracture after each cycle. Any broken specimen was removed. The number of cycles (N) required for fracture to occur was recorded for the first five specimens of each batch. Due to the extreme scatter in data, N for the lower value of ΔT could not be determined for the sixth to ninth specimen within practical time limits.

Under the quenching conditions just described, the maximum value of tensile thermal stresses occur in the surface during the cooling cycle. This assures the maximum effect of the water environment on fatigue life. On the heating part of the cycle, the thermal stresses in the surface are compressive and are not expected to contribute to the fatigue.

Silicon Nitride

The thermal fatigue resistance of the silicon nitride, as determined by Ammann et al [12], consisted of cycling the specimens between an electrically heated laboratory oven and fluidized bed at 40°C. The specimen was specifically selected such that, for the heat transfer characteristics of the fluidized bed, the temperature and thermal stress history of the specimen was similar to that experienced by a vane in a turbine engine undergoing rapid shutdown. As calculated by finite element analysis, the vane, originally at 1200°C and suddenly subjected to compressor air at 410°C, experiences a transient thermal stress at the forward edge as shown in Fig. 1a with a peak value of approximately $3.0 \times 10^8 \text{ Nm}^{-2}$, also included in Fig. 1a. The transient temperature of the specimen at the forward edge is shown in Fig. 1b.

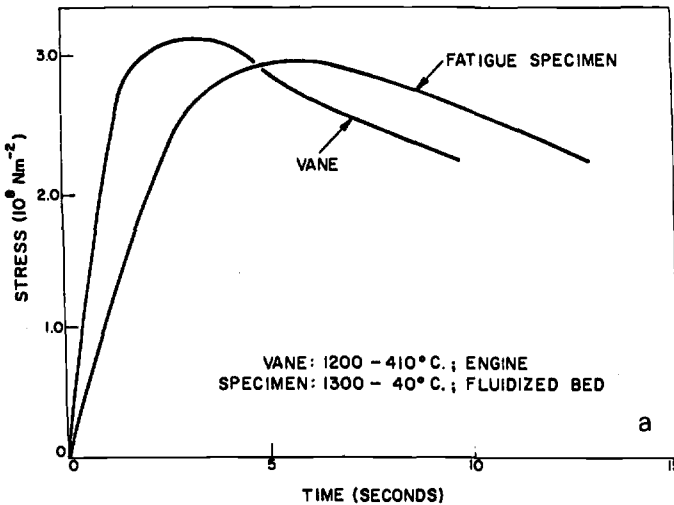


FIG. 1a—Transient thermal stress history of silicon nitride fatigue specimen quenched into fluidized bed and vane in turbine engine subjected to rapid shutdown.

Prediction of Thermal Fatigue Life

The failure prediction of the thermal fatigue life followed the general procedure and assumptions used by Badalian et al [10] for calculations of crack growth during a single-cycle quench, based on the numerical integration of the slow crack growth equation over the period of the ther-

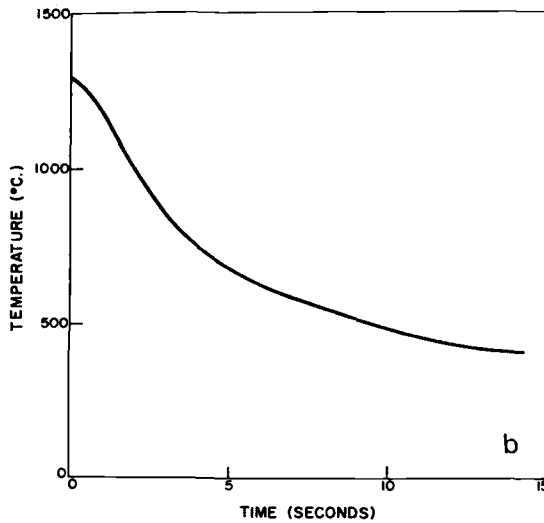


FIG. 1b—Transient temperature in forward edge of thermal fatigue specimen.

mal quench. The crack depth was assumed to be much smaller than the specimen size, such that the crack configuration is closely approximated by an edge crack in a semi-infinite solid. Also, it was assumed that the presence of the crack did not affect the transient temperature field. Finally, in view of the shallow crack depth relative to the specimen size, it was assumed that the crack “sees” a uniform temperature and stress field calculated to exist at the surface of the rod. This latter assumption was shown [15] to be valid for the ratios of flaw depth to specimen size of the present study. For the glass rods, the temperature and stresses were calculated directly from general equations given in the literature for infinitely long rods of circular cross section. For the silicon nitride specimens, the analytical expressions for the temperature and stresses in a cylindrical rod were used by adjusting the appropriate parameters such that the actual temperatures and stresses were closely matched to those shown in Fig. 1. The use of analytical expressions for the transient temperatures and thermal stresses considerably simplifies the calculations of slow crack growth for the silicon nitride specimens.

The transient surface temperatures, $T(R, t)$ of the rod under condition of convective heat transfer is given by [16]

$$T(R, t) = T_0 + (T_1 - T_0) \sum_{n=1}^{\infty} \frac{2\beta_n J_1(\beta_n)}{(m^2 + \beta_n^2) J_0(\beta_n)} \exp(-\beta_n^2 \kappa t / R^2) \quad (3)$$

where

- R = cylinder radius,
 T_0 = temperature of quenching medium,
 T_1 = initial uniform temperature of the cylinder,
 m = Biot's modulus with $m = Rh/k$,
 h = heat transfer coefficient,
 k = thermal conductivity,
 κ = thermal diffusivity with $\kappa = k/\rho c$,
 ρ = density,
 c = specific heat,
 t = time,
 J_0 and J_1 = Bessel functions of the zero and first order,
 β_n = the root of

$$mJ_0(\beta_n) - \beta_n J_1(\beta_n) = 0, \quad n = 1, 2, 3, \dots \quad (3b)$$

From the distribution of the transient temperatures in the rod, the transient thermal stresses at the surface of the rod for the state of generalized plane strain are [17]

$$\sigma_r(R, t) = 0$$

$$\sigma_\theta(R, t) = \sigma_z(R, t) = \frac{E\alpha(T_1 - T_0)}{(1 - \nu)} \left\{ 2 \sum_{n=1}^{n=\infty} \frac{J_1(\beta_n)}{(m^2 + \beta_n^2) J_0^2(\beta_n)} \right. \quad (4)$$

$$\left. [2J_1(\beta_n) - \beta_n J_0(\beta_n)] \exp(-\beta_n^2 \kappa t / \beta^2) \right\}$$

where

- E = Young's modulus of elasticity,
 ν = Poisson's ratio, and
 α = coefficient of thermal expansion.

For the water quench, the heat transfer coefficient, $h \approx 0.1 \text{ cal} \cdot \text{cm}^{-2} \cdot \text{s}^{-1} \cdot \text{C}^{-1}$ was established by Evans et al [15]. The corresponding value of the Biot modulus for this value of h and rod radius of 0.236 cm is $m \approx 10$. For the silicon nitride subjected to thermal fatigue in the fluidized bed, a peak value of thermal stress of $3.0 \times 10^8 \text{ Nm}^{-2}$ for a value of $\Delta T = 1260^\circ\text{C}$ corresponds to an effective Biot modulus, $m_{\text{eff}} \approx 0.65$. Similarly, the time dependence of the transient temperature and thermal stress corresponds to that of a circular cylinder with effective radii of $R_{\text{eff}} = 0.60$ and 1.135 cm, respectively. These values of m_{eff} and R_{eff} are consistent with the average specimen dimensions and the heat transfer coefficient of the fluidized bed with $h \approx 850 \text{ W} \cdot \text{m}^{-2} \cdot \text{C}^{-1}$.

The thermal stress-intensity factor, K_I , is related to the thermal stress by [18]

$$K_I = 1.1215 (R, t) \sqrt{\pi a} \quad (5)$$

In general, the crack depth (a) at any time t can be obtained by integration of Eq 1 or 2, that is

$$a(t) = a_0 + \int_0^t V dt \quad (6)$$

where a_0 is the initial crack-depth at $t = 0$ at the beginning of a thermal cycle. Substitution of Eq 4 into Eq 5, followed by substitution into Eq 1 or 2, with subsequent substitution into Eq 6 results in a nonlinear integral expression for crack depth as a function of time within a given thermal cycle. In order to overcome the mathematical complexity of the resulting expression, a computer program was developed which numerically calculates the crack depth and stress-intensity factor as a function of time for a given number of thermal cycles, as described in detail by Badaliane et al [10]. Whenever the stress-intensity factor (K_I) exceeds K_{Ic} , the specimen is assumed to have failed. If failure did not occur within a given thermal cycle, the procedure was repeated, and the number of cycles required to meet the condition $K \geq K_{Ic}$ was recorded as the thermal fatigue life. For simplicity, the calculations assume that all pertinent properties were independent of temperature. This assumption is quite reasonable for the temperature ranges considered in this study for the glass and silicon nitride. For the glass, the properties listed in Table 1 correspond approximately to 50 to 100°C. For the silicon nitride, the properties listed in Table 2 correspond to approximately 1000°C, which is the estimated average temperature at the time of maximum thermal stress in the fatigue experiments.

Preliminary results showed that, for good agreement with measured fatigue life, predicted fatigue life had to be calculated on the basis of a greater value of flaw depth than the value from the strength test. This is not surprising since it is well known that the strength of brittle materials is controlled by statistical variables and depends on specimen volume or surface area as well as the stress distribution. Such effects were formulated by Weibull [19] on the basis of the concept of the weakest link. For the glass, a similar approach was followed in the present study using the assumption that failure resulted from a surface flaw distribution. This resulted in the value of the ratio of the average strength in the quench test (σ_q) to the average strength in the bend test (σ_b)

$$\sigma_q / \sigma_b \approx 0.59 \quad (7)$$

For $\sigma_b = 2.38 \times 10^8 \text{ Nm}^{-2}$ and a value of $K_{Ic} = 8.7 \times 10^5 \text{ Nm}^{-3/2}$ at liquid N_2 temperature as reported by Wiederhorn [20], an initial flaw depth, $a_0 \approx 8.6 \mu\text{m}$ can be calculated from Eq 5. This value of initial flaw depth should correspond approximately to the flaw depth of the fifth specimen out of nine to fail by thermal fatigue.

No such statistical analysis was carried out for the strength data of the silicon nitride since the number of data points available was insufficient to obtain a reliable value of the Weibull parameter q . For a critical stress intensity factor, $K_{Ic} = 4.7 \text{ MN} \cdot \text{m}^{-3/2}$ [21] at room temperature, the strength values reported earlier correspond to flaw depths ranging from about 40 to 95 μm , with a value of flaw depth of approximately 50 μm for the average value of strength.

Results and Discussion

The experimental and calculated fatigue data for the glass at the bath temperatures of 33 and 65°C are shown in Figs. 2a and 2b, respectively. The fifth specimen to a first approximation represents the average specimen of the nine tested for a given batch. Since the initial flaw depth of the average specimen, $a_0 \approx 8.6 \mu\text{m}$, the agreement between predicted and experimental fatigue behavior must be considered excellent.

In comparing the thermal cycles to failure for the two bath temperatures, it may be noted that the thermal fatigue life at a given ΔT , or the ΔT for a given fatigue life, is less for the bath temperature of 65 than for 33°C. The reason for this is that, although, for a given ΔT , the thermal stresses are independent of bath temperature, the rate and total extent of crack growth per cycle will be higher for the bath temperature of 65°C with its higher specimen temperature than for the bath temperature of 33°C. It is for this reason also that the slope of the ΔT versus N curve for a given bath temperature is controlled by the simultaneous effects of decreasing values of ΔT . It may also be noted that, at the bath temperature of 33°C, the scatter in experimental data for fatigue life at a given value at ΔT is greater than for the bath temperature of 65°C. This probably is the result of the higher rates and extent of crack growth at the higher bath temperature. Included in Figs. 2a and b are the values of the fatigue limits (that is, the temperature differences) below which no thermal fatigue failure will occur. These fatigue limits correspond to those temperature differences, and corresponding stress intensity factor (K_1) is less than the value of stress intensity factor (K_0 , see Table 1) below which no crack growth occurs. These fatigue limits are independent of temperature since K_0 was assumed independent of temperature, in view of the lack of further information.

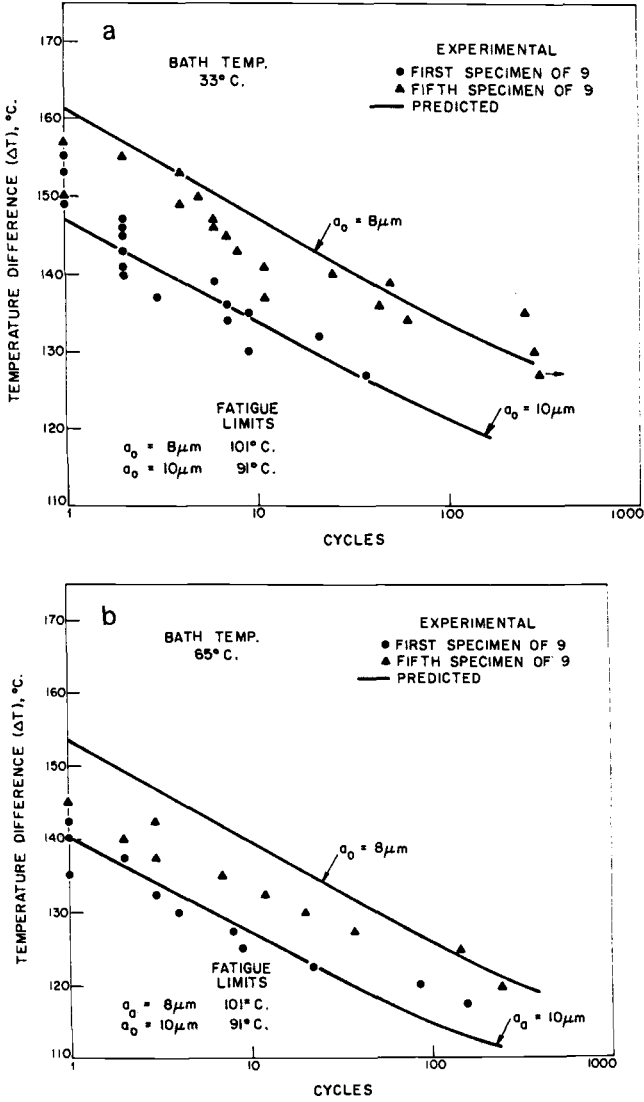


FIG. 2—Predicted and experimental number of cycles-to-failure of glass rods with initial flaw-depth $\approx 8.6 \mu m$ subjected to thermal fatigue into water at (a) 33°C and (b) 65°C.

Figure 3 shows the predicted and observed thermal fatigue behavior of the silicon nitride. In general, the range of flaw depth for the predicted data covers the range of flaw depth of the specimens. However, quantitative agreement with the predicted data occurs for values of initial flaw

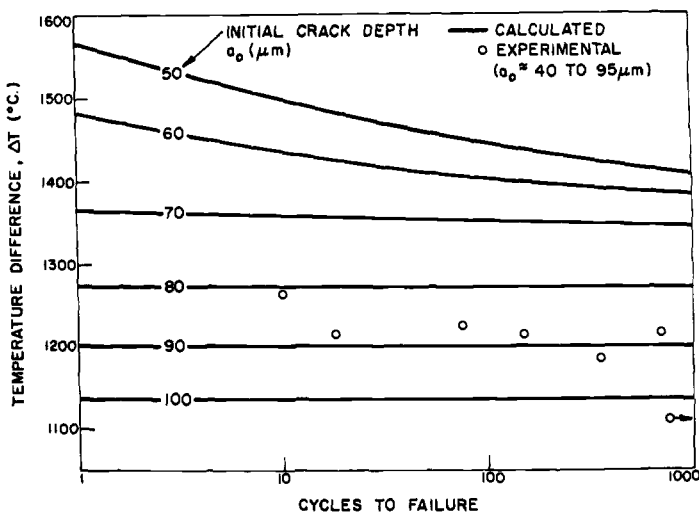


FIG. 3—Experimental and predicted thermal fatigue behavior of silicon nitride subjected to thermal cycling from high temperature into a fluidized bed at 40°C .

depth much higher than the flaw depth corresponding to the average strength of the set of specimens discussed earlier. Again, this discrepancy is likely to be due to the statistical nature of brittle fracture referred to earlier. In Fig. 3, as expected, the slope of the predicted curves corresponding to the lower values of initial crack depth and higher temperatures are steeper than those for the larger values of initial crack-depth. Again, this is due to the simultaneous decrease in temperature as well as level of thermal stress with decreasing temperature difference. For initial crack depths of 80, 90, and $100\ \mu\text{m}$, the temperature levels and thermal stresses are sufficiently low such that the crack growth per cycle is less than $10^{-6}\ \mu\text{m}$. This implies that for these values of a_0 , the specimen stress is just below the fracture stress, even at the first cycle. For these flaw sizes, even a very small decrease in ΔT can make the specimens last almost indefinitely. However, the low slopes of thermal fatigue curves imply that, for accurate thermal fatigue predictions, thermal stresses, temperatures, crack depths, and crack-growth behavior need to be established precisely.

The results for the glass and silicon nitride as just presented indicate that reasonably accurate estimates of thermal fatigue resistance can be made. However, the relative complexity of making such failure predictions is clearly indicated from Table 1, which, including the initial temperature of the specimen, lists a total of 17 values of physical properties, crack propagation behavior, and thermal environment required for such

predictions. This number can be reduced to some extent by describing crack growth behavior by Eq 2 rather than Eq 1. On the other hand, if the temperature dependence of all the physical and environmental variables were included, the degree of complexity of the fatigue calculations would increase manyfold. Also, the cumulative error as the result of the uncertainty in the numerical value for each variable can cause large discrepancies between predicted and observed fatigue life. Especially in view of its semiempirical nature, estimating the proper flaw depth by use of the Weibull theory introduces the largest uncertainty in estimating fatigue life.

In this respect, it should be noted that using the approach outlined in this paper, differences in predicted life for different thermal environments should be more reliable than predicted values of fatigue life for any given simple condition. As a specific example, for the glass rods, for a given fatigue life at low N , the observed decrease of approximately 7°C for the two bath temperatures is correctly predicted. For this reason, the computational technique developed for this study can be successfully coupled to experimental fatigue studies and thereby increase the reliability of the fatigue life predicted for some other condition. Such an approach becomes very useful in comparing calculated and observed fatigue life under controlled conditions in order to predict fatigue life for a thermal environment not easily duplicated in the laboratory. In this manner, for instance, the initial slope of the thermal fatigue curve at small values of N may be determined experimentally, from which the thermal fatigue behavior for higher values of N may be predicted by using the present technique. As a further example, for the silicon nitride, one can compute the critical temperature differences (ΔT_c) required for catastrophic failure in one cycle for flaw sizes smaller than those considered in the present study. Such results are shown in Fig. 4, which indicate that near the values of $a_0 = 10$ m, ΔT_c is virtually independent of crack size. This suggests that decreasing crack size to a value of $10\ \mu\text{m}$, which is expected to result in large increases in strength at room temperature, nevertheless will not permit major increases in engine operating temperatures. For comparison, ΔT_c in the absence of crack growth is shown in Fig. 4 by the dotted line. The large differences in ΔT_c especially at the lower value of a_0 , are the direct result of the slow crack growth. This observation suggests that a reduction in the rate of crack growth in order to increase operating temperatures is preferred to reduction in flaw size. At low engine temperatures at which crack growth is negligible, of course, reductions in flaw size should prove beneficial in that impact strength, etc., should be significantly increased.

Similar approaches become especially useful for full-scale engineering applications on which actual experimental testing would be highly impractical. As a result, computer simulation of thermal fatigue in conjunction with an experimental program can constitute a powerful technique in

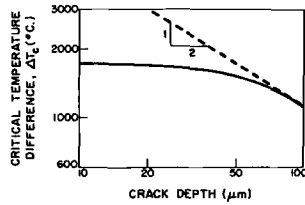


FIG. 4—Predicted critical temperature difference required to cause catastrophic failure in silicon nitride as a function of flaw depth.

making reliable estimates of thermal fatigue resistance of brittle materials.

In summary, a potentially useful technique was developed to calculate the thermal fatigue behavior of brittle materials and was applied successfully to predict the thermal fatigue resistance of soda-lime-silica glass and silicon nitride.

Acknowledgment

This study was conducted as part of a long-range research program on thermal stress fracture of brittle materials supported by the Army Research Office, Durham, under grant DA-ARO-A-31-124-73-G45.

References

- [1] Williams, L. S., *Transactions of the British Ceramic Society*, Vol. 55, 1956, p. 287.
- [2] Krohn, D. A. and Hasselman, D. P. H., *Journal of the American Ceramic Society*, Vol. 55, 1972, p. 208.
- [3] Gurney, C. and Pearson, S., *Proceedings*, Physics Society, London, Section B, Vol. 62, 1958, p. 537.
- [4] Kossowsky, R., *Journal of the American Ceramic Society*, Vol. 56, 1973, p. 531.
- [5] Sarkar, B. K. and Glinn, T. G. J., *Transactions of the British Ceramic Society*, Vol. 69, 1970, p. 199.
- [6] Tumanov, V. I., Goldberg, Z. A., Chernyshev, V. V., and Pavlova, V. I., *Poroshkovaya Metallurgiya*, Vol. 10, 1966, p. 71.
- [7] *Fracture Mechanics of Ceramics*, Vol. 2, *Microstructure, Materials and Applications*, Bradt, R. C., Hasselman, D. P. H. and Lange, F. F., Eds., Plenum Press, New York, 1974.
- [8] Evans, A. G., *Journal of Materials Science*, Vol. 7, 1972, p. 1137.
- [9] Evans, A. G. and Fuller, E. R., *Metallurgical Transactions*, Vol. 5, 1974, p. 27.
- [10] Badaliane, R., Krohn, D. A., and Hasselman, D. P. H., *Journal of the American Ceramic Society*, Vol. 57, 1974, p. 432.
- [11] Wiederhorn, S. M. and Bolz, L. H., *Journal of the American Ceramic Society*, Vol. 53, 1970, p. 543.
- [12] Armann, C. L., Doherty, J. E., and Nessler, C. G., *Journal of Materials Science*, to be published.
- [13] Evans, A. G., Russell, L. R., and Richerson, D. W., *Metallurgical Transactions*, Vol. 6A, 1975, pp. 707-716.
- [14] Nessler, C. G., *Transactions of the American Society of Mechanical Engineers*, to be published.

- [15] Evans, A. G., Linzar, M., Johnson, H., Hasselman, D. P. H., and Kipp, M. E., *Journal of Materials Science*, to be published.
- [16] Carslaw, H. S. and Jaeger, J. C., *Conduction of Heat in Solids*, Clarendon Press, Oxford, England, 1969.
- [17] Boley, B. A. and Weiner, G. H., *Theory of Thermal Stresses*, Wiley and Sons, New York, 1960.
- [18] Sih, G. C., *Handbook of Stress Intensity Factors*, Lehigh University, Bethlehem, Pa., 1973.
- [19] Weibull, W., *Akad. Handl.*, No. 151, 1939.
- [20] Wiederhorn, S. M., *Journal of the American Ceramic Society*, Vol. 52, 1969, p. 99.
- [21] Wiederhorn, S. M. in *Fracture Mechanics of Ceramics*, Bradt, R. C., Hasselman, D. P. H., and Lange, F. F., Eds., Plenum Press, New York, 1974.

D. A. Spera¹ and E. C. Cox¹

Description of a Computerized Method for Predicting Thermal Fatigue Life of Metals

REFERENCE: Spera, D. A. and Cox, E. C., "Description of a Computerized Method for Predicting Thermal Fatigue Life of Metals," *Thermal Fatigue of Materials and Components*, ASTM STP 612, D. A. Spera and D. F. Mowbray, Eds., American Society for Testing and Materials, 1976, pp. 69-85.

ABSTRACT: A computer program called TFLIFE which can be used to predict the thermal fatigue life of metals and structural components from conventional metal properties is described. This program is used as a subroutine with a main program supplied by the user. The main program calculates input cycles of temperature and total strain for TFLIFE which then calculates a stress cycle, creep and plastic strain damage, and cyclic life. A unique feature of TFLIFE is that it calculates lives according to several different failure criteria for the same input data. These criteria are surface crack initiation, interior crack initiation, and complete fracture of both unnotched and notched fatigue specimens. Sample output tables are shown, together with results for two typical problems: (a) thermal-mechanical fatigue of bar specimens of the tantalum alloy T-111 and (b) thermal-stress fatigue of wedge specimens of the nickel alloy B-1900. Thermal fatigue lives calculated using TFLIFE have been verified by comparison with a variety of laboratory test data on different types of alloys. The computer program is now ready for more extensive evaluation on structural components as well as additional laboratory specimens.

KEY WORDS: thermal fatigue, fatigue (metals), crack initiation, computer programs, thermal stress, life prediction, creep

This paper describes a fatigue life calculation system utilizing a computer program called TFLIFE. TFLIFE calculates the low-cycle fatigue life of metals subjected to simultaneous thermal and strain cycling. In conjunction with an elastic structural analysis program, TFLIFE can be used to predict the fatigue life of complete components in high-temperature equipment such as engines and heat exchangers. This paper contains a general description of the program, typical output tables, and results for two sample laboratory test problems.

¹ Consultant, Fatigue Branch, and mathematician, Computer Services Division, respectively, Lewis Research Center, Cleveland, Ohio 44135.

The original version of TFLIFE was written more than eight years ago to aid in the development of a creep damage theory for thermal fatigue [1,2].² Since that time, it has grown in scope and function, serving as a useful tool for research on high-temperature metals [3]. It now includes recent developments in creep-fatigue theory and input/output formats which make it suitable for general use. To date, TFLIFE results have been verified by thermal fatigue tests on laboratory specimens such as bars, tapered disks, wedges, and simulated turbine blades [1-4]. In these tests, thermal and mechanical loads were applied by fatigue machines, fluidized beds, and burner rigs to specimens of nickel, iron, cobalt, and tantalum alloys. TFLIFE is now ready for more extensive evaluation by the technical community on complete components as well as laboratory specimens.

A unique feature of TFLIFE is that it calculates thermal fatigue lives according to each of three failure criteria, based on one set of input data. These criteria are (a) surface crack initiation, (b) interior crack initiation (applicable to coated metals), and (c) complete fracture of thermal-mechanical fatigue specimens, both unnotched and notched. Including these three criteria in a single computer program produces a very general and complete analysis of thermal fatigue resistance.

A complete set of the equations used in TFLIFE is given in Ref 5, together with derivations. Computer time for a typical problem is 8 to 17 s on a time-sharing system (IBM 360/67). Required storage capacity is approximately 12 000 words.

General Description of TFLIFE

Figure 1 is a schematic diagram which describes the general sequence of operations performed by the life calculation system. TFLIFE is a subroutine which is called by a user-supplied main program. This main program, discussed later, contains all calculations of temperature and total strain specific to the specimen or component being analyzed. Initially, the main program calls TFLIFE which reads its own input data (Block I) and divides both the heating and cooling periods into approximately 100 increments. The input data for TFLIFE are of two types: (a) conventional mechanical properties which describe the monotonic tensile and creep-rupture behavior of the metal and (b) optional empirical constants based on cyclic data. The conventional metal properties must be given for a range of temperatures which includes the thermal cycle being analyzed. The optional empirical constants pertain to cyclic strain hardening, strain concentration, and time-independent fatigue behavior. Nominal values for these constants are contained in TFLIFE for cases in which cyclic data are not available. Input data can be in any of the following three systems of units for stress and

² The italic numbers in brackets refer to the list of references appended to this paper.

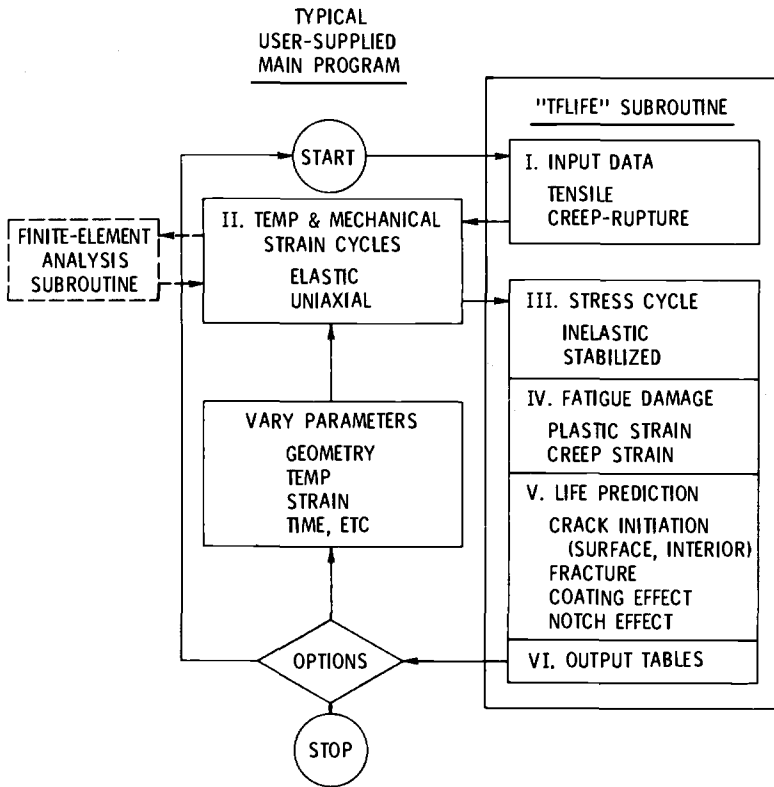


FIG. 1—Schematic diagram of computer program for predicting thermal fatigue life.

temperature: (a) pounds per square inch and Fahrenheit degrees, (b) grams per square millimeter and Celsius degrees, or (c) newtons per square centimeter and Kelvin degrees. SI (Systeme International) units can be specified for the bulk of the output, irrespective of the input unit system. TFLIFE then returns to the main program.

Temperature, Strain, and Stress Cycles

At Block II in the main program, cycles of temperature and mechanical strain (total strain less free thermal expansion) must be calculated for a potential failure location in the specimen or structure. The complexity of these computations can vary greatly, depending on the structure being analyzed. For a strain-cycled thermal-mechanical fatigue specimen, Block II may be required only to generate saw-tooth or sinusoidal cycles. For a thermal-stress fatigue specimen, it may be necessary to calculate transient

temperature distributions and the strains which result from them. In this case, a linear elastic analysis is usually sufficient, according to the hypothesis of total strain invariance proposed in Ref 6. This hypothesis states that, under conditions of thermal stress, the displacements in a body are substantially independent of local inelastic strains. Thus, displacements obtained by a linear elastic analysis can be used to calculate mechanical strains which can later be divided into elastic, plastic, and creep components. For a complex component, it may be necessary for the main program to call a finite-element analysis subroutine. In all cases, a local temperature and a local uniaxial mechanical strain are calculated for each time increment. The system then calls TFLIFE a second time.

In Block III, an incremental stress-strain analysis is performed which divides the mechanical strain cycle into elastic, plastic, and creep components. This analysis is repeated until shakedown occurs, when the stress-strain hysteresis loop becomes stable and repetitive. In this way, a stress, a plastic strain increment, and a creep strain increment are calculated for each time increment. Approximately two thirds of TFLIFE's computing time is used in these calculations. Upon completion of Block III, the mechanical behavior of the material at the potential failure location has been described thoroughly in terms of temperature, stress, and strain. Fatigue damage can now be calculated.

Fatigue Damage and Life Predictions

In Block IV, TFLIFE calculates the fraction of the metal's life consumed in one cycle. This calculation uses a fatigue damage model which we call the generalized damage fraction theory [5]. The model is so named because it integrates elements from the work of many investigators into a unified, practical method of life analysis. This theory uses Palmgren's linear cumulative damage hypothesis [7] as modified by Taira to include time as a variable [8]. Fatigue damage is assumed to be of two types: (a) elastic-plastic strain damage which is independent of time and (b) creep strain damage which is time-dependent.

Elastic-plastic strain damage is calculated using an empirical fatigue equation of the exponential type, derived from equations proposed by Basquin [9], Manson [10,11], and Coffin [12]. Equations for creep strain damage combine contributions by Robinson [13], Hoffman [14], Taira [8], Swindeman [15], and Spera [1-5].

In Block V, life predictions are now made for each of the following three failure criteria: (a) surface crack initiation, (b) interior crack initiation, and (c) complete fracture. The first criterion applies mainly to thermal-stress fatigue of an uncoated material. The second criterion can be used to predict the thermal-stress fatigue life of a coated material in which the fatigue life of the coating exceeds that of the substrate material. The third criterion is

limited to thermal-mechanical fatigue testing in which strains and temperatures are nominally uniform in the test section of the specimen. The program provides for three strain concentration factors so that the user can calculate the effect of notch severity on fatigue life. One of these factors is always unity, representing the unnotched condition. The other two factors may be specified arbitrarily by the user or nominal values of two and three will be supplied by the program. For notched specimens, the input temperature and mechanical strain cycles are considered to be nominal rather than local. Thus, five cyclic lives are calculated in Block V for one pair of temperature and mechanical strain cycles, as calculated in Block II. This is a unique feature of the TFLIFE computer program.

Output Tables

In Block VI, the results of the life analysis are printed in the form of six tables. Samples of some of these tables are shown in Fig. 2 for a thermal-mechanical fatigue problem which will be discussed later. A table which is not shown documents the applied cycle in terms of the mechanical strainrange plus temperature, strain, and time limits. Figure 2*a* contains the actual life predictions. These are presented for each of the three failure criteria just discussed. This figure also contains damage fractions which show the theoretical proportions of the damage associated with creep strain and elastic-plastic strain for each predicted life. The sum of the two damage fractions is always unity. Also, interior crack initiation and complete fracture are assumed to occur simultaneously in a thermal-mechanical fatigue specimen because of the nominally uniform strain and temperature conditions in the test section.

Figure 2*b* presents temperature, strain, and stress as functions of time during heating and cooling. If the user wishes, this figure can be doubled or tripled in length, resulting in smaller time increments and more detailed data on the cycle. Figure 2*c* contains the monotonic tensile data for the material as a function of temperature. This figure is constructed from the actual input data using linear interpolation. The number, order, and spacing of temperatures for which property data are given are arbitrary.

The cyclic hardening ratio in the footnote to Fig. 2*c* relates cyclic and monotonic stress-strain data. This ratio is an optional scaling factor for proportionately increasing or decreasing yield and ultimate tensile stress values at all temperatures. It is specified by the user according to one of the following three criteria: (a) If no cyclic stress-strain data are available, the hardening ratio is unity, which represents neutral hardening. Also, unity is the nominal value used by the program in the absence of a specified value. (b) If partial cyclic stress-strain data are available (for example, at only one temperature) the hardening ratio is adjusted until first-order differences between calculated and observed stresses are eliminated. (c) If complete

FAILURE CRITERION		STRAIN CONC. FACTOR	CYCLES TO FAILURE	DAMAGE FRACTIONS	
				PLASTIC	CREEP
CRACK INITIATION	SURFACE	1.00	41	0.042	0.958
	INTERIOR	1.00	41	0.042	0.958
COMPLETE FRACTURE (THERMAL-MECHANICAL FATIGUE ONLY)		1.00	41	0.042	0.958
		2.15	36	0.167	0.833
		3.00	31	0.271	0.729

(a) Fatigue life and damage predictions.

FIG. 2—Sample output tables (in-phase thermal-mechanical fatigue of the tantalum alloy T-111).

TIME, MIN	TEMP, DEG K	STRAIN			STRESS, N/SQ CM
		MECH.	PLASTIC	CREEP	
0.000	478	-0.009570	-0.000000	0.000000	-56118
0.039	506	-0.008622	-0.000000		
0.078	535	-0.007662			
0.117	563				
			0.009365	0.002253	42962
			0.009365	0.002792	40846
		0.008740	0.009365	0.003317	38684
1.290	1421	0.009138	0.009365	0.003228	36739

(b) Thermal, strain, and stress cycles, heating half cycle.

FIG. 2—Continued.

TEMP, DEG K	YOUNG'S MODULUS, N/SQ CM	YIELD STRESS (.002), N/SQ CM	ULTIMATE TENSILE STRESS, N/SQ CM	TENSILE DUCTILITY	POISSON'S RATIO	THERMAL EXPANSION FROM RT, PER DEG K
200	18.7E 06	56000	63500	0.800	0.265	6.05E-06
269	18.3E 06	51000	60100	1.000		
339	18.1E 06	48075	57000			
408	17.9E 06	46000	54000			
		43500	49500	1.160	0.280	7.09E-06
		40000	47800	1.255	0.290	7.14E-06
		37000	46100	1.350	0.300	7.19E-06
1799	15.2E 06	12000	15000	1.450	0.316	7.25E-06

1 RATIO OF CYCLIC TO MONOTONIC YIELD AND ULTIMATE STRESSES = 1.43

(c) Monotonic stress and strain properties.

FIG. 2—Continued.

cyclic stress-strain data are available, they are used to calculate equivalent monotonic data for a cyclic hardening ratio of unity.

Figure 2d is a summary of the empirical equations which are used in TFLIFE to calculate creep and rupture times [1]. The coefficients are calculated from test data by means of regression analysis. Most of the commonly used time-temperature parameters are included in these general equations as special cases, either exactly or to a close approximation. In this way, the equations in Fig. 2d represent an attempt to select the optimum

$\text{LOG}(Z) = A + B \cdot \text{LOG}(X) + C \cdot X + D \cdot X^2 + E \cdot Y \quad Z = T1 \wedge TR$						
T1 = TIME TO 1 PCT CREEP, HR			TR = TIME TO RUPTURE, HR			
CREEP RATE = 0.01/T1, HR ⁻¹			X = STRESS/1000 N/SQ CM			
Y = (TEMP/1000 K) ^{BETA} OR LOG(TEMP/1000 K), IF BETA = 0						
Z	A	B	C	D	E	BETA
T1	-9.198	-4.6670	0.00000	-.001569	23.791	-1.00
TR	-7.729	-4.6670	0.00000	-.001569	23.478	-1.00

(d) Monotonic creep-rupture behavior.

FIG. 2—Continued.

time-temperature parameter for the available data. If only limited creep rate data are available, simplifying assumptions can be made by the user so that some of the curve-fit constants in the equation for time to 1 percent creep are the same as those in the equation for time to rupture.

A final table (not shown) contains data which document the iterations required to achieve convergence. Each iteration is a new calculation of the stress and inelastic strain cycles. The stress at the end of the cooling cycle is carried forward to start the incremental stress analysis for the next iteration. A residual inelastic strain is recorded which is the sum of the plastic and creep strains at the end of each iteration. (Both these quantities are set to zero at the start of each iteration.) A residual inelastic strain of zero represents a completely stable, repetitive stress-strain hysteresis loop. When the residual strain becomes less than ten microunits, a curve-fit procedure is used to accelerate convergence, and iteration is terminated after two additional cycles.

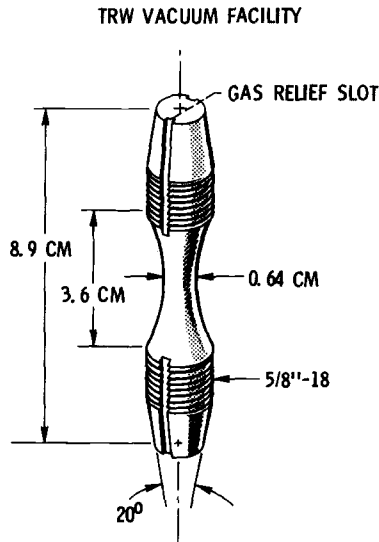
Options

After output tables have been printed for one set of input data, there is a minimum of three options which the user can choose to include in the main

program: (a) terminating the program, (b) starting the solution to a new problem by reading a new set of data, or (3) varying parameters in the input data which are already stored in the computer and starting the solution to a modified problem. The third option enables the user to perform a parametric study from a single set of input data. As mentioned previously, the operations in the main program are determined by the needs of the user. The TFLIFE system, shown schematically in Fig. 1, includes sufficient flexibility to satisfy a wide variety of such needs.

Sample Results

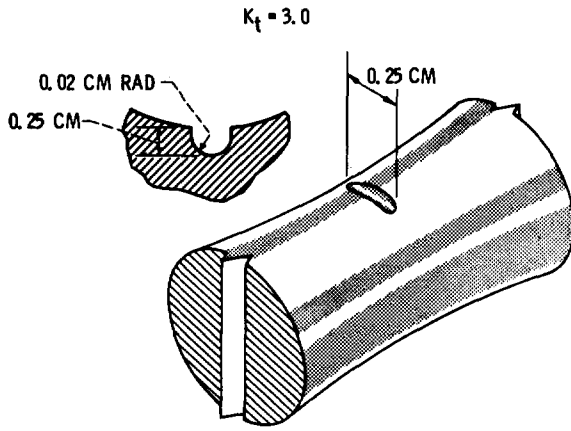
The application of TFLIFE to different types of thermal fatigue conditions will now be illustrated by showing some typical results for the following two problems: (a) thermal-mechanical fatigue of bar specimens of the tantalum-base alloy T-111 tested in vacuum [16] and (b) thermal-stress fatigue of wedge specimens of the nickel-base alloy B-1900 tested in fluidized beds [17,18]. Figure 3 shows the geometry of these two types of specimens. The slot notch shown in Fig. 3b has a theoretical elastic stress (or strain) concentration factor of 3.0 [19]. Predicted lives are given for un-notched and notched bars of T-111 as a function of imposed strain range



(a) Thermal-mechanical fatigue bar specimen [16].

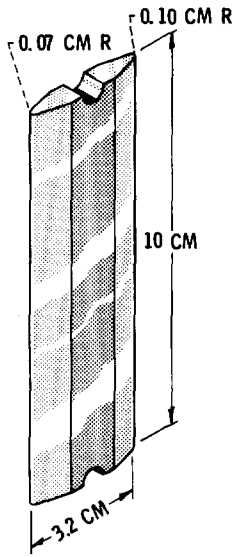
FIG. 3—Geometry of specimens in sample problems.

combined with either isothermal or in-phase thermal cycling. The B-1900 wedge specimen calculations include a study of the effects of changes in



(b) Detail of tangential slot notch.

FIG. 3—Continued.



(c) Thermal-stress fatigue wedge specimen [17,18].

FIG. 3—Continued.

cycle time and edge radius for both the uncoated and aluminide-coated conditions of the alloy.

Thermal-Mechanical Fatigue of T-111 Bars

T-111 was selected as a sample alloy because of the variety of thermal-mechanical fatigue data reported on it in Ref 16. Also, its stress-strain behavior is as complex as any which the user is likely to encounter. Therefore, T-111 provides an excellent test of the capabilities of TFLIFE with respect to thermal-mechanical fatigue. The output tables presented in Fig. 2 are taken from one of the T-111 test cases.

Figure 4 shows the simple type of mechanical strain and temperature cycles programmed for these tests. When diametral strain is the control variable, the normal input variable of axial strain is usually unknown prior

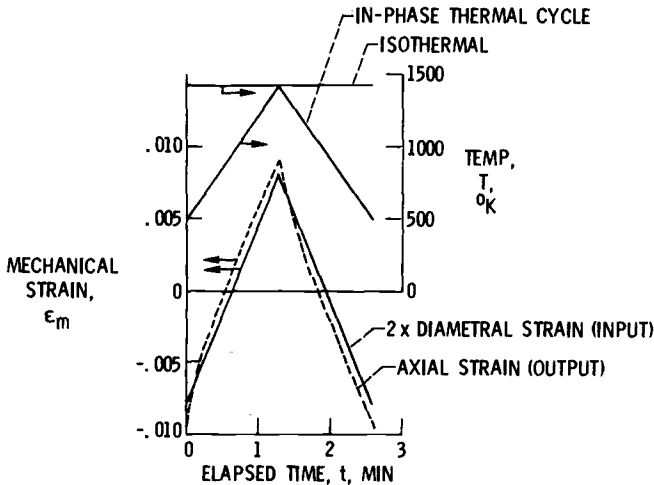


FIG. 4—Typical thermal and strain cycles applied during thermal-mechanical fatigue testing of the tantalum-base alloy T-111.

to the stress analysis (Fig. 1, Block III). TFLIFE resolves this difficulty by using an equivalent axial strain equal to twice the diametral strain plus an equivalent elastic modulus equal to Young's modulus divided by twice Poisson's ratio [5].

Figure 5 illustrates the stress-strain behavior calculated for both the isothermal and in-phase thermal cycles with equal strain ranges. The significantly different shapes of these two calculated hysteresis loops are confirmed by test data [16]. Cyclic hardening ratios were selected according to the criteria described previously for cases with partial cyclic stress-strain data (see output tables). Two different cyclic hardening ratios were required

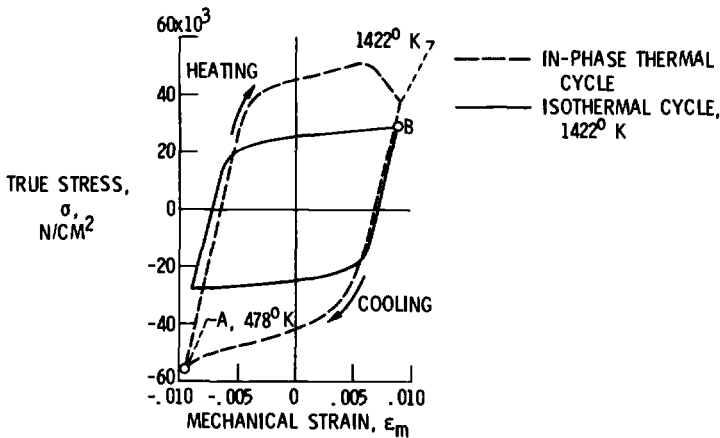


FIG. 5—Typical calculated stress-strain behavior during thermal-mechanical fatigue testing of the alloy T-111.

for these two cycles because the stresses in the in-phase thermal cycle were found to be significantly larger than those in the isothermal cycle for equal strain ranges. A hardening ratio of 1.43 was needed to correlate calculated and observed stresses at Point A in the in-phase loop. A much smaller factor, 1.08, matched the calculated stress amplitude in the isothermal loop (Point B) to the measured value. These hardening ratios reflect the complex cyclic hardening which has been observed in T-111. For behavior of this type, an accurate estimate of the hardening ratio is essential to accuracy in the prediction of creep damage and life.

Figure 6 shows the results of the life calculations for isothermal cycling as a function of axial mechanical strain range. The failure criterion for these tests was complete fracture of the bar specimen. Predicted behavior with a strain concentration factor of unity is in good agreement with the unnotched specimen data, as shown by the open symbols. This correlation between theory and experiment gives a measure of confidence in the extrapolated behavior for lives greater than 1000 cycles. For the notched specimens (closed symbols), predicted behavior is somewhat conservative when the strain concentration factor is equated to its theoretical elastic value of 3.00. The available data were best fit using an empirical strain concentration factor of 2.15. Life predictions based on this factor are given by the dashed line in Fig. 6. In the absence of notched specimen data, the theoretical elastic strain concentration factor would be used as input in TFLIFE.

In Fig. 7, predicted and observed lives are compared for tests with in-phase thermal cycling. Unlike the isothermal tests, the in-phase tests of T-111 showed little notch effect. The TFLIFE predictions are in agreement

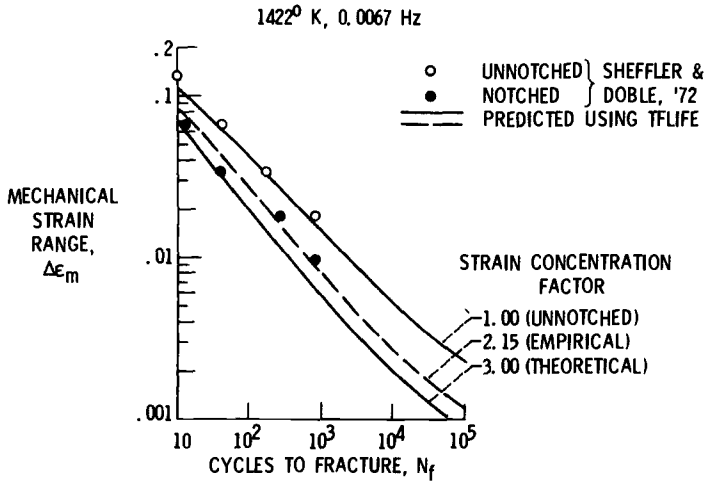


FIG. 6—Comparison of predicted and observed fatigue lives for isothermal cycling of the alloy T-111 in the unnotched and notched conditions (1422 K, 0.0067 Hz).

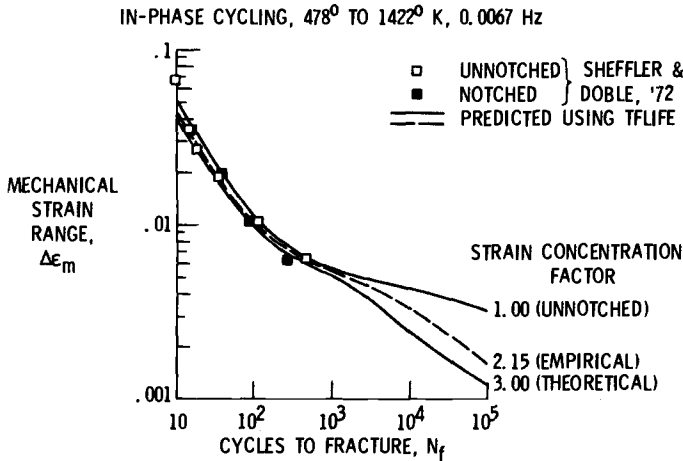


FIG. 7—Comparison of predicted and observed fatigue lives for in-phase thermal cycling of the alloy T-111 in the unnotched and notched conditions (478 to 1422 K, 0.0067 Hz).

with the data, whether the strain concentration factor is assumed to be 1.00, 2.15, or 3.00. This insensitivity to strain concentration is related directly to an assumption in the creep damage model in TFLIFE. The assumption is that interior creep damage is not affected by a surface strain concentration but depends only on the nominal stress. Thus, the strain concentration affects only the elastic-plastic strain component of damage. During in-phase

thermal cycling at relatively large strain ranges (lives less than 1000 cycles) most of the damage results from creep (Fig. 2a). Therefore, the model indicates that strain concentration has only a minor effect on the predicted lives at these strain ranges for in-phase cycling. However, as the strain range decreases below about 0.004, elastic-plastic strain damage becomes dominant over creep damage and a significant notch effect is predicted for this alloy. Figure 7 is an example of an extrapolation of data by TFLIFE that indicates a notch effect at long life which is not present in the short-life data.

Thermal-Stress Fatigue of B-1900 Wedges

Rapid heating and cooling of the wedge specimens shown in Fig. 3 produces edge cracks similar to those often found in turbine blades and vanes. The sequence of calculations required for predicting the initiation period for such cracks is illustrated by the results shown in Figs. 8–11. In contrast to the simple cycles shown in Fig. 4, the transient temperature and

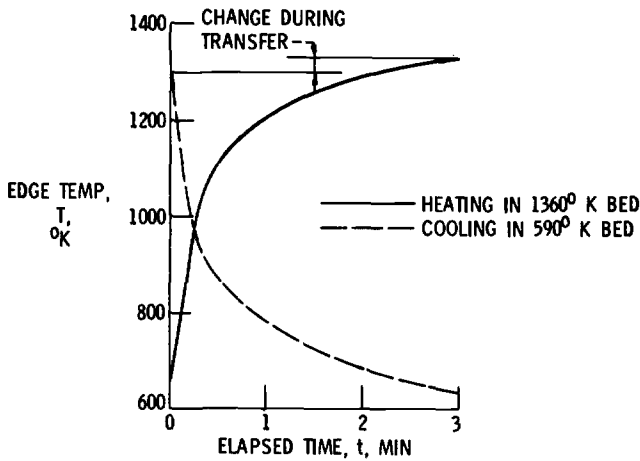


FIG. 8—Typical temperature transients at the edge of wedge specimens of the alloy B-1900 during thermal-stress fatigue testing.

strain inputs for thermal-stress fatigue problems are quite complex. Consequently, Block II in the main program (Fig. 1) is much more complex for thermal-stress fatigue than for thermal-mechanical fatigue problems. For instance, in this B-1900 problem, thermocouple data taken at several points in the interior of the wedge specimen are curve-fit in Block II for each of the approximately 100 time increments during heating and the same number of time increments during heating and the same number of time increments

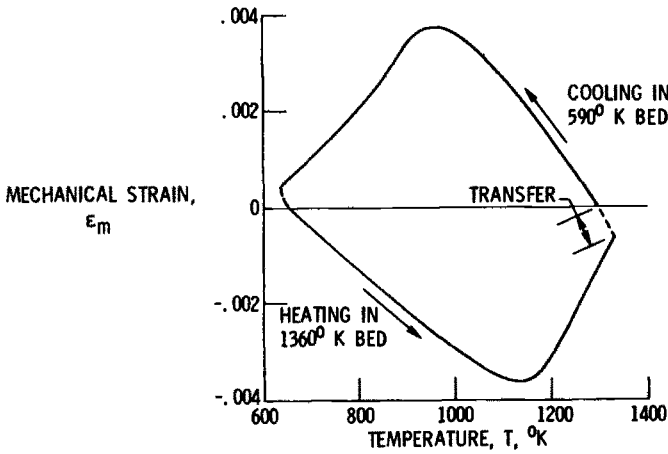


FIG. 9—Typical calculated strain-temperature behavior during thermal-stress fatigue testing of the alloy B-1900.

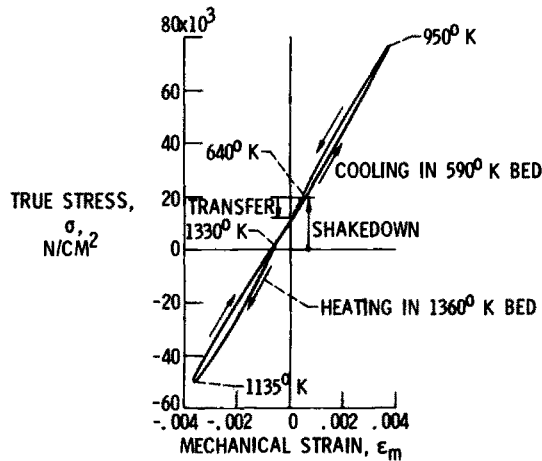
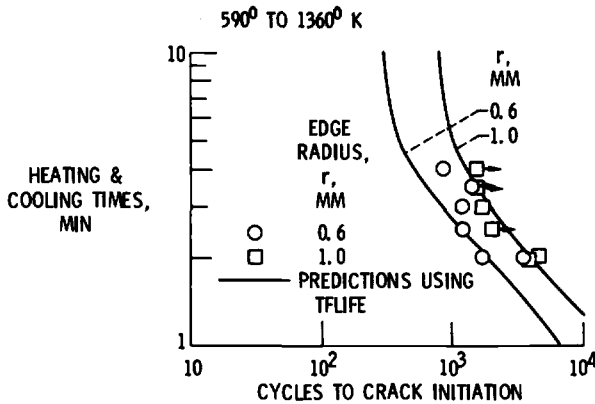
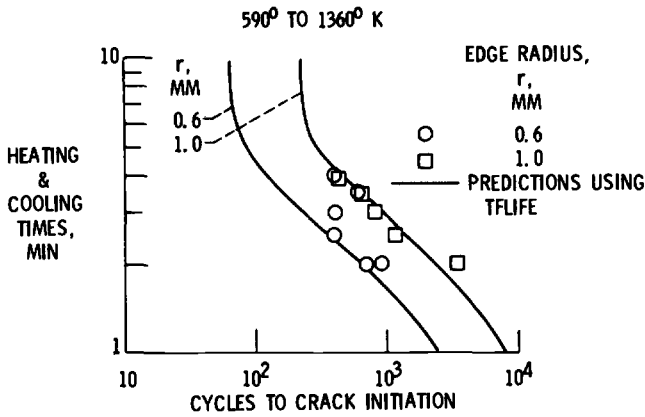


FIG. 10—Typical calculated stress-strain behavior during thermal-stress fatigue testing of the alloy B-1900.

during cooling, as described in Ref 18. These curve-fits are then used to calculate the temperature and mechanical strain cycles at the specimen edges.

Figure 8 shows typical edge temperature transients during heating and cooling. Note that the length of the heating and cooling periods is not sufficient for the temperatures to reach steady-state levels equal to the bed tem-



(a) Uncoated condition.
(b) Aluminide-coated condition.

FIG. 11—Comparison of predicted and observed thermal-stress fatigue lives for the alloy B-1900 (wedge specimens tested in fluidized beds at 590 and 1360 K; data from Ref 17).

peratures. In Fig. 9, transient mechanical strain is plotted versus edge temperature rather than versus time. This is often a convenient way to display transient data and to ensure that calculated strain and temperature cycles are compatible. Changes during one of the transfer periods are also noted in Figs. 8 and 9 when the specimen is moved from the cooling to the heating bed.

A typical stress-strain hysteresis loop for thermal-stress fatigue is presented in Fig. 10. A cyclic hardening ratio of unity (that is, neutral hardening) was used to calculate this loop in the absence of pertinent cyclic stress-strain

data. Comparison of Figs. 5 and 10 shows the wide variety of stress-strain behavior possible during thermal fatigue. The hysteresis loop in Fig. 10 has a figure-eight shape which is produced by changes in elastic modulus with temperature combined with the presence of only small amounts of inelastic strain. The shakedown process during iteration is shown to produce an increase in this cycle's mean stress.

Figure 11 summarizes the dependence of the number of cycles required to initiate edge cracks on the parameters of cycle time and edge radius, for uncoated and aluminide-coated conditions. Comparison of predicted curves with test data indicate that TFLIFE can correctly model thermal-stress fatigue life on the basis of thermocouple data and monotonic material properties. Furthermore, TFLIFE can be used to predict behavior outside the range of the test parameters.

Conclusions

The TFLIFE computer program has been found to be a useful tool for analyzing thermal fatigue data in terms of conventional metal properties and for predicting the thermal fatigue life of metals. It contains models for the major damaging phenomena which occur during a general thermal-fatigue cycle, at least to a first-order approximation. Thermal fatigue lives calculated using TFLIFE have been verified by comparison with a variety of laboratory test data on different types of alloys. This computer program is ready for more extensive evaluation by the technical community, not only on additional laboratory specimens but also on structural components.

References

- [1] Spera, D. A., "A Linear Creep Damage Theory for Thermal Fatigue of Materials," Ph.D. thesis, University of Wisconsin, Madison, 1968.
- [2] Spera, D. A., "Calculation of Thermal-Fatigue Life Based on Accumulated Creep Damage," NASA TN D-5489, National Aeronautics and Space Administration, Oct. 1969.
- [3] Spera, D. A. and Grisaffe, S. J., "Life Prediction of Turbine Components: On-going Studies at the NASA Lewis Research Center," NASA TM X-2664, National Aeronautics and Space Administration, Jan. 1973.
- [4] Spera, D. A. in *Fatigue at Elevated Temperatures*, ASTM STP 520. American Society for Testing and Materials, 1973, pp. 648-657.
- [5] Spera, D. A., "Equations for Predicting Thermal Fatigue Life," NASA TM (to be published), National Aeronautics and Space Administration.
- [6] Mendelson, A. and Manson, S. S., "Practical Solution of Plastic Deformation Problems in Elastic-Plastic Range," NACA TN 4088, National Advisory Committee for Aeronautics, Sept. 1957.
- [7] Palmgren, A., *Zeitschrift des Vereines Deutscher Ingenieure*, Vol. 68, No. 14, April 1924, pp. 339-341. (English translation, NASA TT F-13460, National Aeronautics and Space Administration, March 1971.)
- [8] Taira, S. in *Creep in Structures*, N. J. Hoff, Ed., Springer Verlag, Berlin, 1962, pp. 96-124.

- [9] Basquin, O. H., *Proceedings*, American Society for Testing and Materials, Vol. 11, 1910, pp. 625, 630.
- [10] Manson, S. S., "Behavior of Materials under Conditions of Thermal Stress," NACA TN-2933, National Advisory Committee for Aeronautics, 1953.
- [11] Manson, S. S., *Experimental Mechanics*, Vol. 5, No. 7, July 1965, pp. 193-226.
- [12] Coffin, L. F., Jr., *Transactions*, American Society of Mechanical Engineers, Vol. 76, Aug. 1954, pp. 931-950.
- [13] Robinson, E. L., *Transactions*, American Society of Mechanical Engineers, Vol. 74, 1952, pp. 777-781.
- [14] Hoffman, C. A., *Proceedings*, American Society for Testing and Materials, Vol. 56, 1956, pp. 1063-1080.
- [15] Swindeman, R. W., *Proceedings*, Joint International Conference on Creep, Institution of Mechanical Engineers, London, 1963, pp. 3-71 to 3-76.
- [16] Sheffler, K. D. and Doble, G. S., "Influence of Creep Damage on the Low Cycle Thermal-Mechanical Fatigue Behavior of Two Tantalum-Base Alloys," NASA CR-121001, National Aeronautics and Space Administration, May 1972.
- [17] Howes, M. A. H., "Thermal Fatigue Data on 15 Nickel- and Cobalt-Base Alloys," NASA CR-72738, National Aeronautics and Space Administration, May 1970.
- [18] Spera, D. A., Howes, M. A. H., and Bizon, P. T., "Thermal-Fatigue Resistance of 15 High-Temperature Alloys Determined by the Fluidized-Bed Technique," NASA TM X-52975, National Aeronautics and Space Administration, March 1971.
- [19] Manson, S. S. and Hirschberg, M. H., "Low Cycle Fatigue of Notched Specimens by Consideration of Crack Initiation and Propagation," NASA TN D-3146, National Aeronautics and Space Administration, June 1967.

M. A. H. Howes¹

A Study of Thermal Fatigue Mechanisms

REFERENCE: Howes, M. A. H., "A Study of Thermal Fatigue Mechanisms," *Thermal Fatigue of Materials and Components, ASTM STP 612*, D. A. Spera and D. F. Mowbray, Eds., American Society for Testing and Materials, 1976, pp. 86-105.

ABSTRACT: The thermal fatigue resistance of materials has been evaluated in a series of investigations using the fluidized bed method of thermal cycling. The factors that influence thermal cracking were studied for many materials and definite patterns of behavior observed. Particular attention was paid to H13 tool steel and an 18Ni maraging alloy as these represent materials with distinctly different mechanisms of heat treatment response.

KEY WORDS: thermal fatigue, fluidized bed processing, thermal cycling tests, nickel alloys, steel, crack propagation, plastic deformation

At the present time, thermal fatigue testing is not standardized to the same degree as tension testing, creep testing, or fatigue testing, and it is difficult to compare thermal fatigue results by different investigations. Part of the difficulty results from the fact that a temperature cycle may not produce the same stress cycle because of specimen geometric differences and heat input variations due to the testing method. It would be convenient, therefore, to predict thermal fatigue behavior from the results obtained by more standardized tests. One problem is that thermal fatigue involves mechanisms that do not appear to the same extent as in other testing methods. For example, cyclic oxidation often occurs during thermal fatigue testing, but continuous oxidation occurs in creep tests. It is believed that a better understanding of thermal fatigue failure mechanisms would improve the accuracy of predictive equations and make them more applicable to a wide range of materials.

This investigation used the fluidized bed method of thermal cycling. The objective was to improve the understanding of the thermal fatigue mechanism by control of the test environment and analysis of the test results. The experimental work has been carried out on H13 and 18Ni mar-

¹ Director, Metals Division, Illinois Institute of Technology Research, Chicago, Ill. 60616.

aging alloy, but examples of microstructures obtained in other investigations are also referred to.

Test Procedure

The equipment used for thermal fatigue evaluation consists of two fluidized beds, one heated and one cooled. The specimens are cycled between the two beds at preset intervals. A full description of the equipment is contained in an earlier paper [1].²

The specimens are disk-type configurations 16.35 cm diameter and 1.27 cm thick. The fin section is approximately 3 mm thick. These specimens are used either unnotched or notched [1]. A notched specimen has two V-notches of the same dimensions as the notch in a Type A Charpy impact bar at 180 deg. The stress intensification factor of this type of notch is approximately 2.8.

Thermal fatigue testing often requires attempting the duplication of both the stress and thermal cycles that occur in an actual component situation. In this investigation, it was desired to find the range of stress variation that could be produced with the same thermal excursion limits. This would be done by varying the fluid bed test conditions, making accurate temperature measurements throughout the thermal fatigue specimen test section, and using a computer program to calculate the stress gradients. The stress levels would then be compared with the thermal fatigue results to determine if the stress level to which the specimens are subjected causes cracking. Test results from other programs would also be examined where mechanistic effects had occurred.

The specimens used for the stress determinations were made from two materials chosen to be representative of steels requiring a hardening and tempering treatment and materials requiring solution treatment and aging. The compositions are shown in Table 1.

The materials were processed in the following way: the starting point for each material was a 15-cm-square billet. From this billet, transverse samples were removed at or near the midradius position for tension testing. A portion of the billet was press forged to a 7-cm-round bar and used for thermal fatigue specimens. The remainder of the 15-cm billet was reduced by forging and rolling to a 2.5-cm-diameter round bar for use in creep, strain tempering, and static tempering tests. In this way, all material of one composition came from the same billet, ingot, and heat.

The mechanical properties of both materials were measured up to 700°C and are shown in Figs. 1 and 2. Creep data are given in Fig. 3 and 4. Tempering and aging curves are shown in Figs. 5 and 6.

The specimens were all thermally cycled in a manner that caused the

²The italic numbers in brackets refer to the list of references appended to this paper.

TABLE 1—Materials used for stress determinations.

Description	Analysis, %	
	H13	18Ni
C	0.399	0.018
Mn	0.33	<0.10
P	0.018	<0.01
S	0.003	0.007
Si	0.93	<0.01
Cr	5.27	ND
Mo	1.13	5.10
V	1.00	ND
Ni	0.17	18.2
W	<0.01	ND
Al	ND ^a	0.10
Ti	ND	0.65
Co	ND	8.8
Zr	ND	<0.01
B	ND	0.003
Melting conditions	air melted	induction vacuum melted and vacuum arc melted

^aND = not determined.

outer periphery of the fin to fluctuate between 593 and 204°C. However, the temperature excursion was produced in two different ways.

1. A severe heating cycle was produced by immersing the specimens in a hot bed at 1038°C and removing them when the outer edge of the fin had reached 593°C.

2. A mild heating cycle was produced by immersing the specimen in the hot bed at 649°C and removing them when the outer edge of the fin reached 593°C. In addition, a lower degree of bed fluidization was used.

The thermal fatigue test conditions are given in Table 2. It is seen that there is a considerable difference in total cycle time between the two cycles.

Temperature Calibration and Calculation of Stresses

Temperature profiles were established using fin specimens equipped with ten thermocouples. Calibration was carried out on specimens that had been preoxidized since the oxide film would affect heat transfer characteristics. The sheathed chromel-alumel thermocouples used for the curves shown in Figs. 7 and 8 and H13 were approximately 0.025 mm diameter to ensure a rapid response to temperature change. Figure 7 shows the severe cycle where very large gradients are produced. Figure 8

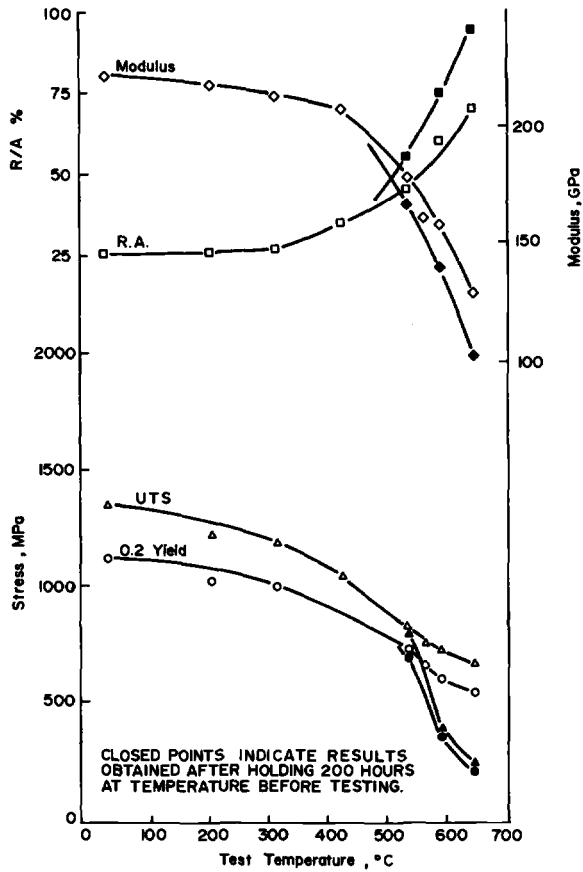


FIG. 1—Mechanical properties of H13 tool steel.

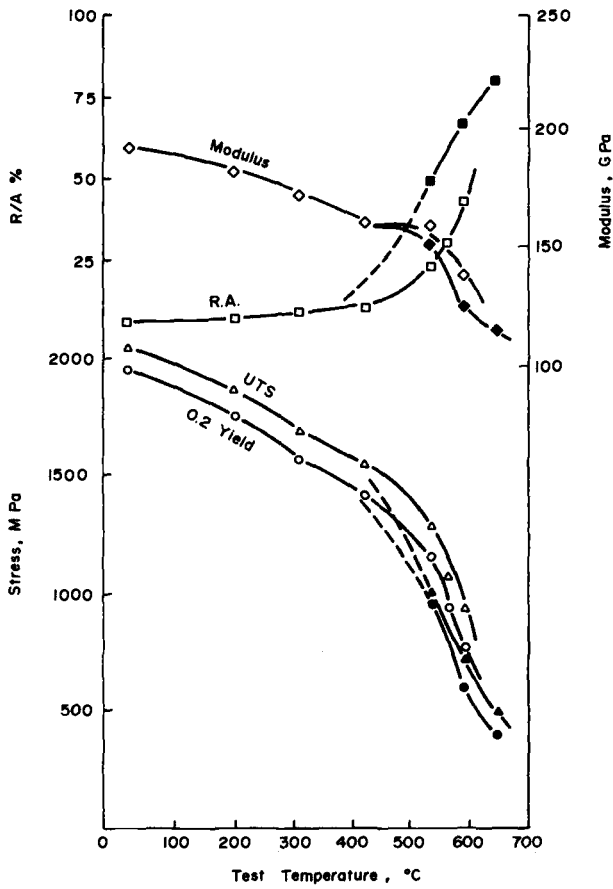


FIG. 2—Mechanical properties of 18Ni maraging alloy.

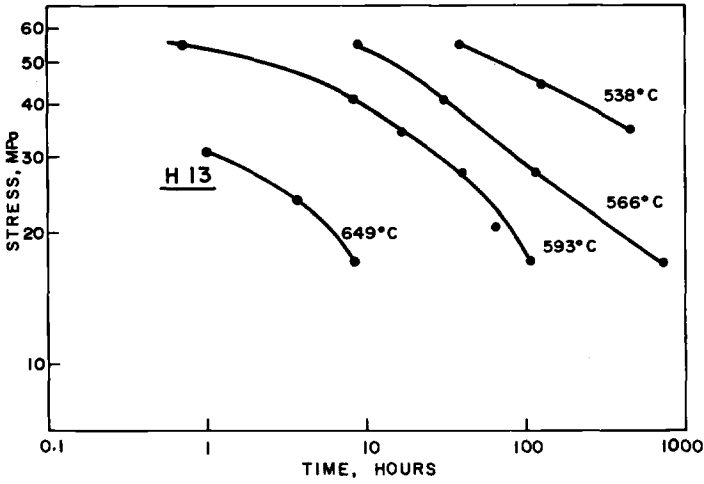


FIG. 3—H13 creep rupture data.

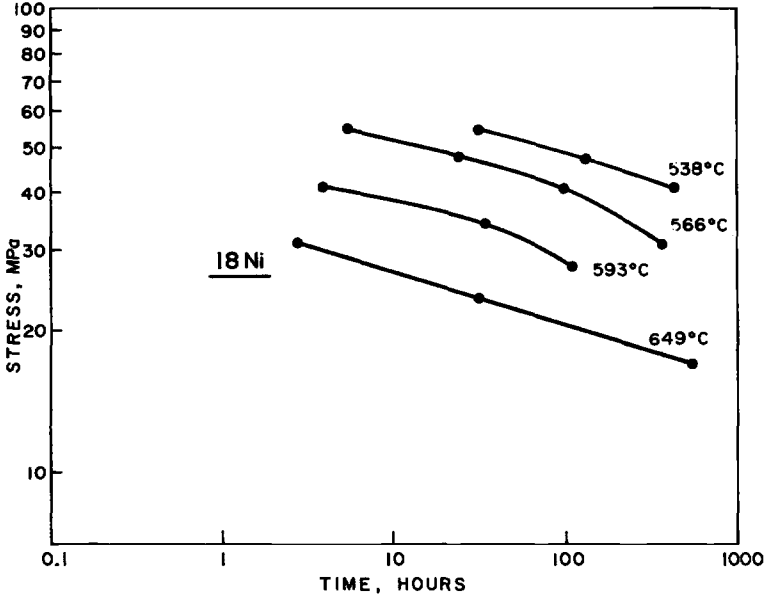


FIG. 4—18Ni maraging alloy creep rupture data.

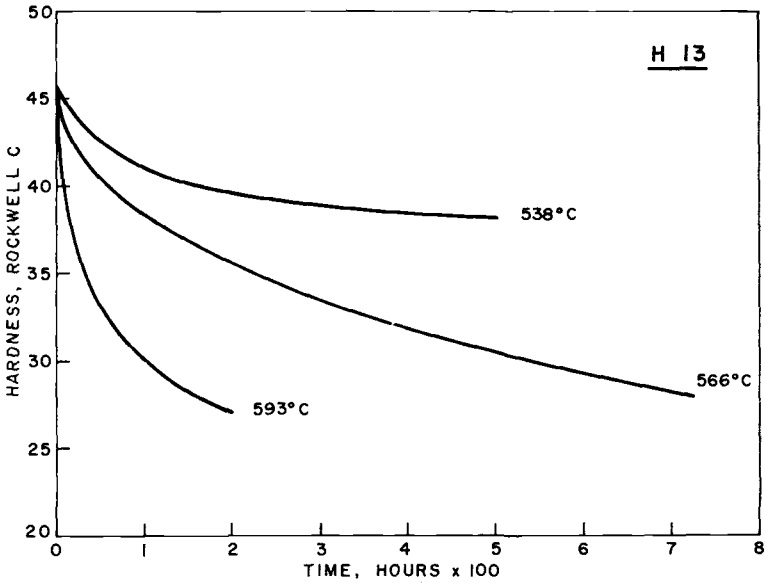


FIG. 5—Tempering of H13.

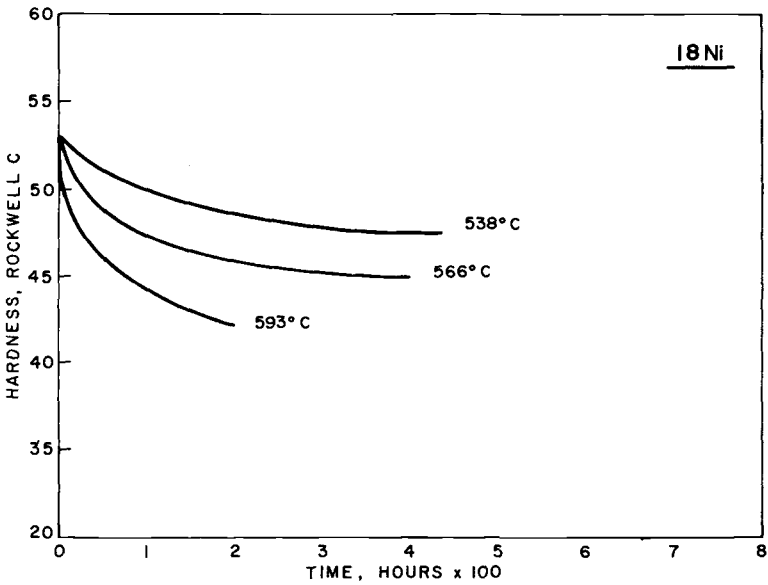


FIG. 6—Aging of 18Ni maraging alloy.

TABLE 2—*Thermal fatigue test conditions.*

Cycle	Material	Bed	Temperature, °C	Time, s	Air Flow Measured at Bed Temperature, m ³ /m ² /h
Mild	18Ni	heating	649	156	600
		cooling	43	85	1200
	H13	heating	649	178	600
		cooling	43	86	1200
Severe	18Ni	heating	1038	3¼	750
		cooling	43	22	1500
	H13	heating	1038	4	750
		cooling	43	24	1500

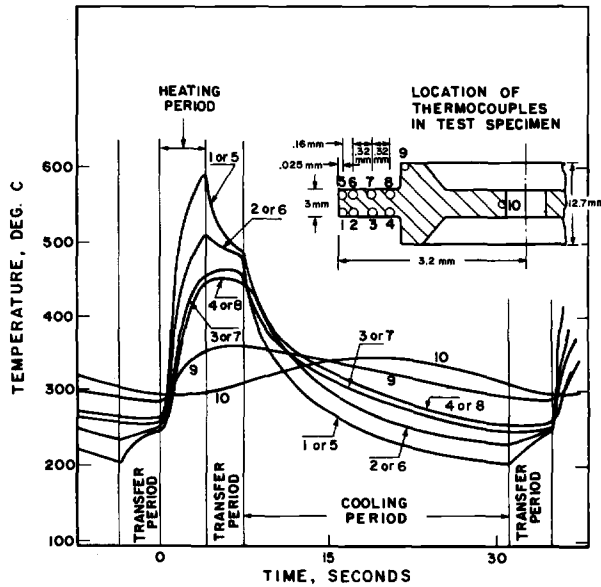


FIG. 7—*Heating and cooling of H13 thermal fatigue specimen fin during the severe cycle.*

shows the mild cycle where temperature changes are much less severe. In many cases, the temperature changes at the top edge of the fin are identical to changes at the bottom edge.

The temperature data are not of prime interest in themselves but are obtained in order to predict stress levels in the specimen. This can be done using finite element technique to calculate both thermal and stress gradients throughout the specimen.

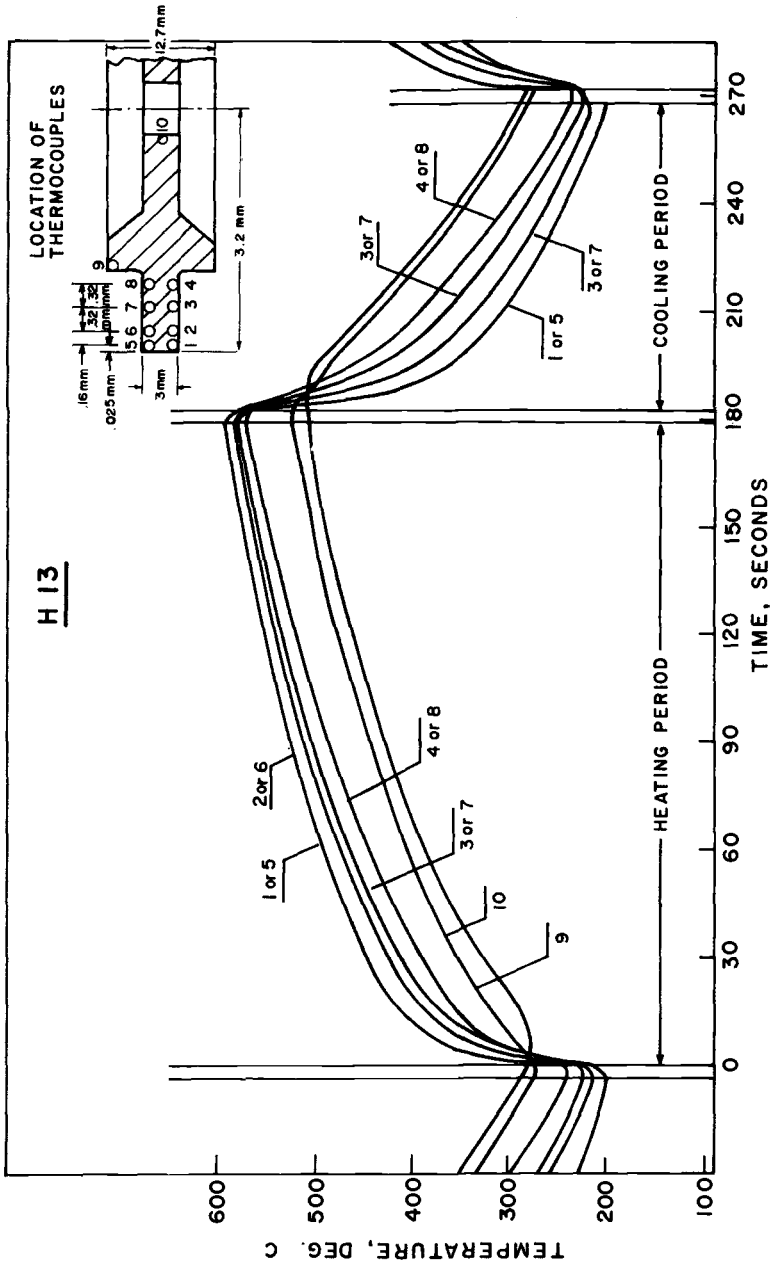


FIG. 8—Heating and cooling of H13 thermal fatigue specimen, fm during the mild cycle.

Figure 9 shows the mesh configuration representing the specimen. It consists of 157 nodes and 123 elements. Six thermocouples (for location, see Fig. 9) recorded temperature changes during the test. The method followed was to determine the temperature distribution with the first nine temperature couple readings as input source and the tenth temperature reading as a check against the computed temperature at the same location. With a known temperature field, a thermal stress field can thus be calculated.

The temperature and thermal stress computations involved modified versions of existing finite element analyses for axisymmetric solids. The same finite element mesh was utilized for both the temperature and stress calculations.

Temperature distributions were calculated according to the procedures described in Ref 2. Steady-state temperature field was determined first using all ten thermocouple temperature readings as input source. Transient temperature distributions were then obtained employing previous steady-state temperatures as initial temperatures and the first nine thermocouple readings as input temperatures. Results were stored in digital form for subsequent thermal stress calculations.

The thermal stress analysis was based on the finite element formulations of Farhoomad and Wilson [3] with modifications to the solution procedures and materials formulation.

Results show that the fin is under high tensile stresses during the heating cycle, but the sign of stresses is reversed during the cooling cycle.

The stress cycles are shown for H13 for both the severe and mild cycle in Figs. 10 and 11. The maximum stress levels experienced in both materials are summarized in Table 3.

Thermal Fatigue Results for H13 and 18Ni Maraging Alloy

The stress results show that, at 593°C, even the severe thermal cycle will not cause plastic strain to occur at the start of testing. However, as discussed later, the properties of H13 degrade and, after about 8000 to 16 000 cycles, the strength has decreased to a point where plastic deformation becomes possible in an unnotched specimen using the severe thermal cycle.

Thermal fatigue results are shown in Figs. 12 and 13. The approximate cycles to initiate cracks are shown in Table 4. Failure did not occur within the test cycles under conditions not involving plastic working. A possible exception is the notched 18Ni specimen tested under the mild cycle. In this specimen, the calculated stress at the notch is 538 MPa, while the yield strength at 593°C is 758 MPa. The strength degraded during testing but was still 600 MPa even after 200 h (28 000 cycles). Thus, at crack initiation (3000 cycles), the crack has apparently started in a zone subject to

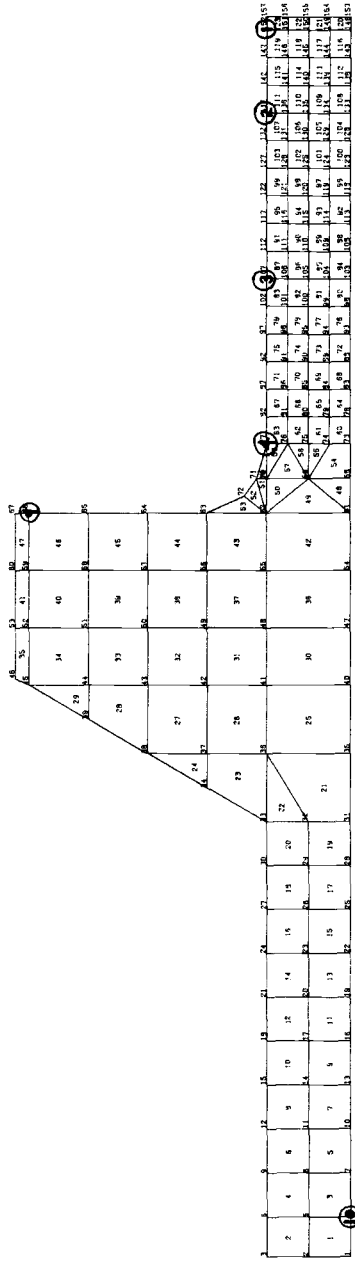


FIG. 9—Mesh configuration representing half of the thermal fatigue specimen entire mesh, view in direction of Y , Z axis.

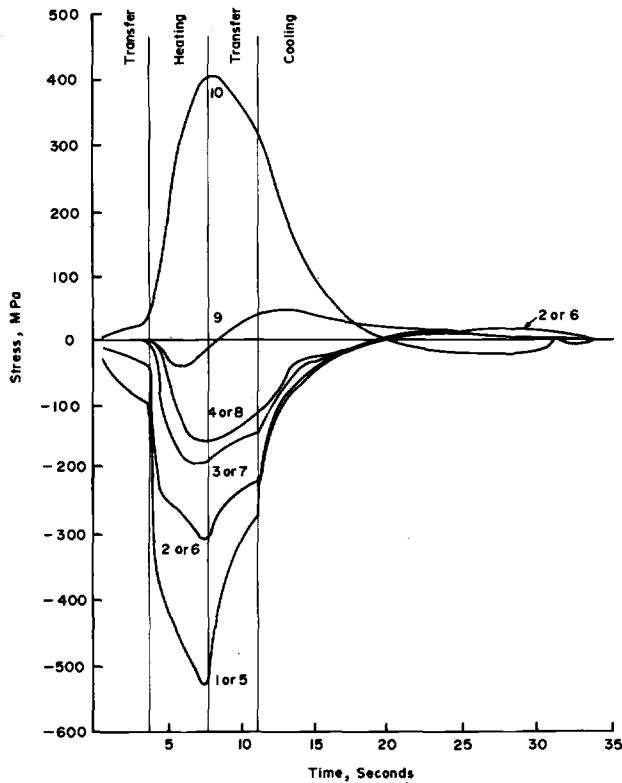


FIG. 10—Stress cycle of H13 specimen fin during the severe cycle.

elastic strain but at a stress level near the point of plastic working. A possible explanation is that the stress concentration at the notch was higher than expected.

During testing, additional specimens were cycled and removed at intervals until sufficient data had been obtained to observe the hardness changes across the fin section. Specimens were removed at 250, 500, 1000, 2000, 4000, 8000, and 16 000 cycles. The specimens were sectioned and microhardness surveys performed on the fin. These hardnesses were converted to Rockwell C values, and isohardness curves were drawn across diagrams representing the fins. The information is summarized in Fig. 14. This figure also gives an estimate of the equivalent time that the outer edge of the fin has spent at 593°C. The estimates were made from tempering curves by summing the effects of small temperature increments from 204 to 593°C.

If the change in hardness (Fig. 14) is compared with the tempering

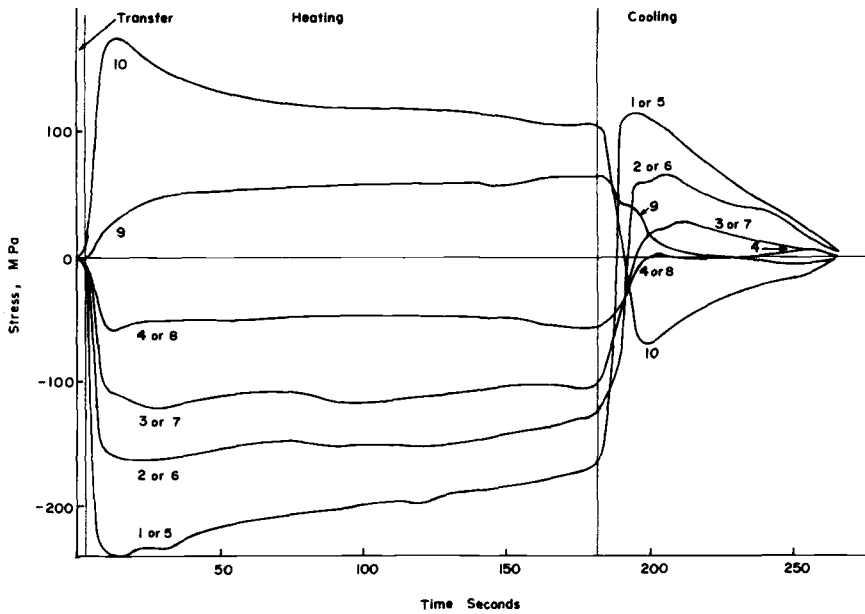


FIG. 11—Stress cycle of H13 specimen during the mild cycle.

TABLE 3—Maximum stress levels at the surface of the thermal fatigue specimens.

Alloy	Stress, MPa				Ultimate Tensile Strength at 593 °C	0.2% Yield at 593 °C
	Severe Cycle		Mild Cycle			
	Plain	Notched	Plain	Notched		
H13	537	1504	241	674	737 (400) ^a	606 (372)
18Ni	400	1120	192	538	930 (716)	758 (600)

^a Values in parentheses are for specimens tested after a 200 h exposure at 593 °C. 200 h is equivalent to 25 000 mild cycles or 3.2×10^6 severe cycles for H13 and 28 500 mild cycles or 3.9×10^6 severe cycles for 18Ni maraging alloy.

curves in Figs. 5 and 6, it will be seen that stress acts to accelerate the normal tempering changes in the structure. In the case of the 18Ni maraging alloy cycled under the severe thermal cycle, there is evidence that strain hardening occurs in the body of the fin due to the high stresses imposed in this cycle. The effect observed in the H13 tool steel and in 18Ni

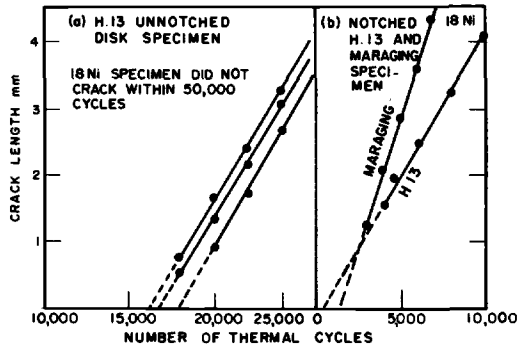


FIG. 12—(a) Crack growth of successive cracks in one unnotched H13 specimen. (b) Average crack growth of four cracks in H13 and 18Ni notched specimens. Specimens cycled between 593 and 204°C under the severe conditions.

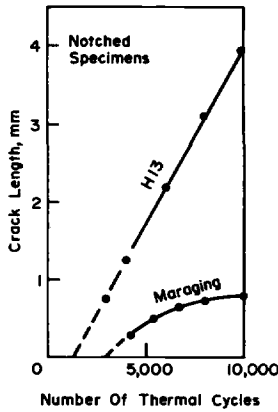


FIG. 13—Average crack growth of successive cycles in four notched H13 and 18Ni maraging alloy specimens. Specimens cycled between 593 and 204°C under the mild conditions.

maraging alloy exposed to the mild cycle is one of failure produced by the onset of cracking in plastically deformed material.

Effect of Microstructural Changes

Two sets of six unnotched disk specimens designated A and B were prepared from a steel containing 0.48 percent carbon, 0.62 percent manganese 0.34 percent nickel, and 0.53 percent chromium. Both sets were heat treated by oil quenching from 850°C and tempering at 565°C. However, Set A was heated to the austenitizing temperature and immediately quenched, whereas Set B was held at temperature 30 min before quenching. The structures produced are shown in Figs. 15 and 16. Set A shows

TABLE 4—Approximate thermal cycles to initiate cracking.

Alloy	Severe Cycle		Mild Cycle	
	Plain	Notched	Plain	Notched
H13	16 500	0	>20 000	1500
18Ni	>50 000	1000	>20 000	3000

NOTE—Cracking observations were made with a $\times 30$ microscope.

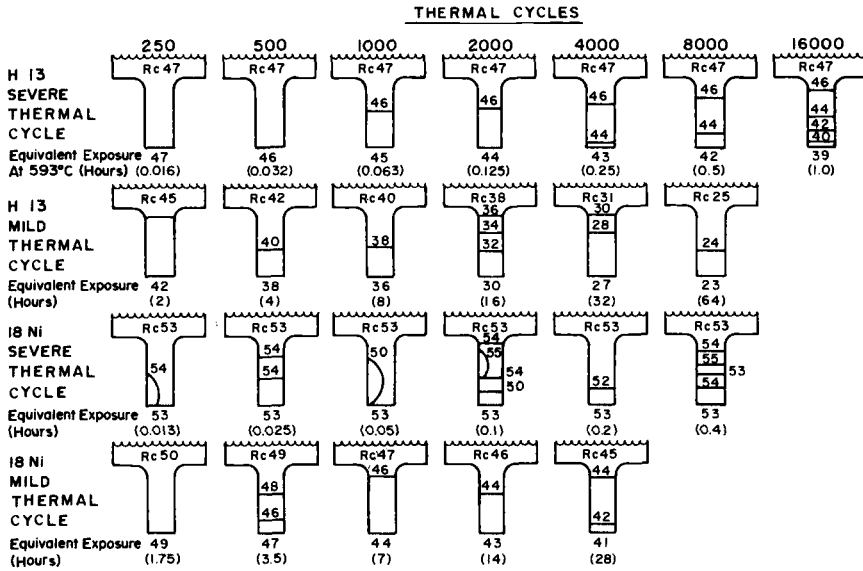


FIG. 14—Hardness changed in thermal fatigue specimen fins after cycling 250 to 16 000 times.

an incompletely hardened structure, but Set B is almost completely tempered martensite. The specimens were then tested by thermally cycling the fin between 550 and 260 °C using a bed temperature of 940 °C; the heating time was 7.5 s, and the cooling time was 27 s. The thermal fatigue results are shown in Fig. 17 where it is seen that all the Set A specimens cracked almost immediately when testing commenced, with the cracks propagating in the weak material at the grain boundaries. Set B specimens initiated cracks in the range of 6000 to 24 000 cycles.

There are many examples of the importance of structure on thermal fatigue results. A paper [4] in this publication discusses the effect of structure on thermal fatigue results obtained with MAR M-509. An example of the effect of structure is given in NASA CR-121212 [5], where a pro-

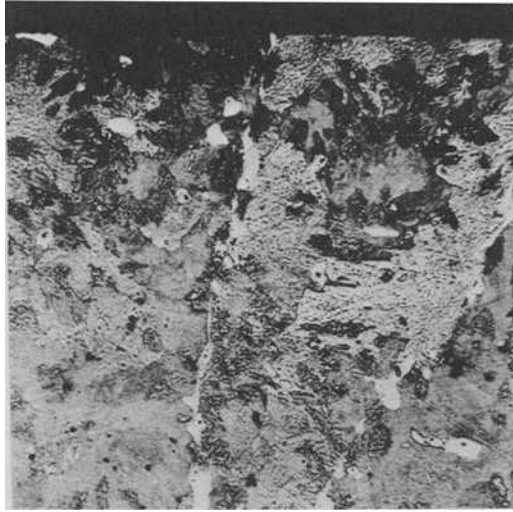


FIG. 15—Steel with slack quenched structure (Set A), $\times 100$.

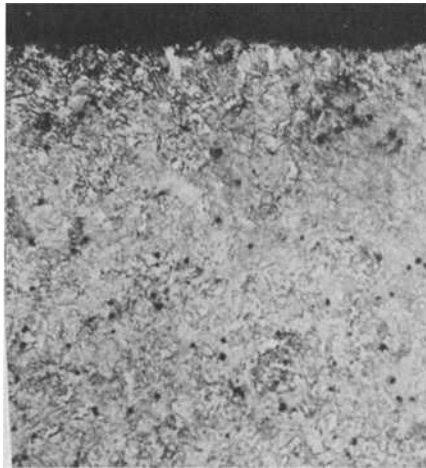


FIG. 16—Steel with correctly quenched structure (Set B), $\times 100$.

nounced dendritic solidification pattern is shown to be detrimental to the thermal fatigue resistance of TAZ-8A.

In general, it is important to give as much attention to processing as to the composition of the alloy. There will be an optimum structure for avoiding points of weakness such as dendrites, porosity, and weak microstructural constituents concentrated at grain boundaries. Structure can be

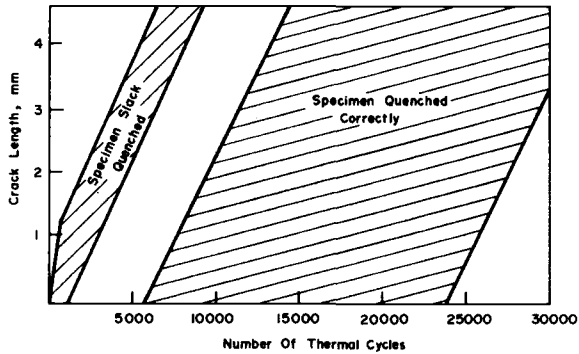


FIG. 17—Effect of structure due to different quench rates in steel specimens on crack initiation during thermal fatigue testing. Specimens cycled between 550 and 260°C.

made to work to improve thermal fatigue resistance, and the prime example of this is directional solidification and single crystal structures. Great improvements have been reported when directional solidification can be used in a cast part [5-7].

Even if it is assumed that a particular composition is processed to produce the structure with the highest thermal fatigue resistance, there is another effect to be considered. During thermal exposure there is often a degradation in properties and potential crack sites can also develop.

Figure 18 shows a section through a double-edged wedge IN-100 specimen that has been subjected to thermal cycling between 1088 and 316°C [6]. It can be seen that the alloy is subject to oxidation and a surface layer of material with a lower content of carbon, chromium, aluminum, and titanium can be produced which is thus of lower strength than the base material. It is less able to resist the stresses produced by the thermal cycling. Furthermore, at the points where the grain boundaries meet the surface, the effect is intensified, and the oxidized or weakened layer tends to penetrate further at these points. This has the effect of creating notches or stress intensification points at the surface, and, when oxidation has proceeded far enough, a crack will initiate and follow the line of least resistance in the structure. The success of coatings in improving thermal fatigue resistance is largely due to their ability to retard oxidation.

This is one reason why there is an apparent incubation period before thermal cracking commences, but another reason is the degradation of the material properties themselves. Most materials are strengthened by a martensitic or an age hardening mechanism. Thus, during thermal cycling, there is a tendency to temper the structure or to cause overaging and thereby lower the strength of the material. The decrease in surface hardness of twelve superalloys during thermal cycling has been reported [6],

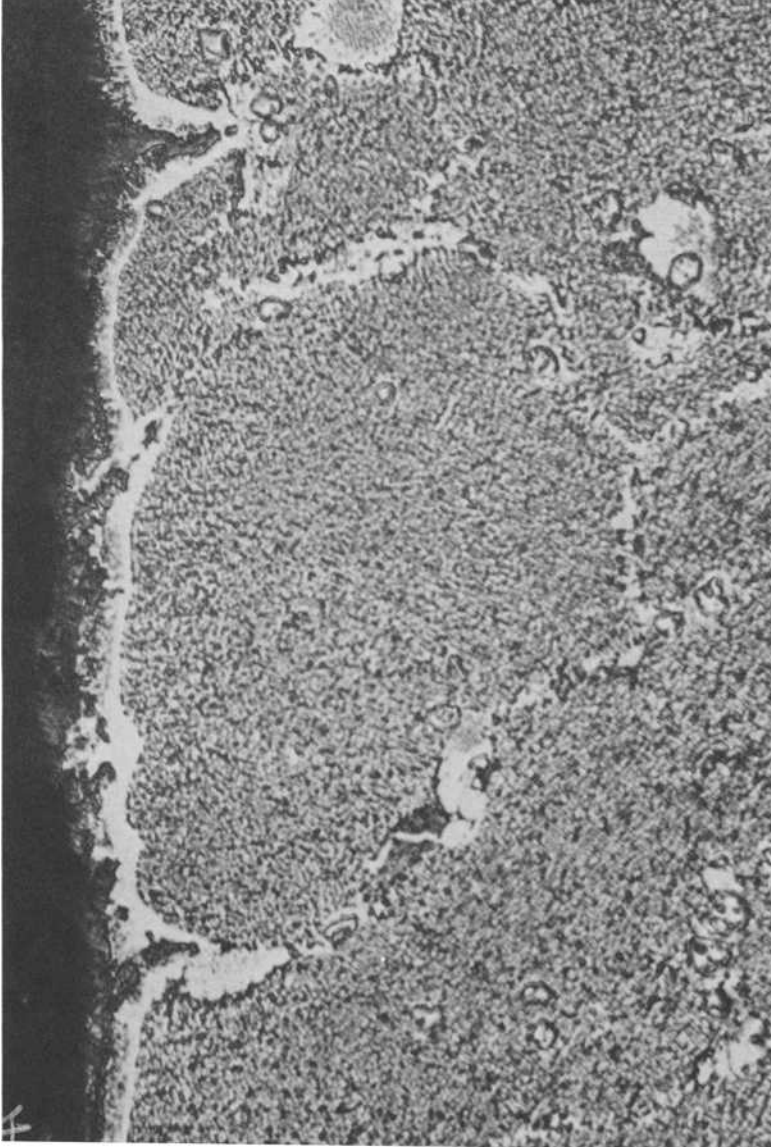


FIG. 18—Surface of an IN-100 thermal fatigue specimen after cycling between 1088 and 316°C, $\times 500$.

and this almost certainly indicates that the strength of the material at the surface has been reduced. A further effect is that tempering and overaging are accelerated by stress [8], and thus the degradation of properties occurs faster while the material is being thermal cycled.

Summary

To summarize the events leading to a thermal fatigue failure, it has been shown that failures occur because the materials have been stressed in the plastic range. If the stresses are purely elastic, then failure would only normally occur after alignment of dislocations during an incubation period causes a void which would exceed the critical crack length and initiate a self-sustaining crack.

Under high stress levels or in situations where stress concentration effects cause a crack to propagate, crack initiation occurs at the start of thermal cycling or very soon thereafter. However, the common experience during thermal fatigue testing is that a definite incubation period is required before cracking commences. It is believed that a number of rate-dependent processes can be in progress during this period, either singly or concurrently, and it is this factor that makes the development of predictive equations very difficult.

One process that occurs is plastic deformation, and it is fairly common to see considerable local plastic deformation on the surface of a specimen before cracking commences. When cracking does occur, it is almost invariably in the areas where plastic deformation was the highest, and this may be regarded as an exhaustion of ductility effect. A further factor is that the strength of the material will be slowly degraded due to overaging or tempering effects, and this will be stress accelerated. At points of maximum stress, it is likely that plastic deformation will occur to a greater extent than in the bulk of the section, and the mechanical properties will therefore be degraded faster in these areas. As the mechanical properties decrease, plastic deformation becomes easier, and thus the weakening process is self-accelerating in individual small areas which will ultimately provide the sites for crack initiation.

A second mechanism that occurs is oxidation depleting the surface of materials at the higher exposure temperature. A nickel-base superalloy can expect to be depleted of carbon, chromium, aluminum, and titanium, at least. Depletion will often be preferential at the grain boundaries, and wedges of low strength material will be formed which act like a notch. After some finite time, the notch will assume the dimensions of the critical crack size, and a thermal crack will initiate and propagate.

Acknowledgments

The author is grateful to Kin Yeung, Edward Welch, and Anne Humphreys who developed the computer program for predicting stresses under thermal cycling conditions.

References

- [1] Howes, M. A. H. in *Fatigue at Elevated Temperatures*, ASTM STP 520, American Society for Testing and Materials, 1976, pp. 242-254.
- [2] Farhoomad, I. and Wilson, E. L., "Nonlinear Heat Transfer Analysis of Axisymmetric Solids," Report PB 199169, University of California, Berkeley, 1970.
- [3] Farhoomad, I. and Wilson, E. L., "A Nonlinear Finite Element Code for Analyzing the Blast Response of Underground Structures," Report No. N-70-1, University of California, Berkeley, 1970.
- [4] Beck, C. G. and Santhanam, A. T., this publication, pp. 123-140.
- [5] Howes, M. A. H., "Additional Thermal Fatigue Data on Nickel- and Cobalt-Base Superalloys," NASA CR-121212, National Aeronautics and Space Administration, Washington, D.C., 15 March 1973.
- [6] Howes, M. A. H., "Thermal Fatigue Data on 15 Nickel- and Cobalt-Base Alloys," NASA CR-72738, National Aeronautics and Space Administration, Washington, D.C., 15 May 1970.
- [7] Howes, M. A. H., "Thermal Fatigue and Oxidation Data on TAZ-8A, MAR-M200, and Udimet 700 Superalloys," NASA Cr-134775, Washington, D.C., 15 Jan. 1975.
- [8] Howes, M. A. H., "Investigation of Stress-Accelerated Tempering and Aging of Ferrous Alloys," presented at XVI International Heat Treatment Conference, Stratford, England, May 1976.

Thermal-Stress Fatigue Behavior of Twenty-Six Superalloys

REFERENCE: Bizon, P. T. and Spera, D. A., "Thermal-Stress Fatigue Behavior of Twenty-Six Superalloys," *Thermal Fatigue of Materials and Components, ASTM STP 612*, D. A. Spera and D. F. Mowbray, Eds., American Society for Testing and Materials, 1976, pp. 106-122.

ABSTRACT: The comparative thermal-stress fatigue resistances of 26 nickel- and cobalt-base alloys were determined by fluidized bed tests. Cycles to cracking differed by almost three orders of magnitude for these materials, with directional solidification and surface protection showing definite benefit. The alloy-coating combination with the highest thermal-stress fatigue resistance was directionally solidified NASA TAZ-8A with an RT-XP coating. Its oxidation resistance was also excellent, showing approximately a ½ percent weight loss after 14 000 fluidized bed cycles.

KEY WORDS: thermal fatigue, thermal stress, oxidation, coatings, nickel alloys, cobalt alloys, fluidized bed, heat resistant alloys, mechanical properties

Thermal-stress fatigue is a potential mode of failure in any component that is exposed to fluctuating temperatures. Resistance to thermal-stress fatigue is one of the major criteria which should be considered when selecting an alloy for a fluctuating temperature application. However, thermal-stress fatigue resistance is not a basic material property such as tensile strength, density, etc., but a structural response. The number of temperature cycles required to cause thermal-stress fatigue cracking depends not only on the alloy but also on the specimen geometry and test conditions. In this investigation, the term "thermal-stress fatigue resistance" is used in a comparative, rather than absolute, sense. Alloys are compared to one another, all having been tested under the same test conditions using the same specimen geometry.

This investigation is part of a program of studies of failure mechanisms and life prediction of turbine components being performed by the Lewis Research Center of the National Aeronautics and Space Administration (LRC/NASA). An overview of this program is given in Ref 1,² together

¹ Materials engineer and fatigue branch consultant, respectively, National Aeronautics and Space Administration Lewis Research Center, Cleveland, Ohio 44135.

² The italic numbers in brackets refer to the list of references appended to this paper.

with a bibliography of NASA-LRC publications on fatigue, oxidation and coatings, and turbine engine alloys. References 2-7 contain incremental portions of the data obtained in the thermal-stress fatigue tests described herein. All significant data from these reports are compiled and described in detail in Ref 8.

The primary objective of this investigation was to determine the comparative thermal-stress fatigue resistance of a large number of nickel- and cobalt-base alloys. A secondary objective was to determine the effects of directional solidification and several coatings on both the thermal-stress fatigue and oxidation resistance of some of these alloys. The alloys selected include those used or proposed for use in the the hottest sections of advanced aircraft gas turbines. Therefore, the test conditions for this evaluation may be more severe than present use conditions for many of the alloys. As an example, the maximum metal temperature during a typical test cycle was about 1074°C (1965°F).

The thermal-stress fatigue tests were carried out in a fluidized bed facility that was designed, built, and operated by the Illinois Institute of Technology Research Institute (IITRI) under contract to NASA-LRC. Fluidized beds were first used for rapidly heating and cooling thermal-stress fatigue specimens by Glenny and his co-workers at the National Gas Turbine Establishment in England in 1958 [9]. Since that time, fluidized bed cycling has become widely used for evaluating the thermal-stress fatigue behavior of both alloys and components [10-15].

In addition to thermal-stress fatigue resistance, some mechanical properties of the alloys were also determined at selected temperatures. The conventional mechanical property tests for the materials included in this investigation were conducted at the LRC.

Materials and Test Specimens

Alloys

The 35 combinations of composition, grain structure, and surface protection which were studied in this program are listed in Table 1. Table 2 lists the compositions of the alloys (chemical analyses provided by vendor or independent laboratory of heats used for specimens) along with the various heat treatments applied to them. Mechanical properties are given in Table 3 for the same heat of alloy that was used for the thermal-stress fatigue specimens.

A new alloy included in this investigation is directionally solidified NASA TAZ-8A. In an earlier investigation [4], the random polycrystalline form of this alloy was found to have the highest resistance to thermal-stress fatigue among 14 uncoated alloys. This indicated that directional solidification or coating or both of TAZ-8A might produce a material with even

TABLE 1—Alloys-coatings investigated (coated and uncoated specimens purchased from vendors except where noted).

NASA TAZ-8A DS + RT-XP coat	B 1900 + Hf + Jocoat ^b
NASA TAZ-8A DS + NiCrAlY overlay	B 1900 + Jocoat
NASA TAZ-8A DS ^a	B 1900
NASA TAZ-8A	
	U 700 cast
	U 700 wrought
NX 188 DS + RT-1A coat ^b	
NX 188 DS ^b	X 40
NX 188 + RT-1A coat ^b	IN 162
NX 188 ^b	TD NiCr
Mar-M200 DS + NiCrAlY overlay	IN 713C
Mar-M200 DS	Mar-M509
Mar-M200 + Jocoat	NASA VI-A
Mar-M200	Rene 80 ^c
	IN 738
IN 100 DS + Jocoat	RBH ^d
IN 100 DS	Mar-M302
IN 100 + Jocoat	WI 52
IN 100	M 22
NASA WAZ-20 DS + Jocoat ^a	
NASA WAZ-20 + Jocoat ^a	

NOTE—DS indicates that the alloy was cast with a directionally solidified grain structure.

^a Specimens cast at NASA Lewis Research Center.

^b Specimens with and without coatings supplied by Pratt & Whitney Aircraft Corp.

^c Specimens supplied by General Electric Corp.

^d Specimens supplied by Cabot Corp.

better thermal-stress fatigue resistance. Specimens with directional polycrystalline structure were then cast from the same alloy heat, both at the LRC and commercially, for evaluation in this investigation.

Surface Protection

Brief descriptions of the four protective coatings used in this study are as follows:

Jocoat—This is a commercial silicon-modified nickel aluminide coating (Pratt and Whitney Aircraft (PWA) proprietary process specified as PWA 47).

RT-1A—RT-1A is a commercial chromium-aluminum duplex coating (Chromalloy American Corporation Research and Technology Division proprietary process similar to specification PWA 32 but with a lower process temperature).

RT-XP—RT-XP is a coating containing an aluminide with a case depth of about 70 μm (2.7 mils) (Chromalloy American Corporation Research and Technology Division proprietary process).

NiCrAlY—This is a commercial Ni-15.2Cr-12Al-0.33Y electron-beam

vapor-deposited overlay coating about 135 μm (5.3 mils) thick (PWA proprietary process specified as PWA 267).

Test Specimens

In this study, two types of specimen configurations (Fig. 1) were used: bars with double-wedge cross sections and round cross-sectional tensile bars. No significant differences were observed in the results of duplicate tests of the double-wedge shape specimens whether end grooves or holes were used for fastening them into the supporting fixtures.

Figure 1 also shows the designs of specimen used to measure conventional tensile and stress-rupture properties. Designs A and B are similar except that Design B has flat grips so that it can be fabricated from 0.635-cm (0.25-in.) plate. The only difference between Designs C and A is the longer gage length in Design C.

All cast alloy specimens were cast to size. For the random polycrystalline specimens, inoculated molds were used to produce fine grain structures. Typical surface grain size at the test sections was about 1.6 mm (0.06 in.) diameter. The directionally solidified polycrystalline specimens were made using a controlled solidification process similar to that detailed in Ref 16. Only directionally solidified specimens with no grain boundaries intercepting the leading edge were tested. Specimens of the two wrought alloys (U 700 and TD NiCr) were machined with the specimen axis parallel to the rolling or extrusion direction. All specimens were given radiographic, fluorescent penetrant, and visual inspections before testing.

Fluidized Bed Facility and Test Procedure

Fluidized Bed Facility

Figure 2 shows groups of specimens in their respective supporting fixtures. The outer two specimens were always dummy test specimens. The supporting fixture using holes is preferred for tests at higher temperatures because of the lower mass of the fixture and because the supporting rods are only partially exposed to the high temperatures. The specimens were loosely supported in both types of fixtures to allow free thermal expansion.

Figure 3 is a drawing showing a cutaway view of the fluidized bed test facility. Both heating and cooling beds consist of retorts filled with 300 to 540- μm (0.012 to 0.021-in.)-diameter alumina particles through which air is pumped. Adjustment of the airflow allows the particles to develop a churning, circulating action, hence, the name "fluidized." The large number of particles in the beds and their fluid action promote uniform, high heat transfer rates. Each group of specimens in the supporting fixture was cycled between the beds by means of an automatically controlled

TABLE 2—Composition and heat treatment (DS indicates that the alloy was cast with a directionally solidified grain structure).

Alloy	Heat Number	Analyzed Composition, % by weight													Other	Heat Treatment		
		C	Mn	Si	Cr	Ni	Co	Mo	W	Al	Ti	Zr	B					
NASA TAZ-8A																		
DS	T-24	0.10	5.85	bal*	...	5.41	3.90	6.40	...	0.52	39 ppm	7.93Ta, 2.44Cb	as cast			
Mar-M200 DS	KD 2012	0.15	<0.02	0.080	9.20	bal	10.25	...	12.55	5.05	2.13	0.048	0.017	0.36Fe, 0.96Cb, <0.01V	816°C (1500°F) for 50 h			
NX 188 DS	EXF 1655	0.033	bal	...	18.03	...	8.13	as cast			
IN 100 DS	KJ 2206	0.17	<0.02	0.11	10.30	bal	15.10	2.96	...	5.45	4.76	0.084	0.016	0.21Fe, 0.97V	1149°C (2100°F) for 2 h; 927°C (1700°F) for 16 h			
NASA WAZ-20																		
DS	...	0.17	bal	20.9	6.28	...	1.2	as cast			
B 1900 + Hf	...	0.09	0.003	0.06	8.13	bal	10.19	5.90	0.04	5.96	0.98	0.04	0.009	4.3Ta, 0.06Fe, 1.64Hf (1650°F) for 10 h	1080°C (1975°F) for 4 h; 899°C (1650°F) for 10 h			
NASA TAZ-8A	67-640	0.01	6.20	bal	...	3.86	3.86	5.96	...	0.88	...	8.01Ta, 2.44Cb	as cast			
X 40	12C6412	0.48	<0.05	0.33	25.59	10.52	bal	0.04	7.87	0.03	0.005	0.46Fe, 0.02N	760°C (1400°F) for 50 h			
B 1900	54V6335	0.10	0.10	<0.10	8.11	bal	10.15	6.11	<0.10	6.09	0.98	0.08	0.013	4.28Ta, 0.16Fe, 4.28V	843°C (1550°F) for 24 h			
IN 162	96317	0.10	0.01	0.04	10.03	bal	0.03	4.05	2.03	6.35	0.93	0.11	0.018	1.97Ta, 0.17Fe, 0.88Cb	as cast			
TD NiCr	1862	0.038	21.39	bal5ThO ₂ , 0.0005N, 0.006S	as cast			
	2858	0.020	19.72	bal	1.9ThO ₂ , 0.004N, 0.007S	as cast			
IN 713C	65611	0.11	<0.10	<0.10	13.40	bal	...	4.50	...	5.95	0.83	0.08	0.009	2.24Cb + Ta, 0.27Fe	as cast			
Mar-M509	T-3008	0.62	<0.1	<0.1	23.4	10.0	bal	...	6.95	...	0.19	0.54	<0.01	3.46Ta, <0.1Fe	as cast			
NX 188	EXF 1655	0.033	bal	...	18.03	...	8.13	as cast			
NASA VI-A	FB 5487	0.11	0.02	<0.10	5.86	bal	7.24	2.11	5.96	5.27	0.95	0.10	0.021	9.03Ta, 0.32Re, 0.39Hf, 0.45Cb, 0.08Fe	899°C (1650°F) for 32 h			
NASA WAZ-20	...	0.17	bal	20.9	6.28	...	1.2	as cast			
Rene 80	101V9494	0.18	0.01	<0.10	14.0	bal	9.91	4.00	3.84	3.11	4.90	0.03	0.014	0.18Fe, <1ppm Ag	1219°C (2225°F) for 2 h; 1093°C (2000°F) for 4 h; 1052°C (1925°F) for 4 h; 843°C (1550°F) for 16 h			
IN 738	94V9529	0.17	0.01	0.11	15.98	bal	8.37	1.81	2.49	3.52	3.39	0.11	0.012	1.95Ta, 0.14Fe, 0.87Cb (1550°F) for 24 h	1121°C (2050°F) for 2 h; 843°C (1550°F) for 24 h			
RBH	70-670-4	0.64	0.43	0.39	20.91	16.00	bal	...	5.46	0.33	0.24	0.16	...	3.20Ta, 0.73Fe, 0.05La	as cast			
Mar-M302	T-272	0.88	<0.10	0.22	21.9	0.49	bal	<0.1	9.89	0.24	<0.01	8.80Ta, 1.11Fe	1232°C (2250°F) for 8 h; 816°C (1500°F) for 24 h			

U 700 cast	85V2416	0.08	<0.10	<0.10	14.24	bal	14.87	4.18	...	4.25	3.26	<0.01	0.012	0.30Fe	760°C (1400°F) for 16 h
WI 52	59-682	0.46	0.21	0.28	20.86	0.23	bal	<0.05	11.06	1.75Fe, 1.87Cb	as cast
IN 100	KJ 2206	0.17	<0.02	0.11	10.30	bal	15.10	2.96	...	5.45	4.76	0.084	0.016	0.21Fe, 0.97V	1149°C (2100°F) for 2 h; 927°C (1700°F) for 16 h
Mar-M200	KD 2012	0.15	<0.02	0.080	9.20	bal	10.25	...	12.55	5.05	2.13	0.048	0.017	0.36Fe, 0.96Cb, <0.01V	816°C (1500°F) for 50 h
U 700 wrought	6541	0.113	0.01	0.02	14.85	bal	17.50	5.10	...	4.55	3.45	<0.02	0.013	0.85Fe	1121°C (2050°F) for 4 h; 843°C (1550°F) for 24 h; 760°C (1400°F) for 16 h
M 22	67-635	0.06	6.35	bal	...	1.96	11.37	6.24	...	0.65	...	2.87Ti	as cast

* Bal = balance.

TABLE 3—Tensile and rupture properties.

Alloy	Specimen Design (see Fig. 1b)	Proportional Limit at 760°C (1400°F) ^a				Ultimate Tensile Strength at 760°C (1400°F) ^a				Stress Rupture at 982°C (1800°F)					
		Percent of Room Temperature Specific Gravity		Divided by Room Temperature Specific Gravity		Percent of Ultimate Tensile Strength		Divided by Room Temperature Specific Gravity		Stress ksi	Life (nominal) 100 h	Reduction of Area, % ^a			
		Yield Stress	0.2% Yield Stress	0.2% Yield Stress	Yield Stress	Strength	Strength	760°C (1800°F)	982°C (1800°F)			h	Nominal (1400°F)	Tensile Rupture	
ksi	ksi	ksi	ksi	ksi	ksi	ksi	ksi	ksi	ksi	h	ksi	ksi			
NASA TAZ-8A DS	C	896	130	93	...	1179	171	110	...	172	25	44, 148	96	5	30
Mar-M200 DS ^b	...	869	126	...	102	14.7	1048	152	...	200	29	6	...
NX 188 DS ^c	C	876	127	77	106	15.5	931	135	79	138	20	60, 55	58	4	25
IN 100 DS	A	841	122	1034	150	107	...	159	23	144, 164	154	16	62
NASA WAZ-20 DS ^c	C	703	102	96	78	11.2	855	124	104	172	25	43, 77	60	9	19
B 1900 + Hf ^c	C	703	102	88	84	12.3	945	137	92	165	169	24.5	66, 34	50	13
NASA TAZ-8A	A	1034	150	...	119	17.3	1200	174	134	124	18	89, 79	84	2	8
X-40	A	386	56	...	45	6.5	593	86	123	76	11	183, >105	183	20	33
B 1900	A	938	136	116	114	16.5	1089	158	114	172	25	99, 95	97	8	11
IN 162	A	896	130	106	111	16.1	1124	163	112	165	24	115, 71	93	11	10
TD NiCr ^{c,d}	B	290	42	105	35	5.0	324	47	107	34 ^e	5 ^f	1268 ^g	...	0.1	6
IN 713C	A	814	118	109	103	14.9	1014	147	108	128	18.6	75, 54	64	12	22
Mar-M609	C	296	43	80	33	4.9	621	90	105	70	10.2	151, 132	141	14	22
NX 188	C	724	105	85	903	131	101	118, 141	130	4	2
NASA VI-A	C	910	132	96	104	15.1	1117	162	102	127	18.5	205	72, 76	74	6
NASA WAZ-20	C	710	103	105	78	11.5	745	108	99	83	12.1	124	18	113, 48	81
René 80	C	758	110	110	93	13.5	1076	156	101	131	19.1	145	21	110, 127	118
IN 738 ^f	C	793	115	100	98	14.2	1014	147	105	125	18.1	138	20	23, 22	22
RBH ^g	...	312	45	...	36	5.1	504	73	...	58	8.3	103	15	...	23
Mar-M302	A	696	101	180	75	11.0	807	117	115	87	12.7	97	14	69, 95	82
U 700 cast	A	745	108	...	94	13.7	1020	148	114	129	18.7	124	18	121, 118	120
W1 52	A	579	84	168	65	9.5	765	111	126	86	12.5	90	13	158, 153	156
IN 100	A	793	115	92	102	14.8	965	140	90	125	18.1	172	25	94, 70	82
Mar-M200	A	855	124	102	100	14.7	1000	145	107	117	17.2	179	26	114, 73	94
U 700 wrought	A	758	110	92	96	13.9	986	143	95	125	18.1	110	16	141, 133	137

M 22 ^a	A	958	139	124	111	16.1	1055	153	116	122	17.7	200	29	7.5, 11	9.3	8	4
-------------------	---	-----	-----	-----	-----	------	------	-----	-----	-----	------	-----	----	---------	-----	---	---

NOTE—Data from same heat as used for thermal fatigue tests except where noted. Test data are for fine grain structure where typical grain sizes were about 1.6 mm (0.63 in.) diameter. DS indicates that the alloy was cast with a directionally solidified grain structure.

^a Average of duplicate tests.

^b Nominal data (specimens of heat used for thermal fatigue test not available).

^c Significantly lower rupture strength than nominal.

^d Nominal data for 0.51-mm (0.02-in.)-thick sheet.

^e Supplementary test.

^f Data for Haynes 1002 alloy which is similar to RBH (specimens of heat used for thermal fatigue tests not available).

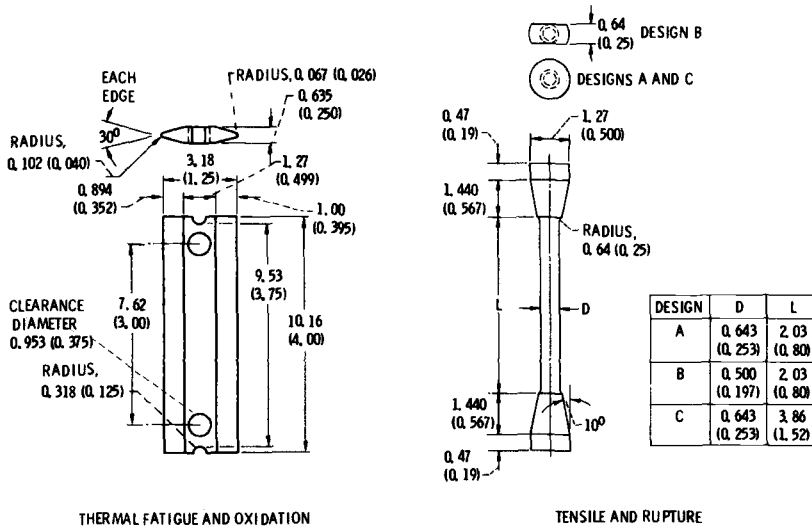


FIG. 1—Geometry of test specimens (all dimensions in cm (in.)).

transfer mechanism operated by pneumatic cylinders. Additional description of the bed and its operation can be found in Ref 17.

Thermal-Stress Fatigue Test Procedure

Comparative thermal-stress fatigue resistance was determined experimentally by simultaneously testing different materials of the same geometry and comparing the number of cycles required to initiate the first crack. A group of up to 18 double-wedge shaped specimens was alternately heated for 3 min and then cooled for 3 min. All materials were tested with the heating bed temperature held at 1088°C (1990°F) and the cooling bed temperature at 316°C (600°F). A typical transient temperature distribution [8] shows that maximum metal temperatures were about 14°C (25°F) less than the heating bed temperature, and minimum metal temperatures were about 33°C (60°F) higher than the cooling bed temperature. The effect on some of the materials of raising both bed temperatures 42°C (75°F) was also evaluated.

Prior to testing and periodically thereafter, both edges of each specimen were examined visually using a microscope with a magnification of $\times 30$. Only the surfaces within ± 3.8 cm (± 1.5 in.) of midlength were examined for cracks. Inspections of most tested specimens were made according to a schedule of 25, 50, 100, 200, 300, 500, 700, and 1000 cycles. Inspection intervals for any series never exceeded 1000 cycles, including the series which was tested the longest (15 000 cycles). For some materials (mostly those with

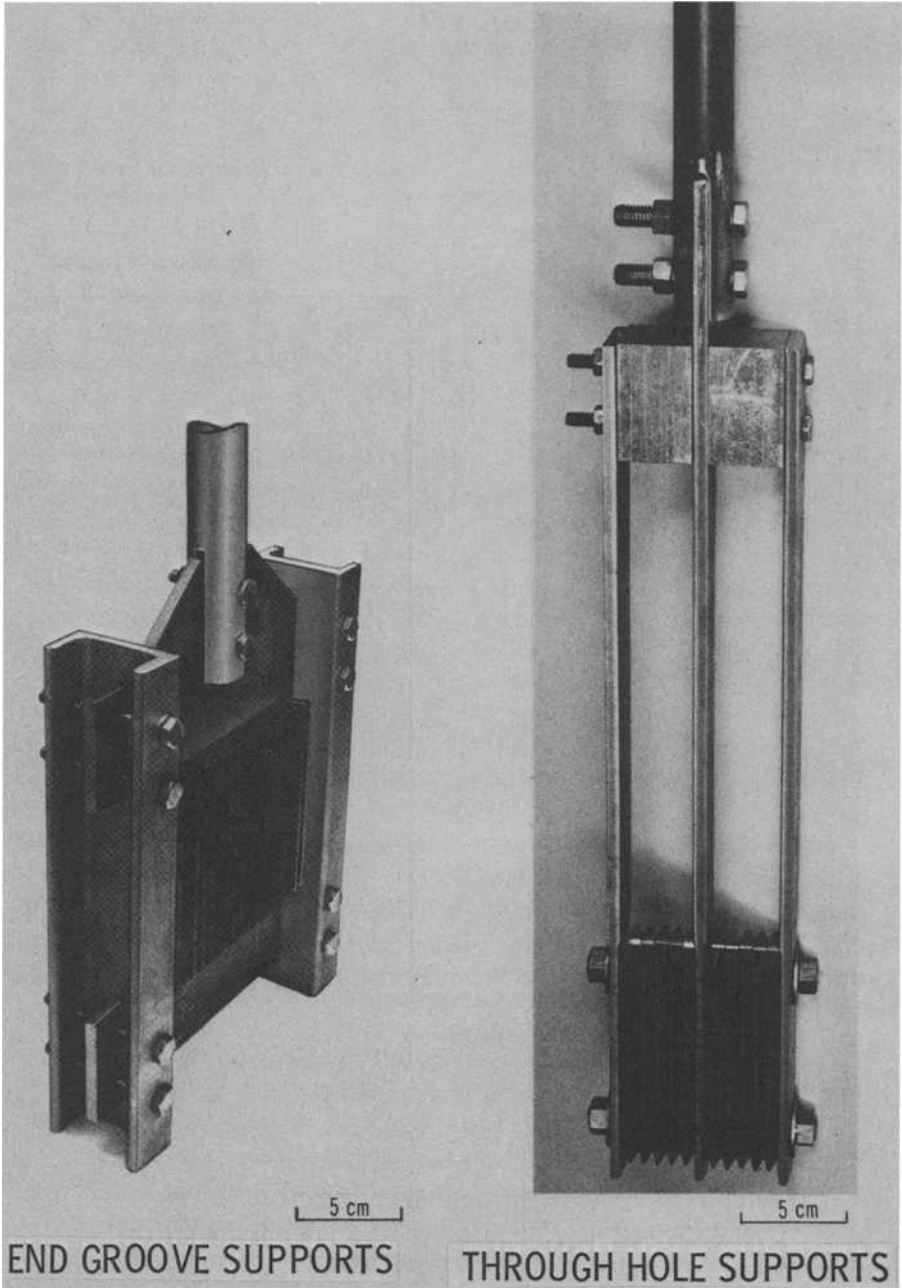


FIG. 2—*Specimen supporting fixture.*

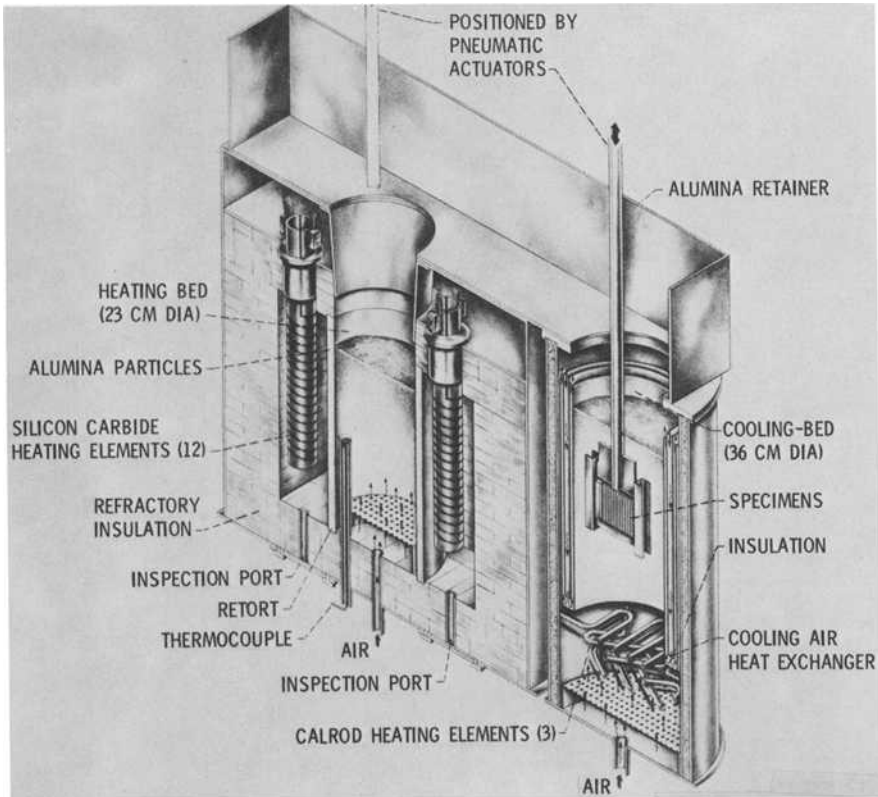


FIG. 3—Fluidized bed test facility at Illinois Institute of Technology Research Institute.

longer lives), duplicate or triplicate tests were run. The number of cycles to crack initiation was taken as the average of the number of cycles at the last inspection without cracks and the number of cycles at the first inspection with a crack.

Results and Discussion

Thermal-Stress Fatigue

The numbers of cycles required to initiate cracks in the 35 combinations of alloys and coatings are shown in Fig. 4. All results are for the 0.635-cm (0.25-in.)-radius edge only. For the same specimen geometry and test conditions, the lives varied from less than 25 to 12 500 cycles. Reproducibility of test data was generally good.

The class of materials having the longest thermal-stress fatigue lives was found to be cast alloys with directionally solidified polycrystalline grain

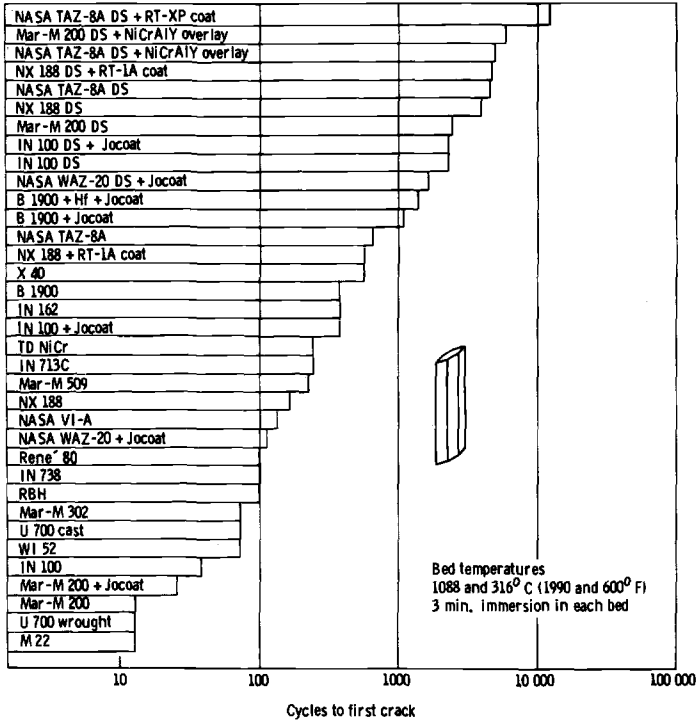


FIG. 4—Comparative thermal-stress fatigue resistances of nickel- and cobalt-base alloys.

structures. The alloy-coating combination with the highest thermal-stress fatigue resistance was directionally solidified NASA TAZ-8A with an RT-XP coating. Its thermal-stress fatigue life was almost double that of the next best alloy-coating combination, directionally solidified Mar-M200 with the overlay coating NiCrAlY. The application of a coating in all cases improved the thermal-stress fatigue resistance of the substrate alloy.

Of all the random polycrystalline alloys tested, hafnium-modified B 1900 with Jocoat had the highest thermal-stress fatigue resistance (1480 cycles). However, of the 19 uncoated random polycrystalline alloys tested, NASA TAZ-8A again had the highest thermal-stress fatigue resistance (700 cycles).

Some of the materials were also tested when both the maximum and minimum temperatures of the fluidized beds were raised by 42°C (75°F). A comparison of the thermal-stress fatigue resistances for materials tested at both bed temperature conditions is presented in Fig. 5. This figure indicates that raising the bed temperatures resulted in only minor changes in relative ordering of the thermal-stress fatigue resistances.

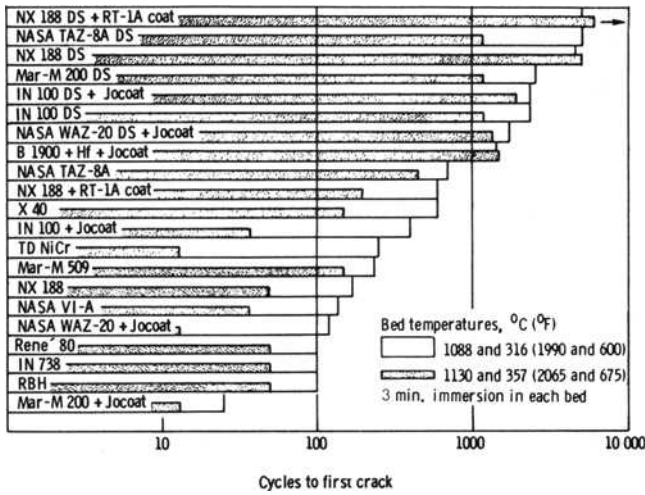


FIG. 5—Comparison of thermal-stress fatigue resistances for alloys tested at both bed temperature conditions.

An interesting observation was made regarding the two alloys NASA TAZ-8A and M 22. Reference to Table 2 shows the similarity of the compositions (considering the refractory elements as a group) of these two alloys. It is apparent from Fig. 4, however, that their thermal-stress fatigue resistances differ widely. It is suggested that further study of these two alloys might serve to identify the microstructural aspects which affect thermal-stress fatigue resistance in nickel-base alloys and perhaps lead to a better understanding of the thermal-stress fatigue process in such materials.

The superior resistance to thermal-stress fatigue of the five directionally solidified polycrystalline alloys in this study may be attributed to two factors: lower modulus of elasticity and an absence of transverse grain boundaries. The modulus of elasticity of a directionally solidified alloy (along the growth direction) can be 30 to 50 percent lower than that of the same alloy in the random polycrystalline form [8], whereas the thermal properties (thermal expansion, conductivity, etc.) are independent of the structure, being dependent only on the composition. Therefore, in specimens of the same composition and geometry under identical test conditions, the directionally solidified specimen will have significantly lower thermal stresses for the same induced strain than a specimen with a random polycrystalline structure. Also, the directional casting process produces long columnar grains aligned in the longitudinal direction of the specimen, and no grain boundaries intercept the specimen leading edge. This removes locations which might serve as crack nuclei. The beneficial

effect of the elimination of transverse grain boundaries can be seen by noting crack propagation in directional alloys. When a crack did initiate, the directional grains tended to be barriers to propagation [8]. Figure 6a shows a macrophotograph of directionally solidified Mar-M200 before and after testing for 2400 cycles at bed temperatures of 1130 and 357°C (2065 and 675°F). Note how the crack turned to grow in the longitudinal direction.

Oxidation

The materials exhibited a wide variation in oxidation resistance. In general, a coating or vapor-deposited overlay on an alloy gave a greatly reduced weight loss. Without surface protection, the directionally solidified alloys oxidized much faster than the same compositions in the random polycrystalline form [8]. The severe oxidation of an uncoated directionally solidified alloy can be seen by referring to Fig. 6b which shows directionally solidified IN 100 before testing and after testing for 2400 and 2900 cycles at bed temperatures of 1130 and 357°C (2065 and 675°F).

Figure 7 shows a comparison of the weight changes for directionally solidified TAZ-8A and Mar-M200, the alloy with the next highest thermal-stress fatigue resistance. All data are for double-wedge specimens tested at bed temperatures of 1088 and 316°C (1990 and 600°F). Results are presented for both alloys without a coating and with the NiCrAlY overlay coating. In addition, data for TAZ-8A with the RT-XP coat are also presented. The much higher weight loss of Mar-M200 compared to that of TAZ-8A in the uncoated condition is apparent. The effect of applying overlay coatings to both alloys is to greatly improve their oxidation resistance. Note that TAZ-8A with the RT-XP coating exhibited only a ½ percent weight loss after 14 000 cycles of testing, indicating excellent resistance to oxidation.

Summary of Results

The comparative thermal-stress fatigue resistances of 26 nickel- and cobalt-base alloys were determined using the fluidized bed technique. A total of 35 combinations of compositions, grain structure, and coatings were studied. All materials were evaluated by thermally cycling double-wedge specimens between two fluidized bed furnaces maintained at 1088 and 316°C (1990 and 600°F). Some materials were also exposed to bed temperatures of 1130 and 357°C (2065 and 675°F). Immersion times were 3 min in both the high and low temperature beds. Thermal-stress fatigue resistance was based on the number of cycles required to initiate a crack. The major results obtained are as follows.

1. Thermal-stress fatigue lives under identical test conditions ranged

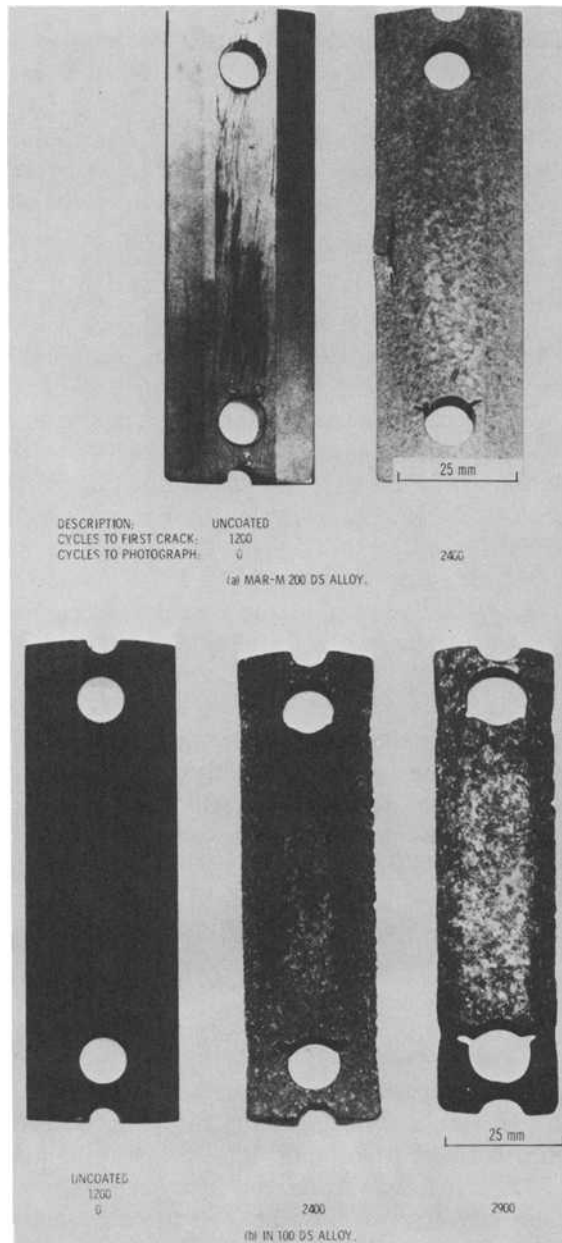


FIG. 6—Directionally solidified thermal-stress fatigue specimens before and after testing at bed temperatures of 1130 and 357°C (2065 and 675 °F).

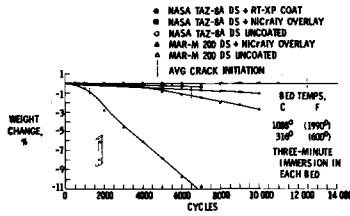


FIG. 7—Weight change for two directionally solidified alloys from fluidized bed tests.

from less than 25 to 12 500 cycles among the 35 combinations of compositions, grain structure, and coatings.

2. The class of alloys having the longest thermal-stress fatigue lives were cast alloys with directionally solidified polycrystalline grain structures.

3. The four coatings employed always increased the thermal-stress fatigue resistance of the substrate alloy. The application of the diffusion coatings or the vapor-deposited overlay coating on the directionally solidified alloys also greatly reduced weight loss.

4. The alloy-coating combination with the highest thermal-stress fatigue resistance was directionally solidified NASA TAZ-8A with an RT-XP coating (proprietary coating containing an aluminide from Chromalloy American Corporation). Its thermal-stress fatigue life was almost twice that of the next best alloy-coating combination. Its oxidation resistance was also excellent. Of the 19 uncoated random polycrystalline alloys tested, NASA TAZ-8A had the highest thermal-stress fatigue resistance.

References

- [1] Spera, D. A. and Grisaffe, S. J., "Life Prediction of Turbine Components: On-Going Studies at the NASA Lewis Research Center," Technical Memorandum X-2664, National Aeronautics and Space Administration, 1973.
- [2] Bizon, P. T. and Oldrieve, R. E., "Thermal Fatigue Resistance of NASA WAZ-20 Alloy With Three Commercial Coatings," Technical Memorandum X-3168, National Aeronautics and Space Administration, 1975.
- [3] Spera, D. A., Howes, M. A., and Bizon, P. T., "Thermal Fatigue Resistance of 15 High-Temperature Alloys Determined by the Fluidized-Bed Technique," Technical Memorandum X-52975, National Aeronautics and Space Administration, 1971.
- [4] Howes, M. A., "Thermal Fatigue Data on 15 Nickel- and Cobalt-Base Alloys," IIT Research Institute, Report IITRI-B6078-38, Report CR-72738, National Aeronautics and Space Administration, 1970.
- [5] Howes, M. A., "Additional Thermal Fatigue Data on Nickel- and Cobalt-Base Superalloys," IIT Research Institute, Report IITRI-B6107-34 (Part 1), Report CR-121211, National Aeronautics and Space Administration, 1973.
- [6] Howes, M. A., "Additional Thermal Fatigue Data on Nickel- and Cobalt-Base Superalloys," IIT Research Institute Report IITRI-B6107-34 (Part 2), Report CR-121212, National Aeronautics and Space Administration, 1973.
- [7] Howes, M. A., "Thermal Fatigue and Oxidation Data on TAZ-8A, Mar-M 200, and Udimet 700 Superalloys," IIT Research Institute, Report IITRI-B6124-21, Report CR-134775, National Aeronautics and Space Administration, 1975.

- [8] Bizon, P. T. and Spera, D. A., "Comparative Thermal Fatigue Resistances of 26 Nickel- and Cobalt-Base Alloys," Technical Note D-8071, National Aeronautics and Space Administration, 1975.
- [9] Glenny, E., Northwood, J. E., Shaw, S. W., and Taylor, T. A., *Journal of the Institute of Metals*, Vol. 87, 1958-9, pp. 294-302.
- [10] Glenny, E. and Taylor, T. A., *Journal of the Institute of Metals*, Vol. 88, 1959-60, pp. 449-461.
- [11] Franklin, A. W., Heslop, J., and Smith, R. A., *Journal of the Institute of Metals*, Vol. 92, 1963-4, pp. 313-321.
- [12] Howes, M. A., *Die Casting Engineering*, Vol. 13, 1969, p. 12.
- [13] Howes, M. A. and Saperstein, Z. P., *Welding*, Vol. 48, 1969, pp. 543-545.
- [14] Rostoker, W., *Journal of Materials*, Vol. 4, No. 1, 1969, pp. 117-144.
- [15] Mowbray, D. F., Woodford, D. A., and Brandt, D. E. in *Fatigue at Elevated Temperatures*, ASTM STP 520, American Society for Testing and Materials, 1973, pp. 416-426.
- [16] Freche, J. C., Waters, W. J., and Ashbrook, R. L., "Application of Directional Solidification to a NASA Nickel-Base Alloy (TAZ-8B)," Technical Note D-4390, National Aeronautics and Space Administration, 1968.
- [17] Howes, M. A. in *Fatigue at Elevated Temperatures*, ASTM STP 520, American Society for Testing and Materials, 1973, pp. 242-254.

Effect of Microstructure on the Thermal Fatigue Resistance of a Cast Cobalt-Base Alloy, Mar-M509

REFERENCE: Beck, C. G. and Santhanam, A. T., "Effect of Microstructure on the Thermal Fatigue Resistance of a Cast Cobalt-Base Alloy, Mar-M509," *Thermal Fatigue of Materials and Components, ASTM STP 612*, D. A. Spera and D. F. Mowbray, Eds., American Society for Testing and Materials, 1976, pp. 123-140.

ABSTRACT: A study was undertaken to determine whether the thermal fatigue response of the cast cobalt-base alloy, Mar-M509, could be modified by changing the casting parameters. Single-edge wedge-type specimens were tested in a fluidized bed using a thermal cycle of 1915/525°F with a cycle time of 6 min divided equally between heating and cooling. The results revealed that the thermal fatigue life of Mar-M509, from the point of view of both crack initiation and propagation, could be significantly improved by changing the casting variables. Cracking was found to be predominantly transgranular and often initiated at interdendritic carbides. A good correlation was obtained between the secondary dendrite arm spacing and the number of cycles for crack initiation, as well as the crack propagation rates. Small dendrite spacings reduced the thermal fatigue life by accelerating both the crack initiation and propagation. Precipitation of MC and M₂₃C₆ carbide occurred during the thermal cycling and affected the crack propagation rate. Based on these results, a model for thermal fatigue cracking in Mar-M509 is presented.

KEY WORDS: thermal fatigue, fatigue (materials), cobalt alloys, microstructure

In gas turbines, critical components such as blades and guide vanes are subjected to rapid changes in temperature during startups and shutdowns. The outer layers and thinner sections of the components respond more quickly to changes in temperature than the interior. The resulting thermal gradients give rise to thermal strains and stresses. Repetition of the stress cycles during service can sometimes cause cracking of the component. This type of cracking under fluctuating temperature conditions is termed thermal fatigue. The susceptibility of blade and vane materials to thermal fatigue is therefore a matter of vital concern to the designer.

¹Engineer and senior engineer, respectively, Westinghouse Research Laboratories, Pittsburgh, Pa. 15235.

The evaluation of the thermal fatigue resistance of a material is a formidable task since it depends on a number of variables such as the maximum and minimum temperature, heating and cooling rate, specimen geometry, environment, etc. One of the methods developed in recent years to simulate the thermal cycles experienced in actual applications is fluidized bed testing [1]² in which a specimen is rapidly heated and cooled in beds of fluidized particles, and the number of thermal cycles required for crack initiation is measured. While a good number of high temperature materials have been ranked on this basis for thermal fatigue resistance [2], very little attention has been given to controlling and optimizing the microstructure for the minimization of thermal fatigue cracking. A study was undertaken to determine whether the thermal fatigue response of the cobalt-base alloy, Mar-M509, could be modified by changing its microstructure.

Experimental

The cobalt-base alloy, Mar-M509, is presently used as one of the guide vane materials for land and air gas turbines. The chemical composition of the heat used is given in Table 1. Specimens were cast using different mold and superheat temperatures which produced variations in grain size, dendrite spacings, and amount of carbides. Single-edge wedge-type specimens with geometry as shown in Fig. 1 were prepared from these castings.

The thermal fatigue testing was carried out in a fluidized bed test facility at the Illinois Institute of Technology Research Institute (IITRI). It consists of a high-temperature bed heated externally with silicon carbide elements and a low-temperature bed equipped with an air- or water-cooled heat exchanger and an internal heat source of low power. The specimens are cycled between the high- and low-temperature beds by means of automatically controlled pneumatic cylinders. The bed consists of alumina particles in the 28 to 48 mesh size range. Air enters from the bottom and keeps the bed fluidized. As a result, the rate of heat transfer to the specimen is high. The heat content of the media is also high, so that a large number of specimens can be heated and cooled rapidly without lowering the bed temperature significantly.

A thermal cycle of 1915/525 °F (1046/274 °C) was used in the present study. The specimens were immersed in each bed for 3 min. Thermocouples were placed at five locations across the specimen section, and the temperatures were recorded during heating and cooling. The time history of the tip (thin trailing edge) temperature and that of the center of the specimen is displayed in Fig. 2. Note that the tip gets heated and cooled more rapidly than the center (Thermocouple Position 3) and gives rise to a transient temperature difference which maximizes at short times. It is this transient tem-

² The italic numbers in brackets refer to the list of references appended to this paper.

TABLE 1—Chemical composition of Mar-M509.

C	Mn	Si	S	Cr	Ni	W	Fe	Ti	Ta	Zr	B	Cu	Pb	Ag	Co
0.62	<0.1	<0.1	0.003	23	10	6.95	0.24	0.18	3.75	0.50	0.006	<0.1	<0.00001	<0.000005	Bal

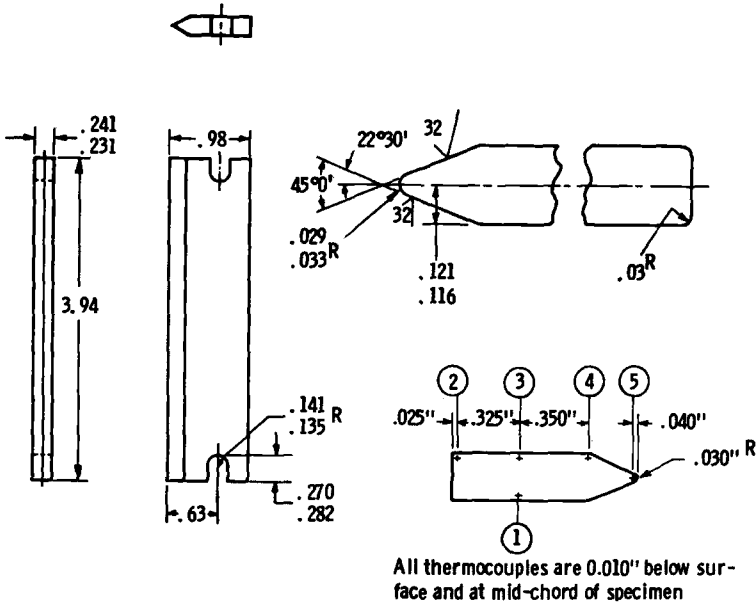


FIG. 1—Fluidized bed thermal fatigue specimen.

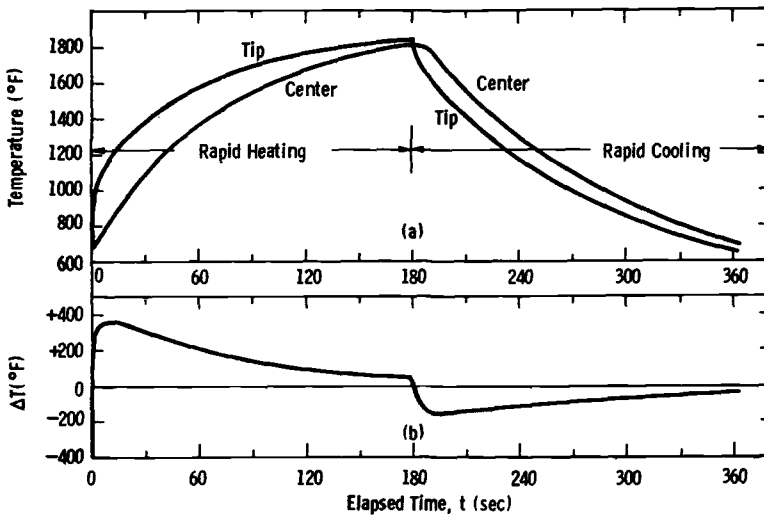


FIG. 2—(a) Measured temperatures during rapid heating and cooling of wedge type specimen of Mar-M509 and (b) transient temperature between the tip and the center of the specimen.

perature difference that gives rise to thermal strains and stresses and consequent cracking of a component.

The specimens were removed from the test rig at regular intervals, and the edges were examined for crack initiation using a $\times 30$ microscope. Inspections were made at 25, 50, and 100 cycles, after every 100 cycles up to 2000 cycles, and at 2500 and 3000 cycles. When a crack was observed, its length from crack tip to specimen edge was measured on both surfaces, and the average value was taken as the crack length.

Crack Initiation and Propagation

The number of cycles required to initiate the first crack and the rate of propagation of the crack were determined for all the specimens representing the different casting conditions. There are several methods by which the number of cycles for crack initiation can be determined. One of the methods suggested by Glennly [3] involves averaging the number of cycles between one inspection cycle when no crack was observed and the next inspection to show a crack. This was determined for all the specimens. Figure 3 illustrates another method in which the average crack length is plotted as a function of the number of cycles, and the curve is back-extrapolated to "zero crack length." (In the present study, the extrapolation was carried to a crack length of 0.01 in.) The thermal fatigue lives calculated by this method were much shorter than those obtained by the averaging method. It was felt that a measurement of crack area would be more appropriate. This was computed from the crack length measurements on both surfaces. Figure 4 shows the crack area as a function of the number of thermal cycles

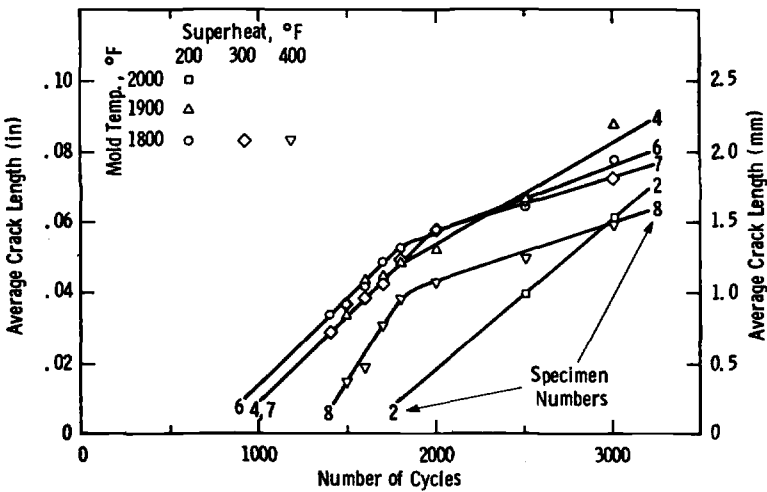


FIG. 3—Crack length versus number of cycles for various casting parameters of Mar-M509.

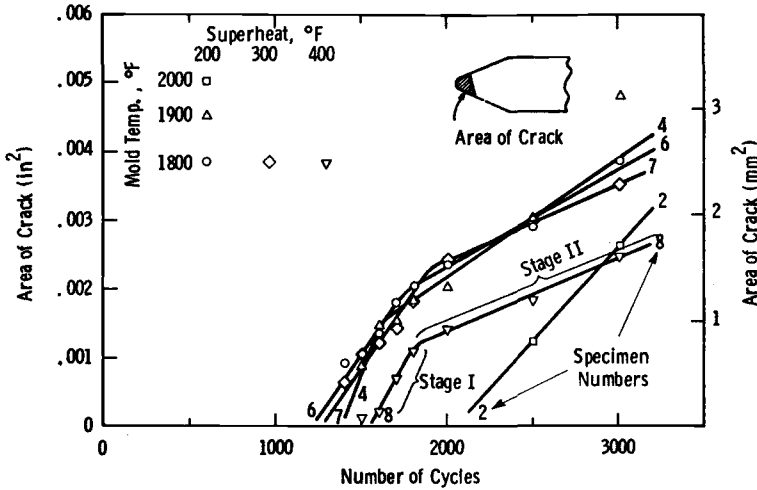


FIG. 4—Area of crack versus number of cycles for various casting parameters of Mar-M509.

for the specimens tested. The thermal cycles required for crack initiation were determined by extrapolating the curves to zero crack area (actually 0.001 in.^2). Figure 4 demonstrates that the specimens representing the different casting variables differ in their response to thermal fatigue. There are differences in both the number of cycles for crack initiation and in the crack propagation rate. Furthermore, crack propagation occurs in two stages. (This is true for all the specimens except Specimen 2 in which only Stage 1 was observed within 3000 thermal cycles.) The first stage crack propagation is faster than the second stage. Table 2 summarizes the crack initiation and propagation data for each of the specimens. As can be seen in this table, based on the measured cracked area, the thermal fatigue lives, from the point of view of crack initiation, varied from 1200 to 2100 cycles. The first stage crack propagation rates differed by a factor of ≈ 1.5 .

Microstructural Aspects

A microstructural study was performed on the specimens before and after the thermal fatigue test with a view to identifying the structural features associated with crack initiation and propagation. The specimens were ground to the midplane, polished, etched, and examined by optical microscopy.

In general, the as-cast microstructure of Mar-M509 consists of five phases:

1. A face-centered-cubic (fcc) cobalt-base matrix.
2. An interdendritic script-like MC carbide.

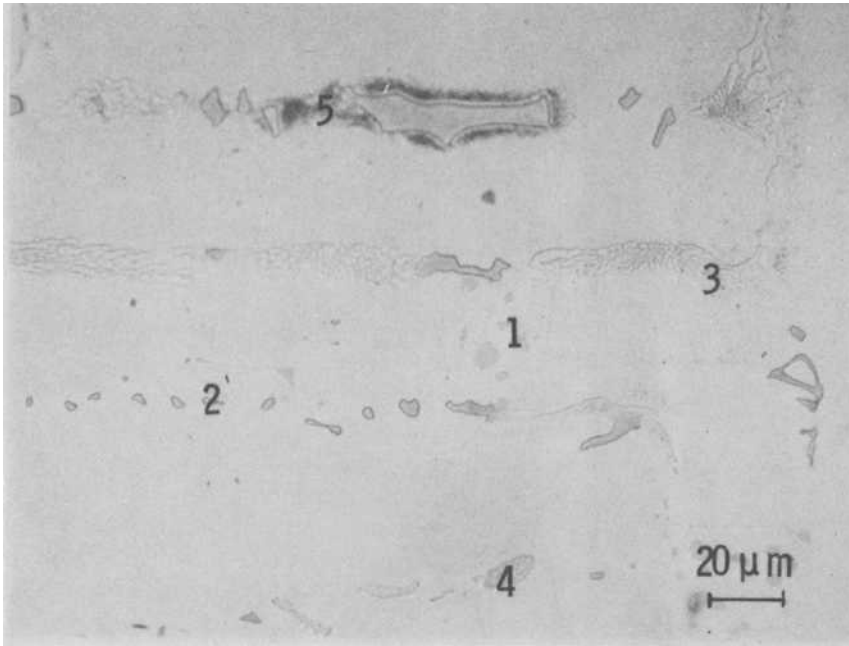
TABLE 2—Summary of crack initiation and propagation data.

Specimen No.	Mold Preheat Temperature, °F	Superheat Temperature, °F	No. of Cycles to Initiate a Crack			Crack Propagation Rate, in. ² /cycle		Dendrite Arm Spacing, μm	Grain Size at Periphery, dia (mm)
			Avg Length ^a	Area ^a	Averaging	Initial	Later		
6	1800	200	920	1220	1350	4.3 × 10 ⁻⁶	1.325 × 10 ⁻⁶	33 to 40	1.5 to 2.0
4	1900	200	1040	1400	1450	3.38 × 10 ⁻⁶	1.540 × 10 ⁻⁶	44 to 48	0.8 to 1.0
2	2000	200	1800	2080	2250	2.80 × 10 ⁻⁶	...	58 to 70	0.6 to 0.8
7	1800	300	1000	1300	1350	4.30 × 10 ⁻⁶	1.022 × 10 ⁻⁶	34 to 40	0.7 to 1.0
8	1800	400	1420	1560	1450	3.60 × 10 ⁻⁶	0.880 × 10 ⁻⁶	38 to 48	1.3 to 1.5

^aCrack initiation criteria: length >0.01 in., area >0.0001 in.².

3. Lamellar eutectic consisting of M_7C_3 carbide and matrix.
4. Another lamellar eutectic made up of $M_{23}C_6$ carbide and matrix.
5. A fine precipitate of $M_{23}C_6$ /MC carbides around large MC carbide particles (see Fig. 5).

A typical microstructure of the specimen after the thermal fatigue test is shown in Fig. 6. Note that the cracks often initiated at interdendritic car-



1. A fcc cobalt-base matrix.
2. An interdendritic script-like MC carbide.
3. Lamellar eutectic consisting of M_7C_3 carbide and matrix.
4. Another lamellar eutectic made up of $M_{23}C_6$ carbide and matrix.
5. A fine precipitate of $M_{23}C_6$ /MC carbides around large MC carbide particles.

FIG. 5—As-cast microstructure of Mar-M509.

bides. Very few cracks initiated at grain boundaries. The crack propagation was predominantly transgranular and occurred in a direction normal to the longitudinal axis of the specimen. This is illustrated in Fig. 7. Varying the grain size from 0.5 to 2 mm did not affect either the crack initiation or propagation as can be seen in Fig. 8.

Figure 9 shows the crack growth path after 3000 thermal cycles for various solidification conditions with associated variation in the secondary dendrite arm spacings.³ Two significant features emerge from this figure:

³ Hereafter, the term "dendrite arm spacing" will be used to denote "secondary dendrite arm spacing."

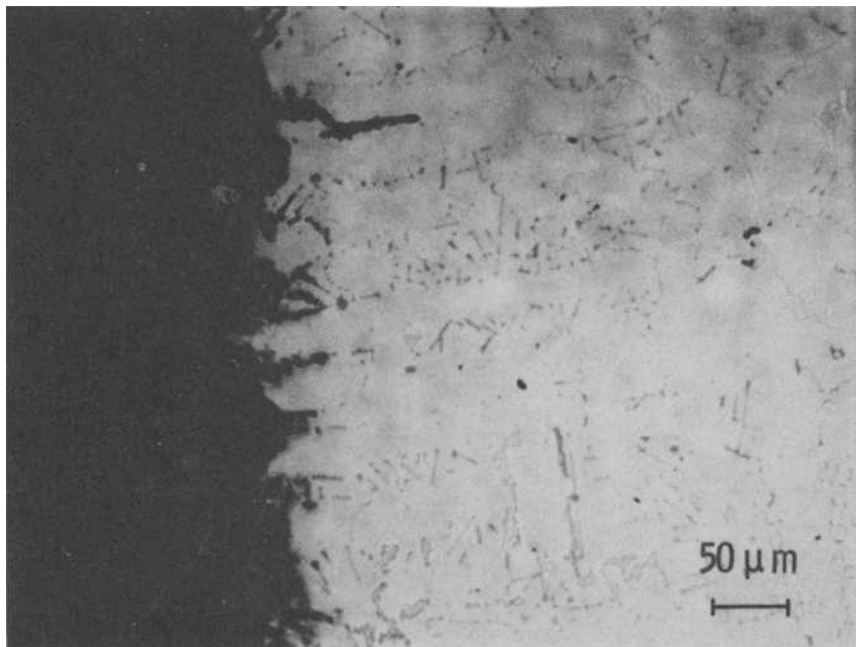


FIG. 6—Crack initiation sites in Mar-M509.

(a) cracks grow both interdendritically and across the dendrites and (b) overall crack length decreases with increasing dendrite arm spacing.

In an attempt to monitor the structural changes that occur during thermal cycling, the various carbide phases were carefully examined. It was observed that the large script-like MC carbides were stable during the thermal cycling test. However, fine $M_{23}C_6$ and MC carbides precipitated within the dendrite areas (Fig. 10). To determine the total amount of carbide precipitated during the test, the matrix was dissolved electrolytically [4], and the insoluble residue was collected, weighed, and identified by X-ray diffraction. Table 3 summarizes the variations in the type and amount of carbides before and after the thermal fatigue test. The as-cast microstructure consists of two MC carbide phases which differ in their lattice parameter (MC #1 > MC #2) and one M_7C_3 carbide phase. During thermal cycling, the metastable M_7C_3 phase decomposes into $M_{23}C_6$ and MC carbides. Both of these carbides also precipitate from the matrix. As a result, for a given dendrite arm spacing, the total amount of carbide increases during thermal cycling. Table 3 shows that there is a greater increase in total carbide in Specimen 6 (smallest dendrite arm spacing) than Specimen 2 (coarsest dendrite arm spacing). Also note that there is a greater increase in the amount of MC #2 carbide in Specimen 6 than in Specimen 2. It was ob-

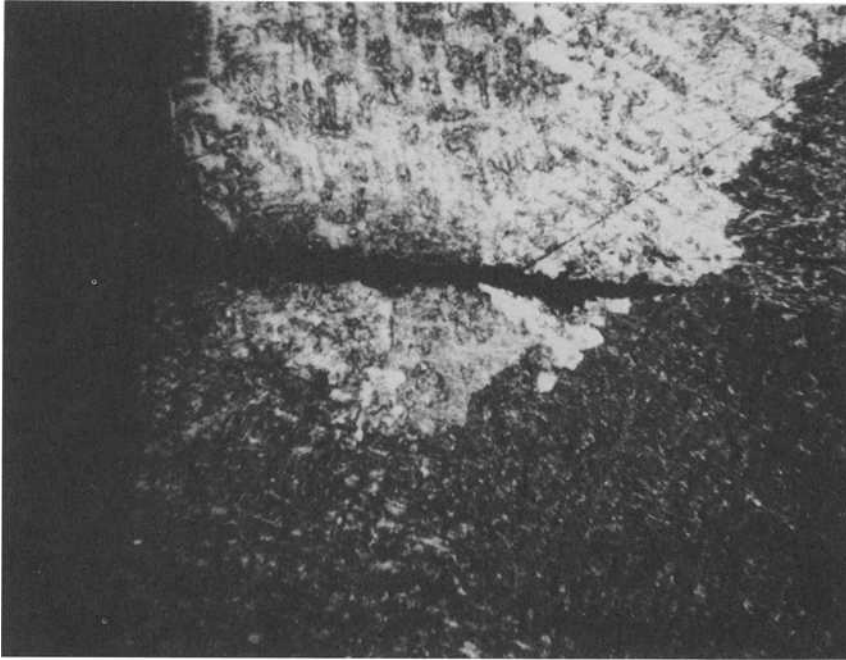


FIG. 7—*Transgranular nature of the crack growth in Mar-M509. The longitudinal axis of the specimen is vertical ($\times 50$).*

served that the MC #2 carbide precipitates preferentially within dendrite areas. The significance of this phase with regard to crack propagation will be discussed later.

Correlating the Microstructure with the Thermal Fatigue Properties

The various solidification conditions employed in this study produced variations in grain size and dendrite spacings. No direct correlation was observed between the grain size and the thermal fatigue resistance. However, the dendrite arm spacings had a significant influence on crack initiation and propagation behavior. This is illustrated in Figs. 11 and 12. Note that small dendrite arm spacings reduce the thermal fatigue life by accelerating both the crack initiation and the initial crack propagation rate.

A previous study of thermal fatigue behavior of Mar-M509 by Howes, using the same thermal cycle as employed in this investigation, indicated that the number of cycles to initiate a crack in this material was between 125 and 350 [5]. The dendrite arm spacing was estimated to be $\sim 10 \mu\text{m}$ from a micrograph given in that reference. The data point is included in Fig. 11. It

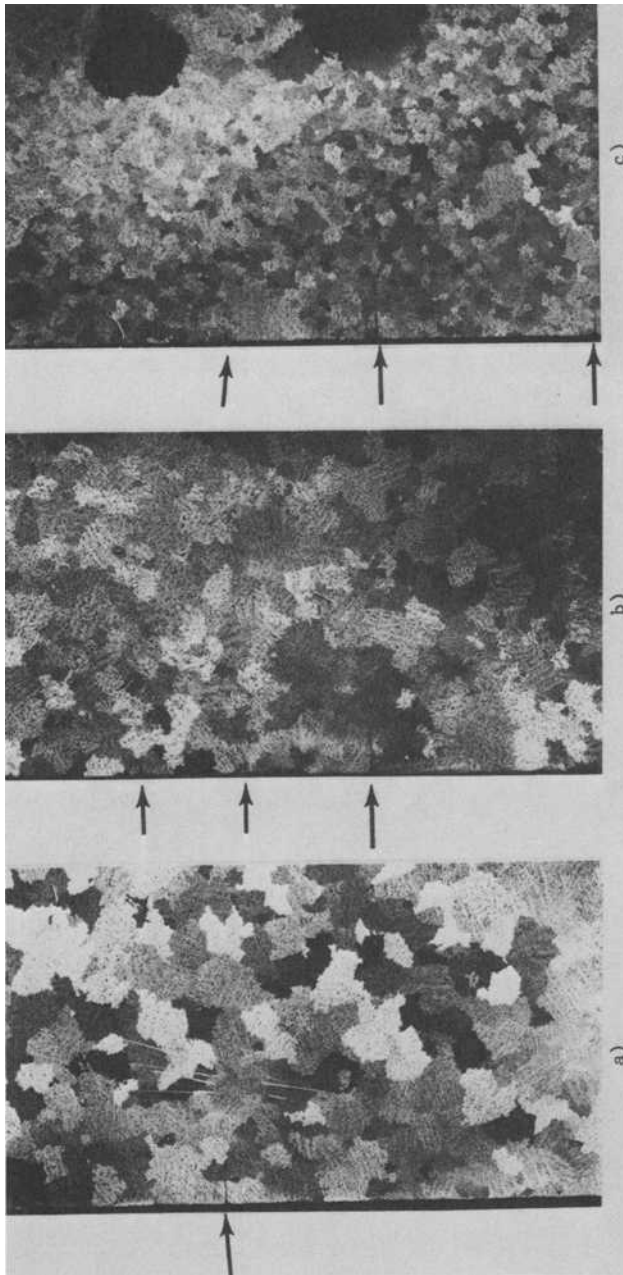


FIG. 8.—Variation in grain size produced by using different mold preheat temperatures. The arrows show the thermal fatigue cracks. (a) 2000°F, (b) 1900°F, and (c) 1800°F ($\times 3.75$).

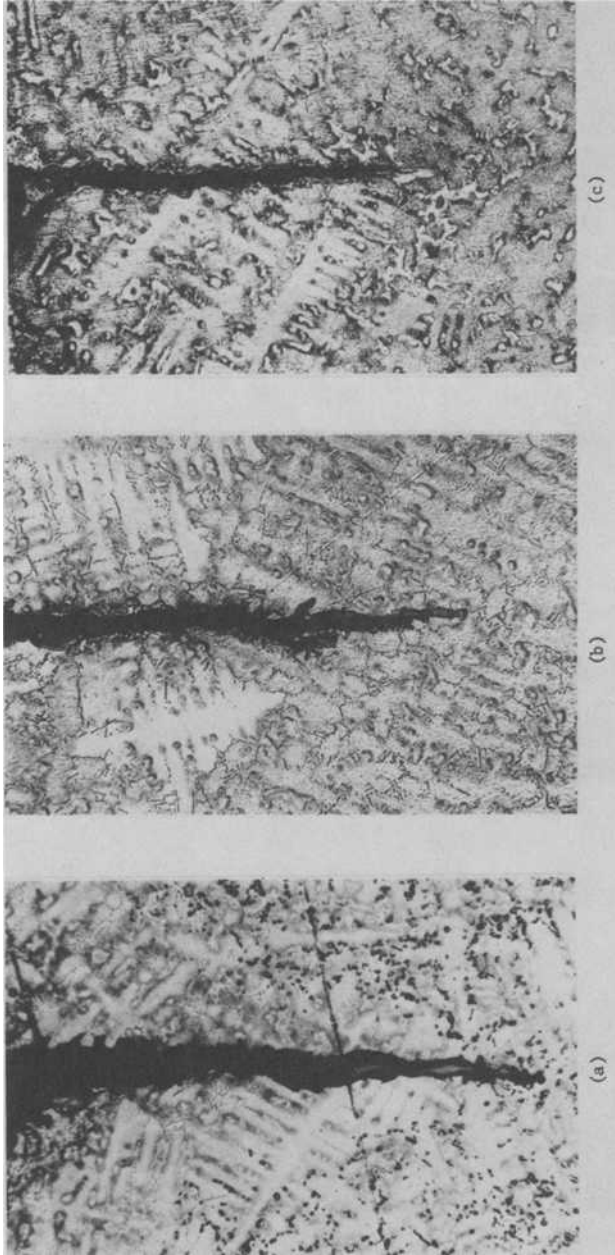


FIG. 9—Crack growth path in Mar-M509 for various dendrite arm spacings: (a) 33 to 40 μm , (b) 44 to 48 μm , and (c) 58 to 70 μm ($\times 68$).

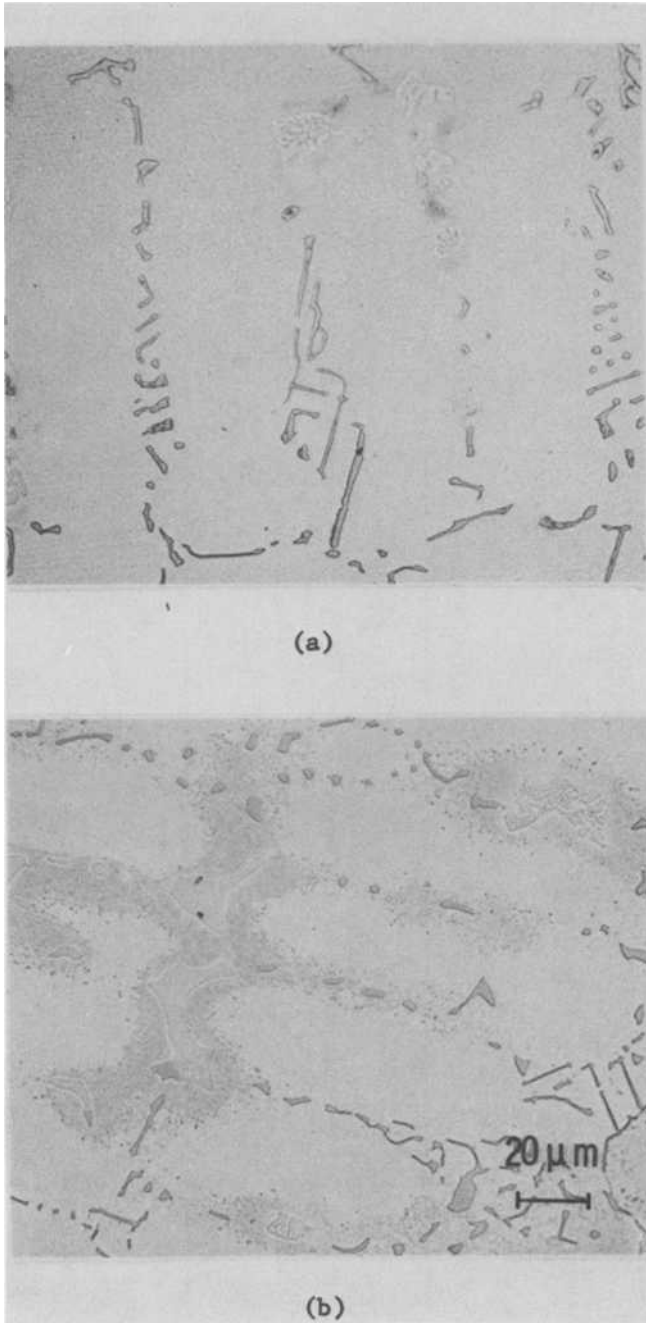


FIG. 10—Effect of thermal cycling on the microstructure of cobalt superalloy Mar-M509.

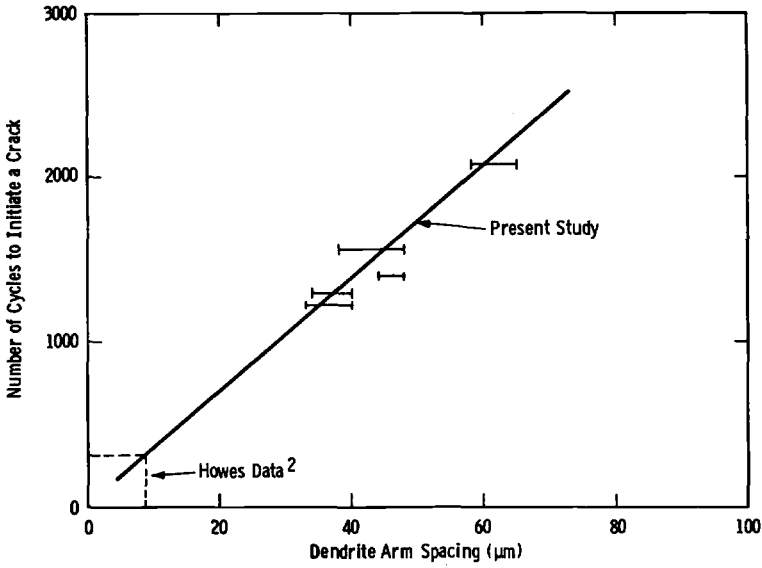


FIG. 11—Correlation between the number of cycles to initiate a crack and the dendrite arm spacing for Mar-M509.

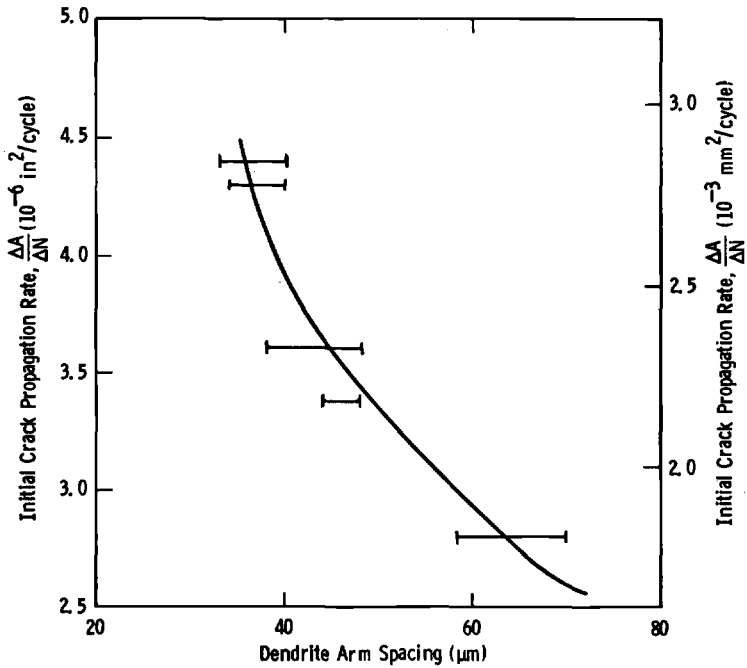


FIG. 12—Correlation between the initial crack propagation rate and the dendrite arm spacing for Mar-M509.

is interesting to note that Howes' data point lies on the line extrapolated from the present data.

The first stage crack propagation rate could also be correlated with the amount of MC #2 carbide phase that precipitates during thermal cycling. This correlation suggests that the effect of dendrite arm spacings on crack growth rate could be an indirect one. No correlation was obtained between the second stage crack propagation rate and the microstructure.

Discussion

The present study demonstrates that the response of a material to thermal fatigue can be changed by changing its microstructure. In particular, it has been shown that in cast cobalt-base alloy, Mar-M509, coarse dendrite arm spacings improve the thermal fatigue resistance by delaying crack initiation and also by reducing the crack propagation rate. It has also been shown that thermal fatigue cracks initiate at the specimen periphery in the interdendritic areas but propagate both interdendritically as well as across the dendrites. Based on these observations, a model for thermal fatigue cracking can be proposed as follows.

Let us consider Fig. 13. In this schematic drawing, two microstructural conditions are depicted. Figure 13a shows a specimen with fine dendrite arm spacing, whereas Fig. 13b refers to a specimen with coarse dendrite arm spacing. In both cases, the cracks are shown to initiate at interdendritic areas but to propagate both inter- as well as transdendritically.

The interdendritic regions contain a large number of script-like MC-type

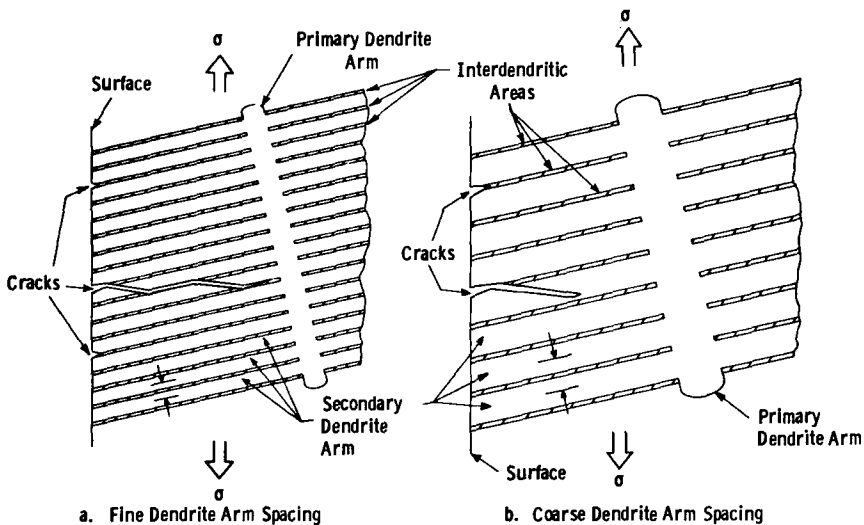


FIG. 13—Schematic of two microstructural conditions depicting a model for thermal fatigue cracking in Mar-M509. Markers indicate secondary dendrite arm spacings.

carbides, (Ta, Zr) carbide, and islands of eutectic M_7C_3 -type carbide (Cr_7C_3). The carbides can act as stress concentrators and provide crack initiation sites. In addition, preferential oxidation of script-like (Zr, Ta)C carbide [6] can promote notch formation at the periphery of the specimens. The likelihood that microporosity will occur is also greater in the interdendritic areas than within the dendrites. The micropores could act as stress raisers and favor crack nucleation. All these arguments suggest that crack initiation is easier in the interdendritic areas. The probability of crack initiation would also be higher in the specimens with fine dendrite arm spacings (larger amount of interdendritic areas) than in the specimens with coarse dendrite arm spacings.

Once a crack initiates at an interdendritic site, it would tend to propagate along the interdendritic area since it contains favorable conditions for crack growth such as the presence of brittle carbide phases. It was shown that the cracks propagate faster in specimens with fine dendrite arm spacings than in specimens with coarse dendrite arm spacings. The schematic drawing shown in Fig. 13 again provides a clue to the observed behavior. If the dendrite arms are inclined to the surface, as shown in Fig. 13, the crack propagation along the carbide network cannot continue indefinitely since the crack is constrained to propagate in a direction approximately normal to the longitudinal axis of the specimen along which the stresses operate. The crack would therefore have to change direction and travel across the dendrite arms. This would imply that, in the specimen with large dendrite arm spacings (Fig. 13), the crack has to travel longer distances across the dendrites before meeting the adjacent carbide network. The rate at which the crack grows across the dendrites would obviously depend on the microstructural features within the dendrite areas. Table 3 shows that precipitation of MC and $M_{23}C_6$ carbides occurs during thermal cycling. Of these, the amount of $M_{23}C_6$ and MC #1 carbides that precipitate during thermal cycling is nearly independent of dendrite spacings; however, a smaller amount of MC #2 carbide precipitates in the specimen with coarse dendrite arm spacing (Specimen 2) than in the fine dendrite arm spacing specimen (Specimen 6). The MC carbides generally precipitate along crystallographic directions within the dendrite areas [7,8]. When aligned favorably, these carbides could provide easy paths for crack propagation. The smaller amount of MC #2 carbide observed in the coarse dendrite arm spacing specimen would therefore provide a less continuous path for crack propagation than the carbides in the fine dendrite arm spacing specimen. This observation, coupled with the fact that the crack has to travel longer distances across the coarse dendrites, would imply that the crack propagation would be slower in the coarse dendrite arm spacing specimen. The experimental evidence for this behavior can be obtained in Fig. 9 which demonstrates that, for the same number of thermal cycles (3000 cycles), the crack is shorter in the specimen with coarse dendrite arm spacing than in the specimen with fine dendrite arm spacing.

Conclusions

1. The thermal fatigue resistance for a given heat of cast Mar-M509 can be improved by employing solidification conditions that result in coarse dendrite arm spacings.

2. This improvement occurs in both the number of cycles to initiate a crack as well as the rate of crack propagation.

3. The carbides at the interdendritic areas act as preferred crack nucleation sites and also provide easy paths for crack propagation.

4. The smaller number of interdendritic sites as well as a lower amount of MC #2 carbide precipitated within the dendrite areas during thermal cycling can explain the superior thermal fatigue resistance of the specimens with coarse dendrite arm spacings.

Acknowledgment

The assistance of P. M. Yuzawich in preparing metallographic specimens is gratefully acknowledged.

References

- [1] Howes, M. A. in *Fatigue at Elevated Temperature, ASTM STP 520*, American Society for Testing and Materials, 1973, pp. 242-254.
- [2] Bizon, P. T. and Spera, D. A., "Comparative Thermal Fatigue Resistances of Twenty-Six Nickel- and Cobalt-Base Alloys," NASA TN D-8071, National Aeronautics and Space Administration, 1975.
- [3] Glenny, E. et al, *Journal of the Institute of Metals*, Vol. 84, 1958-1959, p. 294.
- [4] Donachie, M. J., Jr., and Kriege, O. H., *Journal of Materials*, Vol. 7, No. 3, Sept. 1972, pp. 269-278.
- [5] Howes, M. A. H., NASA Report CR-121212, National Aeronautics and Space Administration, 1973.
- [6] Woulds, M. J. and Cass, T. R., *Cobalt* 42, March 1969, pp. 3-13.
- [7] Sims, C. T., "The Superalloys—Chapter 5," C. T. Sims and W. C. Hagel, Eds., Wiley, New York, 1972.
- [8] Drapier, J. M., Leroy, V., Dupont, C., Coutsouradis, D., and Habraken, L., "Structural Stability of Mar M-509—A Cobalt-Base Superalloy," *International Symposium on Structural Stability in Superalloys*, Seven Springs, Pa., 4-6 Sept. 1968, pp. 436-459.

J. S. Laub¹

Some Thermal Fatigue Characteristics of Mild Steel for Heat Exchangers

REFERENCE: Laub, J. S., "Some Thermal Fatigue Characteristics of Mild Steel for Heat Exchangers," *Thermal Fatigue of Materials and Components, ASTM STP 612*, D. A. Spera and D. F. Mowbray, Eds., American Society for Testing and Materials, 1976, pp. 141-156.

ABSTRACT: Thermal fatigue of mild steel has received little attention until recently even though this material is used extensively in heat exchangers for gas-fired appliances. A survey of the thermal fatigue problem of thin shell mild steel structures subjected to arbitrary temperature fields is given. Data from end-constrained thermally cycled test specimens is also presented. These data have been validated through use in developing production heat exchangers.

KEY WORDS: thermal fatigue, heat exchangers, steels, fatigue (materials)

Nomenclature

- $\Delta\epsilon$ Total strain range, elastic and plastic
- ΔT Temperature range
- T_m Mean cyclic temp, $T_{\max} + T_{\min}/2$
- R Strain ratio $\epsilon_{\min}/\epsilon_{\max}$
- a Weibull location parameter
- c Weibull shape parameter
- $\mu\epsilon$ Microstrain, 10^{-6} unit length/unit length

Ordinary low-carbon mild steels are not normally considered to be high-temperature structural materials; however, large quantities of 16 to 20-gage (1.6 to 0.9-mm-thick) sheet is used every year to make gas-fired appliance heat exchangers. These devices usually take the form of an irregular thin shell, often with a plane of symmetry coincident with flanges used to weld two drawn halves together. Figure 1 shows a typical heat exchanger cell

¹ Senior engineer, Research Division, Carrier Corp., Syracuse, N. Y. 13201.

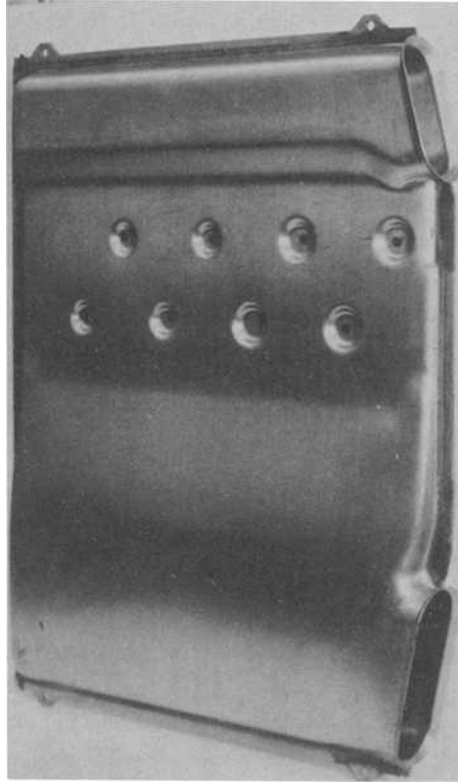


FIG. 1—A typical gas-fired heat exchanger cell.

fired by a gas burner inserted into the lower opening to a thermal rating of 33 000 Btu/h. The upper opening is attached to a flue collector box which transfers the flue gas of this and an arbitrary number of other cells to the stack. Residential and commercial gas furnaces have multiple numbers of these units determined by their capacity.

Heated internally by a gas flame, the cells are cooled by room air circulated in most cases by a fan over their outside surfaces. Internal area variations between adjacent cell surfaces or an outer cell surface and the furnace casing produce variable and arbitrary air flow patterns which combine with the flame thermal pattern to give a complex and time-varying temperature pattern in the material. During typical furnace operation, any given point in the cell will be subjected to a temperature cycle determined by the operational functions plus the timing and duration of the flame and circulating fan. The net result is that the thin shell of an appliance heat exchanger presents one of the most difficult and challenging thermal strain and thermal fatigue problems to be found in engineering practice.

Economic considerations dictate that any new design must be well proven

against thermal fatigue, but, until recently, the only accepted method for doing this was the laborious, time consuming, imprecise, and inefficient life test program. Even life testing is subject to a wide divergence of opinion since any given exchanger may be used in a multiplicity of appliance types (upflow, downflow, crossflow, space heaters, and combination heating and cooling units); and each installation has its own demand peculiarities which determine, to some extent, the cycle and temperatures encountered. Further, by the time a life test program is complete, changing conditions have often dictated new and previously unforeseen uses necessitating a new, long-term test program. Although a component may cost only a few dollars to manufacture, it will be made by the tens or hundreds of thousands per year which necessitates a quicker and more efficient method of proving structural integrity.

Experimental techniques for thermal strain analysis on thin shell structures, while difficult, have been developed in the author's laboratory to the point of providing part of the thermal fatigue problem answer. Over a period of several years, conventional experimental stress analysis methods have been combined, refined, and adapted so that acceptably accurate strain measurements can be made with readily available equipment. Ceramic brittle coatings give initial external surface tensile strain patterns above a threshold strain varying with the local temperature but ranging normally between 600 and 1200 $\mu\epsilon$. Medium temperature foil strain gages with self-temperature compensation can be used in locations of the shell which do not exceed 650°F (343°C). The manufacturer's apparent strain versus temperature correction curve can be incorporated in the data reduction for improved accuracy. For areas of the shell which exceed this temperature, strain measurements require high temperature, wire strain gages applied with flame-sprayed molten ceramic along with special temperature compensation techniques and data reduction programs.

Acceptable strain measurement is one necessary part of the thermal fatigue-reliability problem; the second is an accurate knowledge of the thermal fatigue behavior of the exchanger material. Until recently, very little information was available for ordinary low-carbon or mild steel under conditions of both varying strain and temperature. Some work was published on strain cycling at constant elevated temperatures [1-3],² for example, but this did not really come to grips with heat exchanger operation where strain changes in concert with temperature. As a consequence, thermal fatigue tests were set up on specially constructed equipment following Coffin's earlier work [4-7]. This paper presents the results of these tests. The accuracy of the data has been established by successfully using it in designing and qualifying reliable heat exchangers.

Recently, some new work has been published by Jaske [8] which confirms

² The italic numbers in brackets refer to the list of references appended to this paper.

the general accuracy of these data. His data were generated on equipment allowing constant strain range and ratios and, as such, is more amenable to conventional analysis. The data presented here were generated on much simpler equipment and, consequently, required the proof of time and use. Fortunately, the many uncontrollable and variable factors involved seem to be similar for specimen testing, furnace life testing, and furnace field use. Heat exchangers with reliability proven by service have been produced using these data and the related experimental techniques, while other designs with excessive strain levels were identified early in the development period and corrected or discarded.

Procedure

Completely end-constrained axially loaded plain and notched thin-wall tubes comprised the thermal fatigue specimens in this test. Figure 2 shows the details of the test section. Large brass adapters were silver soldered into

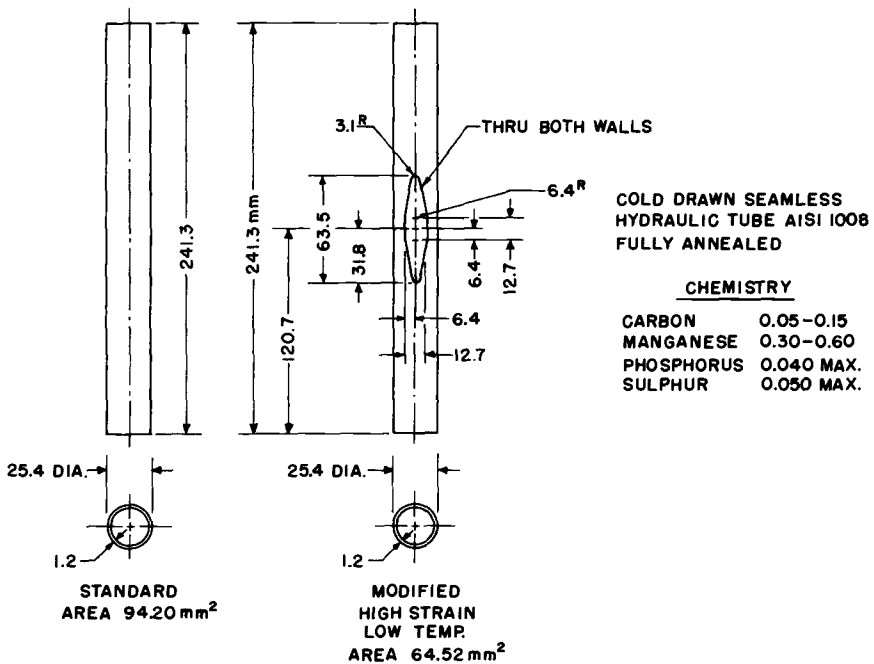


FIG 2—Specimen geometry and material composition.

each end, providing alignment and gripping. These adapters were water cooled to give a constant temperature heat sink at each end of the specimen. They were also drilled axially to allow cooling air to be blown through the tube interior during the cooling portion of the thermal cycle.

A thermal fatigue cycle consists of several more or less separate events which may interact in different ways. We define the initial portion as heating, the next as hot hold time, then cooling, and finally, cold hold time. Each portion has a set time associated with it. In the present data, both hold times were 5 s for all tests. Heating and cooling times were functions of the temperature range, electric heating power, cooling air supply pressure, and cooling air passage area. The latter three were held constant, allowing the heating and cooling times to vary somewhat through each mean temperature series.

The heating portion of the cycle raises the specimen gage length temperature from the minimum to its maximum value. Tensile and compressive strains and, consequently, stresses accompany the temperature change in actual heat exchangers. With axial, end-constraint test equipment, the heating portion necessarily causes compressive strain in the specimen.

Hot hold time affected the specimen fatigue life by allowing compressive stress relaxation. To stabilize this effect in the present data, it was limited to 5 s. This time allowed some redistribution of temperature along the specimen, broadening the high temperature length at the center and raising the temperature profile of the rest of the specimen. The maximum compressive strain was reached at the end of the hot hold time as the maximum tensile strain was similarly reached at the end of the cold hold time. A typical temperature profile at these extremes is shown in Fig. 3. The total thermal strain range, $\Delta\epsilon_t$, may be readily determined from the area between these curves using some simplifying assumptions about the material behavior.

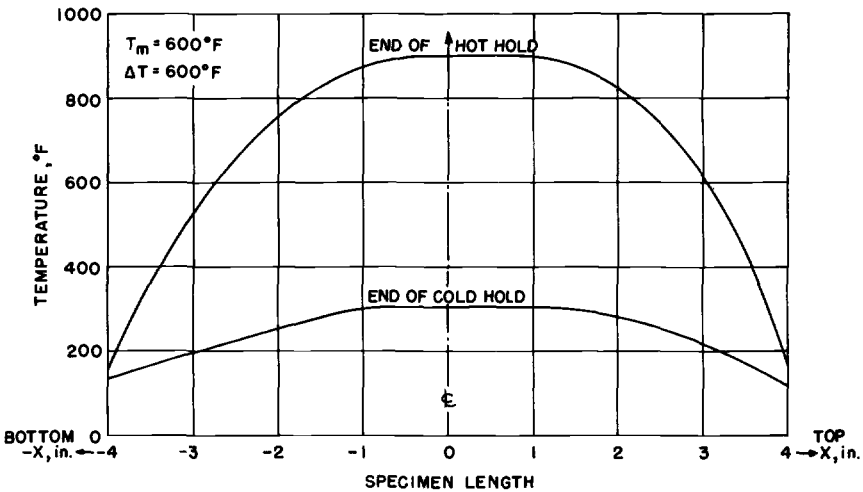


FIG. 3—Specimen temperature profile.

Cooling followed the hot hold time. In these data, the cold hold time power was switched on at the same time as the cooling air. Room temperature air was blown over the outside and through the inside of the specimen until the low cycle temperature value was reached. At this point, the air was switched off and only the cold hold time power applied to the specimen. Redistribution of the low temperature followed for 5 s, allowing the tensile thermal strain and stress to reach their maximum values. This completed one thermal fatigue cycle.

Major restrictions with a test of this type are that compressive strain occurs only by heating and tension by cooling; in order to vary the amount of thermal strain available from a given temperature cycle, the specimen geometry must be changed; and also, the strain ratio, R , is not controlled. For these reasons, the data are presented on the basis of total cyclic strain range, $\Delta\epsilon_t$. R values generally fall between 0 and -0.5 .

On the other hand, the completely constrained test equipment is simple and rugged. The concept was successful enough that other materials were tested on a second similar machine. The total cost of the equipment at the time it was built was approximately \$5000.

Resistive heating was provided by a large transformer, the secondary coil of which consisted of $1\frac{1}{2}$ turns of heavy copper bar. Each end of the bar extended out to provide the connection to the ends of the specimen. A typical electric power level during the heating portion of the cycle was 2500 A at 1.5 V. This power setting resulted in a heating rate at the center of the plain tube specimen of 35°F (20°C)/s. A wide range of control was provided for the transformer so that heating rates could be varied according to the heating time required for a given test series and also to provide for other specimen sections and sizes.

The end-constraint fixture consisted of an upper and lower platen which gripped the specimen end adapters. Massive threaded tie bars and nuts with faces ground parallel to the platen faces positioned the platens. Electrical isolation between the holding fixture ends was accomplished by a set of bakelite shoulder washers between the top platen positioning nuts and the platen.

Specimens were loaded into the fixture platens but not immediately constrained. Several check and adjustment cycles could be run before actually straining the specimen. These were used to obtain the total displacement of the specimen and to make power adjustments when the thermal cycle was changed. The movable platen was always constrained at the end of the hot hold time so that the initial part of the strain cycle was tensile.

After constraint was imposed, no further attention was required until machine shutdown indicated specimen failure or, on rare occasions, failure of some component of the test equipment. Continuous temperature recording at the center of the gage length provided a record for each specimen which could be referred to at the end of the test. Any unusual temperature

excursion shut the equipment down. Excessive temperature in the gage length indicated a crack concentrating the current flow. This provided a shutdown signal, and each fatigue failure recorded here consisted of a crack from 12 to 18 mm in total length. The number of cycles between temperature increase (a noticeable crack) and shutdown varied by no more than 50 cycles and was not considered significant.

Cyclic thermal strain was measured by a noncontacting electro-optical tracker. This instrument used a photomultiplier tube to electronically servo on an optical discontinuity. The optical discontinuity in this case was a light field between dark boundaries produced by two back-lit metal flags attached to pins spot welded to the specimen sides at the gage length extremes. A differential amplifier processed the output signal from the photomultiplier tube giving a voltage proportional to the distance moved by the pins. The total thermal cyclic strain was then the unconstrained displacement of the flags minus the constrained displacement. Single specimens were set up and run through each temperature range at each of the mean cycle temperatures. The total strain range values given with the data are average values obtained after stable cycling had been underway for some time. The measured values were checked against values calculated from specimens which had a series of thermocouples providing the ΔT and profile data similar to the example in Fig. 3. The results of each means of determining thermal strain were comparable within about $\pm 200 \mu\epsilon$, a result considered adequate for the available equipment. The absolute accuracy of the electro-optical device was about $\pm 125 \mu\epsilon$. Alignment changes of the tracker targets during cycling accounted for some additional inaccuracy of the measured values.

Results

Each data point on Fig. 4 consists of the average value of from four to six specimens tested under identical mean temperature and temperature range conditions. All of these data have 5-s hot and cold hold times, while the heating and cooling times vary. On the average, cyclic rate is about 45 cycles/h. At long lives, data are accumulated slowly. This accounts for the scarcity of data beyond 10 000 cycles. Since a major effort was required to obtain the data, a minimum statistical sample at each point was considered necessary.

The data of Fig. 4 covers the area of greatest interest for furnace heat exchangers. While by no means complete, enough of the strain-life field is covered to show general trends and conditions to be avoided if medium- to long-term thermal fatigue reliability is to be achieved. Heat exchangers are warranted for 10 to 15 years of life. From experience, 100 000 cycles is considered an adequate design goal in most cases, so part of the designer's task is to preclude low-cycle fatigue. For cooler areas of the ex-

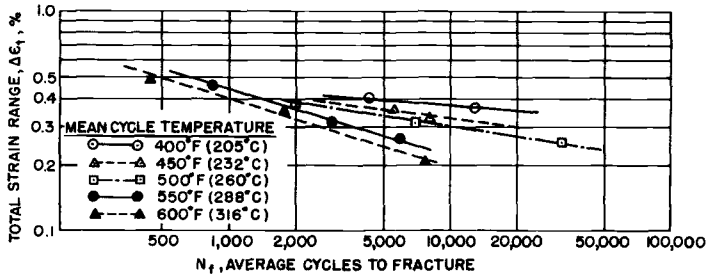


FIG. 4—Thermal fatigue data for low-carbon steel.

changer where the mean cycle temperature is 400°F (260°C) or below, an upper limit of 0.2 percent strain is acceptable. In hotter areas, this must be reduced to 0.1 percent or less.

As would be expected, thermal fatigue strength is greater at 400°F (205°C) than at any higher mean temperature. This corresponds to the highest tensile strength for mild steels. It was necessary to use the second (reduced cross section) type of specimen shown in Fig. 2 for these and the 450°F (232°C) tests since, for plain tube specimens, fatigue cracks occurred at the cool ends under these conditions.

All curves tend to converge in the high strain-short life area where the strain range dominates the other parameters. Here, the cyclic temperature has less influence than at lower strains where temperature and time become stronger factors. No fatigue limit indications are found in this data although, under certain conditions, they may exist. All data shown here are for material which goes well into the plastic range at the cycle extremes. The change in slope between 500°F (260°C) and 550°F (288°C) may be due to material characteristics, or it may be fortuitous. Further testing is needed to clarify this situation.

Approximately 60 specimen tests make up the curves of Fig. 4. The mean life value is presented without probability bounds since the sample size at any given condition is too small to allow reasonably accurate extreme values to be projected. In any case, there is so much uncertainty in other parts of the fatigue analysis that more precision in these data would be of doubtful value. As noted in the discussion section, use of the data against full-scale furnace testing has shown the accuracy to be completely adequate.

Figure 5 is an example of the way the data were treated. It was found in some cases that the data fit the logarithmic normal cumulative distribution function somewhat better than the Weibull distribution. In other test sequences, the two- or three-parameter (including the position parameter) Weibull distribution provided a better fit by the criterion of minimum variance about the regression line. The ordered data for the 600°F (316°C) tests are shown by small dots. Log-normal population parameter estimator

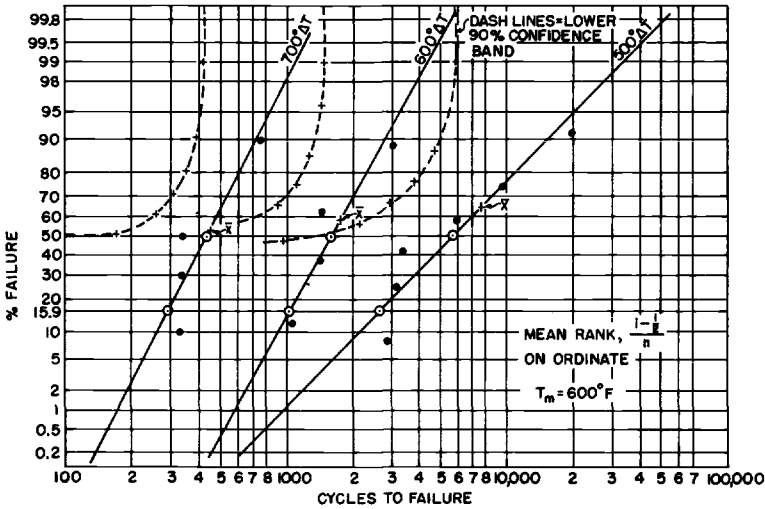


FIG. 5—Log-normal probability of failure with various temperature ranges at 600°F mean temperature. Nonparametric lower 90 percent confidence band shown.

lines found by simple linear regression (least squares) are drawn through these points. The median and one standard deviation below the median value are noted by larger circled points. Population mean estimate points are shown by the crosses denoted \bar{X} . Because of the small sample sizes, it was not considered appropriate to estimate the population extreme value statistics by using an assumed distribution. Lower 90 percent confidence bands (5 percent) obtained by the Kolmogorov-Smirnov nonparametric procedure are shown. Statistical procedures just noted are all standard practice. The details of their use may be found in many texts; Refs 9 and 10 are examples.

For the mean life value, suitable confidence bands are available directly from the log-normal lines. Figure 6 is typical and shows the data of Fig. 5 as they appear in the composite data, Fig. 4, but with the addition of a lower 90 percent confidence band on the mean. A good idea of the mean fatigue life variability of the material can be obtained from this plot. Data from other mean temperatures is similar, showing generally greater variability as life increases at lower strain levels. The host of statistical time-dependent processes increases the data spread as strain severity decreases and testing time increases.

Discussion

The data presented here do not claim to give a complete picture of the behavior of mild steel under thermal fatigue conditions. Thermal fatigue is

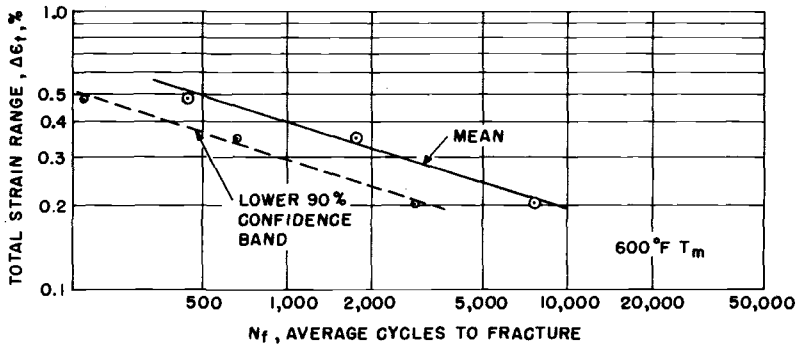


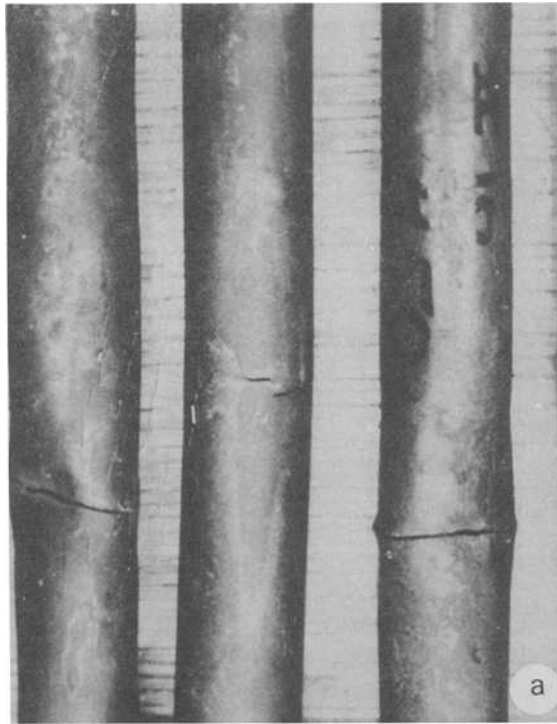
FIG. 6—Average life as a function of strain range at 600°F (315°C) mean temperature.

the result of such a complex set of phenomena that considerable reservation was felt about the usefulness of the data until they were proved in practice. The data in conjunction with experimental strain measurement techniques were tested by use in prediction of failures and failure-free designs. While every effort was made in designing the fatigue test to duplicate as nearly as possible the actual material environment, compromises necessarily placed restrictions on the acceptability of the results. Some of the crucial areas ignored by these tests are now being investigated; among these are the effects of the strain ratio, R . Other materials and coatings are being fatigue tested on more advanced equipment which provides variable strainrange in concert with temperature changes while controlling the strain ratio. The results of these tests may be available in the near future.

Since, until recently, there was little to compare these data to, empirical experience was required to establish their validity. Initially, comparison of test fractures to those found in heat exchangers confirmed that the fracture morphologies were identical. Figure 7 details typical test failures. Figure 7a shows some typical cracks developed on these tests. Once a macrocrack had formed, the area for current flow was reduced, concentrating heating in the material in the same plane as the crack. Depending on the location of the thermocouple with respect to the initial crack, there was some variation in the total length of the crack which could be considered as strictly due to thermal fatigue under the test conditions. This variation in cycle number was small in terms of the test life and has been disregarded in the results.

Figure 7b shows a low power microscopic view of the fracture surface morphology. This appearance is identical with thermal fatigue failures in actual heat exchangers. In areas near the initiation site, the appearance is generally planar, but with variously rounded (oxidized) steps. Macrocracks are formed by coalescence of the small "heat checks" joining together as they reach a critical size by longitudinal shear steps.

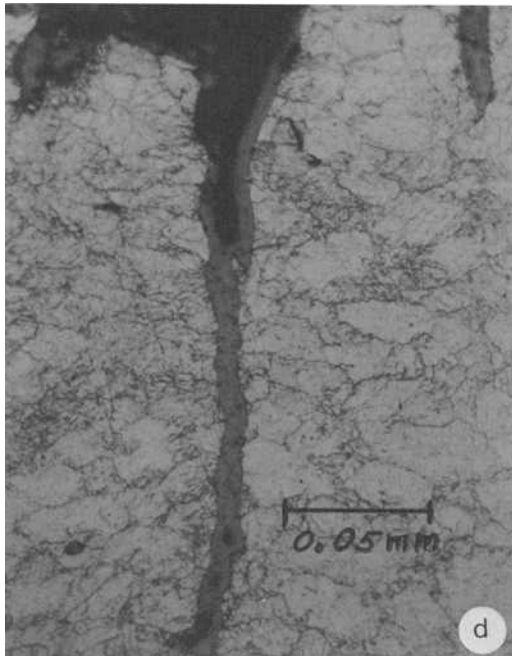
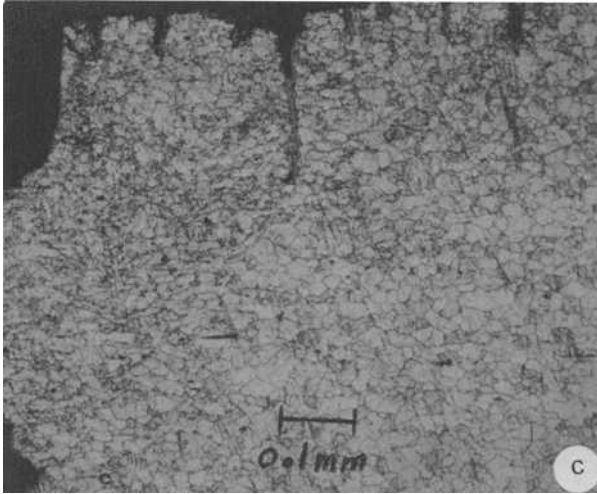
A typical family of heat checks is seen in the metallographic section of



(a) Typical failures showing buckle in high temperature area at crack tip.
 (b) Planar area of flat thermal fatigue ($\times 6$).

FIG. 7—Detail of thermal fatigue test failures.

Fig. 7c. The through crack is at the left, and a series of more or less uniformly spaced surface cracks or checks occur along the top edge, the outer tube surface in this case. These cracks have formed during the cool-



(c) Metallographic cross section adjacent to the through crack ($\sim \times 100$).
(d) Detail of intermediate length crack of Fig. 7c showing oxidation ($\sim \times 400$).

FIG. 7—Continued.

ing (tension) part of the cycle. Bulging in the area of the cracks occurs only after the crack has developed to the point of concentrating current

flow and heat at its ends. Oxidation of the fracture surfaces is a universal feature, as is transgranular cracking. Experience indicates that, if intergranular cracking is found in mild steel exchangers, some other failure mechanism such as corrosion or creep rupture is at work.

Figure 7*d* shows the "oxide wedge" of the intermediate length crack of Fig. 7*c*. Because the oxidation product has a greater volume than the original material, there is a wedging action on the crack tip. In these tests, there is a strong compressive load during heating which attempts to close the cracks. After the oxide wedges have formed, the cracks cannot close, and the effect is to shift *R* toward pulsating tension at the crack tip. It follows that crack growth is not a simple function of the imposed strain cycle. Further, the numerous cracks formed in the relatively uniformly strained gage area interact until the time one crack is clearly dominant. At this point in the tests, failure is only a few cycles away, so there is a gage length size effect determined by the temperature profile which defines the critically strained area. All of these factors influence the fatigue life of the specimen, but they are also involved in actual exchangers, so there are common qualitative effects which are more or less equal in both situations.

Estimation of the fatigue performance of numerous heat exchangers over the past five years has shown that the fatigue data hold up very well. Considering that the accuracy band of experimental strain measurements on operating heat exchangers is fairly broad, great refinement of the thermal fatigue data is not necessary. For strain measurements to about 650°F (343°C), medium temperature foil strain gages give results with an error band about $\pm 100 \mu\epsilon$ wide. High temperature wire gages with special temperature compensation techniques are used from 650 to 1000°F (343 to 530°C) with a considerably wider error band estimated to be about $\pm 300 \mu\epsilon$ on the average. Combination of experimental measurements with the fatigue data to predict the response of several new heat exchangers, as well as existing exchangers used in new applications, has established confidence in both technical areas. Where strain and temperature measurements fall within the limited life region of the data, failures are encountered, generally at lives well within the statistical scatter expected. Usually in furnace life testing, failures are scattered over a much broader life range than for most machine components because of the unavoidable vagaries of burner flame and cooling air flow patterns. Even for very severe strain conditions, the failure rate in life test exchangers rarely exceeds 50 percent within reasonable test times. These statistics are described by positively skew Weibull probability of failure density functions (shape parameter $1.0 < c < 3.5$).

Several very reliable heat exchanger designs have been developed with the help of the data. Furnaces have been manufactured for more than five years which were given a clean bill of health by linear extrapolation as noted in the Results section. Lack of field failures in combination with complete test

series survivals to 100 000 cycles has built confidence and established a sound basis for using these data. Note that field results are a necessary part of the qualification of the thermal fatigue analysis because direct correlation of life testing to operational use is not available.

The most limiting features of completely constrained testing are the lack of a constant compression-tension strain ratio and the difficulty of changing the total strain range without changing the temperature range. New, more sophisticated equipment has overcome these problems to a great extent by providing strain control in a closed-loop feedback circuit. Tests now in progress use a combination of strain and temperature control providing more tractable, conventional low-cycle data on other materials of interest. Because of previously noted shortcomings, no attempt has been made to generalize the data or extract universal trends. There is a danger in this which applies to even the most closely controlled laboratory data because mild steel behaves in a nonhomogeneous, nonlinear manner under high strain and temperature cycling. Even when a short gage length extensometer is used, the average strain measured is only an indication of the section gross behavior once the plastic strain range is entered.

An example of nonhomogeneous behavior is shown in Fig. 8, a specimen

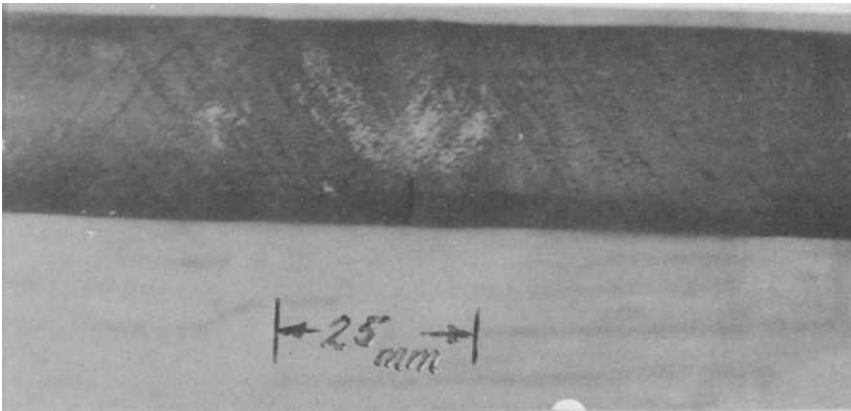


FIG. 8—Maximum thermal strain specimen, 800°F (445°C) ΔT at 600°F (316°C) T_{mean} , $\Delta\epsilon_{total}$ 0.63 percent.

subjected to an above normal temperature range, 800°F (445°C) ΔT at a mean temperature of 600°F (316°C). The oxide scale formed above about 900°F (482°C) provides a visible indication of the plastic behavior not ordinarily available since furnace heat exchangers and hence the test data are restricted to operation below the oxide formation temperature [11]. A slip band was formed during each cycle at arbitrary locations within the maximum temperature zone. Strain hardening along the slip band pre-

vented further yielding of this material for a number of cycles. Under these cyclic conditions, strain aging is nearly complete within the time of one cycle, so the upper yield point returned for the yielded zone by the time the next cycle's yield load was reached, and, as can be seen in the figure, the damage tends to accumulate in the central 25 mm of the specimen. Note that the macrocrack progressed in the direction transverse to the principal tensile stress, directionally unaffected by the slip. The area of strain concentration at the crack tip has shed its oxide scale as a result of the greatly increased strain in this zone.

Conclusions

The data presented in this paper provide one of the engineering elements needed to eliminate thermal fatigue in gas appliance heat exchangers. Another necessary ingredient is a reasonably accurate experimental strain measurement technique which may be applied to operating exchanger shells. Development of a strain measurement procedure has necessarily been carried on concurrently with generation of fatigue data. Although measuring quasistatic strains on thin shell structures at up to 1000°F (538°C) presents great difficulties, techniques have been evolved which give excellent predictive results in combination with the data. Prediction of failure or survival under any normal operating conditions has been assured with confidence through actual operating experience.

Application of these fatigue design techniques still requires a very high level of technical and manual skill. High temperature measurements are time consuming and relatively expensive when compared to the cost of the heat exchanger element and normal experimental strain analysis. Further, actual exchangers, preferably from production tooling, are necessary to do the fatigue analysis. This means that the design is well along, and options for change are limited and expensive by the time fatigue life prediction can be made.

Finite element methods (FEM) have given hope of accelerating the design of reliable heat exchangers by providing an analytical strain field solution before tooling has been set up. This would be ideal because contours could be changed in the computer model with minimal time and expense. To date, however, FEM results obtained by the author's group during heat exchanger development have been disappointing, if not downright misleading. The cause of this is that, to date, only a linear-elastic FEM code has been used. Except for very preliminary indications of problems (where the stress values exceed the local yield strength) this approach is not valid since critical areas of the shells deform plastically and, in most cases, are entering displacement controlled buckling at about the same time. Nonlinear material and geometry properties along with large deflection capabilities are required in the finite element analysis. It remains to be seen if the nonlinear,

large displacement programs which are available will provide an acceptable addition to the experimental procedures.

References

- [1] Mackenzie, C. T. and Benham, P. P., "Push-Pull Low Endurance Fatigue of En 25 and En 32B Steels at 20°C and 450°C," *Proceedings 1965-1966*, The Institution of Mechanical Engineers, Vol. 180, Part I, No. 30, London.
- [2] Mackenzie, C. T., Burns, and Benham, P. P., "A Comparison of Uniaxial and Biaxial Low-Endurance Fatigue Behavior of Two Steels," *Proceedings 1965-1966*, The Institution of Mechanical Engineers, Vol. 180, Part 31, London.
- [3] Benham, P. P., "High-Temperature Low-Cycle Fatigue: Survey of British Work," Paper presented at 1967 Society for Experimental Stress Analysis, Spring Meeting, Ottawa, Ont., Canada.
- [4] Coffin, L. F., Jr., and Wesley, R. P., "Apparatus for Study of Effects of Cyclic Thermal Stresses on Ductile Metals," *Transactions*, American Society of Mechanical Engineers, Aug. 1954.
- [5] Coffin, L. F., Jr., "A Study of the Effects of Cyclic Thermal Stresses on a Ductile Metal," *Transactions*, American Society of Mechanical Engineers, Aug. 1954.
- [6] Coffin, L. F., Jr., "An Investigation of Thermal-Stress Fatigue as Related to High-Temperature Piping Flexibility," *Transactions*, American Society of Mechanical Engineers, Oct. 1957.
- [7] Coffin, L. F., Jr., "Design Aspects of High-Temperature Fatigue With Particular Reference to Thermal Stresses," *Transactions*, American Society of Mechanical Engineers, April 1956.
- [8] Jaske, C. E. and Porfilio, T. L., "Thermal-Mechanical Low Cycle Fatigue of AISI 1010 Steel," Catalog Number H54375, American Gas Association, Cleveland, Ohio, 1975.
- [9] Hald, A., *Statistical Theory with Engineering Applications*, Wiley, New York, 1952.
- [10] Johnson, N. L. and Leone, F. C., *Statistics and Experimental Design in Engineering and the Physical Sciences*, Vol. I, Wiley, New York, 1964.
- [11] USA Standard for Gas Fired Gravity and Forced Air Central Furnaces, ANSI Z21.47-1968, American Gas Association, Cleveland, Ohio, 1968.

S. W. Hopkins¹

Low-Cycle Thermal Mechanical Fatigue Testing

REFERENCE: Hopkins, S. W., "Low-Cycle Thermal Mechanical Fatigue Testing," *Thermal Fatigue of Materials and Components, ASTM STP 612*, D. A. Spera and D. F. Mowbray, Eds., American Society for Testing and Materials, 1976, pp. 157-169.

ABSTRACT: A test method is described for performing uniaxial low-cycle thermal mechanical fatigue tests at elevated temperatures on nickel-base superalloys. Both smooth specimen crack initiation and notched specimen crack propagation testing is discussed. Standard closed loop servohydraulic testing machines with closed loop electric induction heaters are utilized. The temperature and mechanical strain are independently controlled, allowing for a wide range of relationships between temperature and mechanical strain.

Tubular specimens are directly inductively heated in air and cooled with compressed air. The temperature is measured with a radiation pyrometer which eliminates thermocouples and premature failures caused by welded thermocouples. Axial strain in the specimen is measured from machined internal ridges on the specimen utilizing a linear variable differential transformer and a quartz internal extensometer.

An electronic system compensates for the thermal expansion component of strain for both the control loop and the recorders. This system permits direct recording of the load-induced mechanical strain. Load-strain hysteresis loops and strain-temperature plots can simply be recorded during the test.

KEY WORDS: thermal fatigue, mechanical tests, nickel alloys, crack initiation, crack propagation

Thermal fatigue has been defined by Carden [1]² as that process by which cracks originate and are propagated in materials that have both cyclic temperature and cyclic mechanical strain at a critical location. There are essentially two experimental techniques used to obtain such material data. The conventional thermal fatigue (TF) technique entails cycling the test specimen between a hot source and a cold source. With this method, it is the specimen geometry, the heating rate, and the temperature difference which produce the cyclic mechanical strains. The resultant mechanical strains and stresses have to be calculated analytically. For anisotropic materials, such as

¹Presently, mechanical engineer, Failure Analysis Associates, Palo Alto, Calif. 94304; formerly, senior materials engineer, Materials Engineering and Research Laboratory, Pratt & Whitney Aircraft, Middletown, Conn. 06457.

²The italic numbers in brackets refer to the list of references appended to this paper.

gas turbine blade materials, this calculation is extremely complex. The other experimental technique, known as thermal mechanical fatigue (TMF), cycles both the specimen's mechanical strain and its temperature independently. It is this second technique and equipment that will be presented in this paper, with emphasis on those items or procedures which differ from isothermal low-cycle fatigue (LCF) testing.

Before proceeding, definitions of the different types of strains are in order. Thermal strain is defined as a change of specimen dimension caused by thermal expansion at zero load (free thermal expansion) divided by its original dimension. Mechanical strain is defined as that strain which is caused by or which generates stress. Total strain, which is the displacement measured from the specimen divided by the original gage length, is defined as the algebraic sum of both the thermal strain and the mechanical strain.

Experimental Equipment and Procedures

Testing Machine

Presently, there are four TMF machines operating around the clock in the Mechanical Behavior Laboratory of Pratt & Whitney Aircraft. All of these machines are standard closed-loop, servohydraulic systems and are equipped with load, strain, and temperature controllers, along with strain and temperature programmers. One of these systems is shown in Fig. 1. For the most part, this equipment can be purchased from any of the closed-loop fatigue machine manufacturers. These machines were chosen over the commercial screw driven machines because of their ability to control total strain rate and because of their response time. For fast temperature response and good control, a completely electronic closed-loop temperature controller is used which has much better dynamic control than the old-fashioned electrical-mechanical temperature controller that nulls by a slide wire system. The details of how the strains and temperatures are controlled, measured, and programmed will be discussed later.

Loading System and Specimen

The specimen ends and grips used for this testing were selected because they satisfy two major concerns: the grips are stiff enough to maintain alignment in both tension and compression; and the specimen is easily removable after prolonged exposure to high temperatures. This design was originally used by Wells [2], and the details are shown in Fig. 2 with a solid isothermal LCF specimen assembled in one grip.

The specimen design currently in use is shown in Fig. 3. It has the same end design that Wells [2] used for his solid specimens. This tubular design with internal ridges to measure strains was selected for the following

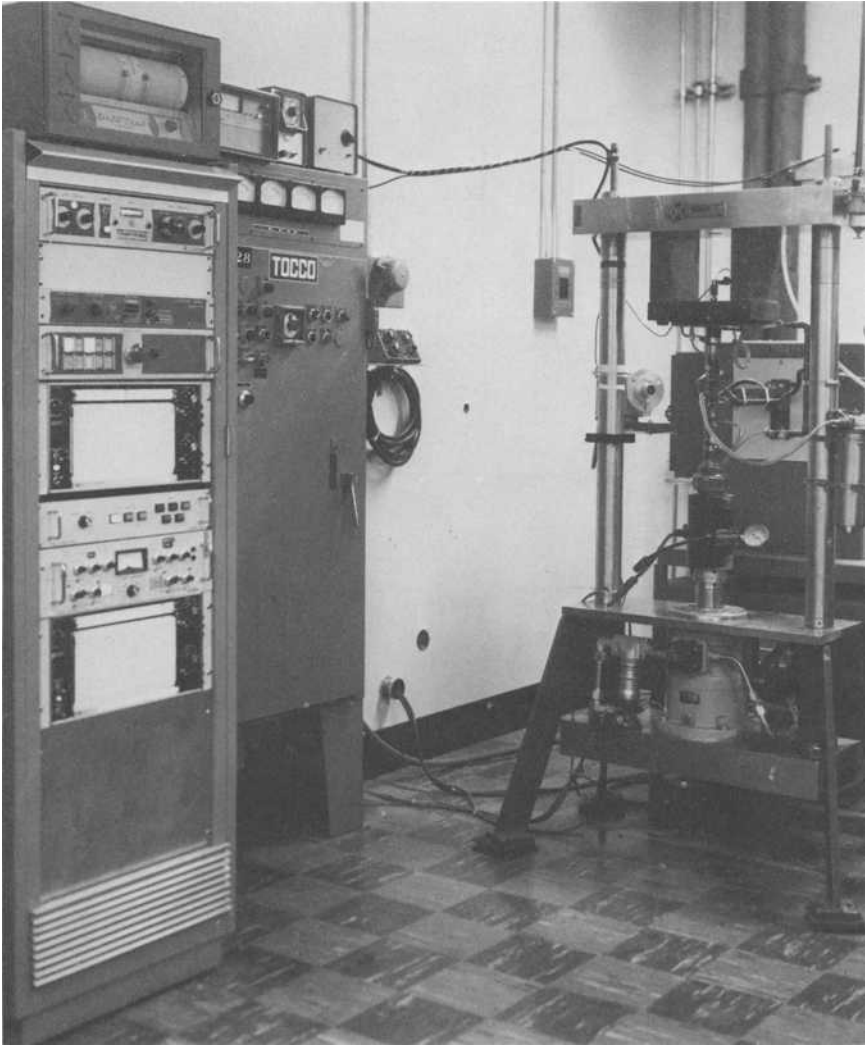


FIG. 1—*Typical closed-loop servohydraulic fatigue machine with a 10 kilohertz induction heater and a pyrometer for temperature measurement used for TMF testing.*

reasons. The thin wall allows for fast heating and cooling cycles with a minimum temperature gradient across the wall thickness. The wall thicknesses can be varied to model a component wall thickness. The strains are measured on the centerline of the specimen which mechanically averages the strains as Tishler and Wells [3] have shown, and the specimen is suitable for both crack initiation and crack propagation testing. The alignment of the loading system is checked and maintained to keep the bending strains within

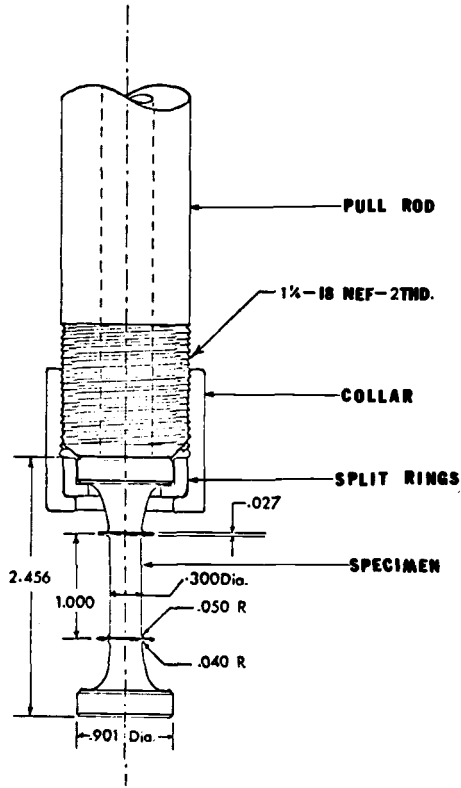


FIG. 2—Solid isothermal LCF specimen with one end assembled in the standard tension-compression gripping system.

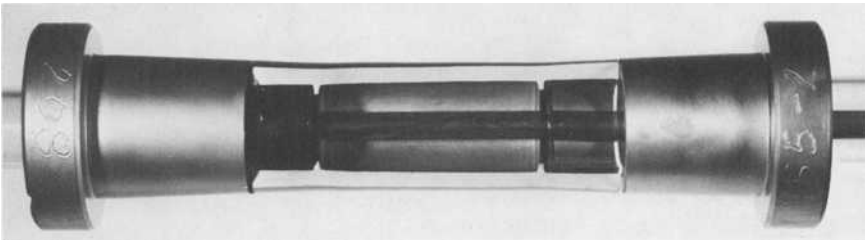


FIG. 3—Strain control tubular fatigue specimen showing the internal ridges and the quartz rod and tube extensometry system.

the specimen to less than 3 percent of the applied axial strain. At small strains where percent bending is meaningless for a stiff gripping system, the bending strains on the specimen's surface are maintained below 10^{-4} .

Extensometry

To minimize the imposed strain errors and measure only displacements in

the gage section of the specimen, fused quartz was chosen for the extensometer material. Fused quartz has a low coefficient of thermal expansion and a high melting temperature, making it ideal for this application. Fig. 4 is a sectional view of the specimen and extensometry. The displacements are measured between the two internal ridges by the quartz rod and tube which are extensions to the linear variable differential transformer (LVDT). There are two high temperature springs: one on the bottom to hold the quartz rod firmly against the lower ridge and one on the top to hold the quartz tube against the upper ridge. Each spring applies less than 5 N force to the ridges. With this technique, the displacements measured reflect only the relative movements of the two ridges.

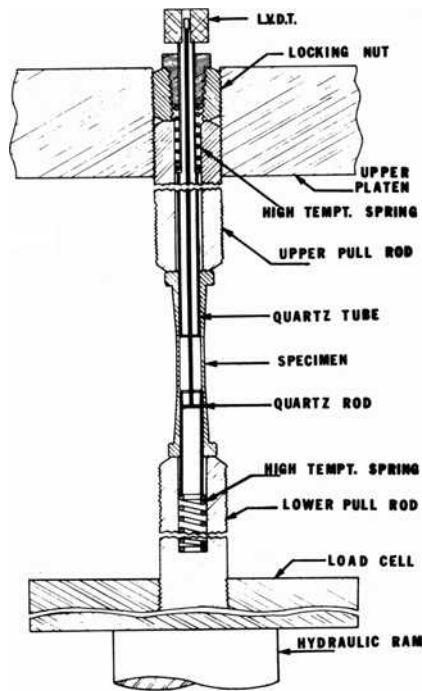


FIG. 4—Sectional view of the loading train with the quartz extensometry installed and the collars and split rings removed.

Load Cell

The loads are measured from a standard load cell in series with the specimen. The cell can be mounted in one of two locations: either above the specimen, attached to the frame, or below the specimen, attached to the hydraulic ram. There are two advantages to mounting the load cell to the hydraulic ram.

1. The temperature of the load cell is easier to maintain. The heat due to

convection is eliminated and the conduction heat is minimized by water cooling the pull rod.

2. It is easier to electrically isolate the load cell from the testing frame. When using high frequency induction heating, multiple connections to ground can cause ground-loop problems. The hydraulic elastomeric seal in the ram isolate the lower pull rod, and Micarta washers and spacers on the top isolate the top pull rod from the testing frame. With this technique, the load cell ground cable remains as the only possible electrical connection to ground.

Heating and Cooling

The specimen is heated with a standard 10 kHz induction heater. Induction heating was chosen because of its fast response. Indirect resistance heating is too slow, and direct resistance heating is not acceptable for crack propagation testing due to the local heating at crack tips. The 10 kHz heater produces a lower wall thickness gradient than do the higher (450 kHz) frequency heaters. Also, ground-loop problems are lessened with 10 kHz heater than with 450 kHz heaters.

The temperature controller is a solid state controller with mean level, amplitude, rate, and reset adjustments. For the feedback loop, an infrared radiation pyrometer sighted on the specimen outer surface is used. This pyrometer, which averages the temperature over 3-mm spot on the specimen, has an output voltage linear with temperature. Welded thermocouples and premature specimen failure due to thermocouples are eliminated.

Compressed air is used to cool the specimen during the cool-down portion of the temperature cycle. The cooling air manifold along with the heating coil are shown in Fig. 5 surrounding the specimen. The amount of air is controlled by a motor-driven cam system and a needle valve. The cam drives the spring-loaded needle valve and is shaped to gradually turn on and off the air. The time for one rotation of the cam system is set to be just less than the time for one complete TMF cycle. After one complete revolution, the cam system stops and waits for an electrical signal from the counter panel. This electrical signal commands the cam system to make an additional revolution. With this technique the air is always synchronized to the temperature cycle and is repeatable. The cooling rate is controlled by the heater ballasting the air blast cooling. This air system is not part of the temperature control loop which consists only of induction heater, specimen, pyrometer, and controller. Therefore, timing problems between two controllers in the same control loop are avoided.

Programmings

The temperature and strain programmers can be a number of different

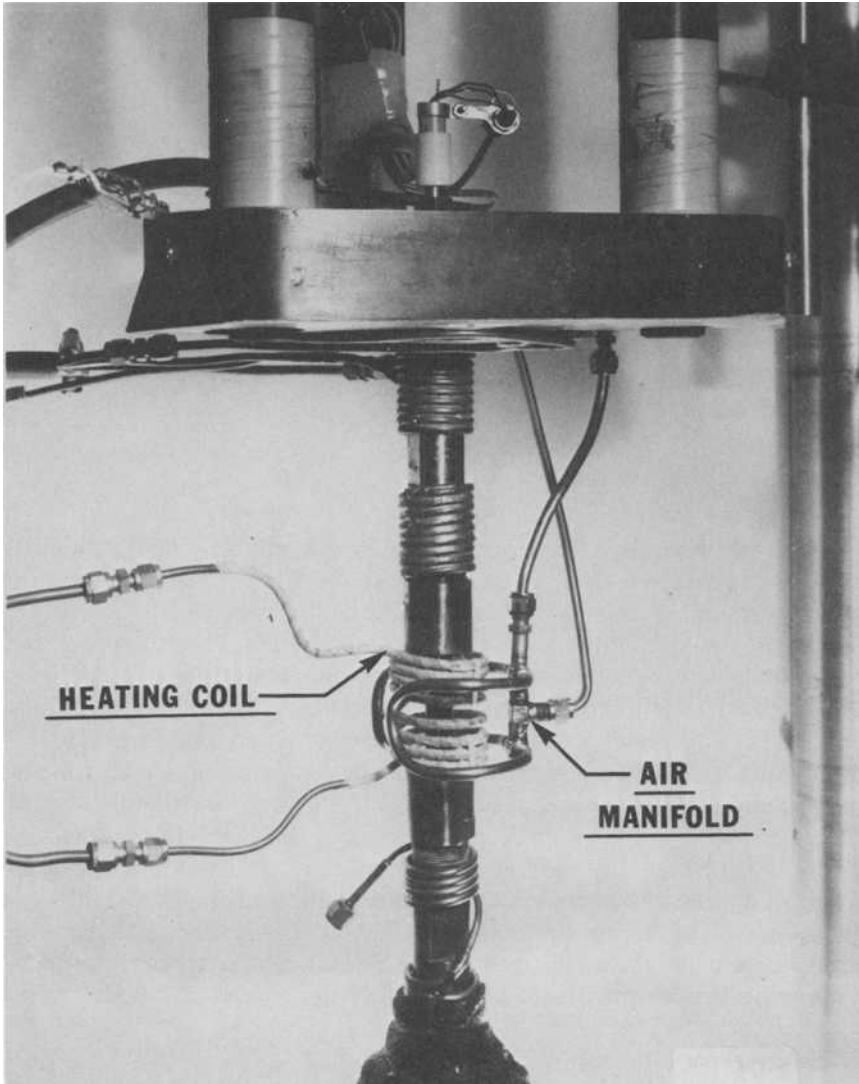


FIG. 5—Typical TMF setup with the cooling air manifold and heating coil surrounding the specimen.

devices depending upon the test frequency and the complexity of the mechanical strain versus temperature curve that is to be programmed. Fig. 6 shows three standard cycles used to obtain material and design data. Cycle I is a linear relationship between strain and temperature with the tensile strain occurring at the lowest temperature and the compressive strain occurring at the highest temperature. Cycle II is also a linear relationship between strain and temperature and is the exact opposite of Cycle I, the tensile strain oc-

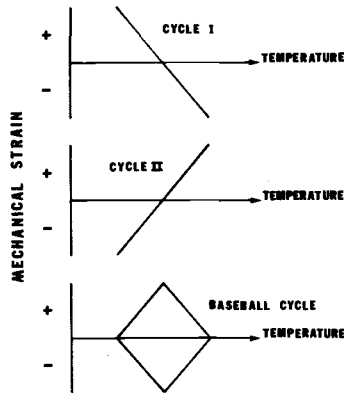


FIG. 6—The three standard TMF cycles conditions used to obtain material and design data, Cycle I, Cycle II, and Baseball cycle.

curing at the maximum temperature. The third standard cycle, the Baseball cycle, is in between a Cycle I and a Cycle II with both the tensile and compressive strains occurring at the same middle temperature.

The original technique uses a dual channel Data Trak³ follower for programming total strain and temperature and is as follows: The temperature versus mechanical strain and temperature versus time relationships are chosen. Following this, the temperature command input curve is hand-drawn on the Data Trak chart and then, the temperature is cycled maintaining zero load on the specimen. During this cycling, the thermal strains are recorded. Having acquired this thermal strain data, the mechanical strain and thermal strain are added algebraically, and the resulting total strain would then be plotted onto the other channel of the Data Trak synchronous with the appropriate temperature. With this procedure, there is no way to ensure that the total strain curve is entirely plotted correctly until the TMF test is started and the loads observed. This entire procedure has to be repeated for each TMF test.

Thermal Expansion Compensator

A new method of strain programming has been developed that minimizes the drawing of different Data Trak program curves. The method utilizes an electronic thermal expansion compensating device which produces an electrical signal analogous to the thermal strain measured from the specimen. This device consists of a nonlinear amplifier as its heart, and two linear amplifiers for scaling as shown in Fig. 7. The linear amplifiers were added to ensure accurate setup and to aid in data reduction. The compensator is

³ T.M. Research Incorporated.

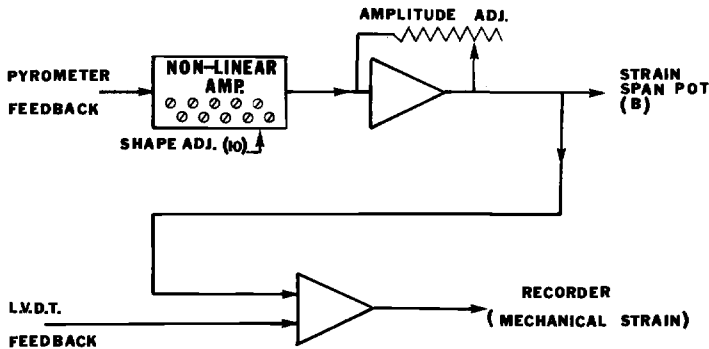


FIG. 7—Thermal expansion compensator used to generate a signal analogous to the thermal strain for closed-loop strain control programming and a signal analogous to mechanical strain for test setup and data reduction.

divided into two parts. The first part uses the temperature feedback signal from the pyrometer as the input and outputs a voltage that is adjusted to match the thermal strain feedback voltage. This adjustable voltage is fed into the closed loop electronics for control through one of the two strain span pots, usually Span Pot B. The mechanical strain signal from the Data Trak is fed into the other span pot, usually Span Pot A. The second part of the compensator has as inputs the adjustable voltage signal and the strain feedback signal from the LVDT. It is wired to subtract the adjustable voltage from the strain feedback signal and produces the resultant mechanical strain signal. Once the adjustable voltage is correctly adjusted, this mechanical strain signal will be zero during thermal cycling at zero load and will be the applied mechanical strain during a TMF test.

In setting up a test utilizing the thermal expansion compensator, the specimen is cycled through the temperature range at the desired test rate. During this time, the loads are maintained at zero, and the thermal strains are measured. These strains are also plotted on an x - y recorder against temperature feedback. This is done to check the strain extensometry system and the temperature gradient. Any hysteresis loops on the x - y recorder indicates one of these items has to be corrected. The extensometry system could either rub against itself or not seat properly against the internal ridges of the specimen, producing a hysteresis loop. Also, a temperature gradient along the gage length of the specimen which is different for the heating and cooling portion of the cycle will produce a hysteresis loop. This is produced because the pyrometer only measures temperature at a point, and the extensometer measures the strain over the gage section. Adjustment of the induction coil corrects this aspect.

Having made the corrections to eliminate the hysteresis loop, the adjustable voltage from the nonlinear amplifier is adjusted to match the ther-

mal expansion feedback signal. This has been achieved when it is observed that the mechanical strain signal will not vary during thermal cycling at zero load. The curve drawn on the strain channel of the Data Trak must now represent the mechanical strain rather than the total strain to be controlled. This minimizes the precision to which the curve needs to be drawn and increases the overall test accuracy.

Digital Computer

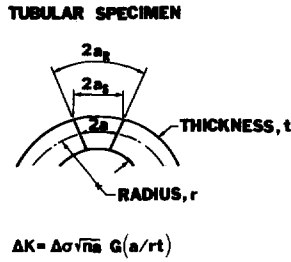
It is difficult to reduce the hysteresis loop of thermal strain versus temperature to exactly zero. With a digital computer as the programmer, this is not necessary. The computer can acquire and store the thermal strains as a function of both temperature and direction, whereas the thermal expansion compensator's output is only a function of temperature and not direction. The computer also allows more complex TMF testing to be conducted with no additional effort from the operator. Such tests may include mode transfers, strain holds for a given time or to a given stress relaxation, and stress holds for a given time or to a given creep strain.

Crack Growth Testing

Since the fatigue life of any component can be divided into a crack initiation phase and a crack propagation phase, data for both phases is necessary to make an accurate fatigue life prediction. Different testing techniques are usually required for each phase; however, the technique and specimen described in this paper are used for both [4,5]. The only difference for a TMF crack propagation test is that a through-the-thickness notch is required. The cracks in these notched tubular specimens were found to propagate in a fan direction, as shown in Fig. 8. Because of this, the surface crack lengths, measured either from a traveling microscope ($2a_s$) or from a cellulose acetate replica ($2a_r$), must be converted to ($2a$) at the mean radius r of the specimen. This change is simply a matter of geometry. The stress intensity factor is given in Fig. 8, where $G(a/Rt)$ is the curvature correction factor from Erdogan and Ratwani [6]. For the strain controlled TMF tests, a strain intensity factor rather than a stress intensity factor is used to reduce the data [4]. This is done by using the mechanical strain range ($\Delta\epsilon_m$) rather than the stress range ($\Delta\sigma$).

Discussion

Three different techniques for programming the strain-temperature-time relationship were mentioned in the previous section: Data Trak only, Data Trak and thermal expansion compensator, and computer. The Data Trak only technique requires a great deal of setup time for each test. The ac-



$$G(a/rt) = 1 + 0.074 \left[\frac{a}{(rt)^{1/2}} \right] + 0.455 \frac{a^2}{rt} - 0.00308 \frac{a^3}{(rt)^{3/2}}$$

FIG. 8—The Erdogan and Ratwani stress-intensity factor used in reducing crack growth data from tubular specimens.

curacy to which these Data Trak curves has to be drawn is quite great, especially for small mechanical strain ranges. The Data Trak and thermal expansion compensator technique reduces the accuracy to which the Data Trak curves must be drawn, reduces the setup time for each specimen, increases the accuracy of the test, and aids in data reduction during the test. However, the computer is still the optimum device to program this type of test.

The accuracy to which the programmed strain curve has to be drawn to has been mentioned a number of times. The following simple calculation will prove this point and show why good temperature control is just as important as good strain control. A typical range in free thermal strain and mechanical strain for a TMF test is 0.012 and 0.003, respectively. If the test needs to be conducted within 10 percent accuracy on mechanical strain, this means that the temperature control must be such that the free thermal strain does not vary more than 0.0003 out of 0.012. This also requires that the temperature and temperature gradient be controlled within 2.5 percent over the entire temperature cycle. If total strain is being programmed from a Data Trak, it must be drawn within 2.5 percent; however, if only mechanical strain is being programmed from a Data Trak, it must be drawn within 10 percent. Obviously running a TMF test to only 10 percent accuracy is not acceptable; however, to run the test within 1 percent accuracy can not be achieved with only Data Trak control. To hand draw the total strain curve on the Data Trak or control the temperature dynamically to within 0.25 percent is virtually impossible. The real accuracy lies between 1 and 10 percent with only Data Trak control depending upon all the control parameters. With the thermal expansion compensator, accuracy is only limited by how closely it is adjusted to zero mechanical strain during the thermal cycling. Obviously, for a given thermal strain error, the test accuracy increases as the mechanical strain range increases.

To conduct these types of tests with a computer is difficult and expensive.

If the job is done correctly, the payoffs are worth the expense. The dynamic accuracy to which load and total strain can be controlled to, with closed-loop equipment, is better than 1 percent. The problem in TMF testing is matching temperature control equipment to heaters for dynamic closed-loop control. As already mentioned, small changes in temperature can translate into large changes in mechanical strain if the total strain is left unchanged. However, a small change in temperature during a cycle without changing the mechanical strain usually does not change the fatigue response of the material. Therefore, a computer should be programmed to take this into account. The computer should almost continuously read the instantaneous temperature and adjust its total strain output to compensate for any temperature error. The frequency at which the computer does this should depend upon the maximum heating rate of the temperature equipment and the accuracy desired from the test. For the materials and strain ranges associated with gas turbine application, the computer has to update its total strain signal for every 2°C of temperature error to maintain a 1 percent accuracy on the mechanical strain. Presently, this type of programmer is being installed to program this equipment.

These control problems never surface for isothermal LCF tests because static temperature control is much better than dynamic temperature control, and any change in temperature that does occur only reflects in a mean strain shift rather than a strain range shift. Fatigue life, measured as either cycles to crack initiation or the crack propagation rate, is affected more by a small change in strain range than it is by the same change in mean strain.

Summary

A TMF test method has been described which has the capability of controlling any mechanical strain-temperature-time cycle. A tubular specimen design was presented that can be used for either crack initiation or crack propagation testing. The axial total strains were measured with a unique extensometry system and separated into two components (thermal strains and mechanical strains) through the use of a thermal expansion compensator. The necessity for precise temperature control was demonstrated in terms of overall testing accuracy, along with how digital computer control can improve this type of testing.

Acknowledgments

The test method described in this paper was developed over a period of years due to the dedicated efforts of numerous people who are or have been associated with the Materials Engineering and Research Laboratory of Pratt & Whitney Aircraft, a division of United Technologies.

References

- [1] Carden, A. E. in *Manual on Low Cycle Fatigue Testing, ASTM STP 465*, American Society for Testing and Materials, 1970, pp. 163-188.
- [2] Wells, C. H. in *Manual on Low Cycle Fatigue Testing, ASTM STP 465*, American Society for Testing and Materials, 1970, pp. 87-99.
- [3] Tishler, D. N. and Wells, C. H., *Materials Research and Standards*, American Society for Testing and Materials, Vol. 6, Jan. 1966, p. 20.
- [4] Rau, C. A., Jr., Gemma, A. E., and Leverant, G. R. in *Fatigue at Elevated Temperatures, ASTM STP 520*, American Society for Testing and Materials, 1973, pp. 166-178.
- [5] Gemma, A. E., Langer, B. S., Leverant, G. R., this publication, pp. 199-213.
- [6] Erdogan, F. and Ratwani, M., *International Journal of Fracture Mechanics*, Vol. 6, No. 4, Dec. 1970, pp. 379-392.

Thermal-Mechanical, Low-Cycle Fatigue of AISI 1010 Steel

REFERENCE: Jaske, C. E., "Thermal-Mechanical, Low-Cycle Fatigue of AISI 1010 Steel," *Thermal Fatigue of Materials and Components, ASTM STP 612*, D. A. Spera and D. F. Mowbray, Eds., American Society for Testing and Materials, 1976, pp. 170-198.

ABSTRACT: This study was undertaken to develop an understanding of the fatigue resistance of AISI 1010 steel under conditions of combined thermal and mechanical strain cycling in air. Comparative evaluations were made with existing thermal-mechanical fatigue data on carbon steels and with results of a comprehensive, companion study of the fatigue behavior of this same steel under isothermal conditions.

Thermal-mechanical fatigue behavior was investigated for constant-amplitude, fully reversed, strain cycling of uniaxially loaded specimens at three ranges of temperature: (a) 93 to 316°C (200 to 600°F), (b) 93 to 427°C (200 to 800°F), and (c) 93 to 538°C (200 to 1000°F). Experiments were conducted both with maximum strain in phase with maximum temperature and out of phase with maximum temperature. Considering differences in experimental techniques and the difficulties associated with conducting these types of experiments, the present data agreed with similar data from the literature in limited instances where comparisons could be made. Thus, these results were considered to be representative of this type of steel, and they provided a significant extension of existing knowledge on the thermal-mechanical fatigue resistance of low-carbon steel.

Dynamic strain aging was observed to cause more cyclic hardening in these experiments than in isothermal fatigue experiments. In terms of total or plastic strain range, out-of-phase cycling was more deleterious than in-phase cycling, and thermal-mechanical fatigue life was much less than isothermal fatigue life. However, on the basis of stable stress amplitude, there was little difference in fatigue life between in-phase and out-of-phase cycling, and the fatigue life was reasonably well correlated with isothermal fatigue results.

KEY WORDS: thermal fatigue, thermal cycling fatigue, alloy steels, tests, precipitation hardening

Nomenclature

- A_T Cross-sectional area of specimen at temperature
 E Elastic modulus

¹Senior researcher, Structural Materials and Tribology Section, Battelle's Columbus Laboratories, Columbus, Ohio 43201.

e_{dt}	Total diametral change in specimen (both thermal and mechanical)
K	Specimen compliance
K'	Cyclic strength coefficient
N_0	Number of cycles where tensile load started to drop just prior to complete fracture
N_5	Number of cycles where tensile load dropped 5 percent just before complete fracture
N_f	Number of cycles to complete fracture
n'	Cyclic strain hardening exponent
ΔP	Load range
T	Temperature
ΔT	Range of temperature
T_e	Equivalent temperature
T_{max}	Maximum temperature
T_{min}	Minimum temperature
t	Time
α	Linear coefficient of thermal expansion
ϵ	Mechanical strain
ϵ_0	Proportional limit strain value in cyclic stress-strain function
$\Delta\epsilon_{de}$	Range of mechanical diametral elastic strain
$\Delta\epsilon_{dp}$	Range of mechanical diametral inelastic strain
ϵ_{dt}	Total diametral mechanical strain
ϵ_{max}	Maximum mechanical strain
ϵ_{min}	Minimum mechanical strain
$\Delta\epsilon_p$	Inelastic mechanical strain range
$\Delta\epsilon_t$	Total mechanical strain range ($\Delta\epsilon_t = \epsilon_{max} - \epsilon_{min}$)
ν	Frequency in cpm
ν_e	Elastic Poisson's ratio
σ	Stress
$\Delta\sigma$	Stress range ($\Delta\sigma = \sigma_{max} - \sigma_{min}$)
σ_{max}	Maximum stress
σ_{min}	Minimum stress
σ_0	Proportional limit stress value in cyclic stress-strain function

Mechanical equipment and structural components are often subjected to cyclic straining while operating at elevated temperature. In some instances, the temperature may be relatively constant, while, in other cases, the cyclic straining may be accompanied by thermal cycling. The problem becomes even more complex when the time relationship between temperature and strain must be taken into account.

Considering the simple case of a bar rigidly restrained at each end, the mechanical strain becomes compressive when the bar is heated and reaches a minimum (maximum negative) value at the maximum temperature. The thermal strain has an equal magnitude and opposite sign to the

mechanical strain because the total strain is zero. The maximum mechanical strain ($\epsilon = 0$) occurs when the temperature returns to the original value, and the corresponding stress is tensile (positive) if yielding occurs. This situation is usually referred to as out-of-phase, thermal-mechanical strain cycling. At the other extreme is in-phase cycling where maximum (positive) strain is at the maximum temperature and minimum (maximum negative) strain is at the minimum temperature. In a complex structure, the strain-temperature relationship may be somewhere between these two extremes.

This paper describes the results of a study where the low-cycle fatigue behavior of AISI 1010 steel was investigated for conditions of combined thermal and mechanical strain cycling. Experiments were limited to the two extreme conditions of in-phase and out-of-phase cycling. Detailed tabulations of data developed during this program and results of a companion study on the isothermal, low-cycle fatigue resistance of this same steel are reported elsewhere [1,2].²

The objective of this study was to obtain information on thermal-mechanical fatigue behavior of a commonly used low-carbon steel. Experiments combining both thermal- and mechanical-strain cycling are more representative of many service conditions than strain cycling at constant temperature. However, since thermal-mechanical fatigue testing is more time consuming, costly, and complicated than isothermal fatigue testing, the approach taken in this program was to conduct a limited study of thermal-mechanical fatigue behavior over the temperature range of 93 to 538°C (200 to 1000°F) for correlation with previous isothermal work [2] on the same material. An upper temperature limit of 538°C (1000°F) was considered to be reasonable for most practical uses of AISI 1010 steel. The lower temperature limit of 93°C (200°F) was chosen as a reasonable approximation of cooling to room temperature. This lower temperature level was well below the blue-brittle temperature range of 149 to 316°C (300 to 600°F) previously observed for this material [2], yet it was high enough to permit thermal cycling at a reasonably fast rate.

Most laboratory studies of thermal-fatigue behavior, as described by King and Smith [3], have been conducted either by thermal cycling of end-restrained specimens or by strain cycling of axially loaded specimens at constant temperature. It was also noted that two other techniques of evaluating thermal-fatigue resistance have been used: (a) testing of components under actual service conditions and (b) thermal cycling of wedges, disks, thick-walled cylinders, and locally heated sheet specimens [3]. Although the testing of components provides very useful and practical data, it is usually not economical at early design stages and does not provide a knowledge of thermal fatigue behavior under well-defined

²The italic numbers in brackets refer to the list of references appended to this paper.

stress-strain conditions. The second type of thermal cycling test is sometimes useful in sorting materials, but stresses and strains developed in the specimens are not well defined and are difficult to determine by analysis.

Carden [4] developed a testing technique for evaluating the behavior of materials under a combination of simple axial loading and temperature cycling. The objective of his approach was to make it possible to evaluate the thermal-mechanical fatigue resistance of materials under well-defined stress-strain conditions by controlling both thermal and mechanical strain independently. This same objective was used in developing experimental procedures for independent control of both thermal and mechanical strain in the present study of AISI 1010 steel.

In recent years, there have been a number of books and symposia either partially concerned with or devoted to the subject of thermal fatigue [5-11]. In addition, there are two extensive bibliographies that list publications on this subject [12,13]. King and Smith [3] have reviewed many of the more recent publications related to thermal fatigue. Since such a large amount of information is already available in published literature, the present brief review will be concerned with only the fatigue behavior of low-carbon steels under thermal or thermal-mechanical cycling. A similar review of isothermal-fatigue data on low-carbon steels is also available [2].

The limited amount of available information on the thermal fatigue behavior of low-carbon steels is summarized in Table 1. Although the work of Kawamoto et al [14] and Udoguchi and Wada [15] was on steels with higher amounts of carbon (0.69 and 0.38 percent, respectively) than were of interest to the present study, it does contain information on behavior under in-phase, thermal-mechanical strain cycling. Kawamoto et al [14] found that, when specimens greater than about 0.64 cm (0.25 in.) diameter were used, the fatigue life decreased, due to triaxial stresses that were developed in the larger specimens. For in-phase cycling between 100 to 300°C (212 to 572°F) and 100 to 400°C (212 to 752°F), Udoguchi and Wada [15] found that 0.30 percent carbon steel had about the same fatigue resistance for both temperature ranges. This thermal-fatigue resistance was slightly less than the isothermal-fatigue resistance at both 200 and 400°C (392 and 752°F).

Lyle [16] presented a limited amount of data on the thermal-fatigue behavior of a low-carbon steel. Similar results for a 0.16 percent carbon steel were reported by Taira and Inoue [17] and Taira [18]. All three of these studies used restrained specimens loaded uniaxially where the mechanical strain was directly proportional to the change in temperature. Since separate control of mechanical strain was not employed, the results have limited application.

Taira and Inoue [17] also obtained multiaxial thermal stresses by cooling a solid cylinder from one end. They were able to correlate the

TABLE 1—Information on the thermal fatigue behavior of low-carbon steels.

Reference Number	Material	Temperature Ranges, °C (°F)	Type of Test	Type of Loading	Remarks
14	0.69% C steel	100 to 300 (212 to 572), 100 to 350 (212 to 662), 100 to 450 (212 to 842), 100 to 500 (212 to 932), and 100 to 600 (212 to 1112)	thermal-mechanical strain cycling	uniaxial	effect of specimen size on thermal fatigue life is reported, and $\Delta\epsilon_r-N_f$ curves are given for cycling with ϵ_{max} at f_{max}
15	0.38% C steel	100 to 300 (212 to 572) and 100 to 400 (212 to 752)	thermal-mechanical strain cycling	uniaxial	$\Delta\epsilon_r-N_f$ curves are given for cycling with ϵ_{max} at f_{max}
16	Low-C steel	between about 50 and 500 (125 and 940)	restrained thermal cycling	uniaxial	using constrained, thin-walled cylindrical specimens, $\Delta\epsilon_r-N_f$ curves were developed for mean temperatures of 204, 232, 260, 288, and 316°C (400, 450, 500, 550, and 600°F)
17	0.16% C steel	between about 195 and 565 (380 and 1050)	restrained thermal cycling	uniaxial and multi-axial	equivalent strain range- N_f curves are reported for a mean temperature of 380°C (716°F): uniaxial specimens were thin-walled cylinders, and multi-axial specimens were solid cylinders cooled from one end: an analytical method was developed to predict the life-time to fatigue-crack initiation in the multiaxial tests from fatigue life data for the uniaxial tests

18	0.16% C steel	200 to 600 (392 to 1112), 300 to 600 (572 to 1112), and 200 to 500 (392 to 932)	restrained thermal cycling	uniaxial	relationship between micro- structural changes and fatigue life was studied for thermal fatigue and related to isother- mal fatigue behavior both $\Delta\epsilon_p N_f$ and $\Delta\epsilon_p N_f$ curves are reported for cycling with ϵ_{min} at T_{max} .
19	0.16% C steel	100 to 400 (212 to 752), 200 to 500 (392 to 932), 300 to 600 (572 to 1112), 150 to 550 (302 to 1022), and 100 to 600 (212 to 1112)	thermal-mechanical strain cycling	uniaxial	

multiaxial with uniaxial fatigue behavior by carrying out an elastic-plastic, thermal stress-strain analysis of the multiaxial specimens.

For the special case of thermal cycling with full end restraint, Taira [18] found that the thermal-fatigue life of a 0.16 percent carbon steel could be predicted from isothermal fatigue data. For cycling at temperatures below about 400°C (750°F), he found that the thermal-fatigue life was about the same as the isothermal fatigue life for the same plastic strain range at the mean temperature of the thermal cycle. When the thermal-fatigue cycle had a maximum temperature of about 500°C (930°F) or more, he found that the thermal-fatigue life was close to that for isothermal-fatigue cycling at the same plastic strain range at the maximum temperature. However, the variety of mechanical strain/thermal cycle conditions studied were limited by use of the restrained specimen, and the minimum temperature of thermal cycling was always about 200°C (400°F) or greater.

The only results on out-of-phase thermal-mechanical cycling of a low-carbon steel were those recently reported by Taira et al [19] for a 0.16 percent carbon steel. The data were well approximated by a linear relationship between $\log \Delta \epsilon_p$ and $\log N_f$, but the slope of this line was much less than -0.5 . The fatigue life values obtained from these experiments were much lower than lives predicted from isothermal-fatigue data using a linear damage theory.

None of the studies just described carried out both in-phase and out-of-phase thermal-mechanical strain cycling on a heat of low-carbon steel with extensive documentation of isothermal-fatigue behavior. Furthermore, cyclic stress-strain data were not reported.

Experimental Procedures

The material for this program was taken from the same heat of special quality hot-rolled, 1.91-cm ($\frac{3}{4}$ -in.)-diameter AISI 1010 steel bar used in the previous study of isothermal low-cycle fatigue behavior [2]. The chemical analysis and tensile properties of this steel were typical of those expected for this alloy and are reported in that same study.

The thermal-mechanical fatigue specimens were machined to the configuration shown in Fig. 1. This is the same external configuration used for the isothermal-fatigue specimens. Use of this specimen configuration allowed the temperature to be controlled at the minimum diameter where strain was measured and reduced the influence of temperature gradients on fatigue life. The present specimens were hollow, rather than solid as for the isothermal studies, to facilitate cooling.

The test section of each specimen was polished with successively finer grades of silicon-carbide paper to produce a surface finish of 0.4 μm (16 $\mu\text{in.}$) rms or better, with finishing marks parallel to the longitudinal

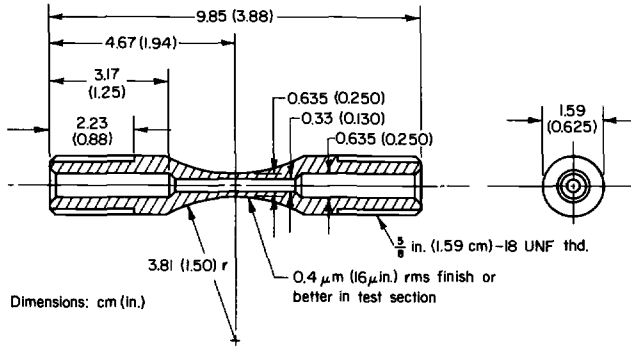


FIG. 1—Configuration of specimen.

axis of the specimen. Specimens were degreased with trichlorethylene, followed by reagent grade acetone before being heated to temperature.

Apparatus

The thermal-mechanical fatigue experiments were conducted using the same basic servocontrolled electrohydraulic test system that was used for isothermal-fatigue experiments [2]. This type of system has been used in numerous low-cycle fatigue studies (for example, see Ref 20). Details of the equipment, method of heating, gripping and alignment procedure, technique of strain measurement, and general experimental procedures are given in any one of several reports [1,2,21]. In the present work, the closed-loop axial strain control system was integrated with a closed-loop temperature control apparatus, as illustrated schematically in Fig. 2. Thus, both the axial mechanical strain and the temperature were controlled throughout each test.

Load was applied to the specimen axially; diametral changes in the specimen were measured using a special diametral extensometer; and load was measured by a strain-gaged load cell in series with the specimen. Diametral mechanical strain was obtained by subtracting the diametral thermal strain from the total diametral strain using a simple analog circuit. The thermal strain was computed from the linear coefficient of thermal expansion and the change in temperature. Diametral mechanical strain and load signals were combined and converted to an axial mechanical strain using an analog computer [22].

The axial mechanical strain and temperature were controlled to follow one of the two basic constant-amplitude waveforms shown in Fig. 3. In Fig. 3a, ϵ_{\max} is in phase with T_{\max} ; whereas, in Fig. 3b, ϵ_{\max} is out of phase with T_{\max} (or ϵ_{\min} is in phase with T_{\max}). The control program waveform was provided by an arbitrary function generator. Heating rate was not constant, but it changed throughout the cycle as shown in Fig. 3. The

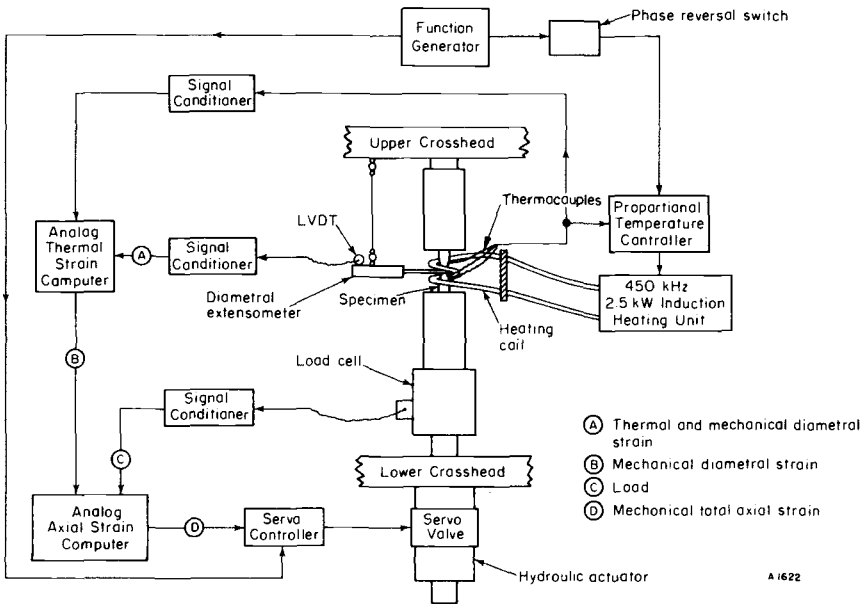


FIG. 2—Schematic diagram of thermal-mechanical fatigue apparatus.

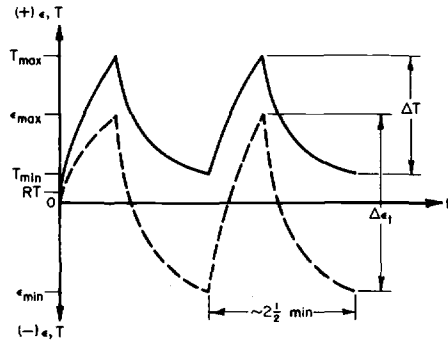
heating rate was determined by the thermal response of the specimen and the heating equipment, with the length of the thermal cycle maintained at about $2\frac{1}{2}$ min. Mechanical strain was programmed through appropriate phasing and scaling of the same waveform used to control temperature. In two of the tests, the waveform was modified by introducing 6-min.-long temperature and strain hold periods at maximum temperature.

Before starting each test, controls of the thermal-strain computer were set to give close to zero diametral mechanical strain when the temperature was cycled with the load at zero. At the start of each test, the specimen was heated to the mean temperature to obtain values of compliance and elastic Poisson's ratio needed in the analog computer. These values at mean temperature were then used throughout the test. Since these values were actually temperature dependent, assuming them to be constant introduced errors, as discussed in the next section of this paper.

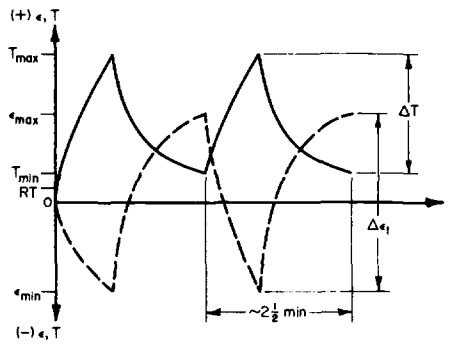
During each fatigue test, load was continuously recorded using a time-base strip-chart recorder. Load versus axial extension hysteresis loops were periodically recorded during each test using an x - y recorder.

Data Acquisition

Use of the hourglass-type specimen (Fig. 1) required that diametral,



(a) Maximum strain in-phase with maximum temperature



(b) Maximum strain out-of-phase with maximum temperature

FIG. 3—Illustration of control waveforms.

rather than axial, strain be measured. Because axial mechanical strain was of prime interest, diametral strain had to be converted before the signal from the diametral extensometer could be effectively used in the control loop. To accomplish this conversion, it was first necessary to compute diametral mechanical strain.

Since diametral thermal strain was simply $\alpha \Delta T$, mechanical diametral strain was given by the following relation

$$\epsilon_{dt} = \epsilon_{dt} - \alpha \Delta T \tag{1}$$

The thermal strain computer (Fig. 2) was designed to compute ϵ_{dt} by Eq 1, using the value of α at the mean temperature of the thermal cycle. Since α is a function of temperature, use of a constant value of α gave an error at temperatures other than mean temperature. As mentioned earlier, the value of α was adjusted experimentally to give minimum error in the computation. This error was controlled to be of equal magnitude at T_{min}

and T_{\max} . The size of this error, in terms of strain, is discussed after the introduction of Eq 2.

To compute axial mechanical strain from diametral mechanical strain, it was then necessary to determine the elastic and plastic components of diametral strain. Once these were obtained, the elastic and plastic components of axial mechanical strain were computed and the results summed to generate the total axial mechanical strain. The necessary equations for the computation of axial strain and the analog circuits of the computer were described in detail by Slot et al [22].

In this study, the value of Poisson's ratio for inelastic deformation was assumed to be 0.5, and the value of Poisson's ratio for elastic deformation was determined for each specimen. The specimen was installed in the test fixture and heated to the mean temperature of the thermal cycle. The value of specimen compliance, K , was then set into the computer by load-cycling the specimen for several cycles at low loads in the elastic region and adjusting the K potentiometer until the value of $\Delta\epsilon_{dp}$ was equal to zero. The value of elastic Poisson's ratio was then determined from the equation

$$\nu_e = \frac{\Delta\epsilon_{de} A_T E}{\Delta P} \quad (2)$$

where the values of $\Delta\epsilon_{de}$ and ΔP were determined from the slope of the load versus diametral extension x - y plot recorded during a few load cycles after setting the value of K . Values of E used in Eq 2 were the average results of the tension tests reported previously [2]. Since values of A_T and E at the mean temperature of the thermal cycle were used to compute ν_e at the mean temperature, an additional error was introduced in the computation of the total mechanical strain at other temperatures.

Considering both the error introduced in Eq 1 by assuming constant value of α and the error introduced in Eq 2 by assuming constant ν_e , the magnitude of total possible errors were computed for each temperature range. For 93 to 316°C (200 to 600°F), it was about 0.03 percent strain; for 93 to 427°C (200 to 800°F), it was about 0.04 percent strain; and for 93 to 538°C (200 to 1000°F), it was about 0.05 percent strain. Thus, for example, at 0.5 percent strain amplitude, these would be relative errors of 6, 8, and 10 percent, respectively. Although these are fairly large errors, they are in the opposite direction for each side of the mean temperature and cause little error in the total strain range. Also, they are likely to have only a small influence on fatigue life for strain ranges with relatively large inelastic strain components. However, if this test procedure is to be used for low-strain range, long-life tests in the future, it must be modified to account for variations in α and ν_e .

Examination of the load-time records revealed changes in the cyclic

deformation resistance of the material. Values of stress amplitude were determined using the load-time histories and the cross-sectional area of the specimen at the mean test temperature. The load-time histories also were used to determine the three measures of fatigue life: N_0 , N_5 , and N_f .

Results and Discussion

Results of all the experiments conducted in this program are summarized in Table 2. Five experiments were conducted with ϵ_{\max} at T_{\max} . However, because out-of-phase cycling was more detrimental than in-phase cycling, the other twelve experiments were with ϵ_{\min} at T_{\max} . As described previously, $\Delta\epsilon_t$ was maintained constant with zero mean strain throughout each test. Values of $\Delta\epsilon_p$ at $N_f/2$ were computed from the relation

$$\Delta\epsilon_p = \Delta\epsilon_t - \frac{\sigma \text{ at } \epsilon_{\max}}{E} - \frac{\sigma \text{ at } \epsilon_{\min}}{E} \quad (3)$$

where E was the value of elastic modulus at which σ at ϵ_{\max} or σ at ϵ_{\min} occurred. For hold-time tests, σ at the end of the hold period was used in Eq 3 instead of σ at ϵ_{\max} for Specimen 79 and instead of σ at ϵ_{\min} for Specimen 78. Thus, listed values of $\Delta\epsilon_p$ are measures of the width of the half-life hysteresis loop for each test and include both time-dependent and time-dependent inelastic strain components.

Cyclic Stress-Strain Response

Even though the strain cycling was fully reversed, the stress cycle was not symmetric about zero because the temperature was different at each extreme of the cycle. For example, Fig. 4 shows this type of stress response for the 92 to 427°C (200 to 800°F) temperature range. This is typical of the cyclic hardening observed in these experiments. In comparison, a smaller amount of cyclic hardening was observed for the 93 to 538°C (200 to 1000°F) experiments, and a larger amount was observed for the 93 to 316°C (200 to 600°F) experiments. For the in-phase cycle (Fig. 4a), the magnitude of peak compressive stress was greater than the magnitude of peak tensile stress, or $|\sigma_{\min}| > |\sigma_{\max}|$. The opposite was true for the out-of-phase cycle (Fig. 4b) where $|\sigma_{\max}| > |\sigma_{\min}|$.

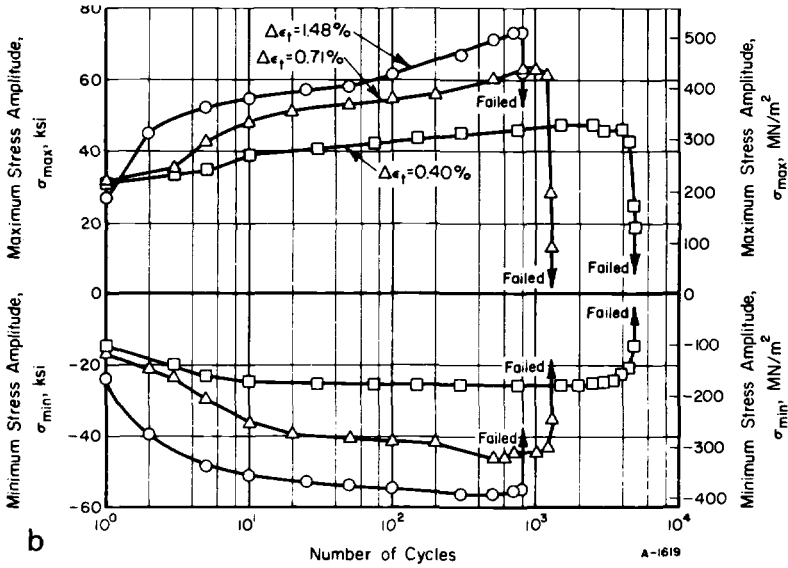
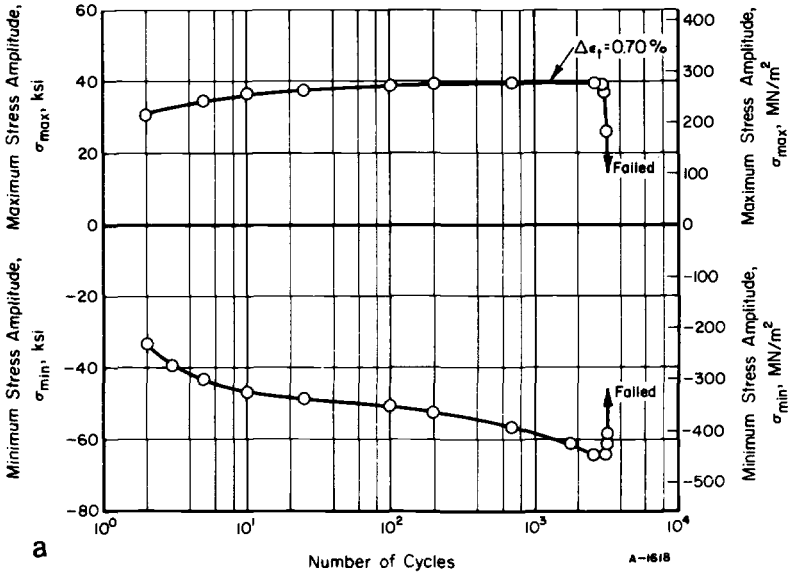
It is also important to note (Fig. 5) that maximum stress (or minimum stress) was not necessarily coincident with the maximum strain (or minimum strain). A detailed tabulation of half-life values of stress at ϵ_{\max} and ϵ_{\min} , as well as values of σ_{\max} and σ_{\min} , are reported in Ref 1. Examination of the data records showed that σ_{\max} (or σ_{\min}) was practically the same as σ at ϵ_{\max} (or σ at ϵ_{\min}), when ϵ_{\max} (or ϵ_{\min}) was at 93°C (200°F). However,

TABLE 2—Summary of thermal-mechanical low-cycle fatigue experiments of AISI 1010 steel conducted in air.

Specimen Number	Temperature-Strain Relationship	Limits of Temperature Cycle, °C (°F)	Total Axial Strain Range, $\Delta\epsilon_1$, %	Inelastic Axial Strain Range at $N_f/2$, $\Delta\epsilon_p$, %		Fatigue Life, cycles		
				$N_f/2$	$\Delta\epsilon_p$	N_0	N_s	N_f
56	ϵ_{\max} at T_{\max}	93 to 538 (200 to 1000)	2.05	1.76	59	73	75	
57	ϵ_{\max} at T_{\max}	93 to 538 (200 to 1000)	1.02	0.75	360	380	489	
62	ϵ_{\min} at T_{\max}	93 to 538 (200 to 1000)	2.00	1.68	107	113	116	
59	ϵ_{\min} at T_{\max}	93 to 538 (200 to 1000)	1.01	0.76	150	156	157	
67	ϵ_{\min} at T_{\max}	93 to 538 (200 to 1000)	0.68	0.44	225	252	262	
68	ϵ_{\min} at T_{\max}	93 to 538 (200 to 1000)	0.41	0.18	570	575	632	
77	ϵ_{\max} at T_{\max}	93 to 427 (200 to 800)	0.70	0.35	3000	3030	3282	
79	ϵ_{\max} at T_{\max}^a	93 to 427 (200 to 800)	1.02	0.72	525	550	575	
70	ϵ_{\min} at T_{\max}	93 to 427 (200 to 800)	1.48	1.12	365	386	403	
71	ϵ_{\min} at T_{\max}	93 to 427 (200 to 800)	1.48	1.08	795	807	811	
73	ϵ_{\min} at T_{\max}	93 to 427 (200 to 800)	1.48	1.07	375	385	386	
69	ϵ_{\min} at T_{\max}	93 to 427 (200 to 800)	0.71	0.35	1200	1207	1307	
72	ϵ_{\min} at T_{\max}	93 to 427 (200 to 800)	0.40	0.15	4000	4130	4890	
78	ϵ_{\min} at T_{\max}^a	93 to 427 (200 to 800)	1.02	0.68	...	429	430	
80	ϵ_{\max} at T_{\max}	93 to 316 (200 to 600)	0.72	0.34	4500	4600	4778	
74	ϵ_{\min} at T_{\max}	93 to 316 (200 to 600)	1.43	0.97	563	565	569	
75	ϵ_{\min} at T_{\max}	93 to 316 (200 to 600)	0.70	0.30	3170	3145	3232	

^a6-min.-hold times at T_{\max}

^bNo noticeable drop in load.



- (a) ϵ_{max} at T_{max} .
- (b) ϵ_{min} at T_{max} .

FIG. 4—Cyclic stress response of AISI 1010 steel under thermal-mechanical strain cycling with a temperature range of 93 to 427°C (200 to 800°F).

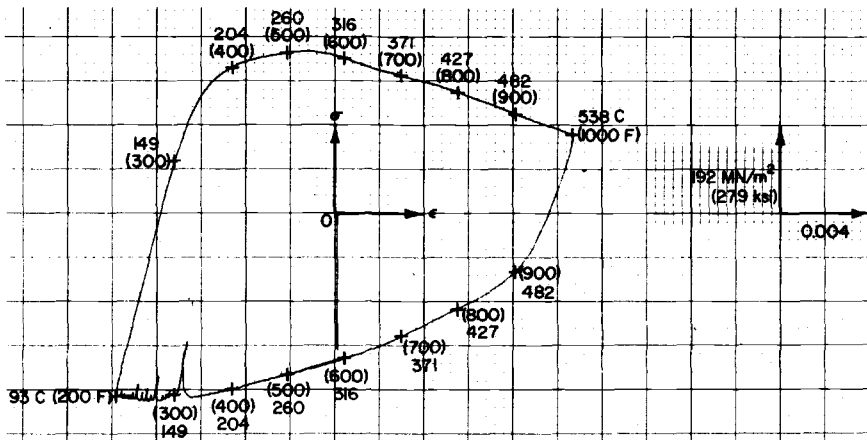


FIG. 5—Stress-strain hysteresis loop for 93 to 538°C (200 to 1000°F) cycle with ϵ_{\max} at T_{\max} (specimen 56 at cycle 40).

when ϵ_{\max} or ϵ_{\min} was at T_{\max} , there was generally a difference between σ_{\max} (or σ_{\min}) and σ at ϵ_{\max} (or σ at ϵ_{\min}). As shown by the cyclic stress-strain curves in Fig. 6, this difference was quite significant at higher temperatures and larger strain ranges. As temperature became lower or strain range became smaller, such differences became much less pronounced.

For out-of-phase cyclic stress-strain response, the difference between σ_{\max} and σ at ϵ_{\max} or between σ_{\min} and σ at ϵ_{\min} was only about 3 percent of σ_{\max} or σ_{\min} for 93 to 538°C (200 to 1000°F) and negligible for the two lower temperature ranges. However, as shown in Fig. 6, there was a difference between such data for in-phase cyclic stress-strain response. For a constant strain amplitude, this difference became larger as the temperature range increased. It also became larger as the strain amplitude increased for a constant temperature range. At 93 to 316°C (200 to 600°F) and 93 to 427°C (200 to 800°F), values of σ at ϵ_{\max} or ϵ_{\min} were still above the isothermal cyclic stress-strain curves for the maximum temperature of that cycle. However, for 93 to 538°C (200 to 1000°F), values of σ at ϵ_{\max} or ϵ_{\min} were about the same as the isothermal cyclic stress-strain curve at 538°C (1000°F).

As shown in Fig. 5, an instability in the stress-strain response was encountered near 149°C (300°F). This sort of instability was related to dynamic strain-aging processes that resulted in discontinuous yielding behavior. These instabilities tended to become less prominent with cyclic hardening for all 93 to 316°C (200 to 600°F) and 93 to 427°C (200 to 800°F) cycles, and no significant instabilities were noted in the stabilized hysteresis loops for these temperature ranges. However, such was not the case for the 93 to 538°C (200 to 1000°F) cycles, where the instabilities

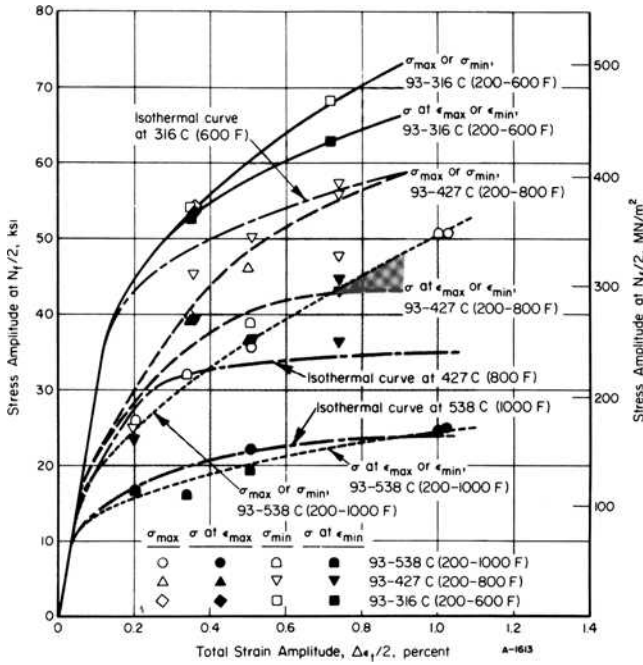


FIG. 6—Cyclic stress-strain behavior of AISI 1010 steel under in-phase thermal-mechanical cycling.

were still observed in the stable loops as shown in Fig. 5. Thus, it was hypothesized that the time at temperatures near 538°C (1000°F) was sufficient to reverse the processes that caused dynamic strain aging at lower temperatures. On the other hand, such was not the case for lower peak temperature cycles.

Although σ_{max} (or σ_{min}) was not always at ϵ_{max} (or ϵ_{min}), the values of σ_{max} and σ_{min} provided a quantitative measure of the cyclic stress-strain response. Therefore, they were used to characterize cyclic stress-strain behavior in the remaining discussion. For the 93 to 427°C (200 to 800°F) (Fig. 4) and the 93 to 538°C (200 to 1000°F), the cyclic stress in phase with T_{max} was relatively stable after the first few cycles and was within 5 percent of the value at $N_f/2$ for more than 90 percent of the cyclic life. In contrast, the out-of-phase stress for these temperature ranges showed continual cyclic hardening and the stress after 10 percent of cyclic life was about 10 percent less than the value at $N_f/2$. The stress response for both in-phase and out-of-phase cycling at 93 to 316°C (200 to 600°F) showed the same trends as that for the out-of-phase cycling at the two higher temperature ranges.

Morrow [23] has shown that it is often possible to express the cyclic

stress-strain curve in terms of a simple power function relating $\Delta\epsilon_p$ to $\Delta\sigma$. However, in the present study, it was found to be more convenient to use the same type of function for relating $\Delta\epsilon_t$ to $\Delta\sigma$ for $\Delta\epsilon_t/2 \leq 1$ percent

$$\Delta\sigma/2 = K' (\Delta\epsilon_t/2)^{n'} \quad (4)$$

where $K' = E$ and $n' = 1$ for $0 \leq \Delta\epsilon_t/2 \leq \epsilon_0$. The parameters E , K' , and n' and ϵ_0 are functions of temperature as listed in Table 3; the parameter σ_0 , also listed in Table 3, is directly related to ϵ_0 ($\sigma_0 = E\epsilon_0$). The thermal-mechanical, cyclic stress-strain curves defined by Eq 4 are shown by the dashed lines in Fig. 7. For comparison, isothermal cyclic curves from Ref 2 are shown in Fig. 7 as solid lines to indicate that more cyclic hardening occurred in the thermal-mechanical than in the isothermal experiments.

Fatigue Resistance

Results of the thermal-mechanical fatigue experiments are compared with the previous isothermal fatigue data [2]

- (a) In terms of $\Delta\epsilon_t$ in Fig. 8.
- (b) In terms of $\Delta\sigma/2$ in Fig. 9.
- (c) In terms of $\sigma_{\max} \Delta\epsilon_t/2$ in Fig. 10.

Based on $\Delta\epsilon_t$ as shown in Fig. 8 (also true for $\Delta\epsilon_p$ as shown in Ref 2), the thermal-mechanical results fell below the isothermal results. This difference became more marked at higher peak temperatures and was greater for out-of-phase cycling than for in-phase cycling. It was also noted that curves for out-of-phase cycling were generally steeper than those for in-phase cycling. Thus, the out-of-phase cycling was more damaging than the in-phase cycling for these conditions.

There may be three main reasons why the thermal-mechanical data fell below the isothermal data. First, thermal-mechanical cycles were applied at a variable and lower strain rate than the isothermal cycles. In the former case, the slowest strain rate was comparable to a frequency of about 0.1 cpm; whereas, in the latter case, depending on the strain range, since strain rate was maintained constant, the frequency was about 6 to 60 cpm. At high temperatures, usually greater than 427°C (800°F), such a reduction in frequency can cause a reduction in fatigue life. For AISI 1010 steel at 500°C (1112°F), Coffin [24] has shown that the effect of frequency can be described by the following equation

$$\Delta\epsilon_t = 0.00291 N_f^{-0.174} \nu^{0.159} + 3.0 N_f^{-0.79} \nu^{0.187} \quad (5)$$

For $\Delta\epsilon_t = 1.0$ percent, this equation predicts (a) $N_f = 860$ cycles at $\nu = 0.1$ cpm, (b) $N_f = 2280$ cycles at $\nu = 5.0$ cpm, and (c) $N_f = 4060$ cycles

TABLE 3—Parameters for thermal-mechanical cyclic stress-strain amplitude curves for AISI 1010 steel.

Limits of Temperature Cycle, °C (°F)	E_s , ° GN/m ² (ksi)	ϵ_0	σ_0 , MN/m ² (ksi)	n'	K' , MN/m ² (ksi)
93 to 316 (200 to 600)	200 (29 000)	0.00176	352 (51.0)	0.255	1770 (257)
93 to 427 (200 to 800)	193 (28 000)	0.00136	262 (38.0)	0.292	1800 (261)
93 to 538 (200 to 1000)	186 (27 000)	0.00115	214 (31.0)	0.286	1480 (215)

^aDetermined from average tensile values at mean temperature of cycle.

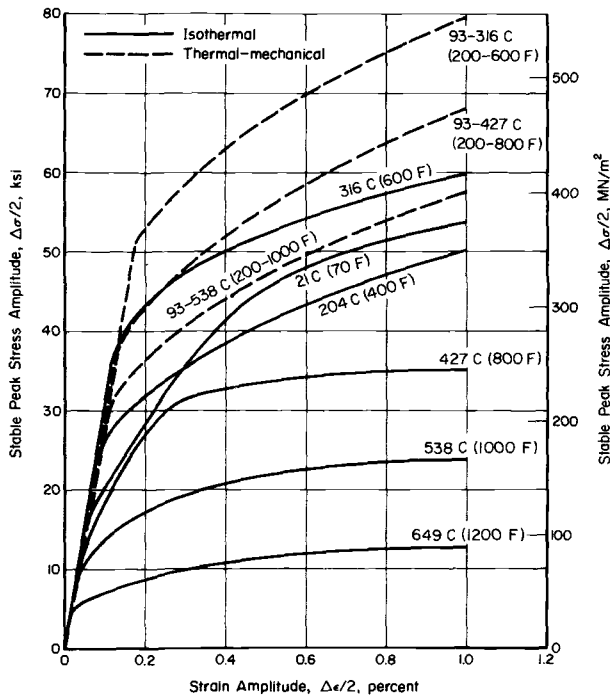


FIG. 7—Comparison of cyclic stress-strain response for thermal-mechanical and isothermal strain cycling of AISI 1010 steel.

at $\nu = 5.0$ cpm. While this effect is significant, it is not nearly large enough to explain the very short lives observed for thermal-mechanical cycling in this study. Furthermore, this effect would become smaller at lower temperatures and would very likely be negligible below 427°C (800°F).

Second, the thermal-mechanical specimens were hollow tubes instead of solid bars as used in the isothermal studies. Once a significant fatigue crack developed in the tube, it might propagate more quickly than in a solid specimen. Although no tubular specimens were included in the previous isothermal work [2], it is believed that, in the present case, such differences were negligible. Low-cycle fatigue experiments using hollow specimens have not shown significant deviations from solid-specimen behavior in work done at other laboratories [5,25,26]. For example, isothermal data for continuous strain cycling of 2¼Cr-1Mo steel [26] agree very well (with about only ± 20 percent difference in cyclic life) with those developed for the AISI 1010 steel over the 316 to 649°C (600 to 1200°F) temperature range [2].

Third, repeated thermal-mechanical cycling through the 120 to 175°C

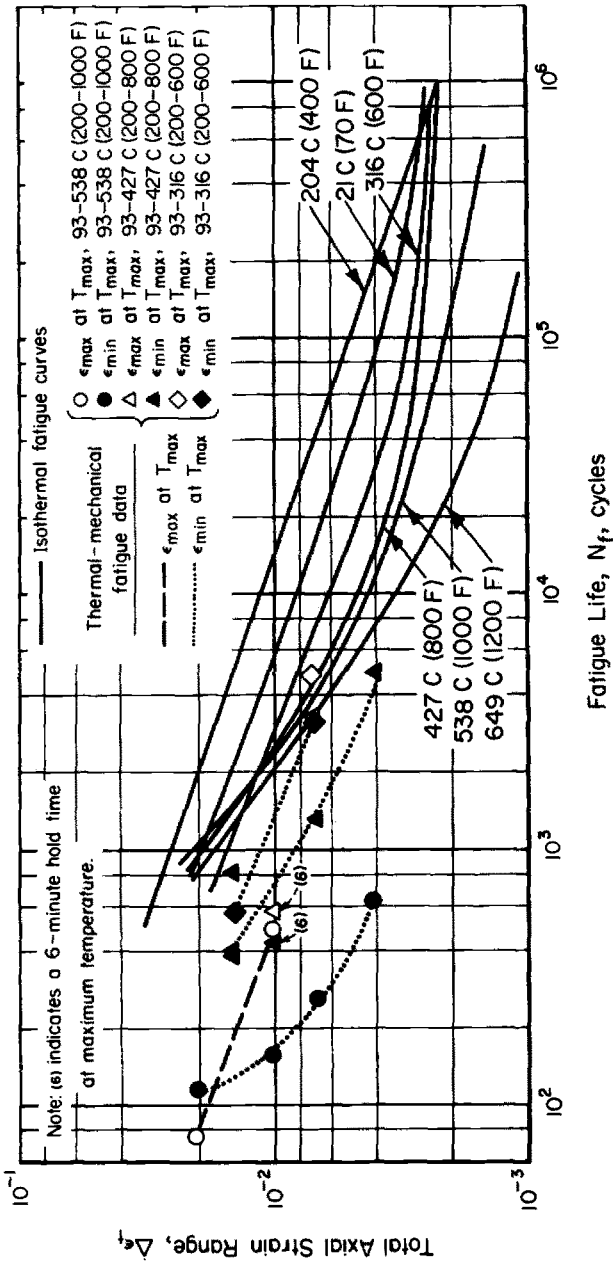


FIG. 8—Comparison of thermal-mechanical and isothermal fatigue resistance of AISI 1010 steel based on total strain range.

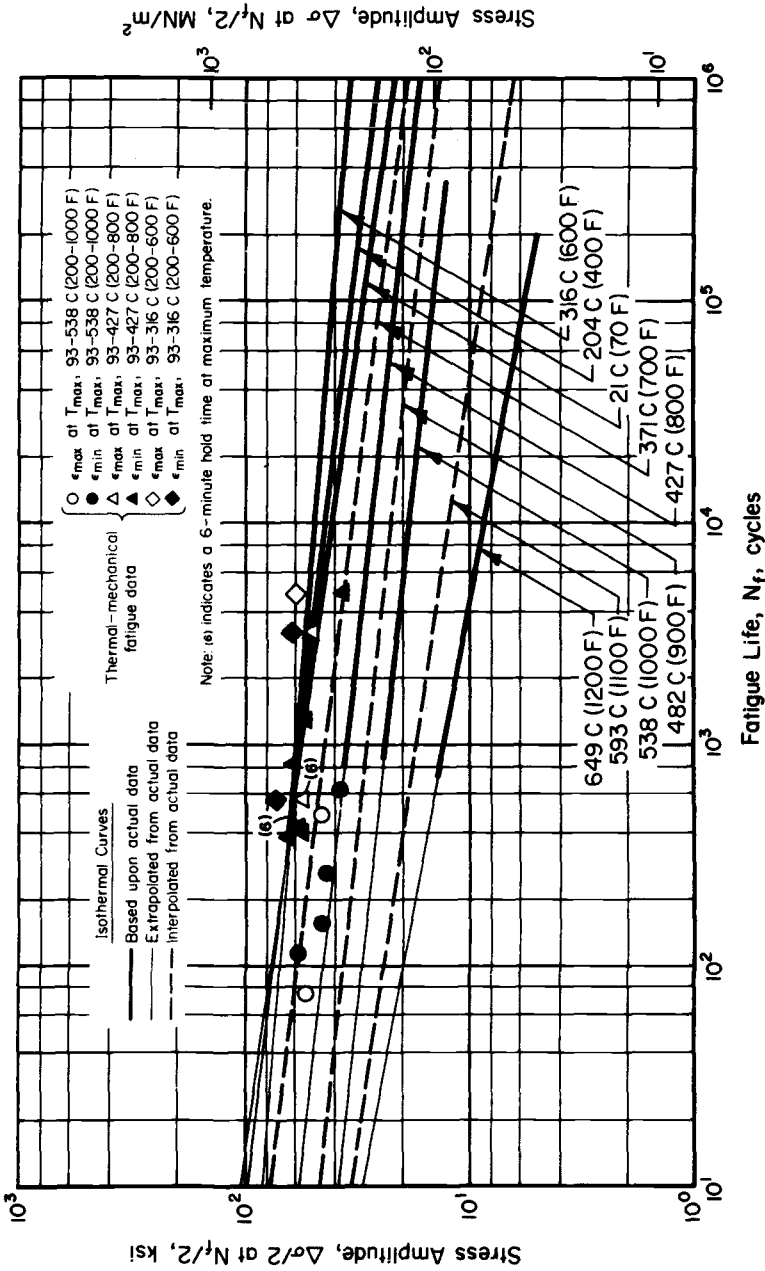


FIG. 9—Comparison of thermal-mechanical and isothermal fatigue resistance of AISI 1010 steel based on stress amplitude.

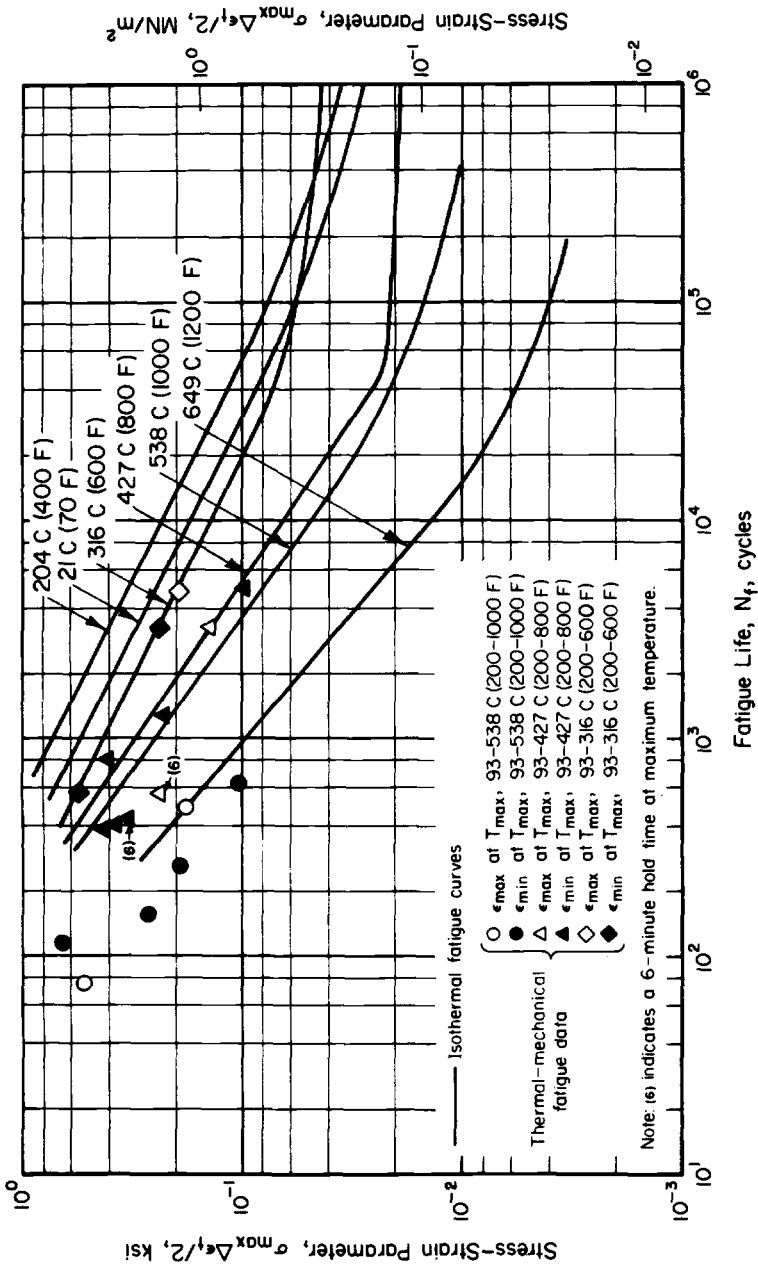


FIG. 10—Comparison of thermal-mechanical and isothermal fatigue resistance of AISI 1010 steel based on a stress-strain parameter.

(250 to 350°F) temperature range allowed dynamic strain aging to take place during each cycle. It is hypothesized that this repeated dynamic strain aging was responsible for the larger amount of cyclic hardening which occurred during the thermal-mechanical tests in comparison with that which occurred during the isothermal tests. If the cyclic hardening caused the stress to be higher for the same strain range without increasing the fatigue resistance of the material, then a shorter fatigue life would be expected for the higher stress level.

To study this hypothesis, the thermal-mechanical data were compared with the isothermal data on the basis of stress amplitude in Fig. 9. There was no significant difference between the in-phase and out-of-phase results when compared on this basis. Data from 93 to 538°C (200 to 1000°F) cycling fell slightly above the 427°C (800°F) isothermal curve; data from the 93 to 427°C (200 to 800°F) cycling fell above the 371°C (700°F) curve; and data from the 93 to 316°C (200 to 600°F) cycling fell above the 316°C (600°F) curve. The isothermal curves were taken from Ref 2 where heavy solid lines are shown in Fig. 9 and were extrapolated as shown by the light lines. The curve at 371°C (700°F) was obtained by logarithmic interpolation between the curves at 21 and 427°C (70 and 800°F). The curves at 482 and 593°C (900 and 1100°F) were obtained in a similar manner using the curves at 427 and 538°C (800 and 1000°F) and at 538 and 649°C (1000 and 1200°F), respectively. To get the 371°C (700°F) curve, the 21°C (70°F) curve was used rather than the 427°C (800°F) curve because it is believed that the strength dropped rapidly between 316 and 371°C (600 and 700°F) and that such a choice was more realistic. In view of these comparisons, it appears that the increased stress due to cyclic hardening was the primary reason for the lower fatigue life observed previously on the basis of $\Delta\epsilon_t$ or $\Delta\epsilon_p$.

Smith et al [27] have used the following empirical parameter to assess the fatigue resistance of metals

$$\sigma_{\max}(\Delta\epsilon_t/2)$$

This parameter is used in Fig. 10 for comparison of the thermal-mechanical with the isothermal fatigue data. For the 93 to 316°C (200 to 600°F) and the 93 to 427°C (200 to 800°F) cycles, the thermal-mechanical fatigue data (plotted symbols) fell close to the isothermal fatigue curves associated with the maximum temperature of the cycle. However, for the 93 to 538°C (200 to 1000°F) cycle, the data fell well below the isothermal curve for 538°C (1000°F). Thus, it appears that this parameter gives a reasonable correlation between thermal-mechanical and isothermal fatigue data for peak temperatures near or below 427°C (800°F), but not for higher peak temperatures where time-dependent mechanisms play a significant role in the damage process. This result was expected because the parameter

is based upon consideration of only time-independent damage processes. Extension of such a parameter to cover time-dependent damage mechanisms should be pursued in future studies.

The thermal-mechanical fatigue data were compared [1] with similar data from other studies [14-17,19]. Because of the limited amount of published information, a complete comparison with present data was not possible. Where comparisons were made, some differences did exist between results of this study and those of other studies, but the overall behavior trends were similar. Thus, it is believed that the present results represent typical thermal-mechanical fatigue behavior of low-carbon steels.

Calculation of Fatigue Life

In order to design or evaluate components operating under combined thermal and mechanical cycling, it is necessary to be able to make reasonable calculations of fatigue life. Two different approaches to life calculation may be considered: (a) development of relationships directly from thermal-mechanical fatigue experiments and (b) development of methods for correlating thermal-mechanical with isothermal fatigue resistance. Although the first approach is more straightforward than the second, it requires the conduction of costly experiments for long periods of time when intermediate or long-life ($>10^4$ cycles) fatigue is of interest. Even in the short-life range of the present study, it was difficult to develop enough data to rely on such an approach. These limitations make it desirable to use the second approach and develop methods of relating the results of thermal-mechanical cycling experiments to isothermal experiments. If such methods can be developed, then they can provide a rational basis for extrapolating the results of relatively short-lived, thermal-mechanical experiments.

In their studies of a 0.16 percent carbon steel, Taira et al [19] tried to predict thermal-mechanical fatigue life using a linear damage theory combined with the isothermal low-cycle fatigue behavior defined in terms of plastic strain range. This attempt was not very successful in that, in most instances, the predicted life was greater than the actual life, an unconservative result from a design viewpoint. Inspection of the data showed that such an approach would give similar results for the present study.

Taira [18] has suggested use of the concept of an equivalent temperature for correlating thermal-fatigue behavior with isothermal-fatigue behavior. This concept states that, for thermal-fatigue cycling between two temperatures, the same fatigue life will be developed by isothermal cycling at the equivalent temperature. For thermal fatigue of 0.16 percent carbon steel, where T_{\min} was greater than or equal to 200°C (392°F), it was shown that the equivalent temperature was defined as follows

$$T_e \cong \frac{T_{\max} + T_{\min}}{2}, \text{ for } T_{\max} < 400^\circ\text{C} (752^\circ\text{F}) \quad (6a)$$

and

$$T_e \cong T_{\max}, \text{ for } T_{\max} > 500^\circ\text{C} (932^\circ\text{F}) \quad (6b)$$

where N_f was related to $\Delta\epsilon_p$. This approach probably worked reasonably well because T_{\min} was above the temperature where dynamic strain aging could occur repeatedly. It would not work for the present study because T_{\min} was low enough to allow dynamic strain aging to take place during each cycle.

In the present program, it was empirically found that the following expression for equivalent temperature would provide a conservative lower bound on fatigue life if thermal-mechanical fatigue life is related to $\Delta\sigma/2$ at $N_f/2$

$$T_e \cong T_{\max}, \text{ for } T_{\max} \leq 316^\circ\text{C} (600^\circ\text{F}) \quad (7a)$$

and

$$T_e \cong \frac{T_{\max} + 316^\circ\text{C} (600^\circ\text{F})}{2}, \text{ for } 316^\circ\text{C} (600^\circ\text{F}) < T_{\max} \leq 538^\circ\text{C} (1000^\circ\text{F}) \quad (7b)$$

This empirical relationship is based only on data for a low-carbon steel for thermal-mechanical strain cycling over temperature ranges employed in this study.

To evaluate this relationship, fatigue life calculations were made for each of the specimens from the present work. The isothermal fatigue curves of Fig. 9 were used in making these calculations, and the results are shown by the open points in Fig. 11. In comparing actual with calculated fatigue lives, it can be seen that in all cases (except one) the calculated life was less than the actual life. The ratio of actual to calculated life gave a quantitative measure of the difference. The average ratio was about 3.4, as indicated in Fig. 11.

Also shown in Fig. 11 (solid points) are calculated fatigue lives using the parameter, $\sigma_{\max}\Delta\epsilon_r/2$, and the isothermal fatigue curves of Fig. 10. The ratio of actual to calculated life was about 0.22 (a factor of 4.5) for the 93 to 538°C (200 to 1000°F) data and was about 0.77 (a factor of 1.3)

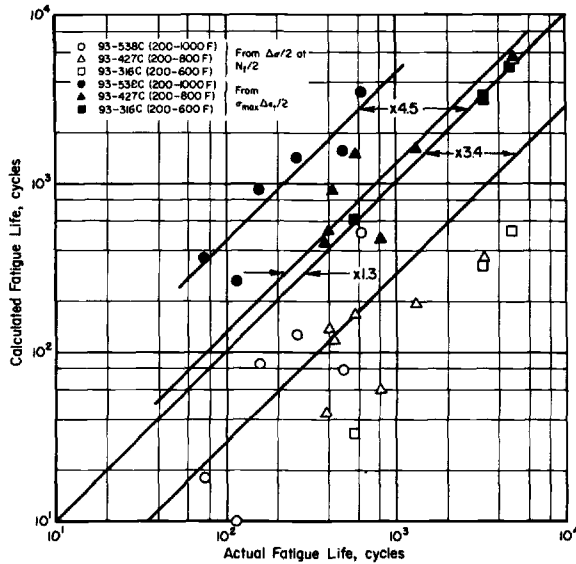


FIG. 11—Comparison of actual thermal-mechanical fatigue life with cyclic life calculated from isothermal fatigue curves.

for both the 93 to 316°C (200 to 600°F) and 93 to 427°C (200 to 800°F) data. Thus, for temperatures of 427°C (800°F) or less, this parameter gave a reasonably accurate assessment of fatigue life, and it could be used successfully in this lower temperature range. However, the calculations were significantly unconservative at 538°C (1000°F). Therefore, life calculations for this steel and these temperature ranges were more consistent when made using the approach based on $\Delta\sigma/2$ and T_e , which gave about the same results for all three temperature ranges and was conservative by a factor of about three on average cyclic life.

At first, it may seem that a factor of three is a large difference, but it is important to consider how such calculations are used in design applications. The designer usually follows one of two approaches: (a) he determines the cyclic stresses and strains in the critical area of the component under consideration and uses them to assess whether or not adequate fatigue life is available or (b) knowing what fatigue life is desired of the component in service, he designs it so that the cyclic stresses and strains will be low enough to assure achievement of desired life. Whichever approach is used, it is always necessary to apply a safety factor to either the stress and strain or to the fatigue life. Safety factors of 1.5 to 2.0 are normally applied to stress or strain, whereas factors of 10 to 20 are usually applied to cyclic life. The reason for larger factors on life than on stress or strain is that fatigue life is usually treated as a logarithmic

variable and small changes in stress or strain produce much greater changes in fatigue life.

When actual cyclic lives from the thermal-mechanical experiments were used to compute $\Delta\sigma/2$ values from the isothermal fatigue curves at T_e , the actual stress amplitudes were only about 18 percent greater than the calculated ones on the average. Thus, a factor of three under calculation of the average number of cycles to failure is not excessive in relation to the relatively small variation in stress amplitude that can cause a factor of three variation in cyclic life. The most important point is that this approach gives a consistent method of computing a lower bound on thermal-mechanical fatigue life of this steel from isothermal fatigue information. Computation of such a lower bound is more valuable for design purposes than is prediction of average fatigue life. Although the actual thermal-mechanical fatigue data might be considered for use, the limited amount of these data makes the statistical confidence in them lower than in the more numerous isothermal data.

It is important to note that either of the two life prediction methods just discussed required a knowledge of the half-life stress amplitude and that strain alone did not provide a sufficient correlation between thermal-mechanical and isothermal fatigue data. In general, a knowledge of both stress and strain were required to make accurate fatigue life predictions. Thus, in studies of thermal-mechanical fatigue behavior of materials, it is necessary to develop information on cyclic deformation behavior as well as on cyclic life. Also, the methods are based upon information for uniaxial loading and are not generally valid for multiaxial loading. Development of a method for complex multiaxial loading situations that are often encountered in design applications should be pursued in future studies.

Summary and Conclusions

During this study, thermal-mechanical fatigue experiments were conducted on AISI 1010 steel for temperature ranges of 93 to 316°C (200 to 600°F), 93 to 427°C (200 to 800°F), and 93 to 538°C (200 to 1000°F). Experiments were under fully reversed strain cycling, where the maximum strain was either in phase or out of phase with the maximum temperature. Where comparisons could be made with a limited amount of published data, present results showed similar trends to those of other studies. Therefore, the present data were considered to be typical of those expected for low-carbon steels in general.

Evaluating the results of the present experiments in comparison with results of comparative isothermal fatigue studies [2] leads to six major conclusions, applicable to the steel and the temperature ranges just mentioned.

1. More cyclic hardening was observed in the thermal-mechanical exper-

iments than in isothermal experiments. Cyclic hardening behavior was noted for all temperature ranges and was greater for the out-of-phase peak stress than for the in-phase peak stress.

2. In terms of $\Delta\epsilon_t$ or $\Delta\epsilon_p$ versus N_f , fatigue life was much lower for thermal-mechanical cycling than for isothermal cycling and out-of-phase cycling was more detrimental than in-phase cycling.

3. Stress-based fatigue curves for thermal-mechanical cycling were comparable to those of isothermal studies. Therefore, it was hypothesized that the added cyclic hardening caused the reduction in fatigue life on a strain basis.

4. On the basis of $\Delta\sigma/2$ at $N_f/2$ versus N_f , little difference was observed between data for in-phase and out-of-phase cycling, and a lower bound on the thermal-mechanical results could be calculated from the isothermal results using an empirically developed effective temperature concept. This method of calculation may be useful in design applications.

5. On the basis of $\sigma_{\max}\Delta\epsilon_t/2$ at $N_f/2$ versus N_f , the thermal-mechanical fatigue life for 93 to 316°C (200 to 600°F) and 93 to 427°C (200 to 800°F) cycles correlated well with the isothermal fatigue life at the peak temperature. However, no such correlation was obtained for the 93 to 538°C (200 to 1000°F) cycle.

6. A knowledge of both cyclic stress and strain was required to obtain an adequate correlation between thermal-mechanical and isothermal fatigue life.

Acknowledgments

The work described in this report was sponsored by the American Gas Association, Inc. (Project No. HA-3-1), and was performed at Battelle-Columbus, Columbus, Ohio. Thanks are extended to Dr. Ab Flowers of the American Gas Association, Inc., for his guidance of the program and to R. W. Newell, G. C. Groff, and O. C. Davis of the advisory committee for their technical assistance.

Appreciation is also extended to the following Battelle-Columbus staff members for their assistance in conducting the experimental work: N. D. Frey, J. J. Parks, and H. J. Malik. T. L. Porfilio, formerly of Battelle-Columbus and presently with Dialight, Brooklyn, New York, assisted in technical conduct and planning of this program. Dr. L. E. Hulbert and H. Mindlin of Battelle-Columbus provided direct technical supervision of the studies.

References

- [1] Jaske, C. E. and Porfilio, T. L., "Thermal-Mechanical, Low-Cycle Fatigue of AISI 1010 Steel," Report to American Gas Association, Inc., Catalog No. H54375, Battelle's Columbus Laboratories, Columbus, Ohio, 14 Feb. 1975.

- [2] Jaske, C. E. and Porfilio, T. L., "Isothermal, Low-Cycle Fatigue of AISI 1010 Steel at Temperatures Up to 1200 F," Report to American Gas Association, Inc., Catalog No. H54975, Battelle's Columbus Laboratories, Columbus, Ohio, 14 Feb. 1975.
- [3] King, R. M. and Smith, A. I. in *Thermal and High-Strain Fatigue*, Monograph and Report Series No. 32, The Metals and Metallurgy Trust, London, 1967, pp. 364-378.
- [4] Carden, A. E. in *Manual on Low-Cycle Fatigue Testing, ASTM STP 465*, American Society for Testing and Materials, 1970, pp. 163-188.
- [5] Manson, S. S., *Thermal Stress and Low-Cycle Fatigue*, McGraw-Hill, New York, 1966.
- [6] "Thermal Fatigue of Metals in Naval Power Machinery," Wash 1178, "Sudostroyeniye" Press, Leningrad, 1967, given to the 1970 U.S. Nuclear Power Reactor Delegation.
- [7] "Thermal and High-Strain Fatigue," Monograph and Report Series No. 32, The Metals and Metallurgy Trust, London, 1967.
- [8] *Fatigue at High Temperature, ASTM STP 459*, American Society for Testing and Materials, 1969.
- [9] International Conference on Thermal Stresses and Thermal Fatigue, Berkeley, England, 1969.
- [10] *Fatigue at Elevated Temperatures, ASTM STP 520*, American Society for Testing and Materials, 1973.
- [11] "International Conference on Creep and Fatigue in Elevated Temperature Applications," American Society for Testing and Materials, American Society of Mechanical Engineers, and Institution of Mechanical Engineers, Philadelphia, 23-27 Sept. 1973.
- [12] Carden, A. E., "Bibliography of the Literature on Thermal Fatigue," N68-23652 (NASA CR-94605), University of Alabama, Huntsville, 1967.
- [13] Wundt, B. M., *Low-Cycle Fatigue Bibliographic Survey, ASTM STP 449*, American Society for Testing and Materials, 1968.
- [14] Kawamoto, M., Tanaka, T., and Nakajima, H., *Journal of Materials*, Vol. 1, No. 4, 1966, pp. 719-757.
- [15] Udoguchi, T. and Wada, T., "Thermal Effect on Low-Cycle Fatigue Strength of Steels," International Conference on Thermal Stresses and Thermal Fatigue, Paper No. 18, Berkeley, England, 1969.
- [16] Lyle, J. M., "Forced Air Furnace Exchangers; Some Design and Reliability Evaluation Considerations," Gas Appliance Engineers Society Meeting, June 1971.
- [17] Taira, S. and Inoue, T., "Thermal Fatigue Under Multiaxial-Thermal Stresses," International Conference on Thermal Stress and Thermal Fatigue, Paper No. 3, Berkeley, England, 1969.
- [18] Taira, S. in *Fatigue at Elevated Temperatures, ASTM STP 520*, American Society for Testing and Materials, 1973, pp. 80-101.
- [19] Taira, S., Fujino, M., and Takashi, M., *Journal of Society of Materials Science, Japan*, Vol. 22, 1973, pp. 235-241.
- [20] Jaske, C. E., Perrin, J. S., and Mindlin, H., *Reactor Technology*, Vol. 15, No. 3, Fall 1972, pp. 185-207.
- [21] Jaske, C. E., Mindlin, H., and Perrin, J. S., "Low-Cycle-Fatigue Evaluation of Reactor Materials," in USAEC Report No. BMI-1928, Battelle's Columbus Laboratories, Columbus, Ohio, July 1972.
- [22] Slot, T., Stentz, R. H., and Berling, J. T. in *Manual on Low-Cycle Fatigue Testing, ASTM STP 465*, American Society for Testing and Materials, 1969, pp. 100-128.
- [23] Morrow, JoDean, in *Internal Friction, Damping, and Cyclic Plasticity, ASTM STP 378*, American Society for Testing and Materials, 1965, pp. 45-87.
- [24] Coffin, L. F., Jr., "A Generalized Equation for Predicting High-Temperature Low-Cycle Fatigue, Including Hold Times," Air Force Conference on Fatigue and Fracture of Aircraft Structures and Materials, Miami Beach, Florida, 1969, (Also General Electric Research and Development Center Report 69-C-401, 1969.)
- [25] Hirschberg, M. H. in *Manual on Low-Cycle-Fatigue Testing, ASTM STP 465*, American Society for Testing and Materials, 1969, pp. 67-86.
- [26] Manson, S. S., Halford, G. R., and Hirschberg, M. H. in *Design for Elevated Temperature Environment*, The American Society of Mechanical Engineers, 1971, pp. 12-28.
- [27] Smith, K. N., Watson, P., and Topper, T. H., *Journal of Materials*, Vol. 5, No. 4, Dec. 1970, pp. 767-778.

A. E. Gemma,¹ B. S. Langer,¹ and G. R. Leverant¹

Thermomechanical Fatigue Crack Propagation in an Anisotropic (Directionally Solidified) Nickel-Base Superalloy

REFERENCE: Gemma, A. E., Langer, B. S., and Leverant, G. R., "Thermomechanical Fatigue Crack Propagation in an Anisotropic (Directionally Solidified) Nickel-Base Superalloy," *Thermal Fatigue of Materials and Components, ASTM STP 612*, D. A. Spera and D. F. Mowbray, Eds., American Society for Testing and Materials, 1976, pp. 199-213.

ABSTRACT: Strain-controlled thermomechanical fatigue tests were performed on two nickel-base superalloys, directionally solidified (DS) Mar-M200 plus hafnium and conventionally cast B-1900 plus hafnium. The DS alloy was tested at various angles (θ) to the direction of grain growth. It was found that crack growth rates were a minimum for the DS alloy tested parallel to the direction of grain growth (crack propagating normal to the direction of grain growth). The crack growth rate increased for other orientations in the sequence $\theta = 15, 30$ or 90 , and 45 deg until equivalence was reached with rates for the conventionally cast alloy, B-1900 plus hafnium. A linear elastic fracture mechanics approach was extended to strain-controlled crack growth as a function of θ for the DS alloy. Prediction of crack growth rates as a function of θ was achieved by normalizing with the elastic modulus. The sequencing of crack growth rates with θ and a smooth-to-rough fracture surface transition are explained on the basis of the orientation dependence of crack opening displacement for a given strain intensity range.

KEY WORDS: thermal fatigue, fatigue tests, nickel alloys, crack propagation

Linear elastic fracture mechanics was extended to fatigue when Paris [I]² showed that the range of the stress intensity could be used to correlate crack propagation data. Since the stress intensity factor is only a function of the applied load, crack, and structure geometry, (that is, it is independent of material properties), the crack data can be used to predict the fatigue behavior of any structure that is subject to the same cyclic environ-

¹ Senior assistant project engineer, senior materials engineer, and group leader, respectively, Pratt & Whitney Aircraft, Middletown, Conn. 06457 and East Hartford, Conn.

² The italic numbers in brackets refer to the list of references appended to this paper.

mental conditions under which the crack growth data has been obtained. The empirical parameters, that is, the pre-exponential term and the exponent of the Paris-type crack growth relationship, encompass the material and environmental information. Some investigators [2-4] have studied the influence of various mechanical properties on fatigue crack propagation; however, Pearson [5] was among the first to recognize the strong influence of Young's modulus on the fatigue crack growth rate. Richards [6] found a correlation between grain orientation and room-temperature fatigue crack growth rate in silicon iron, and he attributed the effects to the variation in the ultimate tensile strength and Young's modulus. Woodford and Mowbray [7] conducted thermal fatigue tests using tapered disks in a fluidized bed. They found that the crack growth rate correlated with grain orientation for directionally solidified IN 738. The variation in crack growth rate was attributed to carbide alignment and dendrite orientation.

Rau, Gemma, and Leverant [8] have shown that, for strain-controlled thermal-mechanical fatigue cycling of high strength turbine alloys, crack growth may be analyzed on the basis of a linear elastic fracture mechanics approach.³ This paper will extend this approach to a directionally solidified nickel-base superalloy tested at various angles to the grain growth direction. It will be shown that the orientation dependence of the modulus of elasticity can be used to normalize the power-type crack propagation relationship. Thus, the dependence of crack growth behavior of an anisotropic alloy on the angle between the grain growth direction and the tensile axis, θ , can be predicted from a single test of longitudinal ($\theta = 0$ deg) material.

Alloy Characterization and Experimental Procedure

The materials investigated were Mar-M200 plus hafnium (PWA 1422) and B-1900 plus hafnium (PWA 1455) which are directionally solidified (DS) and conventionally cast nickel-base superalloys, respectively. The alloys are composed of a γ solid solution matrix precipitation hardened by ordered γ' particles and contain both bulk and grain boundary carbides. The microstructures and chemistries for both alloys are shown in Fig. 1. The Mar-M200 plus hafnium specimens were fabricated from 1 by 4 by 6 in. (2.5 by 10.2 by 15.2 cm) slabs, except the longitudinal (0 deg) specimens which were machined from 1.250 by 5.5 in. (3.2 by 14.0 cm) bars. This alloy was heat treated at 2200°F (1204°C) for 2 h, 1975°F (1079°C) for 4 h,

³ The data in Ref 8 and much of the data in the present study are plotted as a function of the strain intensity range [$\Delta K_e = \Delta \epsilon \sqrt{\pi a f}$ (geometry)] rather than the usual stress intensity range. This is done primarily for convenience since thermal fatigue is a strain-controlled property, and lifetime prediction of components is more easily accomplished when dealing in terms of strain distributions. (As shown later in Fig. 6, the stress intensity factor is still considered to be the prime driving force for crack propagation.)

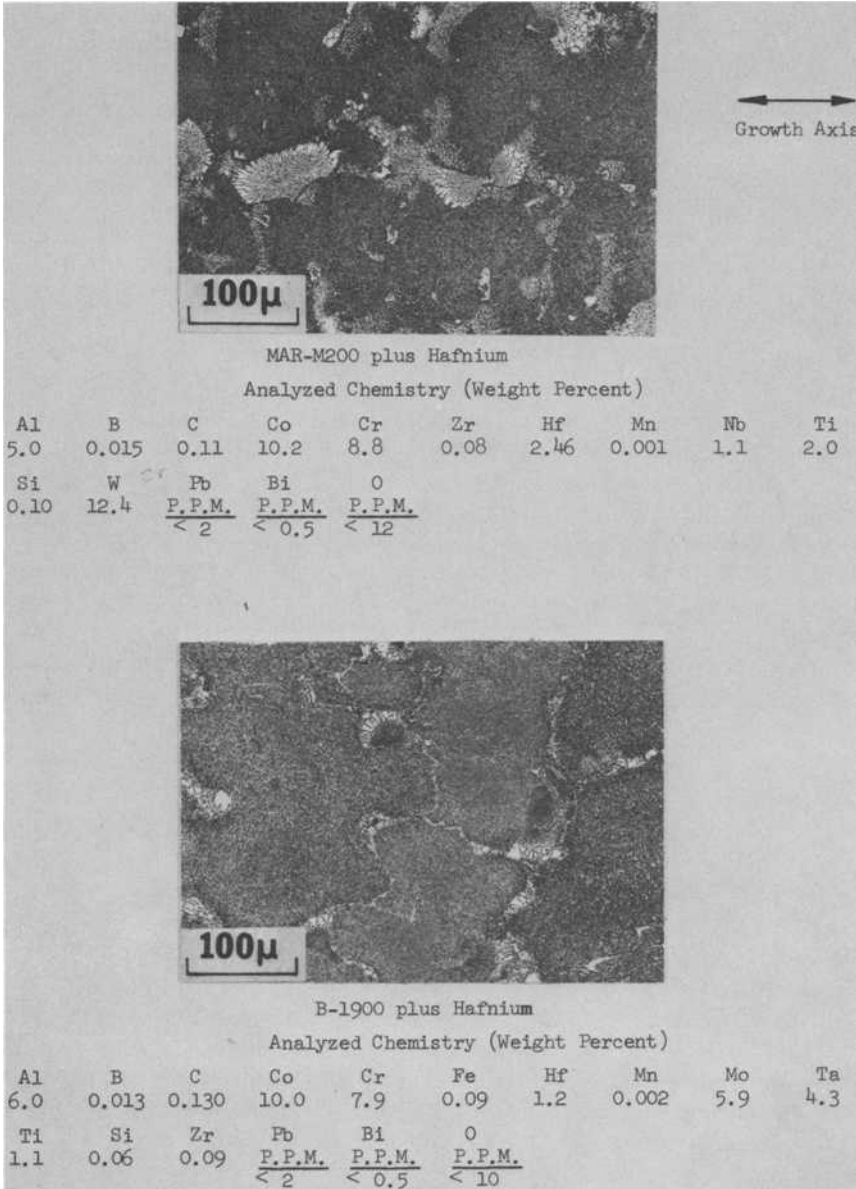


FIG. 1—Microstructure and chemistry.

and 1600°F (871°C) for 32 h prior to machining. The B-1900 plus hafnium specimens were machined from hollow bars and were heat treated at 1975°F (1079°C) for 4 h and 1650°F (899°C) for 10 h. The Mar-M200 plus hafnium grain size ranged from approximately 0.040 to 0.150 in. (1

to 3.8 mm) and the B-1900 plus hafnium grain size was equal to or less than 0.032 in. (0.8 mm) with preferred growth in the radial direction.

Thermal-mechanical fatigue tests were performed in strain control on tubular specimens (Fig. 2a) with a 1 in. (2.54 cm) uniform section gage length in closed loop testing machines. Axial strain was measured with a calibrated linear variable differential transformer (LVDT) and its associated extensometry (coaxial quartz tubes) which rested on ridges machined on the inside diameter of the specimen gage section, as shown in the cut-away view in Fig. 2b. Temperature was controlled and measured with the

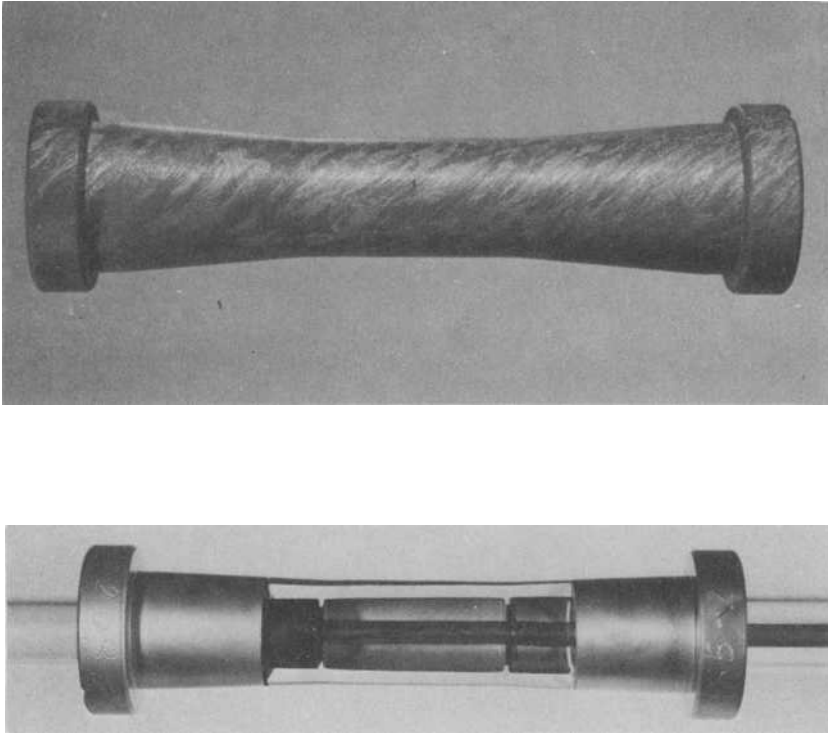


FIG. 2—Strain control fatigue specimen: (a) macroetched Mar-M200 plus hafnium. The angle between the grain growth direction and the tensile axis, θ , is 45 deg and (b) cutaway view of specimen with quartz extensometer in place.

aid of a calibrated infrared temperature comparator, and both the strain and temperature signals were independently controlled by the closed loop servohydraulic systems. To produce the desired strain-temperature histo-

ries, the temperature excursions were obtained by induction heating and forced convective cooling of the outside specimen surface. Total cycle time was $2\frac{1}{4}$ min (0.445 cpm, 0.0074 Hz) with a symmetrical cycle shape maintained for the heating and cooling portions of the cycle.

The fatigue cracks were started from electrical discharge machined slots (0.45/0.030 by 0.007/0.005 in.) (1.14/0.76 by 0.178/0.127 mm) in the center of the gage section. The specimen wall thickness was 0.055 to 0.060 in. (1.40 to 1.52 mm) except for the longitudinal or 0-deg oriented DS Mar-M200 plus hafnium specimens where the wall was 0.040 in. (1.02 mm) thick. Crack extension was monitored with a calibrated micrometer mounted telescope unit. A curve was then fitted to the plot of crack length versus number of cycles. The half-crack extension rate (da/dN) versus strain intensity range (ΔK_e) was calculated by the various methods to be discussed and plotted. All the strain intensity factors were calculated with the aid of a curvature correction [9] and a geometrical correction of true projected length to mean arc length. For all testing, the maximum tensile strain was applied at the minimum cycle temperature (427°C, 800°F) and the maximum compressive strain at the maximum cycle temperature (1038°C, 1900°F), Fig. 3a. The crack growth rates were determined for the conventionally cast B-1900 plus hafnium and for DS Mar-M200 plus hafnium having the grain growth direction oriented 0, 15, 30, 45, and 90 deg from the loading axis. A schematic of the loading and grain growth axis is shown in Fig. 3b.

The cyclic strain ranges employed were less than 50 percent of the yield strain (Table 1), and the appropriate calculations indicate that modification to the measured crack length by the crack tip plastic zone size was negligible.

Experimental Results

Dependence of the Crack Growth Rate of Directionally Solidified Mar-M200 Plus Hafnium on the Angle Between the Grain Growth Direction and Tensile Axis

The Mar-M200 plus hafnium thermal-mechanical fatigue crack propagation rate was a function of the angle between the tensile axis and the grain growth direction. The slowest crack growth rate was obtained for the longitudinal material ($\theta = 0$ deg) and the most rapid crack growth rate for 45-deg off-axis tests. The 15-deg off-axis crack growth rates were 25 to 80 percent faster than the average 0-deg growth rates. The 30 and 90-deg off-axis crack growth rates fell within the same scatterband and were faster than the 15-deg off-axis test. The crack growth rates for the 45-deg orientation were similar to those obtained for conventionally cast B-1900 plus hafnium under identical test conditions (Fig. 4) and were

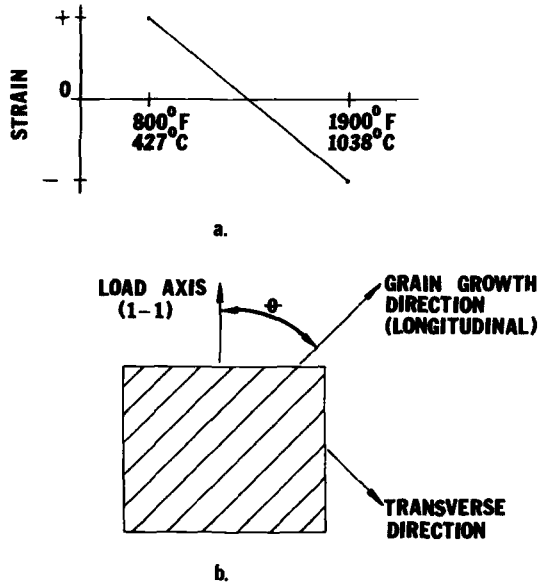


FIG. 3—(a) Schematic of thermal-mechanical fatigue cycle and (b) schematic of loading and grain growth axes.

TABLE 1—Elastic modulus, yield strain, and yield stress of DS Mar-M200 plus hafnium and conventionally cast B-1900 plus hafnium.

Temperature, °F	DS Mar-M200 plus Hf Orientation (θ), deg					B-1900 plus Hf Conventionally Cast
	0	15	30	45	90	
Elastic Modulus (psi $\times 10^6$)						
800	17	20	26	34	20	25.4
1500	14	17	23	30	17	22.2
1700	12	15	20	26	16	20.8
1900	11.5	13	18	23	12.5	19.4
Yield Strain, ^a %						
800	0.97	0.82	0.68	0.60	0.78	0.58
1500	1.02	1.02	0.81	0.65	0.81	0.59
1700	0.85	0.85	0.69	0.52	0.68	0.48
1900	0.66	0.52	0.47	0.41	0.57	0.38
Yield Stress, ksi						
800	130	121	123	133	116	118
1500	115	132	131	136	103	107
1700	85	94	92	84	76	74
1900	58	43	46	43	48	42

^aStrain required to attain the 0.2 percent yield stress.

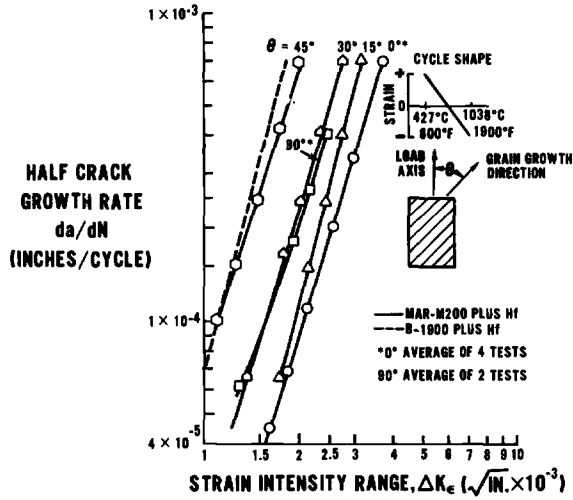


FIG. 4—Dependence of the fatigue crack propagation rate on the angle between the tensile axis and the grain growth direction.

about a factor of eight faster than those for the longitudinal material ($\theta = 0$ deg). Conventionally cast Mar-M200 plus hafnium was not tested in this investigation but would be expected to show crack growth rates similar to conventionally cast B-1900 plus hafnium.

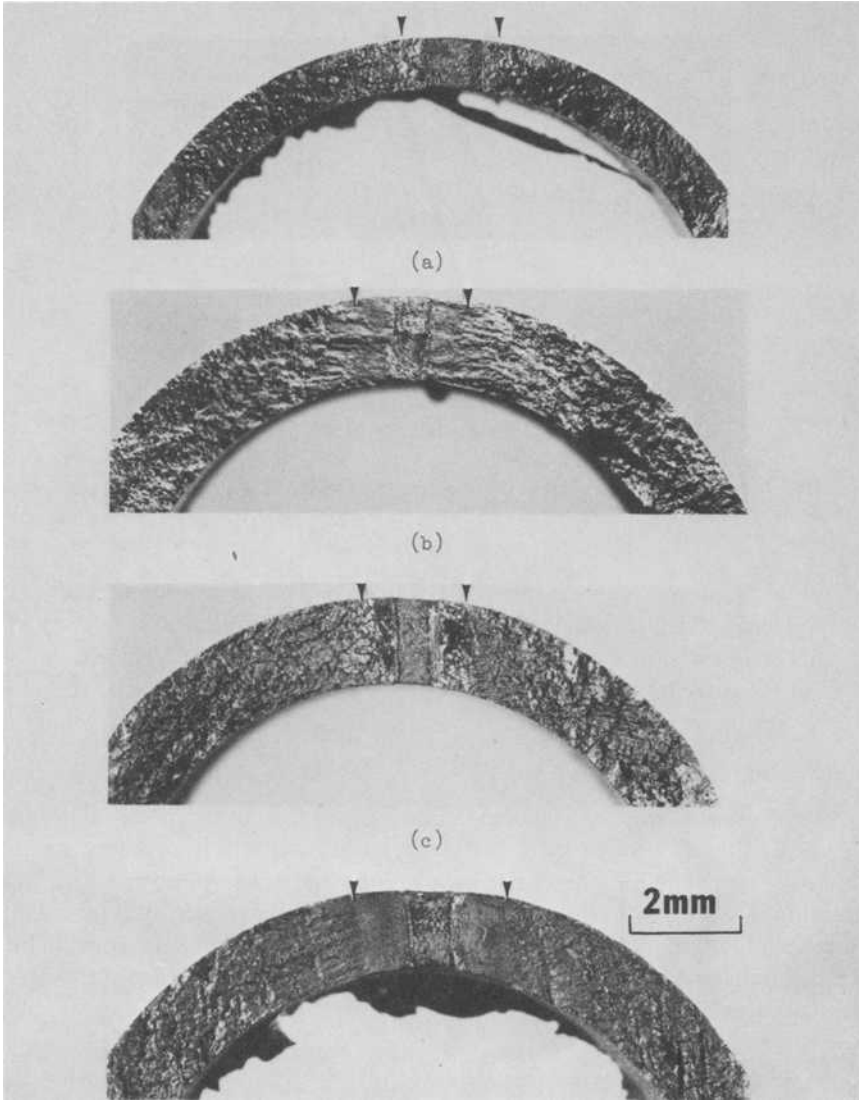
Fractography

Crack growth was transgranular and perpendicular to the tensile axis (Stage 2) for all DS Mar-M200 plus hafnium orientations. At low strain intensity ranges (ΔK_{ϵ}), the crack propagation path was smooth. With increasing ΔK_{ϵ} , Fig. 5, the amount of interdendritic cracking increased, resulting in a much rougher fracture surface for all orientations. The strain intensity range for the smooth to rough fracture surface transition decreased in the following order: $\theta = 0, 15, 30$ or 90 , and 45 deg, Table 2.

Discussion

Background

The stress intensity factor of a crack oriented at an arbitrary angle to the principal material directions of an orthotropic plate is not meaningful within the now classical Irwin approach to fracture mechanics. Wu [10, 11] has shown that the stress intensity factor for a crack in an ortho-



- (a) 0 deg off-axis (longitudinal).
- (b) 30 deg off-axis.
- (c) 45 deg off-axis.
- (d) 90 deg off-axis (transverse).

Arrowheads show the location of the smooth to rough transition.

FIG. 5—Fracture surfaces for various angles between the loading axis and the grain growth direction.

TABLE 2—Values of various fracture mechanics parameters at the transition from a smooth to a rough fracture surface in DS Mar-M200 plus hafnium.

	θ (Angle Between Loading Axis and Growth Direction), deg				
	0	15	30	45	90
Strain intensity range $\Delta K_e, \sqrt{\text{in.}} \times 10^{-3}$	1.76	1.75	1.31	1.23	1.26
	<u>1.96</u>				<u>1.34</u>
	avg 1.86				1.30
Estimated crack opening displacement COD, in. $\times 10^{-5}$	6.0	8.8	6.0	6.0	7.2
	<u>7.6</u>				<u>6.9</u>
	avg 6.8				7.0

tropic plate is reducible to the Irwin approach, that is, uncoupled modes, only if the crack is oriented along one of the principal material directions, and Bowie and Freese [12] allude to the difficulties which arise when lines of elastic symmetry do not coincide with the coordinate axes. Most published analyses are specialized to avoid these difficulties and so fall within the Irwin scheme of fracture mechanics [10–14]. Gandhi's analysis [15] of an arbitrarily oriented crack in a finite orthotropic sheet indicates a strong dependence of the stress field of an inclined crack on material properties and the aspect ratio of the finite orthotropic plate. In addition, Cook and Rau [16] critically examined the concepts of linear elastic fracture mechanics and concluded that orientation and plasticity effects were of significance in fatigue crack extension.

In light of these difficulties, a heuristic approach was taken to estimate the crack propagation behavior of a directionally solidified nickel-base superalloy. The objective of the analysis was to retain the linear elastic isotropic definition of the stress intensity factor by introducing the effects of grain orientation in the Paris-type crack propagation relationship.

Normalization of the Fatigue Crack Propagation Data

As shown in Fig. 4, crack growth rates increased in the following sequence: $\theta = 0, 15, 30$ or 90 and 45 deg. If the driving force for crack propagation is calculated in terms of effective stress intensity⁴ (obtained from the load history during strain cycling) rather than strain intensity,

⁴The effective stress intensity range $(\Delta K_o)_{\text{eff}}$ is derived from the load history of a strain-controlled test and is calculated in exactly the same manner as the standard stress intensity range for load-controlled cycling. It is not strictly equivalent to the stress intensity range calculated from a load-controlled test because of the presence of complex time-dependent plasticity at the crack tip during cycling at elevated temperature. As a result, $(\Delta K_o)_{\text{eff}}$ would not be material independent or independent of orientation for an anisotropic material as required by the linear elastic fracture mechanics definition of stress intensity range.

the data are significantly condensed, as shown in Fig. 6, suggesting that the elastic modulus might be utilized for predictive purposes. For example, it would be desirable to predict all off-axis crack growth behavior from

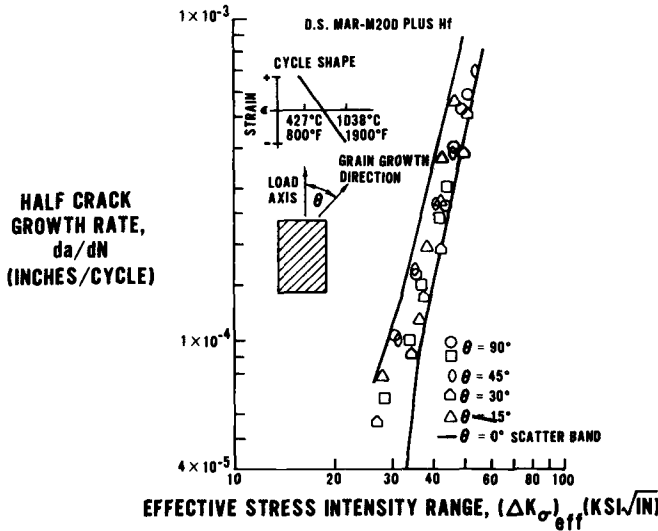


FIG. 6—Convergence of the crack growth rates when plotted as a function of effective stress intensity range.

one test of a specific orientation. The data in Table 1 indicate that there is some relationship between the anisotropic elastic modulus and crack growth rate. This approach is developed as follows.

A plate of directionally solidified alloy may be considered to be approximately transversely isotropic if the transverse columnar grain orientation ($\langle 100 \rangle$ to $\langle 110 \rangle$ in the case of directionally solidified nickel-base superalloys) is random. Thus, any lamina of the plate when loaded uniaxially in the 1-1 direction, is orthotropic. The ratio of the longitudinal modulus, E_L , to the modulus of the load axis, E_1 is [17]

$$\lambda^{-1} = \frac{E_L}{E_1} = \cos^4\theta + \frac{E_L}{E_T} \sin^4\theta + \left(\frac{E_L}{G_{LT}} - 2\nu_{LT} \right) \cos^2\theta \sin^2\theta$$

where

- θ = angle between the load and grain growth axes,
- E_T = transverse modulus ($\theta = 90$ deg),
- G_{LT} = shear modulus, and
- ν_{LT} = Poisson ratio.

A schematic diagram of the loading and grain growth axes is shown in Fig. 3b.

The crack growth law is then normalized with respect to the grain growth direction and has the form $da/dN = A [\lambda (\Delta K_c)]^n$ where A and n are constants that are determined from tests for which the loading and grain growth direction are coincident, that is, $\theta = 0$ deg and $\lambda = 1$. The material constants, E and ν , used in the calculation were obtained at 800°F (427°C) because, at this temperature, the specimen experiences the maximum tensile strain. (Similar results can be obtained using other temperatures as well.) The results are shown in Fig. 7. A very good correlation of the data is achieved with this approach.

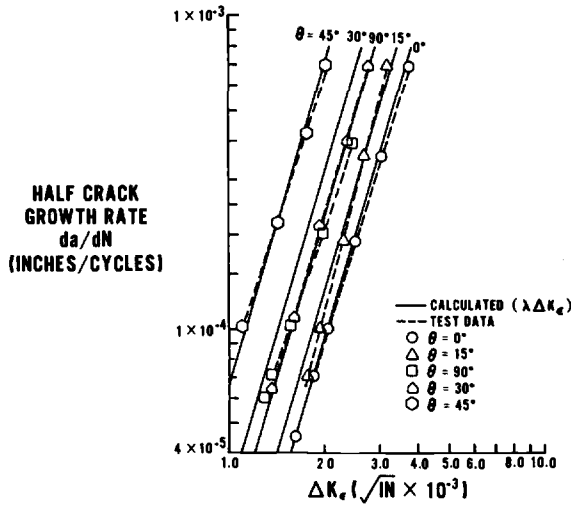


FIG. 7—Predictability of off-axis crack growth rates in DS Mar-M200 plus hafnium by employing a modulus correction factor (λ) where

$$\lambda^{-1} = \frac{E_L}{E_I} = \cos^4\theta + \frac{E_L}{E_T} \sin^4\theta + \left(\frac{E_L}{G_{LT}} - 2\nu_{LT} \right) \cos^2\theta \sin^2\theta.$$

It is generally accepted that fatigue crack growth in a single cycle is proportional to the crack opening displacement (COD) at the crack tip [18]. This suggests that, for a given crack growth rate, COD should be independent of θ . In order to make an estimate of COD, the equation for isotropic and time-independent material's response is employed, for example

$$\text{COD} \cong \Delta K_c^2 / 4E\sigma_y$$

where

$$\begin{aligned} \Delta K_o &= \text{stress intensity range,} \\ E &= \text{Young's modulus, and} \\ \sigma_y &= \text{yield stress [18].} \end{aligned}$$

The values for the estimated COD for various θ calculated with the 800°F material constants are tabulated in Table 3 for a constant crack growth rate of 2.5×10^{-4} in./cycle. The calculated COD is reasonably constant, with the exception of the value for $\theta = 45$ deg.

TABLE 3—Crack opening displacement (COD) for a given crack growth rate.

	θ (Angle Between Loading Axis and Grain Growth Direction), deg				
	0	15	30	45	90
Estimated COD at a constant growth rate of 2.5×10^{-4} in./cycle	1.43×10^{-4}	1.73×10^{-4}	1.53×10^{-4}	0.86×10^{-4}	1.95×10^{-4}

The ability of the elastic modulus to normalize the crack growth data must be associated with the form of the equation for COD. σ_y is a weak function of θ (Table 1), and there is a direct relationship between elastic modulus and stress intensity range experienced by the crack tip. Since the loading conditions for these tests resulted in no net section yielding (the one exception being moderate shakedown in the initial portion of the 45-deg orientation), the elastic modulus and ΔK_o are directly proportional such that the ΔK_o^2 term in the COD equation dominates.

Fractography

It was reported in the results section that the transition from a smooth to a rough fracture surface occurred at decreasing ΔK_e in the order $\theta = 0, 15, 30$ and $90, 45$ deg, Table 2. Calculation of the COD at the transition using the effective stress intensity range shows that the estimated COD is essentially constant (6.0 to 8.8×10^{-5} in.) at this location, Table 2. This is consistent with the observation that COD is the controlling factor in determining the crack growth rate for various θ .

Comparison with Other Studies

It is interesting to compare the results of this investigation with those of Pearson [5], Richards [6], and Rau [19] who have examined the influence of elastic modulus on fatigue crack growth under stress-controlled con-

ditions. In these studies, fatigue crack growth rate decreased with increasing elastic modulus. An example is shown in Fig. 8 for Udimet 700 [19], a superalloy similar to Mar-M200 and B-1900. For stress-controlled

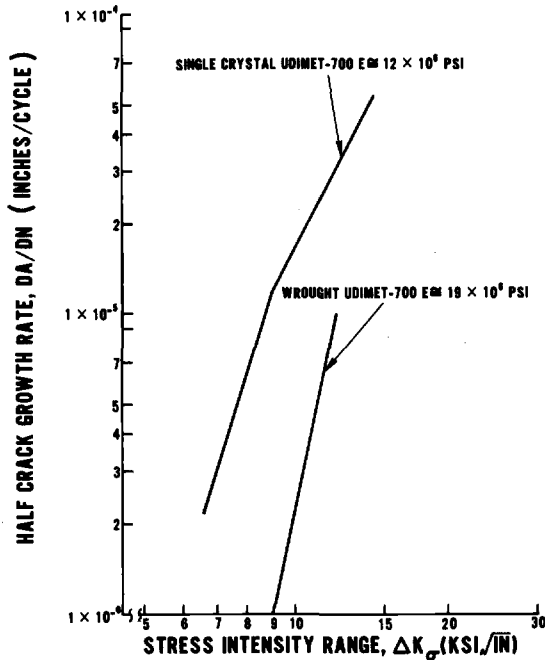


FIG. 8—Crack growth rate as a function of stress intensity range for single crystal and wrought Udimet-700 tested in pulsating tension ($R = 0.1$) at 1700°F (927°C).

cycling, the lower modulus material has a considerably higher crack growth rate compared to the higher modulus form of the same alloy. In contrast, the present work, which was performed under strain-controlled conditions, showed an increasing crack growth rate with increasing elastic modulus, Fig. 4.

This result emphasizes the basic difference between strain- and stress-controlled crack propagation testing at elevated temperatures. Although Fig. 6 would seem to imply that the crack growth rate is insensitive to grain growth direction and elastic modulus for load control tests, the $(\Delta K_{\sigma})_{\text{eff}}$ used to plot that graph is clearly not equivalent to the ΔK_{σ} calculated in a load-controlled test. The primary information to be derived from Fig. 6 is the importance of elastic modulus on crack growth rate. As pointed up previously, because of the complex, time-dependent deformation at crack tips in elevated temperature testing, one cannot deduce that the absence of net section yielding implies that $(\Delta K_{\sigma})_{\text{eff}}$ is equivalent to ΔK_{σ} .

The difference in material's response between stress- and strain-controlled cycling can be explained on the basis of COD. In stress-controlled testing, the denominator of the COD equation ($4E\sigma_y$) dominates because the numerator (ΔK_o^2) is constant. Higher E results in reduced levels of COD and reduced crack growth rates. In contrast, as already discussed, strain-controlled testing of DS Mar-M200 plus hafnium results in dominance of the ΔK_o^2 term in the numerator of the equation for COD, and this leads to an increase in COD and crack growth rate with increasing E .

Thermal fatigue crack propagation rates as a function of the angle between the crack growth path and the grain growth direction have been measured by Woodford and Mowbray [7] in fluidized bed testing of disks of DS IN 738. In contrast to the present results, they found that $\theta = 45$ deg had the most resistance to crack propagation. This orientation dependence was attributed to aligned MC carbides which significantly influenced the crack path and apparently the crack growth rate. In addition, it would be expected that the distribution of strains around the periphery of the disk would be asymmetrical because of the tendency for an anisotropic material to distort under such loading. In DS Mar-M200 plus hafnium, high-density-aligned carbides are not an important factor, and testing for each orientation was performed under uniform loading conditions.

Summary

It has been established that thermomechanical fatigue crack growth rates in a directionally solidified nickel-base superalloy are a minimum for loading parallel to the grain growth direction ($\theta = 0$ deg). Crack growth rates increase for other orientations in the sequence $\theta = 15, 30$ or 90 , and 45 deg until equivalence is reached with rates for conventionally-cast superalloys.

It was demonstrated that a linear elastic fracture mechanics approach can be extended to the prediction of strain-controlled thermomechanical fatigue crack growth in an anisotropic material of this type. Prediction of crack growth rates as a function of the angle between the loading direction and the grain growth direction can be achieved by utilizing the elastic modulus as a normalization factor. The relative crack growth rates as a function of orientation (θ) and the smooth-to-rough transition in fracture surface appearance can be explained by the orientation dependence of the COD.

References

- [1] Paris, P. C., Gomez, M. P., and Anderson, W. E., *The Trend in Engineering*, Vol. 13, Jan. 1961, p. 9.

- [2] Grosskreutz, J. C., *Physica Status Solidi* (b), Vol. 47, No. 1, 1971, pp. 11-31.
- [3] Grosskreutz, J. C., *Physica Status Solidi* (b), Vol. 47, 1971, pp. 359-396.
- [4] Hickerson, J. P., Jr., and Hertzberg, R. W., *Metallurgical Transactions*, Vol. 3, Jan. 1972, pp. 179-189.
- [5] Pearson, S., *Nature*, Vol. 211, Sept. 1966, pp. 1077.
- [6] Richards, C. E., *Acta Metallurgica*, Vol. 19, July 1971, pp. 583-596.
- [7] Woodford, D. A. and Mowbray, D. F., *Materials Science and Engineering*, Vol. 16, No. 1/2, Oct./Nov., 1974, pp. 5-43.
- [8] Rau, C. A., Jr., Gemma, A. E., and Leverant, G. R., in *Fatigue at Elevated Temperatures*, ASTM STP 520, American Society for Testing and Materials, 1973, pp. 166-178.
- [9] Erdogan, F. and Ratwani, M., *International Journal of Fracture Mechanics*, Vol. 6, No. 4, Dec. 1970, pp. 379-392.
- [10] Wu, E. M., *Journal of Applied Mechanics*, Dec. 1967, pp. 967-974.
- [11] Wu, E. M. in *Composite Materials Workshop*, S. W. Tsai, J. C. Halpin, and N. J. Pagano, Eds., Technomic Publishing Co., Stamford, Conn., 1968, pp. 20-43.
- [12] Bowie, O. L. and Freese, C. E., *International Journal of Fracture Mechanics*, Vol. 8, 1972, pp. 49-58.
- [13] Sih, G. C., Paris, P. C., and Irwin, G. R., *International Journal of Fracture Mechanics*, Vol. 1, No. 3, 1965, pp. 189-203.
- [14] Walsh, P. F., *Engineering Fracture Mechanics*, Vol. 4, 1972, pp. 553-541.
- [15] Gandhi, K. R., *Journal of Strain Analysis*, Vol. 7, No. 3, 1972, pp. 157-162.
- [16] Cook, T. S. and Rau, C. A., "A Critical Review of Anisotropic Fracture Mechanics," *Proceedings*, International Conference on Prospects of Fracture Mechanics, Delft University of Technology, Netherlands, 24-28, June 1974.
- [17] Calcote, L. R., *The Analysis of Laminated Composite Structures*, Van Nostrand Reinhold Co., New York, 1969, pp. 29-31.
- [18] Hahn, G. T., Rosenfield, and Sarrate, M., "Elastic-Plastic Fracture Mechanics," AFML-TR-67-143, Part III, Air Force Materials Laboratory, Jan. 1970.
- [19] Rau, C. A., Pratt & Whitney Aircraft, unpublished data.

K. D. Sheffler¹

Vacuum Thermal-Mechanical Fatigue Behavior of Two Iron-Base Alloys

REFERENCE: Sheffler, K. D., "Vacuum Thermal-Mechanical Fatigue Behavior of Two Iron-Base Alloys," *Thermal Fatigue of Materials and Components, ASTM STP 612*, D. A. Spera and D. F. Mowbray, Eds., American Society for Testing and Materials, 1976, pp. 214-226.

ABSTRACT: Isothermal and thermomechanical fatigue tests conducted in ultrahigh vacuum on Type 304 stainless steel and A286 alloy have shown significant effects of frequency and combined temperature-strain cycling on fatigue life. Results of isothermal tests at elevated temperatures in the creep range indicate reduced life with decreasing frequency. Combined temperature-strain cycling further reduces fatigue life with respect to isothermal lives measured at the maximum temperature of the applied thermal cycle. Life reductions observed with in-phase thermal cycling (tensile deformation at high temperature, compressive deformation at low temperature) are attributed to grain boundary ratcheting effects resulting from unreversed tensile grain boundary sliding. Results of out-of-phase tests (compressive deformation at high temperature, tensile deformation at low temperature) were confused in Type 304 stainless steel by the occurrence of geometric instabilities in the hourglass specimens. In the low ductility A286 alloy, where geometric instabilities were not observed, out-of-phase life reductions are attributed to grain boundary cavitation resulting from unreversed compressive grain boundary displacements (ratcheting) which could not be accommodated by intragranular deformation of the high-strength low-ductility matrix.

KEY WORDS: thermal fatigue, fatigue (materials), iron alloys, tests, stainless steels

Thermal fatigue is a recognized failure mode for structures such as gas turbine components which operate with combined temperature and strain cycling. Previous vacuum thermal fatigue work involving independently controlled temperature and strain cycling of two tantalum alloys^{2,3}

¹ Assistant project engineer, Materials Engineering and Research Laboratory, Pratt and Whitney Aircraft, East Hartford, Conn. 06108.

² Sheffler, K. D. and Doble, G. S. in *Fatigue at Elevated Temperatures, ASTM STP 520*, American Society for Testing and Materials, 1973, p. 491.

³ Sheffler, K. D. and Doble, G. S., "Influence of Creep Damage on the Low Cycle Thermal-Mechanical Fatigue Behavior of Two Tantalum-Base Alloys," Final Report, Contract NAS3-13228, NASA-CR-121001, National Aeronautics and Space Administration, May 1972.

showed that tensile deformation imposed at a high temperature in the creep range reversed by compressive deformation imposed at a lower temperature (defined as in-phase cycling) causes a significant fatigue life reduction as compared to isothermal cycling, consistent with concepts of strain range partitioning.⁴ This life debit was attributed to grain boundary ratcheting effects involving high-temperature grain boundary sliding in tension which is not reversed by compressive deformation imposed at lower temperatures where grain boundary sliding does not occur. The effect of out-of-phase cycling (compressive deformation at high temperature reversed by tensile deformation at low temperature) was not clearly defined in the previous study because of geometric instabilities which confused interpretation of the experimental results. The present study extends the concept of in-phase grain boundary ratcheting to two iron-base alloys (Type 304 stainless steel and A286) and provides a clearer interpretation of out-of-phase grain boundary ratcheting effects observed in the A286 alloy which does not exhibit the geometric instability.

Experimental Details

To separate the effects of temperature and environment on fatigue behavior, all tests were conducted in an ion-pumped ultrahigh vacuum chamber at pressures below 1×10^{-7} torr. Elevated temperature isothermal fatigue tests were conducted at two frequencies (0.65 and 0.0065 Hz) to evaluate the contribution of frequency induced creep effects to the fatigue process. Test temperatures for the isothermal tests were 1200°F (922 K) for the Type 304 stainless steel and 1100°F (866 K) for the A286 alloy. Tests with combined temperature and strain cycling were of two types, as illustrated in Fig. 1. The in-phase cycle involved isothermal tensile strain imposed at a high temperature reversed by isothermal compressive strain imposed at a low temperature. The out-of phase cycle was similar except that the temperature-strain phasing was reversed. The upper temperature for each material was the same as the isothermal test temperatures. The lower temperature was 600°F (589 K) for both alloys. Tests were conducted to failure (defined as a separation of the specimen into two pieces) over a range of plastic strain amplitudes which were measured by the width of hysteresis loop at zero load. Fractured specimens were sectioned longitudinally and examined metallographically to evaluate the character of the microstructural damage associated with each of the applied cycle types.

Test procedures were essentially identical to those reported for previous tests.^{2,3} The apparatus was designed to perform completely reversed push-pull fatigue tests on hourglass specimens using independently pro-

⁴ Manson, S. S. in *Fatigue at Elevated Temperatures*, ASTM STP 520, American Society for Testing and Materials, 1973, p. 744.

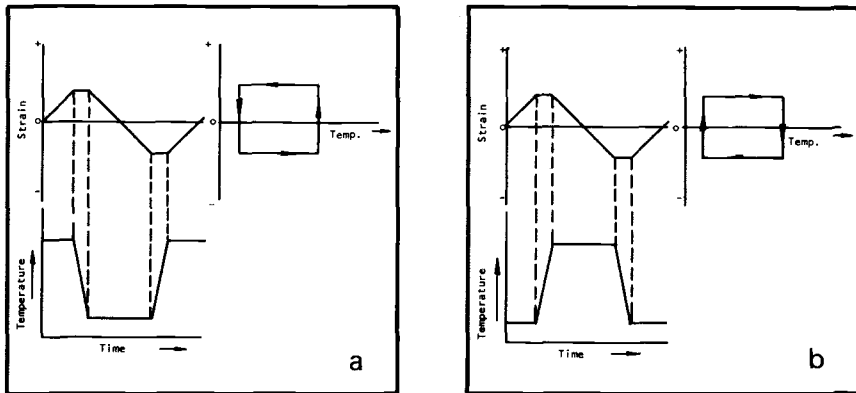


FIG. 1—Schematic representation of the two types of thermal-mechanical cycles applied in this study: (a) in-phase cycle (TCIPS) and (b) out-of-phase cycle (TCOPS).

programmable temperature and strain control. Temperature was programmed using a thyristor-controlled 50 kV a-c transformer for direct resistance heating of the specimen, while diametral strain was controlled directly using a linear variable differential transducer (LVDT) type extensometer coupled to a programmable closed loop electrohydraulic servosystem. For tests with combined temperature and strain cycling, the output of the servoamplifier was electronically compensated for thermal expansion so that net mechanical strain was controlled directly, which allowed temperature changes to be accomplished with mechanical strain held constant, as shown in Fig. 1.

Results and Discussion

Test Results

Typical hysteresis loops generated in Type 304 stainless steel are shown in Fig. 2. The isothermal loops are essentially symmetrical for both materials, with the load range developed at a constant diametral strain range being larger at the higher test frequency. Hysteresis loops observed for A286 were similar except that the inelastic strain ranges were smaller at equivalent total diametral strain ranges because of the larger loads and, consequently, larger elastic strains developed in the higher strength material. Asymmetric hysteresis loops were developed with both types of thermal fatigue cycles as a result of differences in flow stress at different temperatures. In-phase cycling generated loops having a net compressive stress, while out-of-phase cycling caused a mean tensile stress to be developed.

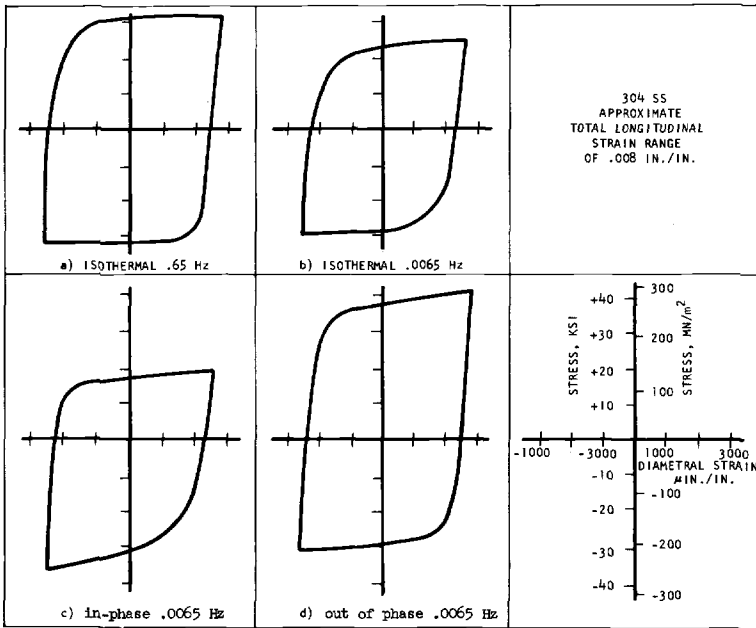


FIG. 2—Typical hysteresis loops observed for Type 304 stainless steel tested with various strain-temperature cycles.

In previous thermal cycled tests on the tantalum alloys, geometry changes occurred which involved thickening of the specimen in locations above and below the minimum diameter with isothermal and in-phase cycling and thinning of the specimen in these same locations with out-of-phase cycling (Fig. 3). Similar geometry changes were observed in Type 304 stainless steel but not in the A286 specimens tested in the current program (Fig. 4). While no definite explanation is available for the occurrence of geometric instabilities in one alloy and not the other, it may be observed that the three materials which have shown pronounced geometry changes in out-of-phase thermal cycling (two tantalum alloys and Type 304 stainless steel) are basically high ductility alloys, whereas A286 has a relatively low ductility. It is not possible to determine from the available results if this qualitative correlation represents a general trend or is merely coincidental. Additional data on a wider range of materials would be desirable to clarify this point.

The geometry changes did not appreciably influence the test results from the isothermal and in-phase tests since the change left the area of controlled maximum strain unchanged. However, the out-of-phase geometry change had a significant influence on fatigue life since this change caused failure to occur at a location separate from the original

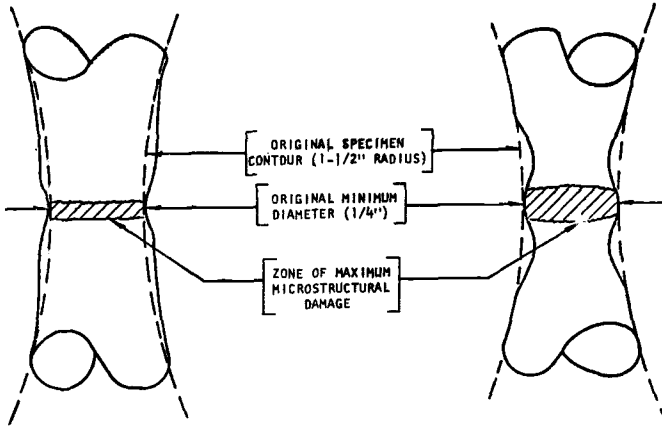


FIG. 3—Schematic illustration of specimen geometry changes produced by thermal-mechanical fatigue cycling: (a) isothermal and in-phase thermal cycling and (b) out-of-phase thermal cycling.

minimum diameter (Fig. 4d) where strain was both unknown and uncontrolled. This qualification applies only to the out-of-phase Type 304 stainless steel results since geometry changes were not observed in the A286 alloy.

Fatigue life results for both alloys are summarized in Tables 1 and 2. Type 304 stainless steel displayed cyclic strain hardening, while the A286 alloy exhibited cyclic strain softening. For both alloys, the majority of hardening or softening occurred during the first few cycles of testing. The stress ranges noted in Tables 1 and 2 represent stabilized loop sizes. For the thermal cycled tests, where asymmetric loops were observed, both tensile and compressive stress values are noted.

The longitudinal inelastic strain ranges noted in Tables 1 and 2 are plotted against life in Figs. 5 and 6. These results indicate definite effects of both frequency and thermal cycling on fatigue life. Decreasing frequency, which increases the potential for creep effects, reduces the isothermal fatigue life of both materials. Combined temperature and strain cycling causes further reductions of fatigue life in both materials as compared to isothermal cycling at the maximum temperature associated with the thermal cycle. For the A286 alloy, in-phase cycling is more damaging than out-of-phase cycling. For Type 304 stainless steel, the reverse at first appears to be true; however, the out-of-phase Type 304 results are confused by the previously noted geometry change and are therefore not considered meaningful.

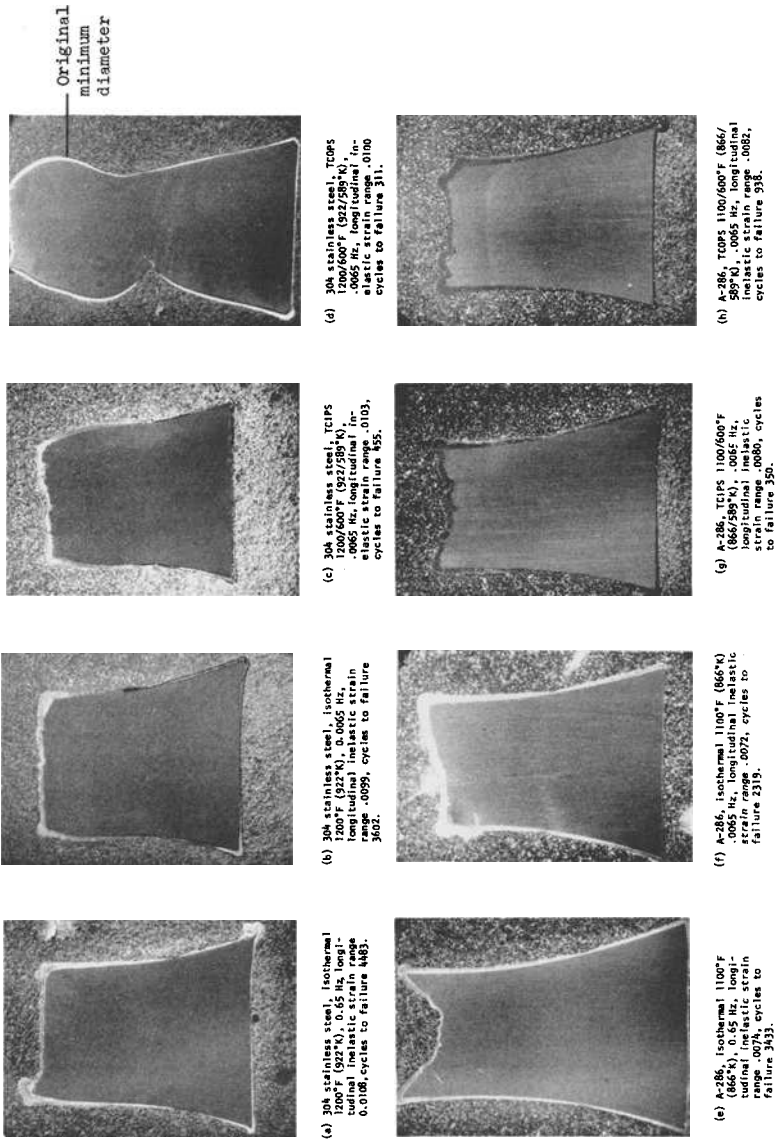


FIG. 4—Illustrating geometry of fatigue tested hourglass specimens. Materials and test conditions as indicated. Note that apparent specimen lengths are not representative of actual length changes which occurred during testing ($\times 2.52$).

TABLE 1—304 stainless steel fatigue results.

Test Number	Cycle Type ^a	Frequency, Hz	Temperature				Longitudinal Inelastic Strain Range (dimensionless)	Stress				Cycle to Failure		
			Upper		Lower			ksi		MN/m ²				
			°F	K	°F	K		Tensile	Compressive	Tensile	Compressive			
A3A	isothermal	0.65	1200	922	0.0212	83.3	...	574	1 219	
A1A	isothermal	0.65	1200	922	0.0108	63.4	...	437	4 483	
A2A	isothermal	0.65	1200	922	0.0052	53.9	...	371	19 016	
A4A	isothermal	0.0065	1200	922	0.0216	70.3	...	484	557	
A12A	isothermal	0.0065	1200	922	0.0099	55.3	...	381	3 602	
A7A	TCIPS	0.0065	1200	922	600	589	0.0220	30.5	43.3	73.8	210	298	508	226
A8A	TCIPS	0.0065	1200	922	600	589	0.0103	21.6	41.0	62.6	149	282	431	455
A5A	TCIPS	0.0065	1200	922	600	589	0.0050	23.6	39.9	63.5	163	275	438	573
A11A	TCOPS	0.0065	1200	922	600	589	0.0209	36.3	32.9	69.2	250	227	477	214
A6A	TCOPS	0.0065	1200	922	600	589	0.0100	38.3	31.3	69.6	264	216	482	311
A9A	TCOPS	0.0065	1200	922	600	589	0.0049	34.8	28.8	63.6	240	198	438	3 612

^aTCIPS = thermal cycled in-phase square wave; TCOPS = thermal cycled out-of-phase square wave.

TABLE 2—A-286 alloy fatigue results.

Test Number	Cycle Type ^a	Frequency, Hz	Temperature				Longitudinal Inelastic Strain Range (dimensionless)	Stress				Cycle to Failure	
			Upper		Lower			ksi		MN/m ²			
			°F	K	°F	K		Tensile	Compressive	Range	Range		
L-42	isothermal	0.65	1100	866	0.0170	...	261	...	1798	432	
L-41	isothermal	0.65	1100	866	0.0074	...	221	...	1523	3 433	
L-43	isothermal	0.65	1100	866	0.0033	...	200	...	1378	40 162	
L-44	isothermal	0.0065	1100	866	0.0167	...	215	...	1481	358	
L-45	isothermal	0.0065	1100	866	0.0072	...	193	...	1330	2 319	
L-50	TCIPS	0.0065	1100	866	600	589	0.0183	115	153	268	792	1054	1846
L-46	TCIPS	0.0065	1100	866	600	589	0.0080	95.6	148	244	660	1020	1680
L-47	TCIPS	0.0065	1100	866	600	589	0.0026	86.3	121	207	594	834	1428
L-51	TCOPS	0.0065	1100	866	600	589	0.0180	153	113	266	1054	779	1833
L-52	TCOPS	0.0065	1100	866	600	589	0.0082	118	111	229	813	765	1578

^a TCIPS = thermal cycled in-phase square wave; TCOPS = thermal cycled out-of-phase square wave.

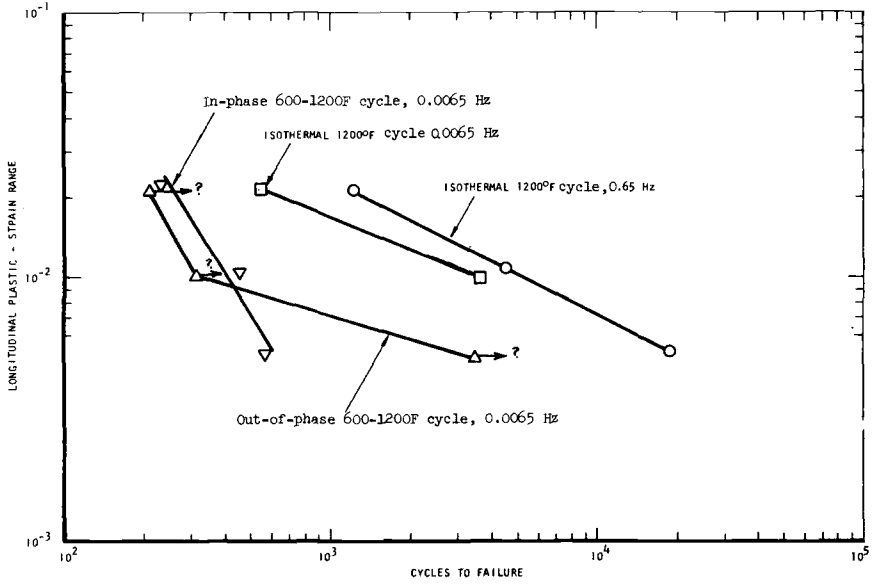


FIG. 5—304 stainless steel fatigue life results.

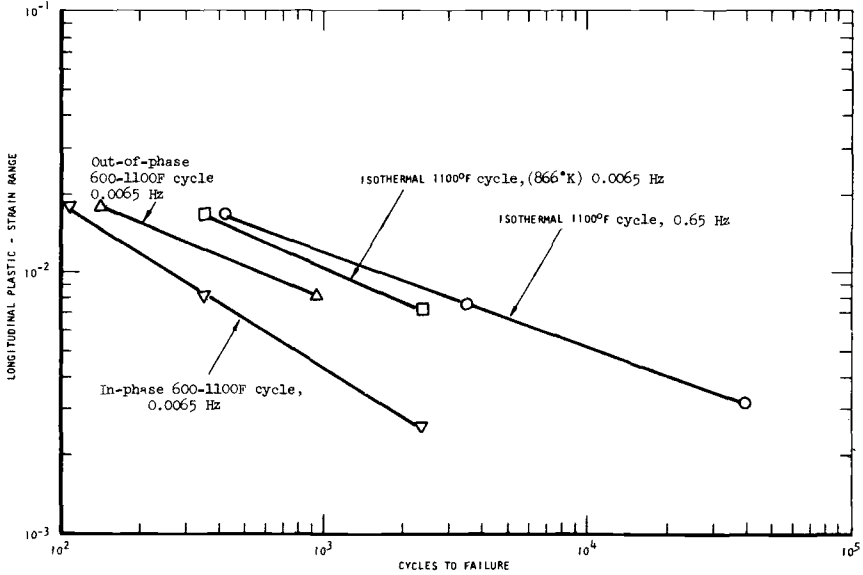
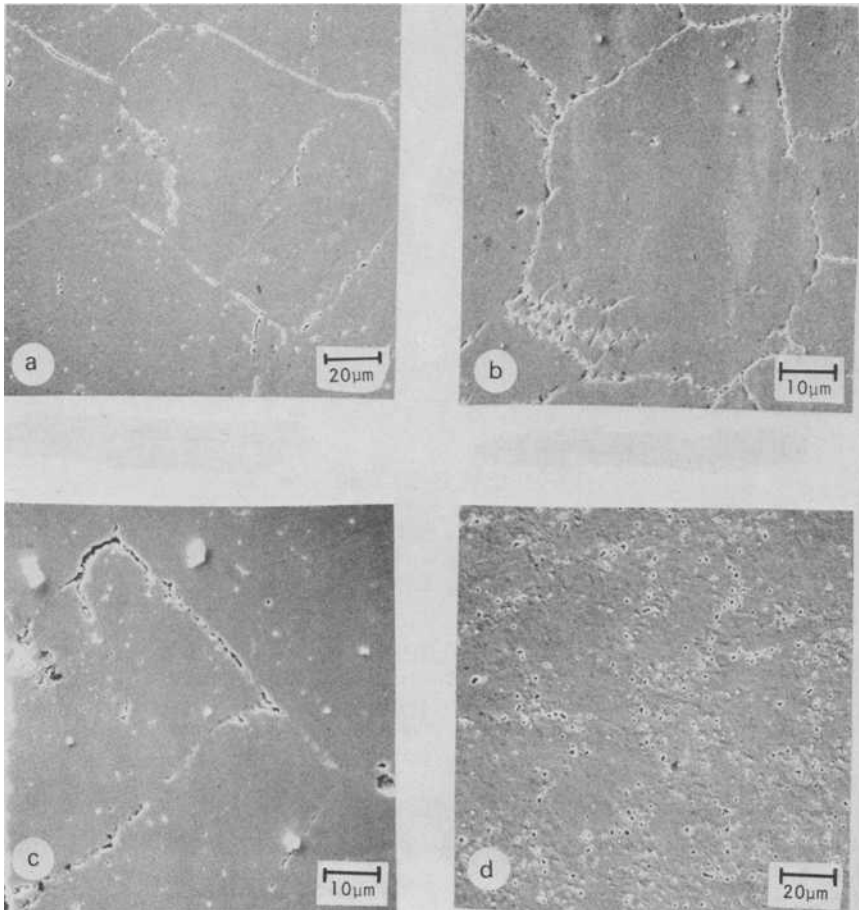


FIG. 6—A286 fatigue results.

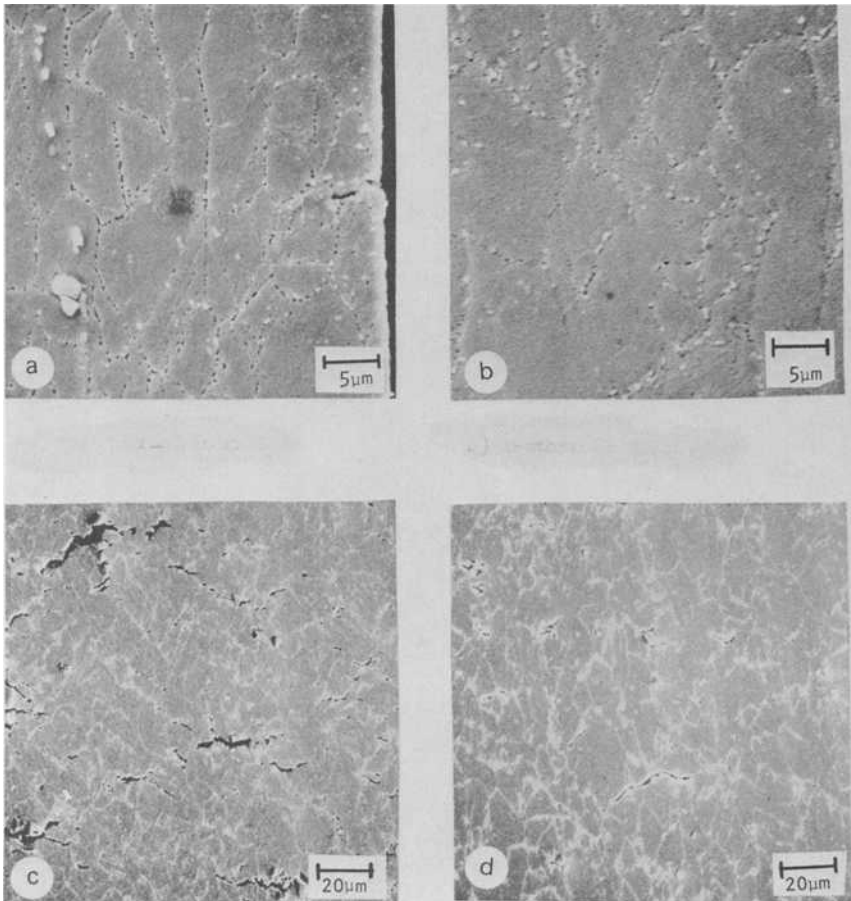
Microstructural Observations

Microstructural damage observed in the fatigue tested specimens varied with both cycle and test material, as shown in Figs. 7-9. In high frequency cycling, both alloys exhibit mixed intergranular and transgranular cracking (Fig. 9) with minimal microstructural damage localized at grain boundaries (Figs. 8*a* and 9*a*). As shown in Fig. 9*d*, some of the secondary cracks found in A286 are associated with carbide inclusions. While carbide cracking is assumed to have some influence on the cyclic life of



- (a) Isothermal 0.65 Hz.
- (b) Isothermal 0.0065 Hz.
- (c) In-phase cycle.
- (d) Out-of-phase cycle.

FIG. 7—Microstructural damage found in Type 304 stainless steel tested with various cycles. Tensile axis vertical.



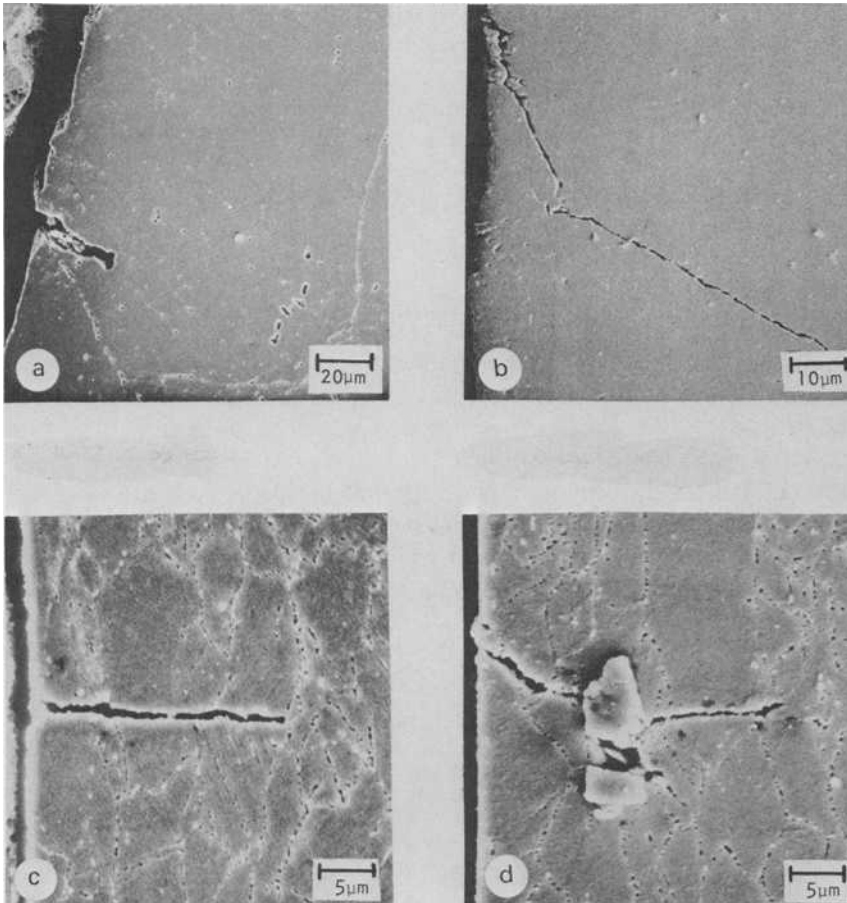
- (a) Isothermal 0.65 Hz.
- (b) Isothermal 0.0065 Hz.
- (c) In-phase cycle.
- (d) Out-of-phase cycle.

FIG. 8—Microstructural damage found in A286 tested with various cycles. Tensile axis vertical.

A286, it is not thought to influence the life differences caused by different types of cycles, since carbide associated cracking was observed in A286 with all cycle types studied.

Reduced frequency isothermal cycling causes a greater degree of localized grain boundary damage in the Type 304 stainless steel (Fig. 7b), with the fracture mode being exclusively intergranular in both alloys.

In-phase thermal cycling causes severe grain boundary cavitation in both alloys (Figs. 7c and 8c). This effect is attributed to the previously



- (a) Type 304 stainless steel, 0.65 Hz.
 (b) Type 304 stainless steel, 0.0065 Hz.
 (c) A286, 0.65 Hz.
 (d) A286, 0.65 Hz.

FIG. 9—Secondary cracks found in various fatigue specimens. Tensile axis vertical.

discussed grain boundary ratcheting mechanism, which is assumed to be responsible for the significant life reduction associated with in-phase cycling.

Significant differences were found between the types of damage developed in out-of-phase A286 and Type 304 stainless steel specimens. Damage in Type 304 alloy is characterized by extensive etch pitting concentrated near grain boundaries (Fig. 7*d*). This pitting presumably represents areas of high dislocation density associated with large localized

intragranular strains required to accommodate accumulated compressive grain boundary displacements (compressive ratcheting). In the higher strength A286 alloy, where unreversed compressive grain boundary displacements cannot be fully accommodated by intragranular deformation, significant intergranular cavitation is found (Fig. 8d). As with in-phase cycling, this cavitation is presumed to be the cause of the life reduction caused by out-of-phase cycling of A286.

Summary

Elevated-temperature, low-cycle thermal-mechanical fatigue tests conducted in vacuum on Type 304 stainless steel and A286 alloy show significant effects of frequency and of combined temperature-strain cycling on fatigue life. At temperatures in the creep range, fatigue lives of both materials are lower at 0.0065 than at 0.65 Hz. Metallographic examination of fractured specimens indicates mixed mode (intergranular and transgranular) fracture at the higher frequency and exclusively intergranular fracture at the lower frequency. In-phase thermal cycling (tension at high temperature and compression at low temperature) causes large life reductions in both materials. These life reductions are attributed to grain boundary cavitation caused by unreversed grain boundary sliding (grain boundary ratcheting). Out-of-phase thermal cycling (tension at low temperature and compression at high temperature) also causes large cyclic life reductions in both materials, but the results from Type 304 stainless steel are confused by the occurrence of geometric instabilities. In the A286 alloy, out-of-phase life reductions are attributed to cavitation damage resulting from unreversed compressive grain boundary displacements (compressive ratcheting) which cannot be fully accommodated by intragranular deformation.

Acknowledgments

Support for this work was provided by the NASA Lewis Research Center, Contract NAS-3-6010, with Dr. G. R. Halford as program manager. Assistance with the experimental effort, provided by J. W. Sweeney, is gratefully acknowledged.

L. F. Coffin¹

Instability Effects in Thermal Fatigue

REFERENCE: Coffin, L. F., "Instability Effects in Thermal Fatigue," *Thermal Fatigue of Materials and Components, ASTM STP 612*, D. A. Spera and D. F. Mowbray, Eds., American Society for Testing and Materials, 1976, pp. 227-238.

ABSTRACT: This paper considers shape changes which develop progressively in hourglass specimens subjected to fully reversed cyclic plastic strain applied in a variety of mechanical and thermal waveforms. While the strain at the minimum diameter is controlled, off-center locations subjected to cyclic plastic strain undergo ratcheting. Two major off-center shape changes have been observed: barreling and necking. The paper discusses the reasons for these changes.

KEY WORDS: thermal fatigue, strains, necking

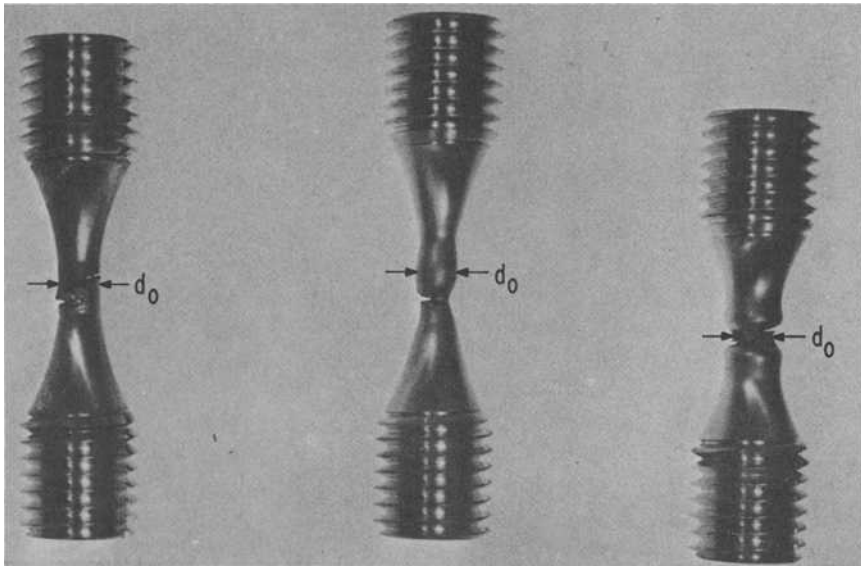
It is observed that uniaxially loaded, cyclically strained hourglass specimens change their shape during the progress of fatigue testing, particularly at high-cyclic strains [1].² At elevated temperature with mixed thermal and mechanical cycling, distinct differences in shape occur, depending on the phase relationship between the mechanical and thermal effects [2]. This paper is addressed to the question and discusses the broader implications to the thermal fatigue problem.

Earlier [1], the author investigated the phenomenon in room-temperature tests. The softer metals, notably 1100 aluminum and, to a lesser extent, OFHC copper, were particularly prone to progressive off-center barreling when the minimum diameter was cycled between prescribed limits [3]. From an analysis [1] of the stress and strain limits at both the minimum diameter and off center, it was shown that the instability came from unequal loads in tension and compression. When the minimum diameter was controlled between equal diametral strain limits of opposite size, a compressive stress bias and a progressive diameter increase developed off center at plastically deforming sections.

¹ Mechanical engineer and Coolidge Fellow, Corporate Research and Development, General Electric Co., Schenectady, N.Y. 12301.

² The italic numbers in brackets refer to the list of references appended to this paper.

Conway, Stentz, and Berling [4] have performed continuous cycling and hold time tests on hourglass specimens of zirconium-copper in argon at 538°C, also utilizing diametral strain control. Figure 1 shows the occurrence of off-center necking during a tension hold and off-center barreling during a compression hold.



R-2-28	R-2-47	R-2-50
482°C	538°C	538°C
6.1%	1.4%	1.4%
no hold time •	56 sec (tens.)	56 sec (comp.)
$N_f = 176$	$N_f = 1,152$	$N_f = 3,180$

FIG. 1—Test specimens of zirconium-copper tested in argon at 538°C. Continuous cycling and strain-hold time tests. See Ref 4.

resulting from compression hold. Here d_0 refers to the position of the diametral extensometer. Using similar specimen geometries and strain control procedures, the author has shown that AISI 304 stainless steel, tested at 650°C with unequal (sawtooth) total longitudinal strain ramp rates, developed similar shapes [5]. With a plastic strain range, $\Delta\epsilon_p$, of 0.02, a period of 10 min, and a ramp whose tension going time was 0.1 min, followed by a compression going ramp time of 9.9 min, off-center necking was found, while reversing the ramp rates produced off-center barreling.

Shape instability was found in thermal fatigue tests performed on axi-

ally constrained, uniform gage length tubular specimens subjected to alternate heating and cooling [6,7]. Those tests revealed a progressive thinning of the wall near the ends of the specimen as cycling proceeded, particularly under the extreme conditions of cyclic temperature (100 to 600°C). Carden and his associates have also studied this problem [8-10]. Sheffler [2] reported shape instabilities in hourglass geometries of AISI 304 stainless steel and A286 at elevated temperatures in high vacuum. (The temperature-mechanical strain program was as shown later in Fig. 7a (in-phase) or 7b, (out-of-phase.) Figure 2 shows the shape changes observed for AISI 304 stainless steel. A286, on the other hand, showed no shape change. Sheffler reports that prior tests [11] on two tantalum alloys showed similar instabilities.

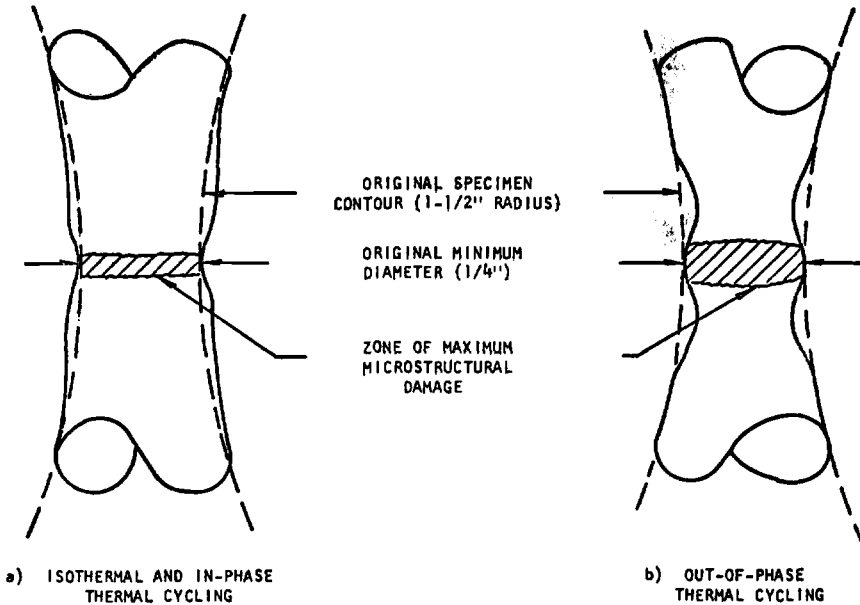


FIG. 2—Schematic of shape changes observed with in-phase and out-of-phase thermal and mechanical cycling of AISI 304 stainless steel. See Ref 2.

It is clear that, aside from being a curious observation, the phenomenon of shape instability has practical importance in the interpretation of test results. It may have other important implications, as will be discussed later.

Monotonic Strain Distribution in Hourglass Geometries

In developing the mechanism for shape instability under cyclic strain,

we consider first the strain distribution in an hourglass-shaped geometry under monotonic loading as a function of such parameters as strain hardening, strain rate, and temperature. In Fig. 3a, the axial plastic strain distributions are compared for two distinct materials at the same temperature and strain rate, but of differing strain hardening coefficients. In Fig. 3b, a given material is tested at two different strain rates, while, in Fig. 3c, the response of the material at two temperatures is considered. As a

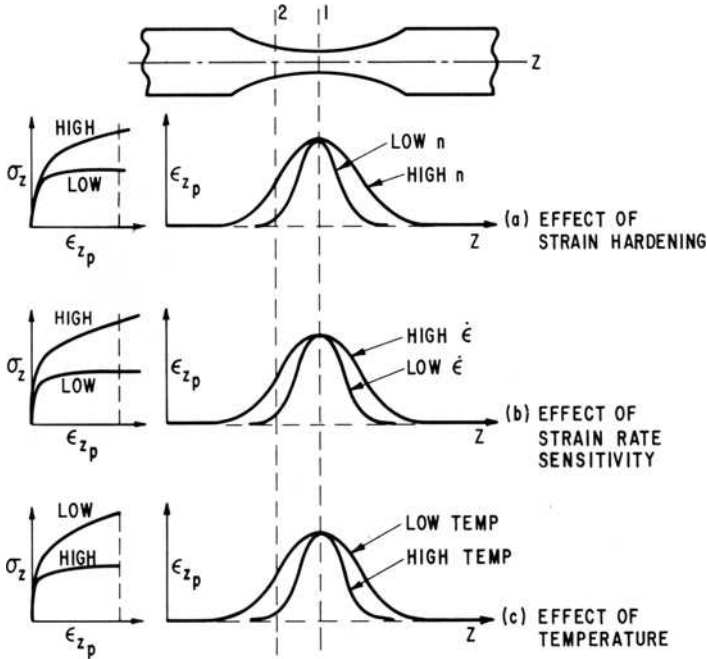


FIG. 3—Strain distributions in hourglass-shaped specimen with monotonic loading, showing effect of strain hardening, strain rate, and temperature.

result of the changes in the flow stress curves for the parameters considered here, the axial strain distribution may be diffuse or localized with application of axial stress. The localization or diffuseness can also be observed by comparing, in each case, the axial strains at Position 2 for equal strains at 1.

Off-Center Dimensional Changes

Assuming now an hourglass-shaped specimen subjected to controlled diametral strain at Position 1, Fig. 3, we now consider how dimensional changes can occur at the off-center Position 2. In doing so, we shall relate

the axial strain distributions shown in Fig. 3 to the separate legs of specific hysteresis loops. Three cases will be considered: (a) isothermal balanced cycling (Fig. 4), (b) isothermal unbalanced cycling (Figs. 5,6), and (c) thermomechanical cycling (Fig. 7c).

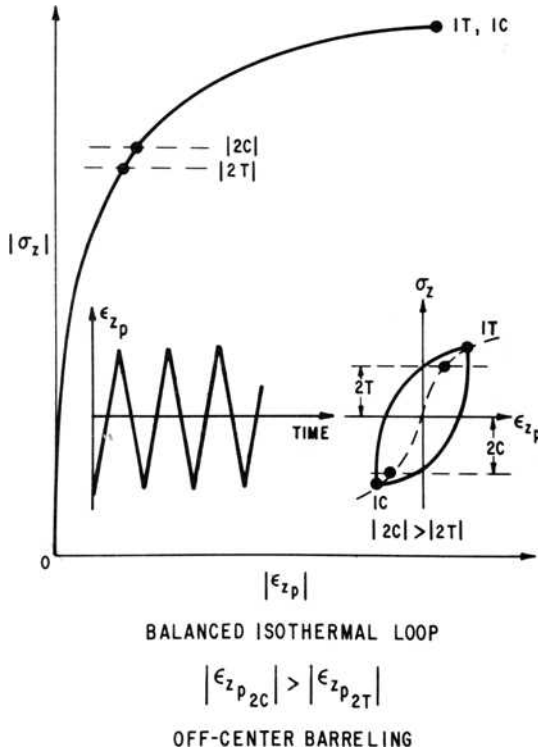


FIG. 4—Cyclic stress-strain behavior and hysteresis loop for balanced isothermal cycling showing conditions for off-center barreling.

Isothermal Balanced Cycling

Consider the stable hysteresis loops of stress versus plastic strain and the waveform illustrated in Fig. 4 for a specimen controlled at its minimum diameter Position 1. The two legs of the loop are closely similar since the temperature, the strain ramp rates, and the strain limits for each leg are of equal magnitude. We next consider the off-center Position 2. As indicated earlier, the tensile load on the specimen is less than the compressive load in order to equate the tensile and compressive true stresses at Position 1. Because the area at 2 is larger and the stress is less, the area correction for stress at 2 is small. Hence, the tensile stress at 2, $2T$, is less than the corresponding compressive stress, $2C$. Referring to the loop of

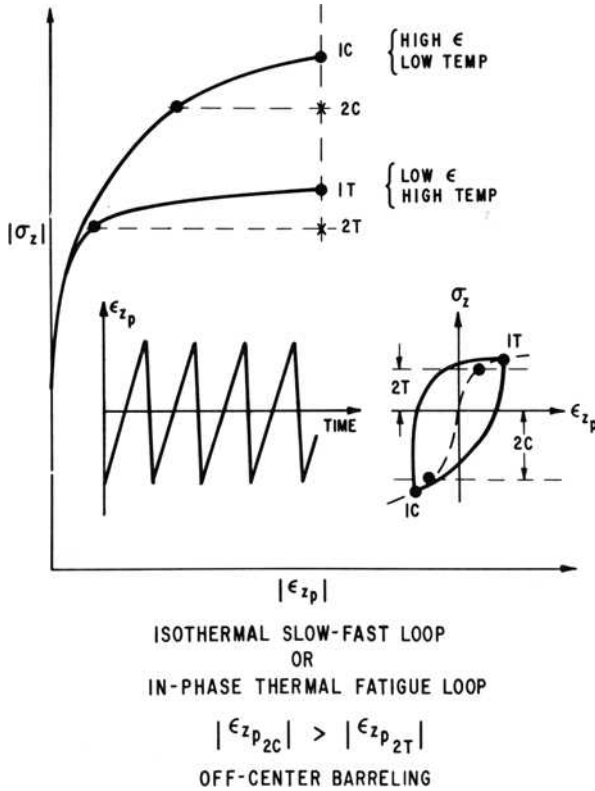
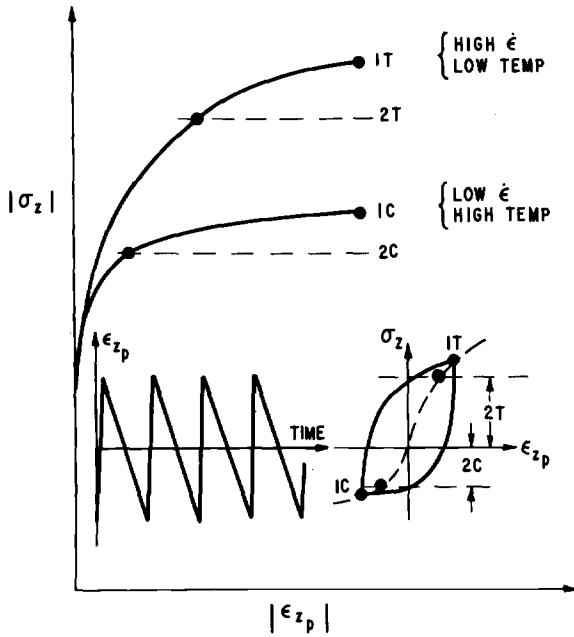


FIG. 5—Cyclic stress-strain behavior and hysteresis loop for unbalanced cycling produced by isothermal slow-fast or in-phase thermal cycling showing conditions for off-center barreling.

Fig. 4, these points are identified. Also shown in Fig. 4 is the cyclic stress-cyclic plastic strain amplitude response of the material, $|\sigma_z|$ versus $|\epsilon_{zp}|$. The Points 2T and 2C are identified. The cyclic stress-strain curve shown is the locus of stable loop End Points 1, either in tension or compression, for all strain ranges. Since the loop is balanced, the tension and compression curves are identical. Now since $|2C| > |2T|$, $|\epsilon_{zp_{2C}}| > |\epsilon_{zp_{2T}}|$. Thus, the loop for Point 2 does not close, but rather a slightly excessive axial compressive strain is produced. This increment of strain accumulates with each cycle leading to progressive off-center barreling.

The ratcheting process described is difficult to predict quantitatively. As the compressive strain accumulates at 2, the flow stress increases and the increment of plastic strain decreases because of strain hardening. Cyclic strain softening limits strain hardening, and a steady-state ratcheting rate is reached.

We can qualitatively determine the response of various materials to



ISOTHERMAL FAST-SLOW LOOPS
OR
OUT-OF-PHASE THERMAL FATIGUE LOOP

$$|\epsilon_{zp_{2T}}| > |\epsilon_{zp_{2C}}|$$

OFF-CENTER NECKING

FIG. 6—Cyclic stress-strain behavior and hysteresis loop for unbalanced cycling produced by isothermal fast-slow or out-of-phase thermal cycling showing conditions for off-center necking.

shape changes under these conditions. First, a high strain hardening coefficient is desirable in order to enhance the off-center strain range. Secondly, pronounced cyclic strain softening is necessary in order that the strain hardening effects which would otherwise limit the ratcheting strains be minimized. Because of these considerations, 1100 aluminium is particularly sensitive to shape changes [1,3].

Isothermal Unbalanced Cycling

We now consider specimen shape changes for isothermal loops of unequal ramp rates, called slow-fast (Fig. 5) or fast-slow (Fig. 6). We first note the hysteresis loop generated for the slow-fast ramp condition illustrated and observe that its unbalanced nature arises from the material's response to strain rate, Fig. 3b [5]. The cyclic stress-plastic strain ampli-

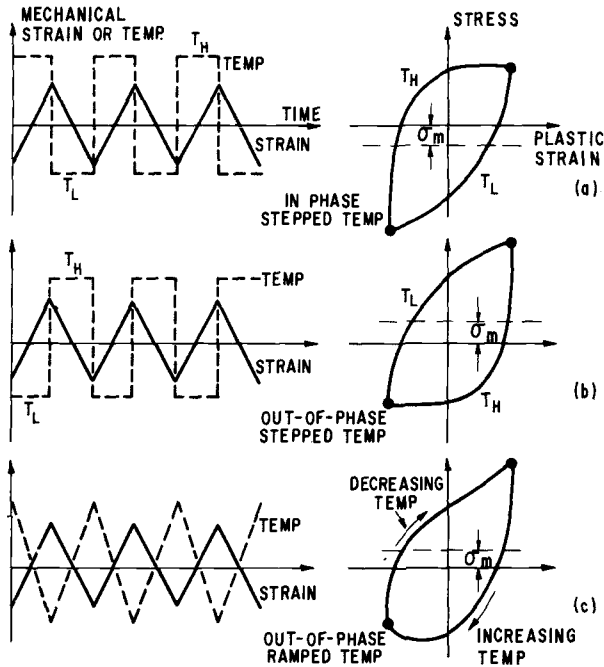


FIG. 7—Waveshapes for mixed mechanical and thermal cycling for in-phase and out-of-phase conditions.

tude curves for the tensile and compressive stress portions of the loop (locus of Points 1T and 1C) are also shown. Since the tensile portion of the cyclic stress-strain curve is controlled by the slow tension-going part of the loop, it differs distinctly from the compressive portion, as indicated. Values of stresses and plastic strain are shown for the off-center Position 2 as indicated, the stress assumed to be 90 percent of the stress at Position 1. No correction has been made for load differences at Position 1 between tension and compression nor for differences in strain rate between Positions 1 and 2. Strain rate difference effects between 1 and 2 can be avoided if the cyclic stress-plastic strain curve is obtained under conditions of constant frequency. From Fig. 5 we note that $|\epsilon_{zp2c}| > |\epsilon_{zp2t}|$; that is, for each closed cycle of strain at Position 1, there is a net compressive strain increment developing at Position 2, causing the specimen to become progressively fatter there. Simultaneously, there will be a net shortening of the specimen.

Conversely, the fast-slow loop produces just the opposite effect, Fig. 6. The unbalanced cyclic stress-strain loci for Point 1 are now reversed, the tensile curve being generated at high strain rate. The off-center stresses are located at 90 percent of the end point values and, because of the slope differences, $|\epsilon_{zp2t}| > |\epsilon_{zp2c}|$. Thus, at Position 2, there is a progressive

elongation and necking, causing the configuration described earlier. The behavior may not be as pronounced as for off-center barreling, for when the stresses at Position 2 are corrected for the load differences between tension and compression at Position 1, $2C$ increases and $2T$ decreases, causing less strain unbalance in each cycle. In fact, with fast-slow loops which are only slightly unbalanced, this later correction may control, and off-center barreling may occur.

Thermal-Mechanical Cycling

A similar approach can be used to describe the instability that develops when stepped temperatures but similar strain rates are employed in the two legs of the loop, shown in Figs. 7a and b. Referring to Figs. 5 and 6, substitution of high temperature for low strain rate and low temperature for high strain rate leads to the same behavior as mentioned previously. For in-phase cycling, that is, for high-temperature tension going, the cyclic stress-strain amplitude curve for tensile stresses is lower and flatter than that for compression. Hence, at remote positions, that is, 2, the strain values, indicated by $2T$ and $2C$, are such that $|\epsilon_{zp2C}| > |\epsilon_{zp2T}|$, and off-center barreling will occur. On the other hand, during out-of-phase cycling, Fig. 6, the tensile part of the cyclic stress-strain curve is higher and steeper such that, at Position 2, $|\epsilon_{zp2T}| > |\epsilon_{zp2C}|$. Consequently, off-center necking develops at Position 2. These predictions fit the observations of Sheffler, Fig. 2.

The case of differing strain rates as well as temperatures can be similarly treated. From the arguments presented, the largest imbalance is developed for the combination of high temperature and low strain rate in one leg and low temperature and high strain rate in the other. The shape change (off-center necking or barreling) will depend on the phasing with mechanical strain. Combinations of high temperature and high strain rate for one leg and low temperature and low strain rate are not predictable because of the offsetting effects of temperature and strain rate.

Special Cases

Earlier, the case of end thinning in axially constrained and thermally cycled tubular specimens was referred to [6]. This situation requires a different treatment since the end thinning (and central thickening) was occurring in a region of uniform stress. Nonuniform temperature along the tube length, especially near the ends, was found and was particularly severe at the higher temperature (600°C) but was insignificant at the lower temperature (100°C). The end thinning and center thickening can be traced to this axial temperature distribution. Since compression exists at high temperature, greater thickening in the wall occurs there rather than at the ends where the flow stress is greater. At the lower temperature and

the accompanying tensile stress, the ends are thinned further because of the now developed nonuniform wall thickness. There is little to prevent the process from continuing.

Another case mentioned earlier is that reported by Conway, Stentz, and Berling [4] for isothermal hold-time tests on zirconium-copper in argon at 538°C. It should first be noted that this temperature is very high for copper alloys. Secondly, the shape changes were reported to occur at 1.4 percent total strain range, but not at 5.0 percent. Hence the behavior is not a general phenomenon. Because of the high temperature and very low strain hardening, most of the plastic deformation during the ramping of the strain is localized to a region very near the specimen center, as illustrated by Fig. 3. Thus, at off-center Position 2, the cyclic plastic strain component is very small. The tensile hold period requires that the total computed longitudinal strain at Position 1 remain constant. The specimen is subjected to a prolonged, relaxing tensile stress, allowing tensile creep deformation to occur at Position 2. Correspondingly, there will be elastic unloading at 2 consistent with the constant total (elastic plus plastic) strain conditions at Position 1. With the next strain reversal, again little plastic deformation occurs at 2, but another creep increment develops during the hold period. Hence, progressive necking develops at 2. As the diameter becomes smaller and the stress increases at 2, the creep effects accelerate, although no indication of this event is evident at the control position. However, the specimen becomes progressively longer.

In the case of compression hold, the same process takes place, but in compression. Off-center barreling develops as a result of repetitive increments of compressive creep. Here, the stress decreases with increasing barreling, so that the process tends to slow down at 2. However, the shape change of the specimen causes the bulging process to move down closer to the specimen center. Eventually the barreling extends almost to the center, and the profile becomes highly localized. The highly concentrated necking and barreling is clearly seen in Fig. 2, together with specimen shortening.

In the case of the hold experiments performed at higher strain ranges, the zone of plastic deformation extends further from the center. The differences in rapid straining in one direction and creep in the other direction are now less, and the shape changes are smaller. Additionally, there are fewer cycles.³

³Note added in proof: attention should also be called to the work of Skelton [13] in which uniform gage length test specimens of 20Cr/25Ni/Nb steel were subjected to longitudinal strain control at 750°C with tension and compression hold periods. It was found that tension hold periods led to barreling at the midgage length position and necking near the end fillets, while compression holds produced midlength necking and barreling near the end fillets. These observations are consistent with those of Conway, Stentz, and Berling [4].

Discussion

The general condition that appears necessary for shape changes and instabilities in mechanical and thermal cycling is a positional variation or gradient in the cyclic stress-strain field caused by geometry, temperature, or material variations. We have cited several examples of geometry variations where hourglass specimen geometries are used and one example of temperature variation, that of the axially constrained and thermally cycled tube. Instability can be minimized by maintaining axial uniformity both in geometry and in temperature distribution wherever cyclic plastic strain is present.

Although the observations and interpretations cited here relate to specific bulk geometries, it is interesting to speculate as to whether similar geometric changes can occur on a much finer scale. Two intriguing questions come to mind. One relates to whether the intense strain localization associated with slip-band extrusion and crack initiation develops as a consequence of progressive microstructural changes in shape of surface grains. Another deals with crack growth and the shape of the crack tip as a function of the wave shape employed. Relative to the latter question, substantial differences in the shape of mildly notched specimens occur depending on the phase relationship between thermal and mechanical loading (Fig. 5). Similar shape changes can be envisaged when the notch sharpens sufficiently to become a propagating crack. Various investigators [2,5] have reported substantial differences in life as a function of wave shape, other conditions being equal. Can these differences be related to differences in crack tip shape changes and thus on crack propagation?

Relative to crack nucleation, McClintock's [12] quantitative model of instability to explain surface roughness and crack nucleation should be recalled. That work was inspired by observations of roughening on cycled plasticine models. Northcott and Baron's studies on thermal fatigue can also be cited, where narrow edges of wedge-shaped specimens were alternately heated and cooled to produce a regular pattern of deep grooves, initiating crack propagation. Crazeing in thermal fatigue and local surface roughening in isothermal fatigue may be closely related to the hourglass specimen shape instabilities reported here. The craze-cracking problem is unquestionably more complicated, dealing with cyclic phase transformations, interplay with oxidation processes, two-dimensional stresses, etc. It is, however, basic to many thermal fatigue problems and should be studied in more detail.

References

- [1] Coffin, L. F., *Transactions, American Society for Mechanical Engineers, Journal of Basic Engineering*, D, Vol. 82, 1960, p. 671.

- [2] Sheffler, K. D., "Vacuum Thermal-Mechanical Fatigue Testing of Two Iron Base Alloys High Temperature Alloys," NASA-CR-134524, National Aeronautics and Space Administration, Lewis Research Center, Cleveland, Ohio, Jan. 1974.
- [3] Raymond, M. H. and Coffin, L. F., *Acta Metallurgica*, Vol. 11, 1963, pp. 801-807.
- [4] Conway, J. B., Stentz, R. H., and Berling, J. T., "High Temperature, Low-Cycle Fatigue of Copper-Base Alloys in Argon," NASA-CR-121260, National Aeronautics and Space Administration, Lewis Research Center, Cleveland, Ohio, Aug. 1973.
- [5] Unpublished General Electric Co. research.
- [6] Coffin, L. F., *Transactions*, American Society of Mechanical Engineers, Vol. 76, 1954, pp. 931-950.
- [7] Coffin, L. F., *Transactions*, American Society of Mechanical Engineers, Vol. 79, 1957, p. 1637.
- [8] Carden, A. E., "Thermal Fatigue—An Analysis of the Experimental Method," ORNL TM-405, Oak Ridge National Laboratory, Oak Ridge, Tenn., 1963.
- [9] Thomas, W. S., "An Investigation of the Stages of Deformation of a Thin-Wall Tube Caused by Cyclic Thermal Stress," M.S. Thesis, University of Alabama, University, Ala., Aug. 1961.
- [10] Hernandez, J. A., "An Analysis of the Thermal Fatigue Characteristics of Inconel," M. S. Thesis, University of Alabama, University, Ala., 1964.
- [11] Sheffler, K. D. and Doble G. S. in *Fatigue at Elevated Temperature*, ASTM 520, American Society for Testing and Materials, 1973, pp. 491-499.
- [12] McClintock, F. A. in *Fracture of Solids*, Interscience Publishers, New York, 1963, pp. 65-102.
- [13] Skelton, R. P., *Materials Science and Engineering*, Vol. 19, 1975, pp. 25-30.

Life Prediction of Thermal-Mechanical Fatigue Using Strainrange Partitioning

REFERENCE: Halford, G. R. and Manson, S. S., "Life Prediction of Thermal-Mechanical Fatigue Using Strainrange Partitioning," *Thermal Fatigue of Materials and Components, ASTM STP 612*, D. A. Spera and D. F. Mowbray, Eds., American Society for Testing and Materials, 1976, pp. 239-254.

ABSTRACT: This paper describes the features of the method of strainrange partitioning that make it applicable to the life prediction of thermal-mechanical strain-cycling fatigue. An in-phase (230 to 760°C) test on Type 316 stainless steel is analyzed as an illustrative example. The method utilizes the recently proposed step-stress procedure of experimental partitioning, the interaction damage rule, and the life relationships determined at an isothermal temperature of 705°C. Implications of the present study are discussed relative to the general thermal fatigue problem.

KEY WORDS: thermal fatigue, intergranular fracture, plastic strain, creep strain, life prediction, strainrange partitioning, stainless steels

Several of the papers in this volume relate to fatigue data obtained by thermal-mechanical strain-cycling (TMSC) involving the simultaneous independent variation of both strain and temperature. TMSC simulates many of the features of the general thermal fatigue problem, yet retains the relative simplicity and ease of data gathering and interpretation associated with axial strain-cycling of smooth laboratory specimens. In a TMSC test, the temperature, strain, and stress can be measured directly at any point within a cycle. Furthermore, any two of these variables can be controlled independently with time.

Cyclic lives associated with thermal fatigue and TMSC are typically observed to be lower than those associated with comparable isothermal cycles. Many investigators have concluded that some form of creep damage is responsible for such adverse effects. As a result, a number of high-

¹Engineer, Lewis Research Center, National Aeronautics and Space Administration, Cleveland, Ohio 44135.

²Professor, Case Western Reserve University, Cleveland, Ohio 44106.

temperature fatigue life prediction approaches [1-8]³ have evolved over the past two decades in attempts to deal rationally with the pernicious nature of creep damage. The earliest attempts did not consider that creep damage might be encountered in more than one form.

In 1968, Spera [5] proposed upper and lower bound criteria for creep damage for use in calculating isothermal and thermal fatigue life. The lower bound criterion based on "monotonic rupture" best fit thermal fatigue results since they tended to exhibit creep damage in only one direction. Isothermal results involving creep damage in both directions usually followed the upper bound or "cyclic rupture" criteria. At that time, however, a methodology was not considered for blending between monotonic and cyclic damage in a general cycle.

The method of strainrange partitioning [8] was proposed in 1971 and provides a methodology for handling any strain cycle composed of creep and plastic strains, including those cycles which give rise to monotonic and cyclic creep damage. Within the framework of this method, damage is contributed by each of four partitioned strainranges in proportion to the amount of each present within a cycle. A damage rule, such as the interaction damage rule [9], provides the means for synthesizing these damage contributions. The partitioned inelastic strainranges are defined as:

$\Delta\epsilon_{pp}$ = tensile plastic strain that is balanced by compressive plastic strain.

$\Delta\epsilon_{pc}$ = tensile plastic strain that is balanced by compressive creep strain.

$\Delta\epsilon_{cp}$ = tensile creep strain that is balanced by compressive plastic strain.

$\Delta\epsilon_{cc}$ = tensile creep strain that is balanced by compressive creep strain.

These strainranges are commonly encountered in a number of applications considered by others [1,5-7,10-14] in dealing with a variety of creep-fatigue problems. Strainrange partitioning simply recognizes these components as generic in that the strain response to any arbitrary history of reversed strain can be synthesized from contributions of these components.

Several features of the method are of special advantage in the treatment of thermal-mechanical cycling. The purpose of this paper is to discuss these features and to illustrate possible application with an example.

Features of the Strainrange Partitioning Method

Although $\Delta\epsilon_{pp}$, $\Delta\epsilon_{pc}$, $\Delta\epsilon_{cp}$, and $\Delta\epsilon_{cc}$ are the four generic strainrange components which comprise all hysteresis loops, the amount of each component present in any one hysteresis loop must be determined by a process referred to as "partitioning." Several procedures have been developed for

³ The italic numbers in brackets refer to the list of references appended to this paper.

accomplishing this process [9,15]. In the present discussion we shall limit consideration to only the "step-stress" method which is an experimental procedure whereby the hysteresis loop is traversed, stopping at a selected number of stress levels to determine creep rates. In Ref 15, this procedure was developed in connection with hysteresis loops at isothermal conditions. However, the same basic partitioning procedure can be applied in thermal-mechanical cycles involving arbitrary temperature variations within the cycle. Several advantages accrue when the analysis is performed according to the strainrange partitioning framework and through the step-stress partitioning procedure.

Accounting for Details of Cycle, Including Creep Induced by Compressive Stress

An important aspect of strainrange partitioning relevant to the subject of thermal fatigue analysis is that it is possible to distinguish between the severity of the different types of strainranges that can be commonly generated during such cycling. For example, if the strain is "in-phase" with the temperature (rising tensile strain while temperature is increasing), the strain-range component developed will be of the $\Delta\epsilon_{cp}$ type. "Out-of-phase" cycling (rising compressive strain with increases in temperature) is conducive to the development of a $\Delta\epsilon_{pc}$ component of strainrange. Since the method associates different effects with each of these strainrange types, it not only provides a means for recognizing the importance of the compressive portion of the cycle (which some alternative methods do not; for example, that currently specified by the American Society of Mechanical Engineers (ASME) Boiler and Pressure Vessel Code Case 1592 [16]), but it also provides a basis for distinguishing between the details of strain and temperature variation within the cycle that can have significant effects on fatigue life.

Separation of the Two Distinct Roles of Temperature

Within the framework of strainrange partitioning, temperature is assumed to exert an influence on low-cycle fatigue in two independent ways: its strong influence on flow behavior (constitutive relationships), and, to a much lesser degree, its influence upon failure behavior (life relationships). A more detailed discussion of these two aspects is given in Ref 17. Any influence the temperature has on the flow behavior is manifested in the size and shape of the hysteresis loop that develops during cycling. When such a loop is partitioned, the amount of creep strain present will be a direct function of the time available and the thermal activation provided by the temperature. Once the hysteresis loop has been partitioned and the pertinent components of strainrange $\Delta\epsilon_{pp}$, $\Delta\epsilon_{cc}$, and $\Delta\epsilon_{cp}$, or $\Delta\epsilon_{pc}$

determined, the method makes use of an appropriate damage rule to combine the effects of two or three strainranges present. In applying this rule, the life relations for each component strainrange become the important material characterization parameters.

For certain materials—for example, Type 316 stainless steel and $2\frac{1}{4}$ Cr-1Mo, which are materials of great technological importance in nuclear pressure vessel applications—the partitioned strainrange versus life relationships are not sufficiently dependent on temperature [17] to require special consideration. Advantages accrue in these cases. First, there is a reduction in the amount of material testing needed to characterize the life relationships. Although this is not too important when only short time results are needed, it is of great importance when very long test times are deemed necessary. Second, temperature insensitivity removes the question of selecting a temperature within the spectrum covered by a temperature variation throughout a cycle that is to be regarded as the most important for the choice of pertinent life relationships.

In treating materials for which there may be a strong dependence of the life relationship on temperature, this advantage is, of course, lost. For such materials, alternate criteria could be assumed. For example, one could use the life relationships at the maximum temperature [16], the relationships at the temperature which produces the lowest lives [18,19], or the temperature at which the dominant strainrange type is imposed.

Provision of Upper and Lower Bounds on Life

The method lends itself well to the determination of bounding values on life. Thus, once the inelastic strainrange has been determined, a lower bound on cyclic life can be obtained by assuming that all of the strainrange is of the most damaging type (for most materials, $\Delta\epsilon_{cp}$, but for some, $\Delta\epsilon_{pc}$). Should the life relationships vary with temperature, the lower bound could, of course, be determined at the temperature producing the lowest lives. Likewise, an upper bound on life can be ascertained by assuming that the entire strainrange is of the most benign type (usually $\Delta\epsilon_{pp}$) and evaluated at the temperature producing the greatest lives. If the bounding values are acceptable, a detailed analysis to determine the actual hysteresis loops and to partition them becomes unnecessary; if not, the need for a more detailed study is indicated. This feature has special merit to designers who may wish to apportion design effort according to the needs of a particular situation rather than always making detailed analyses. It is also of significance to codifying bodies in specifying under what conditions minimal analyses will be required (that is, when the most pessimistic estimate of life associated with the lower bound can be tolerated) and when detailed analyses are needed (that is, when the designer is motivated to take full advantage of the potential life of the part).

Example Analysis

Description of the Problem Treated

As a demonstration of the applicability of the method of strainrange partitioning to the thermal-mechanical strain-cycling problem, an axially loaded, tubular specimen of AISI Type 316 stainless steel was subjected to the in-phase conditions listed in Table 1.

TABLE 1—*Material, specimen, and test conditions for sample problem.*

<i>Material:</i>	AISI Type 316 stainless steel, hot rolled and mill annealed, 19 mm (0.75 in.) diameter bar stock supplied by Viking Steel Co., Cleveland, Ohio. The heat number, exact chemical composition, and annealing details are unknown. Tensile and creep-rupture properties at 705°C are given in Ref 9. An indication of the grain structure can be found in Fig. 5a.
<i>Specimen:</i>	Tubular, hourglass test section [20], specimen number AYY-304.
<i>Extensometer:</i>	Diametral [20].
<i>Strain:</i>	Diametral strain cyclically ramped linearly with time between limits resulting in an axial total mechanical strainrange of 0.00923. The apparent thermal component of strain (0.01381) was measured by temperature cycling the specimen under a controlled zero load condition. This thermal component was subtracted from the total measured strain to determine the mechanical component. The elastic strainrange was subtracted from the total mechanical strain range to get the inelastic strain range of 0.00616. The cyclic period was 30 min.
<i>Temperature:</i>	Silicon carbide internal heating element, temperature ramped linearly with time between temperature limits of 230 and 760°C with a period of 30 min. The temperature was phased with the strain such that the maximum temperature occurred at the peak tensile strain. This is referred to as an "in-phase" thermal-mechanical strain cycle.

Cyclic strain hardening caused an increase in the stress range by about 15 percent during the first 10 to 15 percent of the cyclic life. Thereupon, the hysteresis loop stabilized, and the stress range remained essentially constant until approximately 90 percent of the life was reached. Macrocracking became evident at this time, producing a drop in the stress range and introducing a cusp in the compressive portion of the hysteresis loop.

Failure occurred on the 307th cycle. A hysteresis loop, ABCDEFGHIJKLA, is reconstructed in Fig. 1, using the stress and strain values taken from hysteresis loops on cycles 38, 85, 86, 88, 89, 173, 174, 175, and 176. These were the cycles during which the inelastic strains were partitioned into their creep and plastic components, using the step-stress method.

Separation of the Creep and Plastic Strains

Following the suggestion of Ref 4, the component of steady-state creep for the entire period of the time interval considered is taken as the "creep" strain for use in strainrange partitioning analysis. All the remaining in-

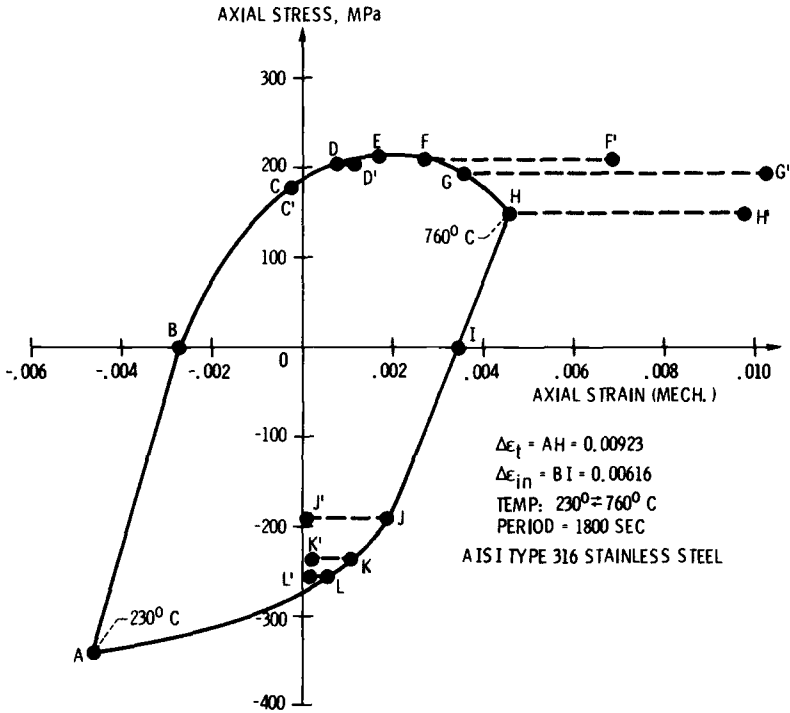


FIG. 1—Stress-strain hysteresis loop for in-phase thermal-mechanical strain cycle illustrating stress levels and creep strains associated with experimental partitioning of strains by the step-stress method.

elastic strain, whether instantaneous or whether occurring as first stage (primary) creep, is taken to be “plasticity.”

The partitioning procedure followed is to temporarily halt the temperature and strain programmers at a selected point, such as F, switch the servocontroller from strain to load control, and hold the stress and temperature constant at the stabilized values associated with Point F while creep strain is measured as a function of time. This condition is held until a reasonably linear creep rate is established. This is taken as an approximation to the steady-state creep condition. At Point F', the controller is switched back to strain control, and the strain and temperature programs are resumed. Before stopping at the next step-stress level, the hysteresis loop is restabilized by traversing one or more cycles. Stability is indicated by observing the hysteresis loop to repeat the path of the previous loops. In the present case, stability was established in the very next cycle following a period of creeping. Table 2 summarizes the steady-state creep rate information measured at each of the stresses and temperatures indicated. Figure 2 illustrates the creep curves measured at various points around the

TABLE 2—*Experimental partitioning results using step-stress method.*

Cycle No.	Point in Cycle	Temperature in Cycle, °C	Time in Cycle, s	Stress in Cycle, MPa	Time Held at Stress, s	Steady State Creep Rate, 10 ⁻⁶ s ⁻¹	Steady State Creep Strain	Total Creep Strain
173	A	230	0	-340	...	0
173	B	325	161	0	...	0
88	C	483	426	177	1300	<0.016	<0.00002	0.00002
88	D	538	522	204	2100	<0.16	<0.00034	0.00034
86	E	594	618	212
38	F	649	711	210	1890	1.3	0.00240	0.00416
89	G	705	804	193	900	6.5	0.00580	0.00664
85	H	760	900	148	560	8.2	0.00460	0.00513
174	I	722	964	0	...	0
175	J	649	1090	-191	2940	0.38	0.00110	0.00180
176	K	594	1184	-238	1890	0.30	0.00057	0.00089
173	L	538	1278	-257	1700	<0.07	<0.00012	0.00035
173	A	230	1800	-340	...	0

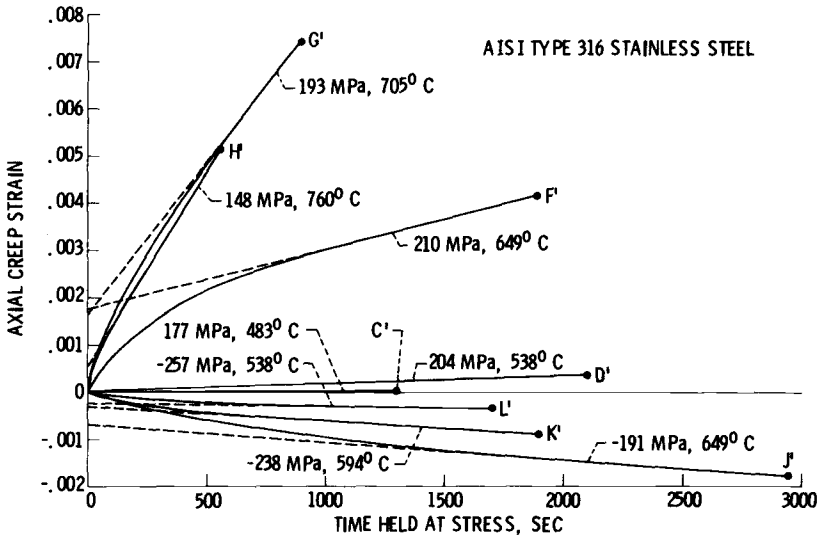


FIG. 2—Creep curves generated during application of step-stress method to partition strains in thermal-mechanical strain cycle (230 to 760°C).

hysteresis loop. Comparison of these cyclic creep data with conventional monotonic data would probably show significant differences in behavior. However, equivalent monotonic data are not presently available. Experimental partitioning procedures have as yet to be worked out for materials that do not exhibit cyclic stability in the sense described here.

A plot of the steady-state creep rate versus time within the thermal-mechanical cycle that each stress and temperature was encountered results in the curve shown in Fig. 3. By integrating the area under this curve, the amounts of tensile and compressive steady-state creep strain can be determined. Areas above the horizontal axis represent tensile creep; those below the horizontal axis represent compressive creep. For the example shown in Fig. 3, the compressive steady-state creep strain is 0.00006. Since the compressive inelastic strain is 0.00616, the compressive plastic strain is 0.00610. Similarly, the tensile creep strain as determined from Fig. 3 is 0.00145. Since the tensile inelastic strain is also equal to 0.00616, the tensile plastic strain is 0.00471. Hence, the partitioned strain ranges [8] are

$$\Delta\epsilon_{pp} = 0.00471, \Delta\epsilon_{cc} = 0.00006, \Delta\epsilon_{cp} = 0.00139 \quad (1)$$

where

$$\Delta\epsilon_{in} = \Delta\epsilon_{pp} + \Delta\epsilon_{cc} + \Delta\epsilon_{cp} = 0.00616$$

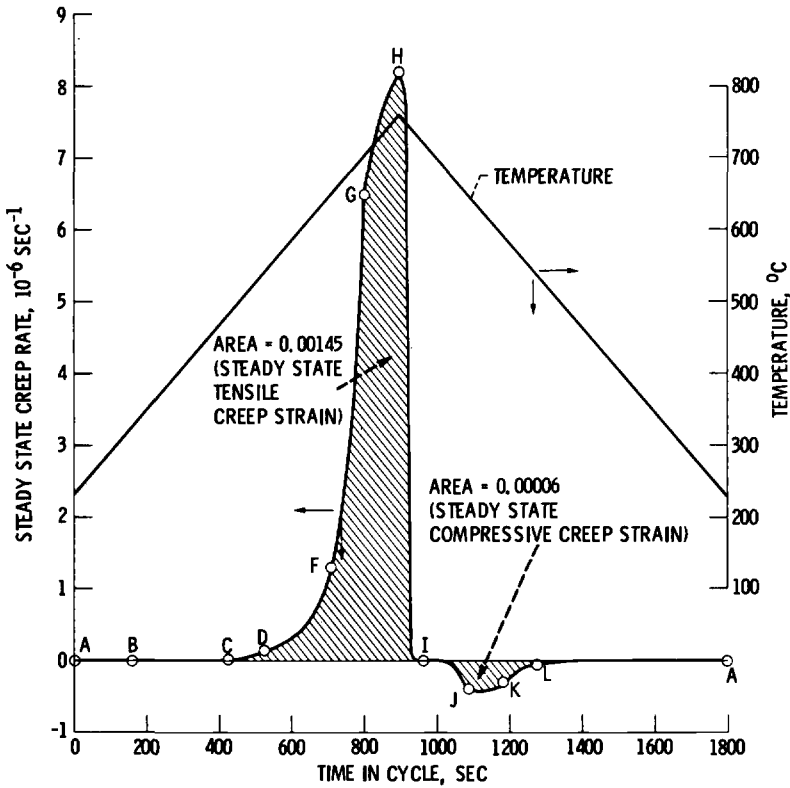


FIG. 3—Accumulation of tensile and compressive steady-state creep strain during in-phase thermal-mechanical strain cycle (230 to 760°C) applied to AISI Type 316 stainless steel.

An assessment of the significance of experimental errors or other sources of variation in the magnitude of these strainranges is given in a later section. The strainrange fractions are

$$F_{pp} = \frac{\Delta\epsilon_{pp}}{\Delta\epsilon_{in}} = \frac{0.00471}{0.00616} = 0.765$$

$$F_{cc} = \frac{\Delta\epsilon_{cc}}{\Delta\epsilon_{in}} = \frac{0.00006}{0.00616} = 0.010 \quad (2)$$

$$F_{cp} = \frac{\Delta\epsilon_{cp}}{\Delta\epsilon_{in}} = \frac{0.00139}{0.00616} = 0.225$$

Damage Rule

The strain fractions are used in the interaction damage rule which is written as follows

$$\frac{F_{pp}}{N_{pp}} + \frac{F_{cc}}{N_{cc}} + \frac{F_{cp}}{N_{cp}} + \frac{F_{pc}}{N_{pc}} = \frac{1}{N_{pr}} \quad (3)$$

where

N_{pp} , N_{cc} , N_{cp} , and N_{pc} = cyclic lives determined from entering the life relationships at a strainrange equal to the entire inelastic strainrange of the cycle of interest, and

N_{pr} = predicted life.

This damage rule is based on assumptions described in detail in Ref 9. Although all of the terms in the equation are linear, we have continued to use the term "interaction" in its designation in order to distinguish it from the linear damage rule used in Ref 8 and because of certain interaction assumptions entering the original derivation.

Life Relationships

The life relationships used in the life prediction of the example thermal-mechanical strain-cycling problem are shown in Fig. 4. These curves are based upon the use of the interaction damage rule and the interpretation of creep strain as being only the steady-state (secondary) portion of the time-dependent strain. All of the tests used to establish these life relationships were conducted at a single isothermal temperature of 705°C.

Prediction of Thermal-Mechanical Strain-Cycling Life

For an inelastic strainrange of 0.00616, the N_{pp} , N_{cc} , N_{cp} , and N_{pc} lives from Fig. 4 are 1330, 405, 94, and 410, respectively. The predicted life, N_{pr} for this cycle, if uninterrupted, is computed from the interaction damage rule as follows

$$\begin{aligned} \frac{F_{pp}}{N_{pp}} + \frac{F_{cc}}{N_{cc}} + \frac{F_{cp}}{N_{cp}} &= \frac{1}{N_{pr}} \\ \frac{0.765}{1330} + \frac{0.010}{405} + \frac{0.225}{94} &= \frac{1}{N_{pr}} \\ 0.000575 + 0.000025 + 0.002395 &= 0.002995 = \frac{1}{N_{pr}} \end{aligned} \quad (4)$$

$$N_{pr} = 334 \text{ cycles}$$

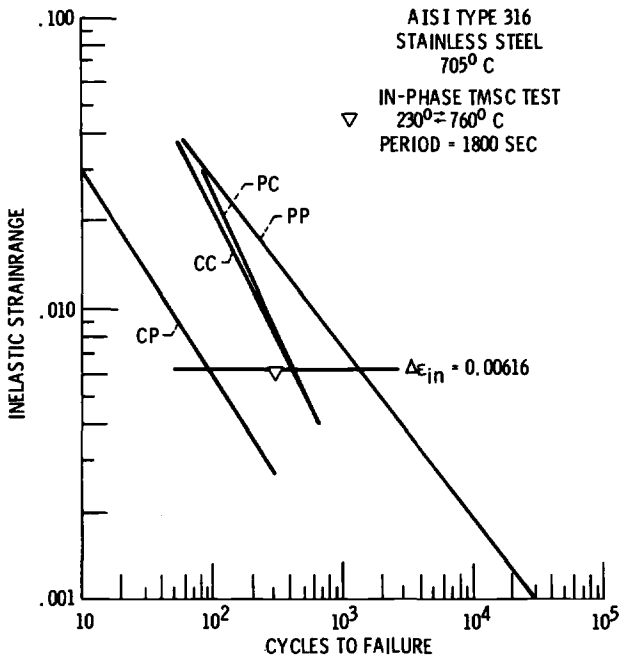


FIG. 4—Strainrange partitioning life relationships based on use of interaction damage rule and steady-state creep strain.

As mentioned earlier, one of the advantages of strainrange partitioning is its ability to recognize the importance of differences in the details of strain cycles. In the sample problem, the considerable amount of tensile creep strain is held responsible for reducing the life from a maximum of 1330 cycles down to the observed life of only 307 cycles. Had the same in-phase thermal-mechanical cycle been run in such a way as to avoid accumulation of creep strain by using a higher frequency or by shifting the temperature range to a lower level, no loss in life would be expected since all of the strain would be of the $\Delta\epsilon_{pp}$ type. With no creep in the cycle, there would also be no expected difference in life between an in-phase and an out-of-phase test. As a case in point, Coffin [10] observed no marked differences in thermal-mechanical fatigue lives of specimens of AISI Type 347 stainless steel tested using in-phase and out-of-phase cycles. Coffin's experiments were run at significantly higher frequencies and at lower temperature levels than those used in the present investigation. However, for the sample problem here, a frequency of 1/30 cycle/min and a temperature range from 230 to 760°C is severe enough to produce significant creep. The method of strainrange partitioning therefore indicates a substantial difference between lives expected for in-phase and out-of-phase thermal-mechanical strain cycles.

Had the sample test been conducted with the temperature and strain

out-of-phase, one could expect exactly the same amount of creep and plastic strain as measured previously but with the role of tension and compression reversed. That is, the term F_{cp}/N_{cp} in Eq 4 would be replaced with F_{pc}/N_{pc} where F_{pc} is 0.225 and N_{pc} is 410 cycles. The predicted life for out-of-phase cycling would be 870 cycles which is 2.6 times greater than the predicted life of 334 cycles for in-phase cycling. The result of this calculation is in line with our experience in conducting a number of other thermal-mechanical strain-cycling tests on AISI Type 316 stainless steel.⁴

Application of the time and cycle fraction approach as used in ASME Code Case 1592 [16] does not differentiate between in-phase and out-of-phase thermal-mechanical straining since compressive creep and tensile creep are taken to be equally damaging. This approach would predict the same life for these two extremes in cycling which can lead to the following undesirable situation: consider that the design curves were established with just the proper amount of conservatism to handle an in-phase thermal-mechanical cycle such as the one just discussed. By applying the same criteria and design curves to an out-of-phase cycle, the designer would predict an unnecessarily conservative life. An inefficient design results.

The foregoing discussion helps to illustrate the emphasis that strain-range partitioning places upon some of the details within thermal-mechanical strain cycles.

Assessment of Error

It should also be pointed up that these calculations do not include an assessment of the added damage to the specimen as a result of the step-stress partitioning procedures. A series of calculations have been made to determine the damage done by having held a constant creep stress for the time intervals listed in Table 2. Each cycle during which the creep

⁴An out-of-phase test conducted at an inelastic strainrange of 0.00484 failed at 1449 cycles. The frequency and temperature range were the same as listed in Table 1. Since this particular test was conducted prior to the development of the step-stress method, the partitioning of the creep and plastic strains was not accomplished. However, since the strainrange is only 20 percent less than that of the in-phase test, it is reasonable to assume that the partitioning would have been approximately the same. Hence, the predicted life is given by

$$\begin{aligned} \frac{F_{pp}}{N_{pp}} + \frac{F_{cc}}{N_{cc}} + \frac{F_{pc}}{N_{pc}} &= \frac{1}{N_{pr}} \\ \frac{0.765}{2022} + \frac{0.010}{524} + \frac{0.225}{540} &= \frac{1}{N_{pr}} \\ 0.000378 + 0.000019 + 0.000417 &= 0.000814 = \frac{1}{N_{pr}} \end{aligned}$$

$$N_{pr} = 1229 \text{ cycles}$$

stress was tensile produced a component of $\Delta\epsilon_{cp}$ strainrange which was greater than would normally have been experienced during that cycle. Likewise, during the cycles with compressive creep stress, there was usually a compressive creep strain greater than the 0.00006 amount normally experienced. In this latter case, the result was to increase the $\Delta\epsilon_{cc}$ strainrange at the expense of the $\Delta\epsilon_{cp}$ strainrange. Since $\Delta\epsilon_{cc}$ straining is less damaging than $\Delta\epsilon_{cp}$, there was less damage done during these particular cycles. The net effect of the hold periods during experimental partitioning was to induce damage in the amount of 0.0240. Thus, 2.4 percent less damage was available for the thermal-mechanical strain cycling. Hence, the N_{pr} value should be reduced by 2.4 percent to a value of 326 cycles to failure. This life can be compared directly with the observed life of 307 cycles to failure for this example problem.

It is also informative to note that the predicted life would have differed by less than 3 percent had an error as large as 100 percent been made in the determination of the compressive creep strain. Had an error of 10 percent been made in the determination of the tensile creep strain, the predicted life would have been altered by less than 8 percent. Furthermore, a 10 percent variation in the inelastic strainrange would produce only an 8 percent change in the predicted life. For the particular problem at hand, a percentage error in determination of strainrange translates into an error in predicted life that is slightly less than that percentage figure.

Bounding the Life Values

Instead of quantitatively determining life by detailed partitioning, an alternate approach is to estimate bounding values on life from a knowledge of the total inelastic strainrange and an estimate of the types of strainrange likely to be present. Here, because of the nature of the cycling, the most damaging type of strainrange is of the $\Delta\epsilon_{cp}$ type. If the entire cycle produced a $\Delta\epsilon_{cp}$ type strainrange, and the $\Delta\epsilon_{cp}$ life relationship is indeed independent of temperature, the life would be 94 cycles to failure. This value is a lower bound on life and can be determined without detailed partitioning. The upper bound on life would have been the N_{pp} value of 1330 cycles to failure. For the out-of-phase test mentioned in the earlier footnote, the upper bound would be the N_{pp} life of 2022 cycles, and the lower bound would be the N_{pc} life of 540 cycles for the inelastic strainrange of 0.00484.

Some Metallurgical Aspects

As was shown in Ref 8, application of a $\Delta\epsilon_{cp}$ type strainrange is conducive to intergranular creep cracking in AISI Type 316 stainless steel.

The photomicrographs of the failed specimen shown in Fig. 5 also reveal intergranular cracking (particularly evident in Fig. 5a), thus substantiating qualitatively the measured presence of a significant amount of $\Delta\epsilon_{cp}$ type strainrange in the present test. Figure 5c shows the wall thickness of the tubular specimen on the side of the tube from which the major crack originated and propagated. This cracking was along grain boundaries. Intergranular secondary cracks are also noted, although there is an indication that these may have initiated in a transgranular mode, possibly by the action of the $\Delta\epsilon_{pp}$ component of strainrange. Figure 5b is a photomicrograph of the wall thickness on the side of the tube opposite to Fig. 5c. The 45 deg shear angle across the thickness illustrates the final tearing-off of the specimen into two pieces on the 307th cycle. This tearing action opened up a number of internal intergranular cracks that had formed

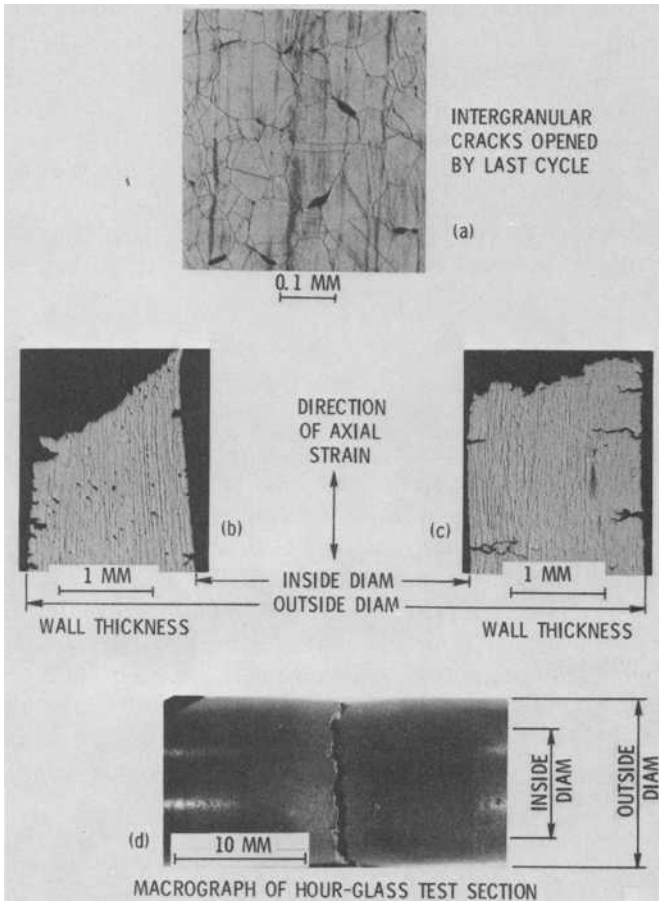


FIG. 5—Photomicrographs of failed specimen of AISI Type 316 stainless steel subjected to thermal-mechanical cycling (230 to 760°C) in phase.

during the thermal-mechanical strain-cycling. It should be noted that the failed specimen is free of cycle-dependent buckling or other geometric instabilities (Fig. 5d).

Conclusions

We have applied the method of strainrange partitioning to a thermal-mechanical strain-cycling problem on AISI Type 316 stainless steel. The sample problem can be used as an initial guide in applying the method to the general thermal fatigue problem. To date, the approach has been limited to cycles in which the inelastic strains can be determined with some degree of confidence. Extension of the method would be required in order to deal with cycles for which the elastic strains dominate and the inelastic strains are too small to calculate or measure accurately.

Although the sample problem involved a material whose life relationships are insensitive to temperature, some suggestions were given for dealing with materials for which this is not the case. Obviously, further experimentation is needed to test out the applicability of these suggestions. Additional research is also needed to guide in the selection of appropriate techniques for analyzing materials that exhibit metallurgical instabilities such as dynamic strain-aging or that experience strong interactions with the environment.

Extension of the method to predict the thermal fatigue life of an actual component would not be a difficult task, provided analyses were available for the temperature and equivalent axial strain histories at critical locations. An axially loaded laboratory specimen could then be programmed to follow these histories. From that point on, the determination of the creep and plastic strains, the partitioned strainrange components, etc., could follow the procedures described in this paper.

Rather than measuring the creep and plastic strains within a cycle as illustrated in this paper, they could be calculated using procedures and constitutive equations such as those proposed by Spera and Cox [19] and Mowbray and McConnelee [21]. Of course, upper and lower bounds on life can be estimated as discussed earlier without having to resort to either experimental or analytical partitioning.

References

- [1] Taira, S. in *Creep in Structures*, N. J. Hoff, Ed., Springer-Verlag, Berlin, 1962, pp. 96-119.
- [2] Manson, S. S. and Spera, D. A., *Quarterly Transactions of the American Society for Metals*, Vol. 58, 1965, pp. 749-751.
- [3] Manson, S. S., *International Journal of Fracture Mechanics*, Vol. 2, 1966, pp. 327-363.
- [4] Manson, S. S. and Halford, G. R. in *Thermal and High Strain Fatigue*, The Metals and Metallurgy Trust, London, 1967, pp. 154-170.

- [5] Spera, D. A., "A Linear Creep Damage Theory for Thermal Fatigue of Materials," Ph.D. thesis, University of Wisconsin, Madison, 1968.
- [6] Coffin, L. F., *Proceedings*, 2nd International Conference on Fracture, Chapman and Hall, London, 1969, pp. 643-654.
- [7] Ellis, J. R. and Esztergar, E. P. in *Symposium on Design for Elevated Temperature Analysis*, American Society of Mechanical Engineers, 1971, pp. 29-43.
- [8] Manson, S. S., Halford, G. R., and Hirschberg, M. H. in *Symposium on Design for Elevated Temperature Analysis*, American Society of Mechanical Engineers, 1971, pp. 12-23.
- [9] Manson, S. S. in *Fatigue at Elevated Temperatures*, ASTM STP 520, American Society for Testing and Materials, 1973, pp. 744-782.
- [10] Coffin, L. F., Jr., *Transactions of the American Society of Mechanical Engineers*, Vol. 79, No. 7, Oct. 1957, pp. 1637-1649.
- [11] Morrow, J. and Halford, G. R., *Proceedings*, Joint International Conference on Creep, Institution of Mechanical Engineers, 1963, pp. 3-43 to 3-47.
- [12] Swindeman, R. W., *Proceedings*, Joint International Conference on Creep, Institution of Mechanical Engineers, London, 1963, pp. 3-71 to 3-76.
- [13] Manson, S. S., Halford, G. R., and Spera, D. A. in *Advances in Creep Design*, A. I. Smith and A. M. Nicolson, Eds., Applied Science Publications Ltd., London, 1971, pp. 229-249.
- [14] Halford, G. R., *Metallurgical Transactions*, Vol. 3, No. 8, 1972, pp. 2247-2256.
- [15] Manson, S. S., Halford, G. R., and Nachtigall, A. J. in *Advances in Design for Elevated Temperature Environment*, American Society of Mechanical Engineers, 1975, pp. 17-28.
- [16] Code Case 1592, Boiler and Pressure Vessel Code, American Society of Mechanical Engineers, April 1974.
- [17] Halford, G. R., Hirschberg, H. M., and Manson, S. S. in *Fatigue at Elevated Temperatures*, ASTM STP 520, American Society for Testing and Materials, 1973, pp. 658-669.
- [18] Manson, S. S., *Thermal Stress and Low-Cycle Fatigue*, McGraw-Hill, New York, 1966.
- [19] Spera, D. A. and Cox, E. C., this publication, pp. 69-85.
- [20] Hirschberg, M. H. in *Manual on Low Cycle Fatigue Testing*, ASTM STP 465, American Society for Testing and Materials, 1969, pp. 67-86.
- [21] Mowbray, D. and McConnelee, J., this publication, pp. 10-29.

Summary

The objective put forward by the committee which organized the Symposium on Thermal Fatigue was to exchange ideas on methods for determining and improving the thermal fatigue resistance of both materials and components. A total of 16 technical papers were presented at the symposium, of which one was a review of terminology and historical developments in the field of thermal fatigue, thirteen were devoted to research on materials, and only two dealt directly with components. Because of the large quantity and variety of information assembled by those who contributed to this symposium, it is appropriate to summarize here the major conclusions offered, to evaluate the success of the symposium in achieving its goals, and to offer some suggestions for future thermal fatigue research.

Summary of Major Conclusions of the Contributed Papers

In the opening address, Spera concluded that it would be convenient and historically correct to view thermal fatigue as one of two categories of low-cycle fatigue, the other being isothermal fatigue. Further subdivision of thermal fatigue into thermal-stress fatigue and thermal-mechanical fatigue was suggested, depending on whether constraint of free thermal expansion was internal or external, respectively. After a brief review of historical developments from 1838 to the present, it was hypothesized that we now have quantitative understanding of the mechanisms of thermal fatigue and that we can make life predictions with factor-of-two accuracy, at least for conventional metals.

Analysis Papers

Mowbray and McConnelee compared the results of two-dimensional finite-element analysis of temperature, stress, and strain (elastic and inelastic) in a thermal-stress fatigue specimen with similar results using a simpler uniaxial, elastic strain invariance (UESI) method and found that stress-strain behavior trends were the same. Moreover, in most temperature regions of the specimen, identical behavior was calculated by the two methods. Therefore, it was concluded that the simpler and less costly UESI method was adequate for further parametric studies of three damage calculation methods.

Gonyea, in one of the two symposium papers devoted to components, proposed that thermal-stress concentration factors (TSCF) can be defined for large, nonuniform shafts which are relatively independent of time and heating rate. Charts for estimating these factors were offered, based on finite-element thermal-stress analysis. Significant differences between thermal and mechanical (bending) stress concentration factors were discussed.

Tepper, in the only other component-oriented paper, proposed a 14-step design approach to achieve reliability in a component susceptible to thermal fatigue failure. It was concluded that, for the purpose of comparing design alternatives, a simple life-fraction rule is sufficient for estimating creep and plastic strain damage. Considerable effort would be required to improve upon this simple analysis. Improvements are usually obtained by compiling a library of creep-fatigue test data. This is an effort which can only be justified under certain conditions, for example, when reliability is marginal or a large number of production units are to be made.

Hasselmann, Badalian, and Chen demonstrated that a fracture-mechanics approach is feasible for predicting the thermal fatigue life of ceramic materials. They concluded that estimating the proper initial flaw depth by use of Weibull theory introduces the largest uncertainty in estimating fatigue life.

Spera and Cox offered a computerized method for predicting thermal fatigue life, using a generalized damage fraction theory. Many of the elements of this computerized analysis also appear in Mowbray and McConnelee's UESI method and Tepper's preliminary LCF analysis. It was claimed that sufficient accuracy is retained in spite of simplifying assumptions to make this computer program a useful tool for calculating thermal fatigue resistance. Application of this method to both thermal-stress fatigue and thermal-mechanical fatigue problems was illustrated.

Papers on Thermal-Stress Fatigue

Howes concluded that the two dominant mechanisms in the formation of a thermal-stress fatigue crack are local plastic strain and oxidation. After an incubation period, cracking almost invariably occurs in areas of highest plastic strain. Oxidation is often preferential at grain boundaries, forming wedges which grow in size until a crack is initiated and begins to propagate. Oxidation also increases the amount of local plastic strain by reducing an alloy's strength through depletion of strengthening elements and phases.

Bizon and Spera used fluidized-bed tests to compare the relative resistances to thermal-stress fatigue of a wide variety of nickel- and cobalt-base alloys. They showed that directional solidification and proper coating are very effective techniques for increasing the thermal fatigue life of these types of alloys, often by two orders of magnitude.

Beck and Santhanam demonstrated that the thermal-stress fatigue resistance of a cast cobalt-base alloy can be significantly improved by changing the casting variables so as to increase the spacing of the dendrite arms in the microstructure. Crack initiation periods were lengthened, and propagation rates were reduced by this technique. This paper and the previous one by Bizon and Spera were the only papers presented at the symposium which dealt directly with methods for improving the thermal-fatigue resistance of materials.

Laub stated that thermal fatigue failures in furnace heat exchangers fabricated from mild steel sheet can now be predicted with confidence. At present, the prediction technique is primarily experimental, combining strain gage data from prototype heat exchangers with thermal fatigue data on tubular specimens. It has not yet been demonstrated that strain gage measurements can be replaced with a finite-element strain analysis. The latter must be capable of modeling the large transverse plate deflections present in furnace heat exchangers.

Papers on Thermal-Mechanical Fatigue

Thermal-mechanical fatigue is primarily a laboratory testing procedure in which external forces are applied to test specimens to produce stresses which simulate the internal thermal stresses in an actual component. According to Hopkins, equipment is now available with which almost any strain-temperature-time cycle of practical interest can be reproduced in the laboratory. Tubular test specimens are useful for both crack initiation and crack propagation studies. Computer control is almost a necessity for achieving acceptable accuracy because of the need to continuously adjust the strain equipment to compensate for small temperature errors.

Jaske found that, in order to correlate in-phase, out-of-phase, and isothermal fatigue test data for a low-carbon steel, a knowledge of both cyclic stress and cyclic strain was necessary. On the basis of stabilized stress range versus cycles to failure, little difference was observed in the behavior of specimens subjected to in-phase and out-of-phase cycles of temperature and strain. However, the cyclic hardening characteristics of the alloy tested were complex, indicating the difficulty in predicting the stabilized stress range.

Gemma, Langer, and Leverant demonstrated that the effect of elastic modulus on crack growth rates during strain-cycling tests is opposite to that during stress cycling. Tests on specimens of a directionally solidified nickel-base alloy with various grain orientations (and therefore moduli) showed that crack growth rates increased with increasing modulus in the loading direction under thermal-mechanical strain-cycling conditions. Good correlation of data for this alloy in all grain orientations was achieved by plotting crack growth rate versus a pseudostress intensity range. This latter

parameter is equal to the product of the modulus in the load direction and the strain intensity range.

Sheffler demonstrated the drastic reductions in life which thermal-mechanical cycling can produce in two iron-base alloys in comparison to isothermal cycling at the maximum cycle temperature. In most cases, the life reductions are attributed to grain-boundary creep damage. A few specimens of a high ductility alloy subjected to out-of-phase cycling showed pronounced geometry changes which led to premature failure. This same behavior has been observed previously in two very ductile tantalum alloys, suggesting that high-ductility alloys may be more susceptible to geometric instability.

Halford and Manson demonstrated the feasibility of extending the techniques of strainrange partitioning to include the calculation of thermal-mechanical fatigue life. It was proposed that further development of this analysis will remove present restrictions such as requirements for measurable inelastic strain, temperature insensitivity of life relations, and metallurgical stability.

According to Coffin, geometric instabilities such as those observed during thermal-mechanical strain cycling must be preceded by a gradient in the cyclic stress-strain field. This gradient may be caused by geometry, temperature, or material variations. It was also suggested that macroscopic geometry changes occurring during thermal-mechanical fatigue may be analogous to microscopic surface roughening and crazing observed during thermal-stress and isothermal fatigue.

Achievement of Symposium Goals

The symposium was successful in fostering an exchange of information on a variety of subjects, all related to thermal fatigue, and, in this respect, its major goal was achieved. The combination of these papers with those recently published in *Fatigue at Elevated Temperatures, ASTM STP 520* provides an excellent set of references on the state of the art in both the isothermal and thermal fatigue categories of low-cycle fatigue. It is hoped that papers on methods for improving the thermal fatigue resistance of actual components will be presented at a symposium in the near future.

Critical Experiment

An important experiment which remains to be performed is the direct comparison between the life of a thermal-stress fatigue specimen and that of a thermal-mechanical fatigue specimen subjected to identical cycles of strain and temperature. While it is convenient to assume that these two lives are roughly equal, correlation between thermal-stress fatigue and thermal-mechanical fatigue has not been critically evaluated in the literature.

However, all the necessary tools are now available, as evidenced by papers presented at this symposium. These tools are (a) equipment for well-controlled thermal-stress fatigue tests, (b) analyses for determining cycles of temperature and stress at crack locations in a thermal-stress fatigue specimen, and (c) thermal-mechanical fatigue machines for faithfully reproducing these cycles in a material test specimen. This critical experiment is important, not only for the technical information which it would produce, but also for the unifying effect it would have on research and development in the field of thermal fatigue.

D. A. Spera

Fatigue Branch, National Aeronautics and Space Administration Lewis Research Center, Cleveland, Ohio; symposium co-chairman and also coeditor of this publication.

Index

- A**
- Analysis (calculation, prediction)
 - Creep strain, 1, 38, 69, 239
 - Fatigue life, 38, 55, 69, 239
 - Finite element, 11, 32, 40, 71, 93, 155
 - Plastic strain, 1, 38, 69, 239
 - Stress, 10, 30, 69
 - Thermal (temperature), 10, 59, 88
 - Thermal stress, 3, 10, 30, 38, 55, 69, 86, 106, 123
 - Fluidized bed, 10, 86, 106, 123
 - Fracture, 55, 199
- C**
- Ceramics, 55
 - Coatings, 70, 106, 143
 - Cobalt alloys, 12, 106, 123
 - Computer program, 11, 32, 42, 62, 69, 166
 - Crack initiation, 69, 157
 - Crack propagation, 55, 86, 157, 199
 - Creep strain, 38, 69, 239
- D**
- Definitions, 3
 - Directional solidification, 107, 199
 - Disk
 - Test specimens, 10, 87
 - Turbine, 31, 38
- F**
- Fatigue
 - Thermal mechanical, 3, 69, 141, 157, 170, 199, 214, 227, 239
 - Heat exchangers, 141
 - Heat resistant alloys, 106
- H**
- I**
- Intergranular fracture, 239
 - Iron alloys, 86, 141, 170, 215, 229, 239
- L**
- Life prediction, 38, 55, 69, 239
- M**
- Materials
 - Ceramic
 - Silicon nitride HS-130, 57
 - Soda-lime-silica glass R-6, 56
 - Cobalt alloys, 106
 - FSX414, 12
 - Mar-M509, 123
 - Copper, zirconium, 228
 - Iron alloys
 - A286, 215
 - AISI 1010, 170
 - H-13, 86
 - Low-carbon mild steel, 141

- Type 304, 215, 229
 - Type 316, 239
 - 18Ni maraging, 86
 - Nickel alloys, 86
 - Astroloy, 39
 - B-1900, 76
 - B-1900 + Hf, 199
 - Mar-M200 + Hf (DS), 199
 - Tantalum alloy, T-111, 76
 - Mechanical properties, 106
 - Mechanical tests, 157
 - Microstructure, 101, 103, 123, 131–135, 152, 201, 223–225
- N**
- Necking, 227
 - Nickel-base alloys, 39, 76, 86, 106, 157, 199
- O**
- Oxidation, 106
- P**
- Plastic strain analysis, 11, 38, 69, 239
 - Plastic deformation, 86
 - Precipitation hardening, 170
- S**
- Shaft, turbine, 30
 - Silica glass, 55
 - Silicon nitride, 55
 - Specimens, test
 - Bar, 76, 217, 228
 - Notched, 76
 - Disk, 12, 87
 - Notched, 87
 - Rod, 56
 - Tube, 144, 160, 177, 202, 243
 - Notched, 144, 203
 - Wedge, 77, 109, 126
 - Steel, 86, 141, 170, 215, 229, 239
 - Strainrange partitioning, 239
 - Stress analysis, 10, 30, 69
 - Stress (or strain) concentration, 30, 50, 73, 76, 87
 - Substructures, 38
- T**
- Tantalum alloy, T-111, 76
 - Test methods
 - Fluidized bed, 10, 86, 106, 123
 - Quench, 55
 - Thermal-mechanical, 4, 141, 157, 170, 199, 214, 227, 239
 - Thermal (temperature) analysis, 10, 59, 88
 - Thermal stress, 3, 10, 30, 38, 55, 69, 86, 106
 - Turbines, 38
- V**
- Vacuum fatigue testing, 214

